Summer 2015

Flight Dynamics Nonlinearity Assessment Across a New Aerodynamic Attitude Flight Envelope

Ayman Muhammad Abdallah
Old Dominion University

FLIGHT DYNAMICS NONLINEARITY ASSESSMENT

ACROSS A NEW AERODYNAMIC ATTITUDE FLIGHT ENVELOPE

by

Ayman Muhammad Abdallah
B.S. December 2002, King Fahd University of Petroleum and Minerals, Saudi Arabia
M.S. May 2007, King Fahd University of Petroleum and Minerals, Saudi Arabia

A Dissertation Submitted to the Faculty of
Old Dominion University in Partial Fulfillment of the
Requirements for the Degree of

DOCTOR OF PHILOSOPHY

AEROSPACE ENGINEERING

OLD DOMINION UNIVERSITY

August 2015

Approved by:

_____
Brett Newman (Director)

_____
Thomas Alberts (Member)

_____
Duc Nguyen (Member)

ABSTRACT

FLIGHT DYNAMICS NONLINEARITY ASSESSMENT
ACROSS A NEW AERODYNAMIC ATTITUDE FLIGHT ENVELOPE

Ayman Muhammad Abdallah
Old Dominion University, 2015
Director: Dr. Brett Newman

A new asymmetric level aerodynamic attitude flight envelope is introduced in this dissertation. The aerodynamic attitude envelope is an angle of attack vs. sideslip angle region which describes the extent of where an aircraft can sustain a steady slipping horizontal flight condition. The new envelope is thus an extension of the more common speed-altitude symmetric level flight envelope. This new envelope can be used for design requirements, dynamic analysis, control synthesis, or performance comparison. Moreover, this envelope provides enhanced insight into trimability-controllability limitations within the aircraft design model. The aerodynamic attitude flight envelope is constructed for a six degree of freedom nonlinear simulation model of a high-performance aircraft. The constructed envelope is found to be asymmetric with respect to positive vs. negative sideslip values, due to the inherent asymmetry in the aerodynamic model database. Asymmetry and offset in the force and moment coefficient data could originate from experimental error, from model fabrication imperfections, from vortex-dominated flow, from data reduction flaws, or from other sources. The literature shows that vortex-dominated flow can cause significant side force, rolling moment, and yawing moment coefficient asymmetries. Details concerning the removal of asymmetry and offset in the aerodynamic data are given. The purpose behind removing the asymmetry and offset is to facilitate analysis of the new aerodynamic attitude flight envelope with an

ideal aircraft model so that fundamental relationships can be more easily observed, and to provide a comparison with the non-ideal case previously computed. Based on the adapted and symmetrized aerodynamic data, a new aerodynamic attitude asymmetric level flight envelope is constructed and introduced.

Further, the six degree of freedom aircraft simulation model is analyzed with nonlinear index theory across this nontraditional flight envelope. Aircraft dynamic properties often change in a nonlinear way across operating conditions. Nonlinear index theory provides a new concept for measuring the strength of these changes for a given set of coordinates and is applied to the asymmetric aerodynamic attitude envelope with the original and the adapted and symmetrized aerodynamic data. This analysis provides new methodology and new insights into aircraft dynamics and control. The index analysis exposes certain flight condition regions in which nonlinearity strength is high. These regions are further investigated with both linear and nonlinear simulations. Because the nonlinearity index is based on the matrix two-norm, the index can sometimes overestimate the nonlinear strength. To circumvent this behavior, indices based on system matrix partitions and normalized state formulations are explored. Nonlinearity is a function of the coordinates used to express the dynamic system. Therefore, the nonlinearity index is also applied to the aircraft model, expressed with three different frame of reference sets for kinetics and kinematics, in order to determine the best, or most linear, coordinates among the three investigated sets.

This thesis is dedicated to my little angels, Youssef and Tulip.

ACKNOWLEDGMENTS

I offer my deep appreciation to Professor Brett Newman, my advisor and dissertation committee chair, for his wise advice, insightful criticism, and patient encouragement. Professor Newman always seeks high quality products, and he challenges his students with creative and innovative ideas. The ideas in this dissertation originated with him, and I consider myself fortunate to have continued upon his suggestions. I owe him a debt of gratitude and thanks and I consider him my mentor during my Ph.D. flight. I will not forget his generosity and kindness for accepting and taking over the advising responsibilities following my previous advisor.

I extend many thanks to the valued dissertation committee members Professor Thomas Alberts and Professor Duc Nguyen for their patience, support, and flexibility, and for the precious time they gave me. It is not an exaggeration when I say that both professors are pioneers in their field of knowledge.

I would like to express my heartfelt thanks to my original advisor Professor Osama Kandil to whom I owe a lot during my early Ph.D. stage. Due to his unforeseen health setback and sudden retirement, the reputable Old Dominion University has lost a genuine and exceptional educator.

I am sincerely thankful to my inspiration in the Aerospace Engineering field, Professor Ahmed Al-Garni. This wonderful professional walked with me, held my hands, and supported me throughout my B.S. and M.S. degrees, and offered moral support during my Ph.D. degree.

I also offer special thanks to King Fahd University of Petroleum and Minerals, my home as both a student and a teacher. Also, my thanks go to the Embassy of Saudi Arabia, represented by the Saudi Arabian Cultural Mission to the United States of America.

I would also like to thank my dear friends, Dr. Ashraf Omran, Faisal Ashour, and El Mehdi Oussir, for their encouragement, support, and friendship.

I am extremely thankful to my wife, Enas Alsisi, and her wonderfully supportive parents, Dr. Ali Alsisi and Mrs. Sahar Jokhadar, whom I regard as my second parents.

Finally, I would like to express a genuine gratitude to my wonderful parents, Engineer Muhammad Abdul-Sattar Khalil and Mrs. Nagma Ahmed, and my siblings Amani, Eman, Ahmed, Ammar, Abrar, and Ebtihaj; without their moral support and prayers I would not have achieved my accomplishments thus far.

NOMENCLATURE

A, B, C, D	State, input, output, and feedforward matrices
$C_{\prime\prime_T}$	Total aerodynamic force and moments coefficients, where $\prime\prime$ denotes x_b, y_b, z_b, l, m, and n
$C_{a/b}$	Transformation matrix (directional cosine) from frame of reference b to frame of reference a
$\bar{c}, \bar{b}$	Wing mean aerodynamic chord and wing span
cg	Center of gravity
D_a	Center of gravity location cross-product matrix
$\mathbf{f}$	Generic function vector
$F_{\prime\prime}$	Force component, including aerodynamic, propulsive, and gravitational, where $\prime\prime$ denotes arbitrary, body-, stability-, or wind-frame of references
$\mathbf{F}_{\prime\prime}$	Total external force vector, including aerodynamic, propulsive, and gravitational, where $\prime\prime$ denotes arbitrary, body-, stability-, or wind-frame of references
g	Acceleration due to gravity
$\mathbf{g}$	Acceleration due to gravity vector, generic function vector
H	Altitude
$\mathbf{H}, \dot{\mathbf{H}}$	Angular momentum and rate of change of angular momentum vectors
I_{xx}, I_{yy}, I_{zz}	Aircraft mass moments of inertia in x, y, and z axes
I_{xy}, I_{yz}, I_{xz}	Aircraft product of inertia about x, y, and z axes
J	Aircraft mass moments of inertia matrix
L, M, N	Total aerodynamic rolling, pitching and yawing moments
M	Mach number

$\mathbf{M}_{''}$	Total external moment vector, including aerodynamic, propulsive, and gravitational, where $''$ denotes arbitrary, body-, stability-, or wind-frame of references
m	Airplane mass
p, q, r	Airplane roll, pitch, and yaw rates
$\bar{q}$	Free-stream dynamic pressure
S	Reference area
t	Time
T	Total instantaneous engine thrust
u, v, w	Velocity components in x, y, and z axes
$\mathbf{v}$	Aircraft velocity vector
V_T	Aircraft total velocity
V_a	Translational velocity cross-product matrix
$\mathbf{x}_0$	Reference state vector
$\delta\mathbf{x}_0$	Bounded deviation vector about reference state
$\mathbf{x}, \mathbf{y}, \mathbf{u}$	State, output, and input vectors
X, Y, Z	Inertial position components
$\dot{X}, \dot{Y}, \dot{Z}$	Inertial velocity components
$x_a y_a z_a$	Arbitrary-frame of reference
$x_b y_b z_b$	Body-frame of reference
$x_s y_s z_s$	Stability-frame of reference
$x_w y_w z_w$	Wind-frame of reference
$X_I Y_I Z_I$	Inertial-frame of reference
α, β	Attack and sideslip angles

χ, γ, σ	Heading, flight-path, and aerodynamic bank angles
$\delta_h, \delta_a, \delta_r$	Horizontal stabilizer, aileron, and rudder control surface deflections
$\delta_{lef}, \delta_{sb}$	Leading-edge-flap and speed-brake control surface deflections
δ_{th}	Throttle deflection
ν	Nonlinearity index
$\boldsymbol{\lambda}$	Varying parameter vector
$\boldsymbol{\rho}$	Center of gravity location vector in the body axis
$\boldsymbol{\omega}$	Angular velocity vector
Ω	Angular velocity cross-product matrix
ϕ, θ, ψ	Roll, pitch, and yaw Euler angles
Φ	Transition matrix
$\Delta_x, \Delta_y, \Delta_z$	Center of gravity location vector in x, y, and z body axes

TABLE OF CONTENTS

Page

LIST OF TABLES

LIST OF FIGURES

CHAPTER 1

RESEARCH DESCRIPTION

1.1 Motivation

The operational range or "flight envelope" for an aircraft is a locus of speed-altitude pairs in which the aircraft is designed in order to sustain symmetric level steady flight. Figure 1.1 shows the typical flight envelope for a fighter aircraft in terms of Mach number vs. altitude. This envelope depicts all of the possible bounding elements of many classes of aircraft. The inner boundary of the envelope is determined by several factors or limits. At the low-speed region, the envelope is bounded by the maximum lift coefficient, which is limited by stall. The highest altitude, or absolute ceiling, is determined by the aircraft's maximum operating thrust. At this flight condition, the aircraft encounters high-drag, due to either a high lift coefficient or a high flight velocity. At the service ceiling, Federal Aviation Regulations, or FARs, require a small rate of climb capability for propeller and jet aircrafts. The usable ceiling, as shown in Figure 1.1, is limited by the pilot ejection survivability. The engine limit presents a safe engine operation, wherein enough air is available to restart the engine, for example, at low-speed and high-altitude. Several structural limits bound the envelope at high-speeds, such as dynamic pressure, duct pressure, and temperature. The external flow dynamic pressure ($\bar{q}$) limit is a design requirement for stress analysis that specifies the structural loads or flutter. The $\bar{q}$ limit varies from 1800 to 2200 psf for fighter aircrafts. The maximum airload pressure inside the inlet duct is accounted for, since it may easily triple the outside dynamic pressure, while the skin aerodynamic heating for structural materials determines the temperature

limit. This envelope is used for design requirement specification and satisfaction, for dynamic analysis over differing flight phases, for control synthesis using scheduling principles, or for comparison of capabilities of different airframes. However, the speed-altitude flight envelope is limited to rectilinear symmetric level flight conditions and does not account for asymmetric flight conditions or provide details on the aircraft control limits in asymmetric flight [1],[2].

The aerodynamic and propulsion characteristics of actual aircraft or of sophisticated theoretical models of aircraft change with altitude and speed across the flight envelope. Principally, the aerodynamic and propulsion characteristics change with the angle of attack and the sideslip angle. The dynamic interaction between the aircraft's inherent design characteristics such as aerodynamics and propulsion, and the externally encountered effects such as pilot input and atmospheric influence may identify a number of nonlinear behavior responses [3]. Many of the unforeseen nonlinear phenomena during the early flight history in the last century caused critical incidents and were even fatal, in some situations. Airframe design and the maneuvering nature play an important role in establishing various dynamic behaviors. This importance comes from the longitudinal-lateral dynamics cross coupling that results from the inertial asymmetry and nonlinearities in the aerodynamics.

Stall dynamics play a critical role in aircraft motion and establish many performance and safety elements. Stalling is a body configuration dependent effect that occurs when the aircraft is flying near the maximum lift coefficient C_L and the air flow is on the verge of detachment from the upper (leeward) surface of the wing. In most cases, stall corresponds to a minimum flight speed and a high angle of attack (α) flight

condition, since most fighter maneuvers occur at high α. Due to the complex air flow patterns at high α, unsteady aerodynamic effects can occur as α increases and enters the prestall, stall, poststall, and superstall regions (see Table 1.1). Such variational effects include unsteady buffeting forces, wing drop, a pitch-up moment effect due to downwash, loss of directional stability, and adverse yaw response to control. Further, variations in the angle of attack strongly affect aerodynamic damping, for instance, as α increases, the pitch and yaw damping effects increase, whereas the roll damping decreases and changes sign in the stall region. Nonlinear aerodynamics at stall complicate the control surface behavior in which their effects diminish or become adverse. At high α, it is possible to lose the aileron effectiveness and produce significant adverse yaw departure motion, leading to the roll-reversal phenomenon. Situations such as a high angle of attack and/or a high sideslip angle (β) complicate the prediction and increase the nonlinearities of the aerodynamics.

Pitch-up is a phenomenon that increases the angle of attack due to an inertially induced pitch-up moment that is caused by stability-axis roll. This phenomenon is sometimes defined as the dumbbell effect. In heavy fuselage aircraft such as modern fighters where $I_{zz} > I_{xx}$, the inertial effect produces positive pitching acceleration and, hence, an increase in α. In this situation, aerodynamic controls could be used to counteract the angle of attack increase. Pitch-up to high α is required in the poststall maneuver; however, control surface effectiveness is also reduced, due to the immersion in the low-energy stalled air flow. Steady-state spin can develop from the inherent autorotation tendency of both unswept wings at $\alpha > \alpha_{\text{stall}}$ and the fuselage depending on its cross-sectional shape. This type of aircraft, usually propeller-driven, experiences an

asymmetric stall due to the autorotation tendency, in which one wing stalls before the other. In general, asymmetric stall, rapid maneuvering, external disturbances, failure of control system, or pilot fault can produce a nose departure. This departure involves pitch, yaw, or roll divergence, probably leading to a fully developed spin, due to high-acceleration. Different aircraft or even the same aircraft spin differently as the nonlinear aerodynamics of the spinning aircraft behave unexpectedly when the flow separates from the wing and tail. Also, the balance between the inertial and the aerodynamic moments is fundamental to the establishment of spin mode behavior. An important point to indicate is that departure and spin are related topics, but they are totally different phenomena. Departure is considered to be a transient occurrence, whereas spin is a quasi-steady condition.

The aerodynamic wing rock mode describes the aircraft dynamic response at high α as self-sustained oscillation about the longitudinal roll-axis. This phenomenon is observed when the aircraft is operating near stall or stall-departure and is explained as the influence of different factors, such as sideslip angle β, roll motion, and vortex shedding on the aircraft nonlinear aerodynamics. However, this occurrence can be suppressed and properly stabilized. The nonlinear oscillatory wing rock motion can be viewed as a limit cycle with constant motion amplitude. In a high-performance aircraft, if the aircraft is harshly roll induced at high-speed flight, the inertia of the asymmetric concentrated fuselage mass distribution overpowers the aerodynamic stabilizing forces, resulting in intense pitch and yaw motion and control loss, dominated by three-dimensional rotation. This longitudinal-lateral coupling is called inertial cross coupling in which the roll mass moment of inertia I_{xx} is significantly smaller than pitch inertia I_{yy} and yaw inertia I_{zz}.

Most of the prescribed nonlinear phenomena are comprehended by extensive experimental research, in-flight test, and/or fortuitous discovery. However, it is demanding to attempt to systematically detect hidden or unknown conditions that are difficult to quantify where the system can experience extreme nonlinear phenomena [4]-[7].

The previous discussion underscores the need for 1) new envelope approaches to address design and analysis focus associated with asymmetric flight conditions, and 2) new identification approaches to expose and quantify aircraft nonlinear behavior across its operational regime. This dissertation investigates flight dynamics nonlinearity assessment across a new aerodynamic attitude flight envelope.

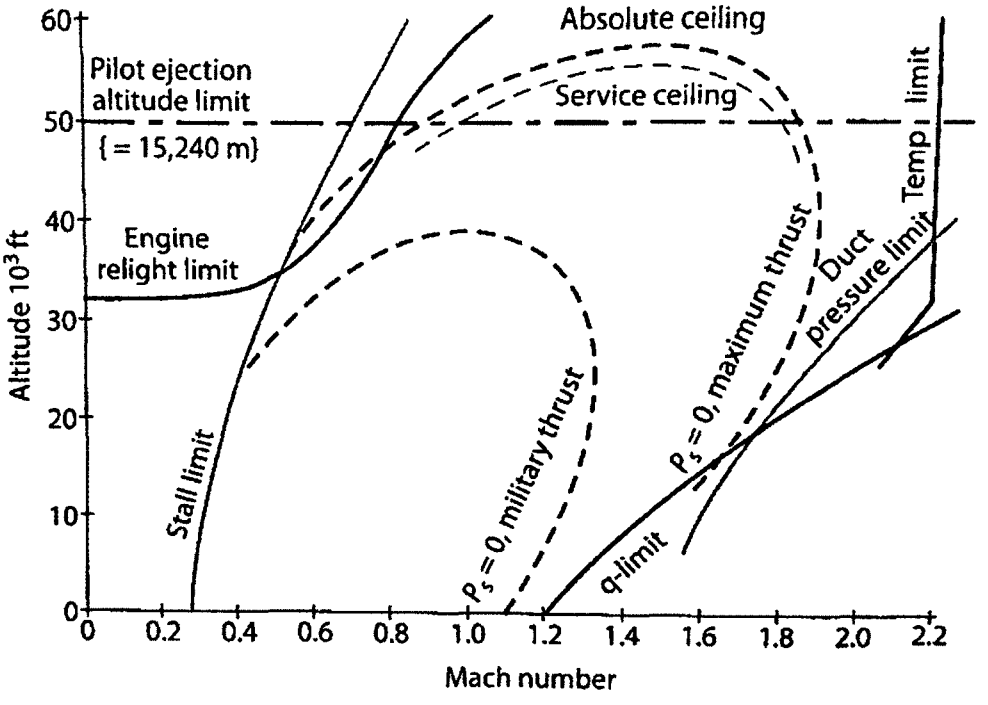

Figure 1.1 Flight envelope [2]

Table 1.1 Typical flight regimes for various aircraft* [4]

Aerodynamic Region	Angle-of-Attack Range (deg)	Possible Flight Attributes
Low Angle of Attack	0–15 (GA, F) 0–10 (JT)	Conventional flight
Prestall	15–20 (GA) 10–15 (JT) 15–25 (F)	Unsteady effects (buffet, wing drop, wing rock)
Stall, Stall Break	20–30 (GA) 15–25 (JT) 25–35 (F)	First lift peak, loss of lift, porpoising, loss of longitudinal and directional stability, adverse yaw
Poststall	30–40 (GA) 25–40 (JT) 35–50 (F)	Departure, post-stall gyrations, incipient spin
Superstall	40–90 (GA, JT) 50–90 (F)	Second lift peak, deep stall, spin, supermaneuverability

*General Aviation (GA), Jet Transport (JT) and Fighter (F)

1.2 Literature Review

The operational range of the aircraft and the various nonlinear aircraft behaviors have been reviewed in the previous section. In this dissertation, the literature review will focus on the speed-altitude flight envelope, selected nonlinear aircraft behavior, and system nonlinearity quantification.

1.2.1 Speed-Altitude Flight Envelope

Several available standard textbooks serve the purpose of estimating the extent of the speed-altitude flight envelope. However, Filippone [1] and Raymer [2] explored the envelope concept in depth. These references elaborately covered all of the physical and mathematical aspects that help in the development of the full-envelope; further, they extensively discussed details concerning envelope limiting boundaries. Departure from the designated flight envelope compromises aircraft safety and causes loss of control. In

the event of anomalous situations, the authors in Reference [8] reported their qualitative and quantitative investigations of flight damage effect on the flight envelope. Moreover, a real-time flight envelope was estimated for a general aerodynamic model that accounts for control and stability surface damages. Richardson et al. [9] presented the probability of an aircraft departure from its flight envelope under the influence of gusts, damage risk, or control loss. Assured techniques were developed to maintain a steady-state flight condition under the action of stochastic wind gusts. The flight envelope for an air-breathing hypersonic vehicle was developed in which requirements of complex coupled balancing is satisfied [10]. Fialho et al. [11] presented a smooth fractional α gain-scheduled controller for the lateral-directional axes of the F-14 aircraft. The linear controller was designed for a powered approach flight phase that accounts for varying α and airspeed. A state-space Youla parameterization interpolation procedure was presented in Reference [12] to develop a locally stabilizing gain-scheduled controller for each operating point of a nonlinear plant. This interpolation method was used to design a gain-scheduled autopilot and was successfully implemented on a pitch-axis missile.

1.2.2 Nonlinear Aircraft Behavior

Examples of various aircraft nonlinear behaviors are mentioned in Section 1.1; those nonlinear behaviors are considered thoroughly in some leading aerospace engineering books and in technical reports published by governmental, academic, and professional organizations [4]-[7]. A few examples, but not all, of nonlinear phenomena are stall, spin, pitch-up, nose slice/departure, shock waves, vortex shedding, engine unstart, fan stall, wing rock, falling leaf, control reversal, and inertial coupling. Kwatny et

al. [13] investigated the nonlinear influences of stall and aircraft dynamics that lead to a loss of control. Various methods of analysis [14], aerodynamic models [15],[16], and nonlinear simulations [17] for investigating the dynamic stall motion are available in the literature. Experimental research [18] has shown that poststall spin has evolved toward partial chaotic motion under an increased high Reynolds number. The development of self-induced oscillations with steady-state roll amplitude "wing rock" and vortex breakdown was experimentally observed by Arena and Nelson [19]. Roll coupling, or the so-called inertial coupling [20], between the lateral and longitudinal-directional motion may cause a jump phenomenon [20] which is an abrupt change from a stability state to a large roll rate and large sideslip state. The jump can be prevented [21] by the proper aileron-rudder interconnect relationship.

1.2.3 System Nonlinearity Quantification

Yana et al. [22] introduced a scale measure and an estimate for the nonlinearity degree of the system between 0 and 1. This scale was based on the input and output time-series signals with included additive observational noise. However, in order to represent different classes of nonlinear functions, a parametrized function "multiplier perceptron" was introduced into the estimation. The degree of nonlinearity of the system approaches 1 when the system cannot be represented by linear representation. Another nonlinearity measuring scale referred as a "nonlinearity index" was discussed by Junkins and Singla [23]. Static/algebraic forms of the nonlinearity index were initially proposed. The nonlinearity index of a linear system is zero, which forms the lowest reference point of the scale. The nonlinearity index is applied to numerous orbital mechanics test cases in

order to provide a rigorous standard for measuring the system's nonlinearity. In the same reference, the nonlinearity index across four different attitude kinematic representations was investigated, and the results indicated that an Euler angle representation has the highest nonlinearity. The four attitude kinematic representations are the Euler angle representation, the classical Rodrigues parameter representation, the modified Rodrigues parameter representation, and the quaternion representation. The degree of nonlinearity of the modified Rodrigues parameter and the quaternion formulations was the same, but it was less than the classical Rodrigues parameter representation. The nonlinearity index showed its usefulness in coordinate selection [24], where it was able to detect the less-nonlinear or near-linear representation. Only coordinate systems resulting in singular nonlinear ordinary differential equations, and coordinates leading to regularized state-space dynamics over very large domains, were reviewed. Results showed it is more advantageous when angular velocity is represented by orthogonal components along axes fixed on a moving N-dimensional rigid body, to realize rigid body classical dynamics cases for general Lagrangian dynamics. Transforming into a quasi-coordinate representation for the velocity along rotating axes of the same rigid body via the Cayley transformation improved the linearity of the dynamical system. The nonlinearity index provides an accurate indication of system nonlinearity strength, since the simulation error between the linear and nonlinear models correlates well with the index results.

The dynamical system nonlinearity index of the Cayley form [25] for an elastic spherical pendulum and a planar satellite example were investigated, based on evaluating the initial condition sensitivity of the state-transition matrix. The Cayley form is a representation for physical systems, in which the dynamical systems were described

using the kinematics and dynamic equations of N-dimensional rotations. Results showed that the Cayley form exhibited lower nonlinearity when compared to traditional representations, particularly those representations with kinematic singularities. Again, the nonlinearity strength of dynamical systems is extended to estimation systems to both a measurement model and a dynamical model in Reference [26]. The nonlinearity measure result showed its practicality in the development of estimation applications for various physical systems.

The abstract development and practical implementation of the nonlinearity index in References [23],[24] has been restricted to initial value problems only, which are well-suited for orbital mechanics and for space vehicle attitude dynamics natural motion. Following Reference [23], the nonlinearity index theory was generalized by Omran and Newman [27] to aircraft flight mechanics analysis, which is the source for the work presented herein. The nonlinearity index theory was generalized by developing four expressions that account for input excitation and parameterized models. Four additional dynamic indices were also developed. The index was applied to a low-order pitch-plunge motion model and showed that it can detect conditions where the system can experience extreme nonlinear phenomena such as limit cycles. The study also investigated the nonlinearity strength of F-16 and T-38 model dynamics over the entire flight envelope, and showed that the F-16 model exhibits double the nonlinearity of the T-38 model. Further, the results indicated that the indices are higher near the low-speed side of the flight envelope. The nonlinearity strength of the T-2C naval trainer aircraft model undergoing stall was investigated in [28]. The results of nonlinearity index theory when applied to the nonlinear pitch-plunge model exposed behavior, such as limit cycling,

which was unobserved by traditional approaches. Further, the nonlinear strength using the F-18 HARV aircraft model was analyzed [29]. Due to a highly nonlinear aerodynamic model of that aircraft, hidden nonlinear phenomena such as chaos and non-repeating quasi-periodic motion were discovered. The theory was able to detect the source of the nonlinearity as the rolling moment derivative with respect to roll rate, C_{l_p}. This coefficient was found to cause an instability in the system.

1.3 Statement and Objectives

The concept of the asymmetric level aerodynamic attitude envelope was initially proposed as a project by Professor Brett Newman at Old Dominion University in his "Atmospheric Flight Dynamics and Control" graduate level course. The goal was to produce an asymmetric level rectilinear flight envelope at different altitudes for the high-performance aircraft model presented in Reference [30]. The nonlinearity index theory [23], which was introduced in 2004, is considered to be a fairly new research subject in the nonlinear dynamical system field. Moreover, this subject has not been investigated extensively by various engineering applications. From that point, along with the non-existence literature on the asymmetric angle of attack vs. sideslip angle flight envelope and the very limited work found on the nonlinearity index theory in the literature, the idea of investigating the nonlinearity index across this flight envelope potentially grew as a dissertation subject.

The dissertation focuses on three main problems concerning 1) extension to a new asymmetric aerodynamic flight envelope, 2) application of the nonlinearity index theory to this new envelope, and 3) linear-nonlinear simulation comparisons. First pertaining to

extension to a new asymmetric aerodynamic flight envelope, the contribution of the study will focus on establishing a methodology to develop the angle of attack vs. sideslip angle envelope using the original aerodynamic model in Reference [30]. This envelope describes the extent of where the airplane can sustain a slipping horizontal flight condition. Fundamentally, this envelope can describe the asymmetric trimability, control power authority, and poststall domain of an aircraft, and thus it can be utilized in similar ways to the traditional flight envelope. Asymmetry and offset issues in the force and moment aerodynamic coefficients will be analyzed and solutions will be provided, in terms of an idealized aerodynamic model. Finally, the envelope will be redeveloped with the ideal aerodynamic model. Second pertaining to the application of the nonlinearity index theory, the primary goal is to investigate the nonlinearity strength of the aircraft model across both the original and the idealized aerodynamic attitude envelopes. Additionally, the nonlinearity index will be also applied to the aircraft kinetics and kinematics model expressed by three different coordinate sets in order to determine the most linear set. Last, indices based on system matrix partitions and normalized state formulations will be explored. The nonlinearity index analysis exposes certain flight condition regions in the envelope, where nonlinearity strength is high. Therefore, the main goal of the third problem pertaining to linear-nonlinear simulation comparisons is to explore regions with high nonlinear index values. The linear-nonlinear simulation will consist of initial condition excitation and control input excitation.

1.4 Dissertation Outline

The dissertation is outlined as follows. Chapter 2 presents a review of topics on the dynamics of atmospheric flight. In this chapter, all mathematical models for the aircraft dynamics are developed. Chapter 3 provides the mathematical foundation of static and dynamic nonlinearity index theory and extends the theory to generalized input excitation and parameterized aerodynamic attitude flight envelope settings. In Chapter 4, the development of the nontraditional angle of attack vs. sideslip angle flight envelope is discussed thoroughly. Numerical results with the high-fidelity F-16 aircraft model used in the study are also presented here. This chapter addresses and provides a solution to the asymmetries in the aircraft aerodynamic model. Chapter 5 implements nonlinearity indices on the aerodynamic attitude flight envelopes and compares the indices for different frames of reference representations. The linear system sub-blocks, sub-indices, and matrix-index are introduced here. In Chapter 6, linear and nonlinear simulation cases are performed in the regions of high nonlinearity index and the results are examined. Finally, overall conclusions and recommendations for future work are drawn in Chapter 7.

CHAPTER 2

DYNAMICS OF AIRCRAFT MOTION

2.1 Introduction

A rigid aircraft body experiences motion in three dimensions. These motions are described as six degrees of freedom (6-DOF) motions; three translational degrees describes the trajectory and three rotational degrees describes the orientation of the aircraft. The motion of the aircraft can be well described by Newton's laws of motion derived in a body referenced frame or coordinate system. In flight dynamics, there are basically three categories of reference frames that must be considered: inertial, aircraft-fixed, and aircraft-carried frames. In this dissertation, all three categories of reference frames are discussed. The choice of frame of reference depends on the classes of the problems or on the assumptions made. Further, it is important to establish a systematic means of transforming the motion components from one frame of reference to another.

In deriving the equations of motion of an aircraft, several assumption are made, such as non-rotating flat Earth, rigid body airframe, no actuator dynamics, and constant mass vehicle. The flat Earth assumption is equivalent to assuming that the Earth is an inertial-frame. The derivation of the equations of motion starts with Newton's laws of motion being applied to a system of particles bounding the rigid body aircraft. Six governing kinetic equations exist for three translational velocities (u,v,w) and three angular velocities (p,q,r). Six governing kinematic equations also exist for three translational positions (X,Y,Z) and three Euler angles (ϕ,θ,ψ).

2.2 Frames of Reference

The aerodynamic forces and moments acting on the aircraft are a function of the aircraft orientation relative to the air flow instantaneous velocity vector (**v**). Therefore, two aerodynamic orientation angles are necessary to specify these forces and moments with respect to **v**. Furthermore, these two angles are the baseline in defining two important special aircraft-carried frames of reference, namely, the stability-frame and the wind-frame. The aerodynamic angles are the angle of attack (α) and the sideslip angle (β) and they are shown in Figure 2.1. The two angles can be defined in terms of the body translational velocities u_b, v_b, w_b as

$$\alpha = \tan^{-1}\frac{w_b}{u_b} \tag{2.1}$$

and

$$\beta = \sin^{-1}\frac{v_b}{V_T} \tag{2.2}$$

where $V_T = \sqrt{u_b^2 + v_b^2 + w_b^2}$.

2.2.1 Inertial-Frame of Reference

An inertial-frame of reference is a frame that describes both time and space and could be moving in a constant rectilinear motion with respect to another inertial-frame. In other words, a frame of reference is inertial if it is experiencing neither rectilinear acceleration nor rotation. This frame of reference is particularly important when dealing with Newton's laws of motion. Aircraft motions are only observed and derived in the inertial-frame. Depending on the flight dynamics problems addressed and the validity of the assumptions made, there are different frames that are assumed to be inertial. For

example, in the analysis of atmospheric flight dynamics vehicles, the accelerations associated with the Earth's rotation around its axis, in addition to the Earth's orbital motion in the solar system, are comparatively small to those resulting on the aircraft. Then, an Earth fixed point can be sufficiently considered to be an accurate inertial-frame of reference. The axes of this frame of reference, as well as the rest of the other frames discussed later, are mutually orthogonal. In general, the axes of the inertial-frame are oriented north, east, and downward to the geometric or mass center of the Earth [31]-[34]. The frame $X_I Y_I Z_I$ in Figure 2.1 is an inertial-frame of reference and is used to track the motion of the aircraft.

2.2.2 Body-Frame of Reference

This type of frame is a noninertial-frame; it is an aircraft-fixed frame and it moves and rotates with the aircraft in a well-defined manner. This frame can be fixed arbitrarily on the aircraft or, as in most of the flight dynamics analysis, it is attached at the center of gravity (cg) of the aircraft. Figure 2.1 shows the body-frame of reference $x_b y_b z_b$ located at the aircraft's center of gravity. The body-frame x_b-axis is aligned with the aircraft fuselage reference line. The y_b-axis is directed along the right wing and the z_b-axis is directed downwards. This frame serves the purpose of defining an aircraft's positions and velocities and is commonly used in aircraft nonlinear simulations. Another example of a body-frame at an arbitrary point a that is not necessarily referenced at the cg of the aircraft is shown in Figure 2.2 and is denoted by $x_a y_a z_a$.

2.2.3 Stability-Frame of Reference

This frame is a special noninertial-frame that is aircraft-carried; it moves with the aircraft but can rotate relative to the aircraft. Usually, this frame is selected for perturbation analysis, in order to simplify the expressions for the aerodynamic forces and moments [33],[34]. This frame is commonly associated with a specific reference flight condition. For example, in steady level flight as a reference flight condition, the stability axes are associated with the reference free-stream velocity vector. The stability-frame of reference $x_s y_s z_s$ is shown in Figure 2.1. The origin of this frame is fixed at the aircraft cg. The stability-frame is established when the body-frame $x_b y_b z_b$ is rotated by the aerodynamic angle of attack α through the negative body y_b-axis. The stability x_s-axis, z_s-axis and the angle of attack α lie in the body $x_b z_b$ plane. The y_s-axis is directed along the right wing.

2.2.4 Wind-Frame of Reference

The wind-frame of reference is also designated as a special aircraft-carried frame, rather than aircraft-fixed, like the body-frame of reference. If the stability-frame of reference is rotated by the aerodynamic sideslip angle β through the stability z_s-axis, a new frame of reference is formed. This frame is called the wind-frame of reference $x_w y_w z_w$ and is shown in Figure 2.1. The wind x_w-axis and the sideslip angle β lie in the stability $x_s y_s$ plane. Further, the wind x_w-axis is always aligned with the aircraft instantaneous velocity vector $\mathbf{v}$. The velocity vector $\mathbf{v}$ is always defined by the aerodynamic angles α and β relative to the body x_b-axis. The y_w-axis is directed along the right wing and the z_w-axis lies in the $x_b z_b$ or $x_s z_s$ plane. The equations of motion

which are derived in the wind-frame are particularly suitable in trajectory or performance analysis and optimization. The wind-frame set of equations is sometimes referred to as the point-mass equations of motion because they govern the three translational, but not the three rotational, degrees of freedom.

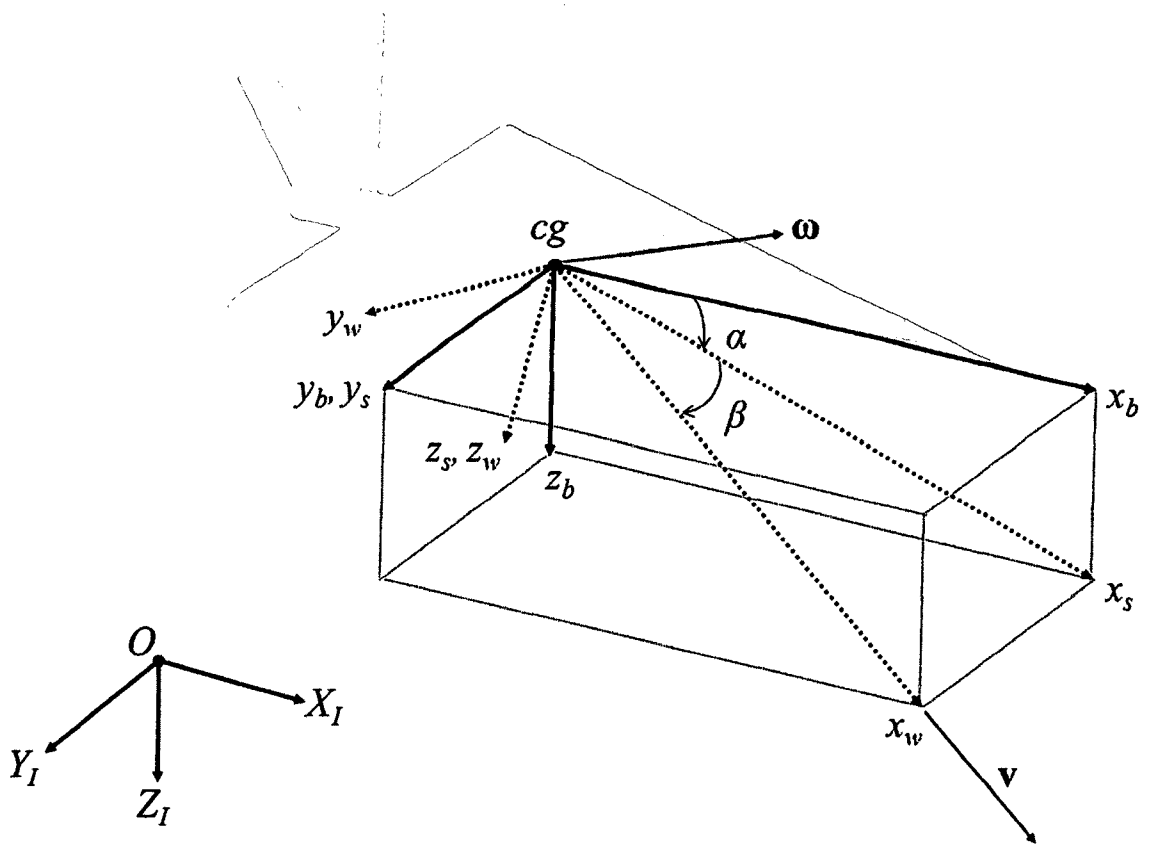

Figure 2.1 Definitions of axes and aerodynamic angles

2.3 Frames of Reference Transformation

2.3.1 Body-Stability-Wind Frame Relationships

Based on the frames of reference described earlier and Figure 2.1, the transformation matrix from body- to stability-frame is

$$C_{s/b} = \begin{bmatrix} \cos\alpha & 0 & \sin\alpha \\ 0 & 1 & 0 \\ -\sin\alpha & 0 & \cos\alpha \end{bmatrix} \tag{2.3}$$

Similarly, the transformation matrix from stability- to wind-frame is

$$C_{w/s} = \begin{bmatrix} \cos\beta & \sin\beta & 0 \\ -\sin\beta & \cos\beta & 0 \\ 0 & 0 & 1 \end{bmatrix} \tag{2.4}$$

Therefore, the transformation matrix from body- to wind-frame becomes

$$C_{w/b} = C_{w/s}C_{s/b} = \begin{bmatrix} \cos\alpha\cos\beta & \sin\beta & \sin\alpha\cos\beta \\ -\cos\alpha\sin\beta & \cos\beta & -\sin\alpha\sin\beta \\ -\sin\alpha & 0 & \cos\alpha \end{bmatrix} \tag{2.5}$$

These transformation matrices are orthogonal, and hence, the wind- to body-frame transformation matrix is simply the transpose of the body- to wind-frame matrix in Equation (2.5).

$$C_{b/w} = C_{w/b}^{T} = \begin{bmatrix} \cos\alpha\cos\beta & -\cos\alpha\sin\beta & -\sin\alpha \\ \sin\beta & \cos\beta & 0 \\ \sin\alpha\cos\beta & -\sin\alpha\sin\beta & \cos\alpha \end{bmatrix} \tag{2.6}$$

2.3.2 Inertial-Body Frame Relationships

The relationship between an inertial-frame of reference fixed on the Earth's surface and a body-frame of reference fixed on an aircraft body is established by a sequence of planar rotations. The common Euler 3-2-1 rotations describe vehicle orientation by the z_b, y_b, x_b rotation sequence, respectively, which transforms the inertial-frame into the body-frame. The rotation sequence is indicated below.

1. Positive yaw (ψ_b), that is right-hand rotation about the z_b-axis.
2. Positive pitch (θ_b), that is right-hand rotation about the y_b-axis.
3. Positive roll (ϕ_b), that is right-hand rotation about the x_b-axis.

Following the established rules, the transformation matrix from inertial- to body-frame is

$$C_{b/I} = \begin{bmatrix} 1 & 0 & 0 \\ 0 & \cos\phi_b & \sin\phi_b \\ 0 & -\sin\phi_b & \cos\phi_b \end{bmatrix} \begin{bmatrix} \cos\theta_b & 0 & -\sin\theta_b \\ 0 & 1 & 0 \\ \sin\theta_b & 0 & \cos\theta_b \end{bmatrix} \begin{bmatrix} \cos\psi_b & \sin\psi_b & 0 \\ -\sin\psi_b & \cos\psi_b & 0 \\ 0 & 0 & 1 \end{bmatrix} \quad (2.7)$$

Carrying out the multiplications, the final result is

$$C_{b/I} =$$

$$\begin{bmatrix} \cos\theta_b \cos\psi_b & \cos\theta_b \sin\psi_b & -\sin\theta_b \\ -\cos\phi_b \sin\psi_b + \sin\phi_b \sin\theta_b \cos\psi_b & \cos\phi_b \cos\psi_b + \sin\phi_b \sin\theta_b \sin\psi_b & \sin\phi_b \cos\theta_b \\ \sin\phi_b \sin\psi_b + \cos\phi_b \sin\theta_b \cos\psi_b & -\sin\phi_b \cos\psi_b + \cos\phi_b \sin\theta_b \sin\psi_b & \cos\phi_b \cos\theta_b \end{bmatrix} \quad (2.8)$$

This transformation matrix is orthogonal, hence, the body- to inertial-frame transformation matrix is simply the transpose of the inertial- to body-frame matrix.

$$C_{I/b} = C_{b/I}^T =$$

$$\begin{bmatrix} \cos\theta_b \cos\psi_b & -\cos\phi_b \sin\psi_b + \sin\phi_b \sin\theta_b \cos\psi_b & \sin\phi_b \sin\psi_b + \cos\phi_b \sin\theta_b \cos\psi_b \\ \cos\theta_b \sin\psi_b & \cos\phi_b \cos\psi_b + \sin\phi_b \sin\theta_b \sin\psi_b & -\sin\phi_b \cos\psi_b + \cos\phi_b \sin\theta_b \sin\psi_b \\ -\sin\theta_b & \sin\phi_b \cos\theta_b & \cos\phi_b \cos\theta_b \end{bmatrix} \quad (2.9)$$

2.3.3 Inertial-Stability Frame Relationships

Similar to the common body-frame Euler 3-2-1 rotations, three additional rotations are defined when transforming from the inertial- to stability-frame. The three rotation sequences are given below.

1. Positive yaw (ψ_s), that is right-hand rotation about the z_s-axis.
2. Positive pitch (θ_s), that is right-hand rotation about the y_s-axis.
3. Positive roll (ϕ_s), that is right-hand rotation about the x_s-axis.

By following the established rules, the transformation matrix from inertial- to stability-frame is constructed directly as

$$C_{s/I} = \begin{bmatrix} \cos\theta_s \cos\psi_s & \cos\theta_s \sin\psi_s & -\sin\theta_s \\ -\cos\phi_s \sin\psi_s + \sin\phi_s \sin\theta_s \cos\psi_s & \cos\phi_s \cos\psi_s + \sin\phi_s \sin\theta_s \sin\psi_s & \sin\phi_s \cos\theta_s \\ \sin\phi_s \sin\psi_s + \cos\phi_s \sin\theta_s \cos\psi_s & -\sin\phi_s \cos\psi_s + \cos\phi_s \sin\theta_s \sin\psi_s & \cos\phi_s \cos\theta_s \end{bmatrix} \tag{2.10}$$

By taking advantage of previous results, the transformation from the inertial- to stability-frame can be indirectly constructed without angles ϕ_s, θ_s, ψ_s using Equations (2.3) and (2.8) as follows.

$$C_{s/I} = C_{s/b}C_{b/I} = \begin{bmatrix} C_{s/I}(1,1) & C_{s/I}(1,2) & C_{s/I}(1,3) \\ C_{s/I}(2,1) & C_{s/I}(2,2) & C_{s/I}(2,3) \\ C_{s/I}(3,1) & C_{s/I}(3,2) & C_{s/I}(3,3) \end{bmatrix} \tag{2.11}$$

Now, equating Equations (2.10) and (2.11), the stability-frame Euler angles are easily found as

$$\begin{aligned} \phi_s &= \tan^{-1}\left(\frac{C_{s/I}(2,3)}{C_{s/I}(3,3)}\right) \\ \theta_s &= -\sin^{-1}\left(C_{s/I}(1,3)\right) \\ \psi_s &= \tan^{-1}\left(\frac{C_{s/I}(1,2)}{C_{s/I}(1,1)}\right) \end{aligned} \tag{2.12}$$

2.3.4 Inertial-Wind Frame Relationships

Again, similar to the common body-frame Euler 3-2-1 rotations, three additional rotations are defined when transforming from the inertial- to wind-frame. The three rotation sequences are given below.

1. Positive yaw (ψ_w), that is right-hand rotation about the z_w-axis.
2. Positive pitch (θ_w), that is right-hand rotation about the y_w-axis.

3. Positive roll (ϕ_w), that is right-hand rotation about the x_w-axis.

Following the established rules, the transformation matrix from the inertial- to wind-frame is generated directly as

$$C_{w/I} = \begin{bmatrix} \cos\theta_w \cos\psi_w & \cos\theta_w \sin\psi_w & -\sin\theta_w \\ -\cos\phi_w \sin\psi_w + \sin\phi_w \sin\theta_w \cos\psi_w & \cos\phi_w \cos\psi_w + \sin\phi_w \sin\theta_w \sin\psi_w & \sin\phi_w \cos\theta_w \\ \sin\phi_w \sin\psi_w + \cos\phi_w \sin\theta_w \cos\psi_w & -\sin\phi_w \cos\psi_w + \cos\phi_w \sin\theta_w \sin\psi_w & \cos\phi_w \cos\theta_w \end{bmatrix} \tag{2.13}$$

By taking advantage of previous results, the transformation from the inertial- to wind-frame can be indirectly generated without angles ϕ_w, θ_w, ψ_w using Equations (2.5) and (2.8) as follows.

$$C_{w/I} = C_{w/b} C_{b/I} = \begin{bmatrix} C_{w/I}(1,1) & C_{w/I}(1,2) & C_{w/I}(1,3) \\ C_{w/I}(2,1) & C_{w/I}(2,2) & C_{w/I}(2,3) \\ C_{w/I}(3,1) & C_{w/I}(3,2) & C_{w/I}(3,3) \end{bmatrix} \tag{2.14}$$

Equating Equations (2.13) and (2.14), the wind-frame Euler angles are found as

$$\begin{aligned} \phi_w &= \tan^{-1}\left(\frac{C_{w/I}(2,3)}{C_{w/I}(3,3)}\right) \\ \theta_w &= -\sin^{-1}\left(C_{w/I}(1,3)\right) \\ \psi_w &= \tan^{-1}\left(\frac{C_{w/I}(1,2)}{C_{w/I}(1,1)}\right) \end{aligned} \tag{2.15}$$

2.4 Arbitrary-Frame Equations of Motion

In this section, rigid body aircraft equations of motion are derived with respect to an arbitrary referenced point a (see Figure 2.2), that is not necessarily the aircraft's center of gravity. These equations of motion are developed based on several assumptions such as non-rotating flat Earth, rigid body airframe, no actuator dynamics, and constant mass vehicle. To fully describe the motion of an aircraft, two sets of equations are required. The first set consists of six kinetic equations to describe three translational velocities and three angular velocities. The other set consists of six kinematic equations to describe three translational positions and three Euler angles. To promote simplicity of notation, physical vector quantities as well as algebraic vector quantities will be denoted by bold letter face, and they are used interchangeably in a mixed fashion in some expressions.

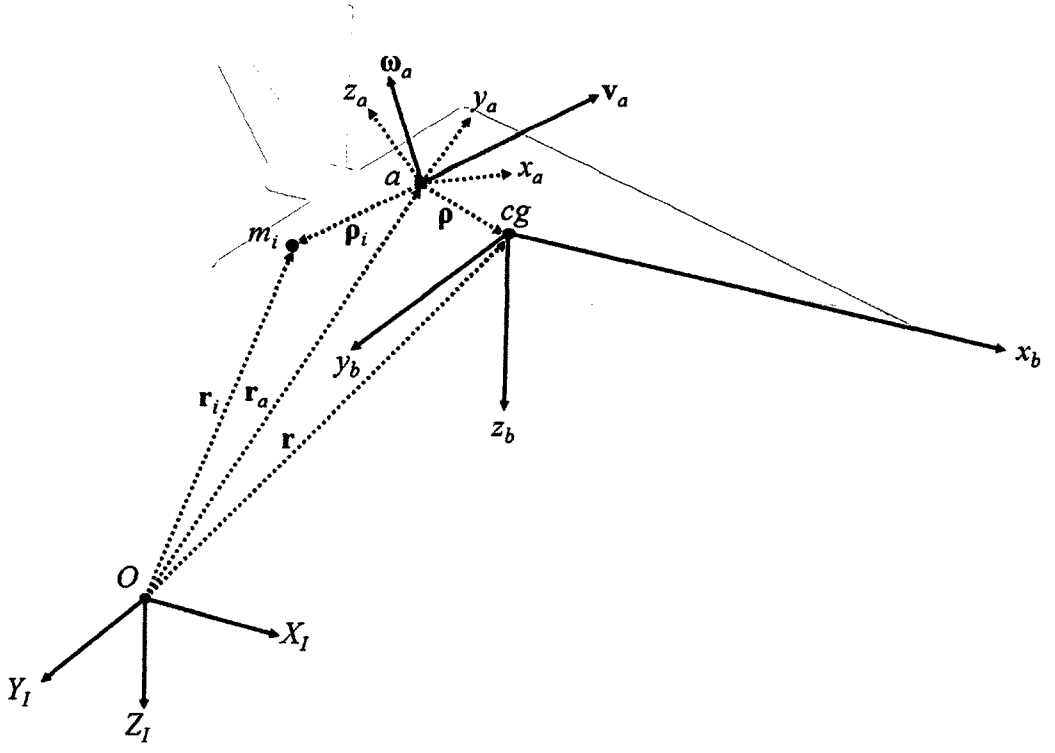

Figure 2.2 Arbitrary referenced rigid aircraft

2.4.1 Kinetic Equations

The aircraft shown in Figure 2.2 has an instantaneous velocity vector $\mathbf{v}_a$ with respect to the arbitrary body-frame $x_a y_a z_a$ located at point a, and an instantaneous angular velocity $\boldsymbol{\omega}_a$ with respect to inertial-frame $X_I Y_I Z_I$. If the location of point a with respect to the inertial-frame and the location of a mass particle m_i with respect to point a are denoted by $\mathbf{r}_a$ and $\boldsymbol{\rho}_i$, respectively, then the location of m_i in the inertial-frame is

$$\mathbf{r}_i = \mathbf{r}_a + \boldsymbol{\rho}_i \tag{2.16}$$

The location of the aircraft center of gravity (cg) from the arbitrary-frame at point a is $\boldsymbol{\rho}$ and $\mathbf{r}$ from the inertial-frame.

The translational motion of the aircraft is derived from Newton's second law in the inertial-frame of reference, mathematically speaking

$$\sum \mathbf{F} = \sum m_i (\ddot{\mathbf{r}}_i)_I = m(\ddot{\mathbf{r}})_I \tag{2.17}$$

where $\sum \mathbf{F}$ is the sum of all external forces acting on the aircraft including aerodynamic, propulsion, and gravity terms and $(\ddot{\mathbf{r}})_I$ is the cg acceleration as observed in the inertial-frame of reference. Further, the relations $m = \sum m_i$ (total aircraft mass), $m\boldsymbol{\rho} = \sum m_i \boldsymbol{\rho}_i$ and $m\mathbf{r} = \sum m_i \mathbf{r}_i$ are satisfied. It is more convenient to write components of Equation (2.17) in a body-fixed frame of reference, such as the arbitrary-frame $x_a y_a z_a$ referenced at a. In order to accomplish this, Equation (2.18), the equation of Coriolis, is used. This equation relates vector derivatives in two different frames through an angular velocity vector $\boldsymbol{\omega}_a$ that describes the angular rotation between the two frames.

$$\left(\frac{d[\mathbf{vector}]}{dt}\right)_I = \left(\frac{d[\mathbf{vector}]}{dt}\right)_a + \boldsymbol{\omega}_a \times [\mathbf{vector}] \tag{2.18}$$

To find the acceleration term in Equation (2.17) in the arbitrary body-frame at a, the first derivative of Equation (2.16) is taken and Equation (2.18) is then applied as follows.

$$(\dot{\mathbf{r}}_i)_I = (\dot{\mathbf{r}}_a)_I + (\dot{\boldsymbol{\rho}}_i)_I$$

or

$$(\dot{\mathbf{r}}_i)_I = (\mathbf{v}_a)_I + (\dot{\boldsymbol{\rho}}_i)_a + \boldsymbol{\omega}_a \times \boldsymbol{\rho}_i$$

If the body derivative notation is dropped, the previous equation becomes

$$(\dot{\mathbf{r}}_i)_I = (\mathbf{v}_a)_I + \dot{\boldsymbol{\rho}}_i + \boldsymbol{\omega}_a \times \boldsymbol{\rho}_i \tag{2.19}$$

Taking the derivative of Equation (2.19) again, the final result is

$$(\ddot{\mathbf{r}}_i)_I = \dot{\mathbf{v}}_a + \boldsymbol{\omega}_a \times \mathbf{v}_a + \ddot{\boldsymbol{\rho}}_i + \dot{\boldsymbol{\omega}}_a \times \boldsymbol{\rho}_i + 2(\boldsymbol{\omega}_a \times \dot{\boldsymbol{\rho}}_i) + \boldsymbol{\omega}_a \times (\boldsymbol{\omega}_a \times \boldsymbol{\rho}_i) \tag{2.20}$$

The relative velocities and accelerations of the mass particles are ignored for a rigid aircraft body, $\dot{\boldsymbol{\rho}}_i = \ddot{\boldsymbol{\rho}}_i = \mathbf{0}$. Therefore, from Equation (2.17), the force equation at a representing the translational motion of the aircraft in physical vector form is

$$\sum \mathbf{F}_a = m(\dot{\mathbf{v}}_a + \boldsymbol{\omega}_a \times \mathbf{v}_a) + \dot{\boldsymbol{\omega}}_a \times m\boldsymbol{\rho} + \boldsymbol{\omega}_a \times (\boldsymbol{\omega}_a \times m\boldsymbol{\rho}) \tag{2.21}$$

Before expanding this equation, vector and matrix components at an arbitrary reference point a that are used to derive the scalar equations of motion are listed in Table 2.1. The angular velocity cross product can be replaced with the cross-product matrix (see Table 2.1). Hence, Equation (2.21) is rewritten in algebraic vector form as

$$\sum \mathbf{F}_a = m\left(\dot{\mathbf{v}}_a + \Omega_a \mathbf{v}_a + \dot{\Omega}_a \boldsymbol{\rho} + \Omega_a^2 \boldsymbol{\rho}\right) \tag{2.22}$$

Expanding the left-hand side (LHS) and the right-hand side (RHS) of this equation and using the proper transformation yields

$$\begin{Bmatrix} F_{x,a} \\ F_{y,a} \\ F_{z,a} \end{Bmatrix} + m \begin{Bmatrix} -g \sin\theta_a \\ g \sin\phi_a \cos\theta_a \\ g \cos\phi_a \cos\theta_a \end{Bmatrix}$$

$$= m \left(\begin{Bmatrix} \dot{u}_a \\ \dot{v}_a \\ \dot{w}_a \end{Bmatrix} + \begin{bmatrix} 0 & -r_a & q_a \\ r_a & 0 & -p_a \\ -q_a & p_a & 0 \end{bmatrix} \begin{Bmatrix} u_a \\ v_a \\ w_a \end{Bmatrix} \right.$$

$$\left. + \begin{bmatrix} 0 & -\dot{r}_a & \dot{q}_a \\ \dot{r}_a & 0 & -\dot{p}_a \\ -\dot{q}_a & \dot{p}_a & 0 \end{bmatrix} \begin{Bmatrix} \Delta x \\ \Delta y \\ \Delta z \end{Bmatrix} + \begin{bmatrix} 0 & -r_a & q_a \\ r_a & 0 & -p_a \\ -q_a & p_a & 0 \end{bmatrix}^2 \begin{Bmatrix} \Delta x \\ \Delta y \\ \Delta z \end{Bmatrix} \right)$$

or

$$\begin{Bmatrix} F_{x,a} \\ F_{y,a} \\ F_{z,a} \end{Bmatrix} + m \begin{Bmatrix} -g \sin\theta_a \\ g \sin\phi_a \cos\theta_a \\ g \cos\phi_a \cos\theta_a \end{Bmatrix}$$

$$= m \left(\begin{Bmatrix} \dot{u}_a \\ \dot{v}_a \\ \dot{w}_a \end{Bmatrix} + \begin{Bmatrix} -r_a v_a + q_a w_a \\ +r_a u_a - p_a w_a \\ -q_a u_a + p_a v_a \end{Bmatrix} \right.$$

$$\left. + \begin{Bmatrix} -(q_a^2 + r_a^2)\Delta x + (p_a q_a - \dot{r}_a)\Delta y + (p_a r_a + \dot{q}_a)\Delta z \\ +(p_a q_a + \dot{r}_a)\Delta x - (p_a^2 + r_a^2)\Delta y + (q_a r_a - \dot{p}_a)\Delta z \\ +(p_a r_a - \dot{q}_a)\Delta x + (q_a r_a + \dot{p}_a)\Delta y - (p_a^2 + q_a^2)\Delta z \end{Bmatrix} \right)$$

Equating the *LHS* and *RHS*, the scalar force equations of motion for the arbitrary body-frame fixed at point a are

$$\begin{aligned} F_{x,a} &= m(\dot{u}_a - r_a v_a + q_a w_a + g \sin\theta_a - (q_a^2 + r_a^2)\Delta x + (p_a q_a - \dot{r}_a)\Delta y \\ &\quad + (p_a r_a + \dot{q}_a)\Delta z) \\ F_{y,a} &= m(\dot{v}_a + r_a u_a - p_a w_a - g \sin\phi_a \cos\theta_a + (p_a q_a + \dot{r}_a)\Delta x \\ &\quad - (p_a^2 + r_a^2)\Delta y + (q_a r_a - \dot{p}_a)\Delta z) \\ F_{z,a} &= m(\dot{w}_a - q_a u_a + p_a v_a - g \cos\phi_a \cos\theta_a + (p_a r_a - \dot{q}_a)\Delta x \\ &\quad + (q_a r_a + \dot{p}_a)\Delta y - (p_a^2 + q_a^2)\Delta z) \end{aligned} \tag{2.23}$$

Table 2.1 Vector and matrix definitions for arbitrary-frame

Force, Moment and Gravity:

$$\sum \mathbf{F}_a = \begin{Bmatrix} F_{x,a} \\ F_{y,a} \\ F_{z,a} \end{Bmatrix} + m\mathbf{g}_a, \quad \sum \mathbf{M}_a = \begin{Bmatrix} L_a \\ M_a \\ N_a \end{Bmatrix} + \boldsymbol{\rho} \times m\mathbf{g}_a$$

$$m\mathbf{g}_a = C_{a/I} m\mathbf{g} = C_{a/I} m \begin{Bmatrix} 0 \\ 0 \\ g \end{Bmatrix}$$

where $C_{a/I}$ denotes the transformation matrix from the inertial- to arbitrary-frame based on Euler angles ϕ_a, θ_a, ψ_a

Linear Velocity, Angular Velocity and cg Location:

$$\mathbf{v}_a = \begin{Bmatrix} u_a \\ v_a \\ w_a \end{Bmatrix}, \quad \boldsymbol{\omega} = \boldsymbol{\omega}_a = \begin{Bmatrix} p_a \\ q_a \\ r_a \end{Bmatrix}, \quad \boldsymbol{\rho} = \begin{Bmatrix} \Delta x \\ \Delta y \\ \Delta z \end{Bmatrix}, \quad \mathbf{r}_a = \begin{Bmatrix} X_a \\ Y_a \\ Z_a \end{Bmatrix}$$

Cross-Product Matrix:

$$\boldsymbol{\omega}_a \times (\cdot) = \Omega_a(\cdot) = \begin{bmatrix} 0 & -r_a & q_a \\ r_a & 0 & -p_a \\ -q_a & p_a & 0 \end{bmatrix} (\cdot)$$

$$\boldsymbol{\omega}_a \times \left(\boldsymbol{\omega}_a \times (\cdot)\right) = \Omega_a^2(\cdot) = \begin{bmatrix} 0 & -r_a & q_a \\ r_a & 0 & -p_a \\ -q_a & p_a & 0 \end{bmatrix}^2 (\cdot)$$

$$\boldsymbol{\rho} \times (\cdot) = \mathrm{D}_a(\cdot) = \begin{bmatrix} 0 & -\Delta z & \Delta y \\ \Delta z & 0 & -\Delta x \\ -\Delta y & \Delta x & 0 \end{bmatrix} (\cdot), \quad \mathbf{v}_a \times (\cdot) = \mathrm{V}_a(\cdot) = \begin{bmatrix} 0 & -w_a & v_a \\ w_a & 0 & -u_a \\ -v_a & u_a & 0 \end{bmatrix} (\cdot)$$

Inertia Matrix:

$$\mathrm{J}_a = \begin{bmatrix} I_{xx}^a & -I_{xy}^a & -I_{xz}^a \\ -I_{xy}^a & I_{yy}^a & -I_{yz}^a \\ -I_{xz}^a & -I_{yz}^a & I_{zz}^a \end{bmatrix}$$

$$\mathrm{J}_a^{-1} = \frac{1}{\Delta^a} \begin{bmatrix} I_{yy}^a I_{zz}^a - \left(I_{yz}^a\right)^2 & I_{yz}^a I_{xz}^a + I_{xy}^a I_{zz}^a & I_{xy}^a I_{yz}^a + I_{xz}^a I_{yy}^a \\ I_{yz}^a I_{xz}^a + I_{xy}^a I_{zz}^a & I_{zz}^a I_{xx}^a - (I_{xz}^a)^2 & I_{xy}^a I_{xz}^a + I_{yz}^a I_{xx}^a \\ I_{xy}^a I_{yz}^a + I_{xz}^a I_{yy}^a & I_{xy}^a I_{xz}^a + I_{yz}^a I_{xx}^a & I_{xx}^a I_{yy}^a - \left(I_{xy}^a\right)^2 \end{bmatrix} = \frac{1}{\Delta^a} \begin{bmatrix} k_1^a & k_2^a & k_3^a \\ k_2^a & k_4^a & k_5^a \\ k_3^a & k_5^a & k_6^a \end{bmatrix}$$

$$\Delta^a = I_{xx}^a I_{yy}^a I_{zz}^a - 2 I_{xy}^a I_{yz}^a I_{xz}^a - I_{xx}^a \left(I_{yz}^a\right)^2 - I_{yy}^a (I_{xz}^a)^2 - I_{zz}^a \left(I_{xy}^a\right)^2$$

where I_{xx}^a, I_{yy}^a, I_{zz}^a denote moments of inertia and I_{xy}^a, I_{yz}^a, I_{xz}^a denote products of inertia for the arbitrary-frame

The rotational motion of the aircraft about an arbitrary point is described by the moment equations about a. The sum of external moments about point a is equal to the rate of change of the angular momentum about a as observed in the inertial-frame of reference. Therefore, the absolute angular momentum about a is defined as

$$\mathbf{H}_a = \sum(\boldsymbol{\rho}_i \times m_i \mathbf{v}_i) \tag{2.24}$$

where $(\dot{\mathbf{r}}_i)_I = (\mathbf{v}_i)_I$. The rate of change of the angular momentum about a as observed in $X_I Y_I Z_I$ is

$$\left(\dot{\mathbf{H}}_a\right)_I = \sum((\dot{\boldsymbol{\rho}}_i)_I \times m_i \mathbf{v}_i) + \sum(\boldsymbol{\rho}_i \times m_i (\dot{\mathbf{v}}_i)_I) \tag{2.25}$$

Here, $(\dot{\boldsymbol{\rho}}_i)_I = (\dot{\mathbf{r}}_i - \dot{\mathbf{r}}_a)_I$, $(\dot{\mathbf{v}}_i)_I = (\ddot{\mathbf{r}}_i)_I$ and since $(\dot{\mathbf{r}}_i)_I \times \mathbf{v}_i = \mathbf{0}$, then,

$$\left(\dot{\mathbf{H}}_a\right)_I = -(\dot{\mathbf{r}}_a)_I \times \sum m_i \mathbf{v}_i + \sum(\boldsymbol{\rho}_i \times m_i (\dot{\mathbf{v}}_i)_I) \tag{2.26}$$

The sum of all external moments about the arbitrary body-fixed frame at point a is defined as

$$\sum \mathbf{M}_a = \sum(\boldsymbol{\rho}_i \times m_i (\dot{\mathbf{v}}_i)_I) \tag{2.27}$$

Using Equation (2.26), Equation (2.27) is rewritten as

$$\sum \mathbf{M}_a = \left(\dot{\mathbf{H}}_a\right)_I + (\dot{\mathbf{r}}_a)_I \times \sum m_i \mathbf{v}_i \tag{2.28}$$

or, since $\sum m_i \mathbf{v}_i = m\mathbf{v}$ and $\mathbf{v} = \mathbf{v}_a + (\dot{\boldsymbol{\rho}})_I$, then Equation (2.28) is written as

$$\sum \mathbf{M}_a = \left(\dot{\mathbf{H}}_a\right)_I + \mathbf{v}_a \times m(\dot{\boldsymbol{\rho}})_I \tag{2.29}$$

Now using Equation (2.19) and noting that for a rigid body $\dot{\boldsymbol{\rho}}_i = \mathbf{0}$, Equation (2.24) is expressed in the arbitrary body-fixed frame at a as

$$\mathbf{H}_a = \sum\left(\boldsymbol{\rho}_i \times m_i (\mathbf{v}_a + \dot{\boldsymbol{\rho}}_i + \boldsymbol{\omega}_a \times \boldsymbol{\rho}_i)\right) \tag{2.30}$$

or

$$\mathbf{H}_a = \sum m_i \boldsymbol{\rho}_i \times \mathbf{v}_a + \sum \boldsymbol{\rho}_i \times m_i(\boldsymbol{\omega}_a \times \boldsymbol{\rho}_i) \tag{2.31}$$

The second term on right in the previous equation is equal to the algebraic vector $\mathrm{J}_a\boldsymbol{\omega}_a$ [35]. The mass moment of inertia matrix of the rigid body aircraft J_a as well as all of the vectors in the previous equation are expressed in the body-fixed arbitrary-frame at a. Now, Equation (2.31) has the form

$$\mathbf{H}_a = m\boldsymbol{\rho} \times \mathbf{v}_a + \mathrm{J}_a\boldsymbol{\omega}_a \tag{2.32}$$

The derivative of this equation can be expressed in the inertial-frame by using the vector derivative relationship from Equation (2.18), so

$$\left(\dot{\mathbf{H}}_a\right)_I = \left(\dot{\mathbf{H}}_a\right)_a + \boldsymbol{\omega}_a \times \mathbf{H}_a \tag{2.33}$$

or, in an expanded form,

$$\left(\dot{\mathbf{H}}_A\right)_I = \mathrm{J}_a\dot{\boldsymbol{\omega}}_a + \boldsymbol{\omega}_a \times \mathrm{J}_a\boldsymbol{\omega}_a + m\boldsymbol{\rho} \times \dot{\mathbf{v}}_a + \boldsymbol{\omega}_a \times (m\boldsymbol{\rho} \times \mathbf{v}_a) \tag{2.34}$$

Noting that $(\dot{\boldsymbol{\rho}})_I = \boldsymbol{\omega}_a \times \boldsymbol{\rho}$ and substituting Equation (2.34) in Equation (2.29) yields

$$\sum \mathbf{M}_a = \mathrm{J}_a\dot{\boldsymbol{\omega}}_a + \boldsymbol{\omega}_a \times \mathrm{J}_a\boldsymbol{\omega}_a + m\boldsymbol{\rho} \times \dot{\mathbf{v}}_a + m\boldsymbol{\omega}_a \times (\boldsymbol{\rho} \times \mathbf{v}_a) + m\mathbf{v}_a \times (\boldsymbol{\omega}_a \times \boldsymbol{\rho}) \tag{2.35}$$

Finally referring to Table 2.1, the right-hand side of this equation can be expressed in cross-product matrix form as

$$\sum \mathbf{M}_a = \mathrm{J}_a\dot{\boldsymbol{\omega}}_a + \Omega_a\mathrm{J}_a\boldsymbol{\omega}_a + m\mathrm{D}_a\dot{\mathbf{v}}_A + m\Omega_a\mathrm{D}_a\mathbf{v}_A - m\mathrm{V}_a\mathrm{D}_a\boldsymbol{\omega}_a \tag{2.36}$$

Equation (2.36) is expanded into three scalar moment equations as

$$
\begin{aligned}
L_a = {} & I_{xx}^a \dot{p}_a - I_{xy}^a \dot{q}_a - I_{xz}^a \dot{r}_a + I_{xy}^a p_a r_a - I_{xz}^a p_a q_a + \left(I_{zz}^a - I_{yy}^a\right) q_a r_a \\
& + (r_a^2 - q_a^2) I_{yz}^a + m(p_a v_a - q_a u_a + \dot{w}_a - g cos\theta_a cos\phi_a)\Delta y \\
& + m(p_a w_a - r_a u_a + \dot{v}_a + g cos\theta_a sin\phi_a)\Delta z \\
M_a = {} & -I_{xy}^a \dot{p}_a + I_{yy}^a \dot{q}_a - I_{yz}^a \dot{r}_a + I_{yz}^a p_a q_a - I_{xy}^a q_a r_a + (I_{xx}^a - I_{zz}^a) p_a r_a \\
& + (p_a^2 - r_a^2) I_{xz}^a + m(q_a u_a - p_a v_a - \dot{w}_a + g cos\theta_a cos\phi_a)\Delta x \\
& + m(q_a w_a - r_a v_a + \dot{u}_a + g sin\theta_a)\Delta z \\
N_a = {} & -I_{xz}^a \dot{p}_a - I_{yz}^a \dot{q}_a + I_{zz}^a \dot{r}_a + I_{xz}^a q_a r_a - I_{yz}^a p_a r_a + \left(I_{yy}^a - I_{xx}^a\right) p_a q_a \\
& + (q_a^2 - p_a^2) I_{xy}^a + m(r_a u_a - p_a w_a + \dot{v}_a - g cos\theta_a sin\phi_a)\Delta x \\
& + m(r_a v_a - q_a w_a - \dot{u}_a - g sin\theta_a)\Delta y
\end{aligned}
\tag{2.37}
$$

2.4.2 Kinematic Equations

The inertial translational positions (X_a, Y_a, Z_a) of an aircraft referenced at point a are obtained by relating the body-fixed translational velocities to the inertial velocities by the appropriate transformation matrix. Using the form of Equation (2.9), the inertial velocities are easily obtained as follows

$$
\begin{Bmatrix} \dot{X}_a \\ \dot{Y}_a \\ \dot{Z}_a \end{Bmatrix} = C_{I/a} \begin{Bmatrix} u_a \\ v_a \\ w_a \end{Bmatrix} \tag{2.38}
$$

or

$$
\begin{aligned}
\dot{X}_a = {} & (cos\,\theta_a\, cos\,\psi_a)u_a + (-cos\,\phi_a\, sin\,\psi_a + sin\,\phi_a\, sin\,\theta_a\, cos\,\psi_a)v_a \\
& + (sin\,\phi_a\, sin\,\psi_a + cos\,\phi_a\, sin\,\theta_a\, cos\,\psi_a)w_a \\
\dot{Y}_a = {} & (cos\,\theta_a\, sin\,\psi_a)u_a + (cos\,\phi_a\, cos\,\psi_a + sin\,\phi_a\, sin\,\theta_a\, sin\,\psi_a)v_a \\
& + (-sin\,\phi_a\, cos\,\psi_a + cos\,\phi_a\, sin\,\theta_a\, sin\,\psi_a)w_a \\
\dot{Z}_a = {} & (-sin\,\theta_a)u_a + (sin\,\phi_a\, cos\,\theta_a)v_a + (cos\,\phi_a\, cos\,\theta_a)w_a
\end{aligned}
\tag{2.39}
$$

The orientation of the arbitrary body-fixed frame at a can be described relative to an inertial-frame by a sequence of Euler rotations similar to the discussion in Section 2.3.2. The Euler angle rates ($\dot{\phi}_a$, $\dot{\theta}_a$, $\dot{\psi}_a$) can be resolved into components relative to the body-fixed angular velocities as shown in Reference [33].

$$\begin{Bmatrix} p_a \\ q_a \\ r_a \end{Bmatrix} = \begin{bmatrix} 1 & 0 & -\sin\theta_a \\ 0 & \cos\phi_a & \sin\phi_a \cos\theta_a \\ 0 & -\sin\phi_a & \cos\phi_a \cos\theta_a \end{bmatrix} \begin{Bmatrix} \dot{\phi}_a \\ \dot{\theta}_a \\ \dot{\psi}_a \end{Bmatrix} \tag{2.40}$$

or

$$\begin{Bmatrix} \dot{\phi}_a \\ \dot{\theta}_a \\ \dot{\psi}_a \end{Bmatrix} = \begin{bmatrix} 1 & \tan\theta_a \sin\phi_a & \tan\theta_a \cos\phi_a \\ 0 & \cos\phi_a & -\sin\phi_a \\ 0 & \sin\phi_a/\cos\theta_a & \cos\phi_a/\cos\theta_a \end{bmatrix} \begin{Bmatrix} p_a \\ q_a \\ r_a \end{Bmatrix} \tag{2.41}$$

The three Euler body rotation relationships in individual form are

$$\begin{aligned} \dot{\phi}_a &= p_a + (\tan\theta_a \sin\phi_a) q_a + (\tan\theta_a \cos\phi_a) r_a \\ \dot{\theta}_a &= (\cos\phi_a) q_a - (\sin\phi_a) r_a \\ \dot{\psi}_a &= (\sin\phi_a/\cos\theta_a) q_a + (\cos\phi_a/\cos\theta_a) r_a \end{aligned} \tag{2.42}$$

In general, the complete motion of an aircraft is described by the three body linear translational velocities (u_A, v_A, w_A) and the three body angular velocities (p_a, q_a, r_a). However, to track the path and orientation of the aircraft, three inertial linear positions (X_a, Y_a, Z_a) and three angular attitudes (ϕ_a, θ_a, ψ_a) are used. Therefore, the complete state vector of a nonlinear aircraft model for the arbitrary body-fixed frame at point a is

$$\mathbf{x}_a = [u_a \quad v_a \quad w_a \quad \phi_a \quad \theta_a \quad \psi_a \quad p_a \quad q_a \quad r_a \quad X_a \quad Y_a \quad Z_a]^T$$

2.5 Body-Frame Equations of Motion

The body-fixed frame is referenced at the center of gravity (cg) of an aircraft, as shown in Figure 2.2. This frame can be interpreted as a special case of the arbitrary-frame when point a is exactly located at the aircraft cg, and the position vector of the cg relative to a is zero. Throughout this dissertation, the body-frame is used to indicate a frame of reference that is centered at the cg of the aircraft. Table 2.2 lists the vector and matrix components that are used in the derivation of equations of motion in this frame of reference. Further simplifications to the body-frame equations of motion can be made by assuming inertial symmetry about the $x_b z_b$ plane; however, these simplifications are carried out in a later section, but not here.

2.5.1 Kinetic Equations

The general equations of motion derived in Section 2.4 are revisited here; however, the subscript a is replaced by b to indicate the body-frame at the aircraft cg position and the terms involving vector $\boldsymbol{\rho}$ are deleted from the expressions. With these simplifications in mind, the force equation, Equation (2.22), is rewritten here as

$$\sum \mathbf{F}_b = m(\dot{\mathbf{v}}_b + \Omega_b \mathbf{v}_b) \tag{2.43}$$

The linear acceleration vector can now be expressed explicitly as

$$\dot{\mathbf{v}}_b = -\Omega_b \mathbf{v}_b + \frac{1}{m}\sum \mathbf{F}_b \tag{2.44}$$

After substituting and expanding, three scalar linear accelerations equations are obtained.

$$\dot{u}_b = r_b v_b - q_b w_b - g\sin\theta_b + \frac{1}{m}F_{x,b}$$

$$\dot{v}_b = -r_b u_b + p_b w_b + g\sin\phi_b\cos\theta_b + \frac{1}{m}F_{y,b} \tag{2.45}$$

$$\dot{w}_b = q_b u_b - p_b v_b + g\cos\phi_b\cos\theta_b + \frac{1}{m}F_{z,b}$$

Similarly, the moment equation represented by Equation (2.36) is rewritten here as

$$\sum \mathbf{M}_b = \mathrm{J}_b\dot{\boldsymbol{\omega}}_b + \Omega_b \mathrm{J}_b\boldsymbol{\omega}_b \tag{2.46}$$

This relation can be expressed in terms of the angular acceleration vector.

$$\dot{\boldsymbol{\omega}}_b = \mathrm{J}_b^{-1}(-\Omega_b \mathrm{J}_b\boldsymbol{\omega}_b + \sum \mathbf{M}_b) \tag{2.47}$$

Substituting and expanding yields three scalar angular accelerations equations.

$$\begin{aligned}
\dot{p}_b = \frac{1}{\Delta^b}\big[&k_1^b\{(I_{yy}^b - I_{zz}^b)q_b r_b + I_{yz}^b(q_b^2 - r_b^2) + (I_{xz}^b q_b - I_{xy}^b r_b)p_b + L_b\} \\
&+ k_2^b\{(I_{zz}^b - I_{xx}^b)p_b r_b + I_{xz}^b(r_b^2 - p_b^2) + (I_{xy}^b r_b - I_{yz}^b p_b)q_b + M_b\} \\
&+ k_3^b\{(I_{xx}^b - I_{yy}^b)p_b q_b + I_{xy}^b(p_b^2 - q_b^2) + (I_{yz}^b p_b - I_{xz}^b q_b)r_b + N_b\}\big] \\
\dot{q}_b = \frac{1}{\Delta^b}\big[&k_2^b\{(I_{yy}^b - I_{zz}^b)q_b r_b + I_{yz}^b(q_b^2 - r_b^2) + (I_{xz}^b q_b - I_{xy}^b r_b)p_b + L_b\} \\
&+ k_4^b\{(I_{zz}^b - I_{xx}^b)p_b r_b + I_{xz}^b(r_b^2 - p_b^2) + (I_{xy}^b r_b - I_{yz}^b p_b)q_b + M_b\} \\
&+ k_5^b\{(I_{xx}^b - I_{yy}^b)p_b q_b + I_{xy}^b(p_b^2 - q_b^2) + (I_{yz}^b p_b - I_{xz}^b q_b)r_b + N_b\}\big] \\
\dot{r}_b = \frac{1}{\Delta^b}\big[&k_3^b\{(I_{yy}^b - I_{zz}^b)q_b r_b + I_{yz}^b(q_b^2 - r_b^2) + (I_{xz}^b q_b - I_{xy}^b r_b)p_b + L_b\} \\
&+ k_5^b\{(I_{zz}^b - I_{xx}^b)p_b r_b + I_{xz}^b(r_b^2 - p_b^2) + (I_{xy}^b r_b - I_{yz}^b p_b)q_b + M_b\} \\
&+ k_6^b\{(I_{xx}^b - I_{yy}^b)p_b q_b + I_{xy}^b(p_b^2 - q_b^2) + (I_{yz}^b p_b - I_{xz}^b q_b)r_b + N_b\}\big]
\end{aligned} \tag{2.48}$$

Table 2.2 Vector and matrix definitions for body-frame

Force, Moment and Gravity:

$$\Sigma \mathbf{F}_b = \begin{Bmatrix} F_{x,b} \\ F_{y,b} \\ F_{z,b} \end{Bmatrix} + C_{b/I} m\mathbf{g}, \quad \Sigma \mathbf{M}_b = \begin{Bmatrix} L_b \\ M_b \\ N_b \end{Bmatrix}, \quad \mathbf{g} = \begin{Bmatrix} 0 \\ 0 \\ g \end{Bmatrix}$$

Linear Velocity and Angular Velocity:

$$\mathbf{v} = \mathbf{v}_b = \begin{Bmatrix} u_b \\ v_b \\ w_b \end{Bmatrix}, \quad \boldsymbol{\omega} = \boldsymbol{\omega}_b = \begin{Bmatrix} p_b \\ q_b \\ r_b \end{Bmatrix}, \quad \mathbf{r} = \mathbf{r}_b = \begin{Bmatrix} X_b \\ Y_b \\ Z_b \end{Bmatrix}$$

Cross-Product Matrix:

$$\boldsymbol{\omega}_b \times (\cdot) = \Omega_b(\cdot) = \begin{bmatrix} 0 & -r_b & q_b \\ r_b & 0 & -p_b \\ -q_b & p_b & 0 \end{bmatrix} (\cdot)$$

$$\boldsymbol{\omega}_b \times \left(\boldsymbol{\omega}_b \times (\cdot)\right) = \Omega_b^2(\cdot) = \begin{bmatrix} 0 & -r_b & q_b \\ r_b & 0 & -p_b \\ -q_b & p_b & 0 \end{bmatrix}^2 (\cdot)$$

Inertia Matrix:

$$\mathrm{J}_b = \begin{bmatrix} I_{xx}^b & -I_{xy}^b & -I_{xz}^b \\ -I_{xy}^b & I_{yy}^b & -I_{yz}^b \\ -I_{xz}^b & -I_{yz}^b & I_{zz}^b \end{bmatrix}$$

$$\mathrm{J}_b^{-1} = \frac{1}{\Delta^b} \begin{bmatrix} I_{yy}^b I_{zz}^b - \left(I_{yz}^b\right)^2 & I_{yz}^b I_{xz}^b + I_{xy}^b I_{zz}^b & I_{xy}^b I_{yz}^b + I_{xz}^b I_{yy}^b \\ I_{yz}^b I_{xz}^b + I_{xy}^b I_{zz}^b & I_{zz}^b I_{xx}^b - (I_{xz}^b)^2 & I_{xy}^b I_{xz}^b + I_{yz}^b I_{xx}^b \\ I_{xy}^b I_{yz}^b + I_{xz}^b I_{yy}^b & I_{xy}^b I_{xz}^b + I_{yz}^b I_{xx}^b & I_{xx}^b I_{yy}^b - \left(I_{xy}^b\right)^2 \end{bmatrix} = \frac{1}{\Delta^b} \begin{bmatrix} k_1^b & k_2^b & k_3^b \\ k_2^b & k_4^b & k_5^b \\ k_3^b & k_5^b & k_6^b \end{bmatrix}$$

$$\Delta^b = I_{xx}^b I_{yy}^b I_{zz}^b - 2 I_{xy}^b I_{yz}^b I_{xz}^b - I_{xx}^b \left(I_{yz}^b\right)^2 - I_{yy}^b (I_{xz}^b)^2 - I_{zz}^b \left(I_{xy}^b\right)^2$$

where I_{xx}^b, I_{yy}^b, I_{zz}^b denote moments of inertia and I_{xy}^b, I_{yz}^b, I_{xz}^b denote products of inertia for the body-frame

2.5.2 Kinematic Equations

The inertial translational positions (X_b, Y_b, Z_b) of an aircraft referenced at the cg are obtained by relating the body-frame translation velocities to the inertial velocities by the appropriate transformation matrix. The inertial velocities are similar to Equation (2.39) and are repeated here with the appropriate Euler angles.

$$\begin{aligned}
\dot{X}_b &= (\cos\theta_b \cos\psi_b)u_b + (-\cos\phi_b \sin\psi_b + \sin\phi_b \sin\theta_b \cos\psi_b)v_b \\
&\quad + (\sin\phi_b \sin\psi_b + \cos\phi_b \sin\theta_b \cos\psi_b)w_b \\
\dot{Y}_b &= (\cos\theta_b \sin\psi_b)u_b + (\cos\phi_b \cos\psi_b + \sin\phi_b \sin\theta_b \sin\psi_b)v_b \\
&\quad + (-\sin\phi_b \cos\psi_b + \cos\phi_b \sin\theta_b \sin\psi_b)w_b \\
\dot{Z}_b &= (-\sin\theta_b)u_b + (\sin\phi_b \cos\theta_b)v_b + (\cos\phi_b \cos\theta_b)w_b
\end{aligned} \tag{2.49}$$

The orientation of a body-fixed frame at the cg can be described relative to an inertial-frame by a sequence of Euler rotations, as discussed in Section 2.3.2. The Euler angle rates ($\dot{\phi}_b$, $\dot{\theta}_b$, $\dot{\psi}_b$) can be resolved into components relative to the body-frame angular velocities. Hence, the three Euler body rotation relationships are

$$\begin{aligned}
\dot{\phi}_b &= p_b + (\tan\theta_b \sin\phi_b)q_b + (\tan\theta_b \cos\phi_b)r_b \\
\dot{\theta}_b &= (\cos\phi_b)q_b - (\sin\phi_b)r_b \\
\dot{\psi}_b &= (\sin\phi_b/\cos\theta_b)q_b + (\cos\phi_b/\cos\theta_b)r_b
\end{aligned} \tag{2.50}$$

Here, the complete motion of an aircraft is described by the three body linear translational velocities (u_b, v_b, w_b) and the three body angular velocities (p_b, q_b, r_b). However, to track the path and orientation of the aircraft, three inertial linear positions (X_b, Y_b, Z_b) and three angular attitudes (ϕ_b, θ_b, ψ_b) are used. Therefore, the complete state vector of a nonlinear aircraft model for the body-fixed frame at the cg is

$$\mathbf{x}_b = [u_b \quad v_b \quad w_b \quad \phi_b \quad \theta_b \quad \psi_b \quad p_b \quad q_b \quad r_b \quad X_b \quad Y_b \quad Z_b]^T$$

2.6 Stability-Frame Equations of Motion

The stability-frame is a special aircraft-carrried frame that is referenced at the aircraft center of gravity and undergoes a left-handed rotation α about the body y_b-axis, as shown in Figure 2.1. The stability-frame experiences an angular velocity of $-\dot{\alpha}$ with respect to the body-frame $x_b y_b z_b$. The angle of attack derivative $\dot{\alpha}$ can be obtained by direct differentiation of Equation (2.1).

$$\dot{\alpha} = \frac{u_b \dot{w}_b - w_b \dot{u}_b}{u_b^2 + w_b^2} \tag{2.51}$$

More discussion of this frame was provided in Section 2.2.3. Table 2.3 lists the vector and matrix components that are used in the derivation of equations of motion in the stability-frame of reference. Note that the velocity vector now lies in the $x_s y_s$ plane, and hence, the z_s velocity component is zero ($w_s = 0$).

2.6.1 Kinetic Equations

From Equation (2.21), the force vector equation in the body-frame $x_b y_b z_b$ referenced at the cg is

$$\frac{1}{m}\sum \mathbf{F}_b = \dot{\mathbf{v}}_b + \boldsymbol{\omega}_b \times \mathbf{v}_b \tag{2.52}$$

The acceleration term $\dot{\mathbf{v}}_b$ can be expressed in the stability-frame by utilizing the vector derivative rule (Equation (2.18)) and the body-stability transformation matrix (Equation (2.3)). Equation (2.52) can be written in the stability-frame $x_s y_s z_s$ as

$$\frac{1}{m} C_{s/b} \sum \mathbf{F}_b = C_{s/b} \frac{d}{dt}\left(C_{s/b}^T \mathbf{v}_s\right) + \left(C_{s/b}\boldsymbol{\omega}_b\right) \times \left(C_{s/b}\mathbf{v}_b\right)$$

or

$$\frac{1}{m}\sum \mathbf{F}_s = \left(C_{s/b}C_{s/b}^T\dot{\mathbf{v}}_s + C_{s/b}\dot{C}_{s/b}^T\mathbf{v}_s\right) + \boldsymbol{\omega}_s \times \mathbf{v}_s$$

or

$$\frac{1}{m}\sum \mathbf{F}_s = \dot{\mathbf{v}}_s + \Omega_{s/b}\mathbf{v}_s + \boldsymbol{\omega}_s \times \mathbf{v}_s$$

Therefore, the linear acceleration vector in the stability-frame $x_s y_s z_s$ can now be expressed explicitly as

$$\dot{\mathbf{v}}_s = -\Omega_{s/b}\mathbf{v}_s - \boldsymbol{\omega}_s \times \mathbf{v}_s + \frac{1}{m}\sum \mathbf{F}_s \tag{2.53}$$

or

$$\dot{\mathbf{v}}_s = -\Omega_{s/b}\mathbf{v}_s - \Omega_s\mathbf{v}_s + \frac{1}{m}\sum \mathbf{F}_s \tag{2.54}$$

The acceleration vector term $-\Omega_{s/b}\mathbf{v}_s = [0 \quad 0 \quad -\dot{\alpha}u_S]^T$ is an additional term due to the rotary motion of the stability-frame, when Equation (2.54) is compared to Equation (2.44). This vector represents tangential acceleration components arising from the mutual interaction of the linear components of velocity $\mathbf{v}_s$ with the components of angular velocity $\boldsymbol{\omega}_{s/b}$. Substitute and expand to get three scalar linear accelerations equations.

$$\begin{aligned}
\dot{u}_s &= r_s v_s - g(\cos\alpha \sin\theta_b - \sin\alpha \cos\phi_b \cos\theta_b) + \frac{1}{m}F_{x,s} \\
\dot{v}_s &= -r_s u_s + g(\sin\phi_b \cos\theta_b) + \frac{1}{m}F_{y,s} \\
\dot{\alpha} &= q_s - \frac{p_s v_s}{u_s} + \frac{g}{u_s}(\sin\alpha \sin\theta_b + \cos\alpha \cos\phi_b \cos\theta_b) + \frac{1}{mu_s}F_{z,s}
\end{aligned} \tag{2.55}$$

If the transformation $C_{s/l}$ is used instead of $C_{s/b}C_{b/l}$ for the gravity term, then Equation (2.54) becomes

$$\dot{u}_s = r_s v_s - g\sin\theta_s + \frac{1}{m}F_{x,s}$$

$$\dot{v}_s = -r_s u_s + g\sin\phi_s\cos\theta_s + \frac{1}{m}F_{y,s} \tag{2.56}$$

$$\dot{\alpha} = q_s - \frac{p_s v_s}{u_s} + \frac{g}{u_s}\cos\phi_s\cos\theta_s + \frac{1}{mu_s}F_{z,s}$$

Similarly, the moment equation represented by Equation (2.35) is rewritten here in the body-frame $x_b y_b z_b$ and is expressed in terms of the angular acceleration vector as

$$\dot{\boldsymbol{\omega}}_b = \mathrm{J}_b^{-1}(-\boldsymbol{\omega}_b \times \mathrm{J}_b\boldsymbol{\omega}_b + \sum\mathbf{M}_b) \tag{2.57}$$

Equation (2.57) can be replaced by an equation in the stability-frame as

$$\dot{\boldsymbol{\omega}}_s + \boldsymbol{\omega}_{s/b} \times \boldsymbol{\omega}_s = \mathrm{J}_s^{-1}(-\boldsymbol{\omega}_s \times \mathrm{J}_s\boldsymbol{\omega}_s + \sum\mathbf{M}_s) \tag{2.58}$$

or, in terms of cross-product matrices

$$\dot{\boldsymbol{\omega}}_s = -\Omega_{s/b}\boldsymbol{\omega}_s + \mathrm{J}_s^{-1}(-\Omega_s\mathrm{J}_s\boldsymbol{\omega}_s + \sum\mathbf{M}_s) \tag{2.59}$$

Substitute and expand to get three scalar angular accelerations equations.

$$\begin{aligned}
\dot{p}_s = (r_s\dot{\alpha}) + \frac{1}{\Delta^s}\big[&k_1^s\{(I_{yy}^s - I_{zz}^s)q_s r_s + I_{yz}^s(q_s^2 - r_s^2) + (I_{xz}^s q_s - I_{xy}^s r_s)p_s + L_s\} \\
&+ k_2^s\{(I_{zz}^s - I_{xx}^s)p_s r_s + I_{xz}^s(r_s^2 - p_s^2) + (I_{xy}^s r_s - I_{yz}^s p_s)q_s + M_s\} \\
&+ k_3^s\{(I_{xx}^s - I_{yy}^s)p_s q_s + I_{xy}^s(p_s^2 - q_s^2) + (I_{yz}^s p_s - I_{xz}^s q_s)r_s + N_s\}\big] \\
\dot{q}_s = \frac{1}{\Delta^s}\big[&k_2^s\{(I_{yy}^s - I_{zz}^s)q_s r_s + I_{yz}^s(q_s^2 - r_s^2) + (I_{xz}^s q_s - I_{xy}^s r_s)p_s + L_s\} \\
&+ k_4^s\{(I_{zz}^s - I_{xx}^s)p_s r_s + I_{xz}^s(r_s^2 - p_s^2) + (I_{xy}^s r_s - I_{yz}^s p_s)q_s + M_s\} \\
&+ k_5^s\{(I_{xx}^s - I_{yy}^s)p_s q_s + I_{xy}^s(p_s^2 - q_s^2) + (I_{yz}^s p_s - I_{xz}^s q_s)r_s + N_s\}\big] \\
\dot{r}_s = (-p_s\dot{\alpha}) + \frac{1}{\Delta^s}\big[&k_3^s\{(I_{yy}^s - I_{zz}^s)q_s r_s + I_{yz}^s(q_s^2 - r_s^2) + (I_{xz}^s q_s - I_{xy}^s r_s)p_s + L_s\} \\
&+ k_5^s\{(I_{zz}^s - I_{xx}^s)p_s r_s + I_{xz}^s(r_s^2 - p_s^2) + (I_{xy}^s r_s - I_{yz}^s p_s)q_s + M_s\} \\
&+ k_6^s\{(I_{xx}^s - I_{yy}^s)p_s q_s + I_{xy}^s(p_s^2 - q_s^2) + (I_{yz}^s p_s - I_{xz}^s q_s)r_s + N_s\}\big]
\end{aligned} \tag{2.60}$$

Table 2.3 Vector and matrix definitions for stability-frame

Force, Moment and Gravity:

$$\sum \mathbf{F}_S = \begin{Bmatrix} F_{x,s} \\ F_{y,s} \\ F_{z,s} \end{Bmatrix} + C_{s/I} m\mathbf{g}, \quad \sum \mathbf{M}_S = \begin{Bmatrix} L_s \\ M_s \\ N_s \end{Bmatrix}, \quad \mathbf{g} = \begin{Bmatrix} 0 \\ 0 \\ g \end{Bmatrix}$$

Linear Velocity and Angular Velocity:

$$\mathbf{v}_S = \begin{Bmatrix} u_s \\ v_s \\ 0 \end{Bmatrix}, \quad \boldsymbol{\omega}_S = \begin{Bmatrix} p_s \\ q_s \\ r_s \end{Bmatrix}, \quad \boldsymbol{\omega}_{s/b} = \begin{Bmatrix} 0 \\ -\dot{\alpha} \\ 0 \end{Bmatrix}, \quad \mathbf{r} = \mathbf{r}_S = \begin{Bmatrix} X_s \\ Y_s \\ Z_s \end{Bmatrix}$$

Cross-Product Matrix:

$$\boldsymbol{\omega}_S \times (\cdot) = \Omega_S(\cdot) = \begin{bmatrix} 0 & -r_s & q_s \\ r_s & 0 & -p_s \\ -q_s & p_s & 0 \end{bmatrix} (\cdot)$$

$$\boldsymbol{\omega}_S \times \left(\boldsymbol{\omega}_S \times (\cdot)\right) = \Omega_S{}^2(\cdot) = \begin{bmatrix} 0 & -r_s & q_s \\ r_s & 0 & -p_s \\ -q_s & p_s & 0 \end{bmatrix}^2 (\cdot)$$

$$\boldsymbol{\omega}_{s/b} \times (\cdot) = \Omega_{s/b}(\cdot) = \begin{bmatrix} 0 & 0 & -\dot{\alpha} \\ 0 & 0 & 0 \\ \dot{\alpha} & 0 & 0 \end{bmatrix} (\cdot)$$

Inertia Matrix:

$$\mathrm{J}_s = C_{s/b} \mathrm{J}_b C_{s/b}^T = \begin{bmatrix} I_{xx}^s & -I_{xy}^s & -I_{xz}^s \\ -I_{xy}^s & I_{yy}^s & -I_{yz}^s \\ -I_{xz}^s & -I_{yz}^s & I_{zz}^s \end{bmatrix}$$

$$\mathrm{J}_s^{-1} = \frac{1}{\Delta^s} \begin{bmatrix} I_{yy}^s I_{zz}^s - \left(I_{yz}^s\right)^2 & I_{yz}^s I_{xz}^s + I_{xy}^s I_{zz}^s & I_{xy}^s I_{yz}^s + I_{xz}^s I_{yy}^s \\ I_{yz}^s I_{xz}^s + I_{xy}^s I_{zz}^s & I_{zz}^s I_{xx}^s - (I_{xz}^s)^2 & I_{xy}^s I_{xz}^s + I_{yz}^s I_{xx}^s \\ I_{xy}^s I_{yz}^s + I_{xz}^s I_{yy}^s & I_{xy}^s I_{xz}^s + I_{yz}^s I_{xx}^s & I_{xx}^s I_{yy}^s - \left(I_{xy}^s\right)^2 \end{bmatrix} = \frac{1}{\Delta^s} \begin{bmatrix} k_1^s & k_2^s & k_3^s \\ k_2^s & k_4^s & k_5^s \\ k_3^s & k_5^s & k_6^s \end{bmatrix}$$

$$\Delta^s = I_{xx}^s I_{yy}^s I_{zz}^s - 2 I_{xy}^s I_{yz}^s I_{xz}^s - I_{xx}^s \left(I_{yz}^s\right)^2 - I_{yy}^s (I_{xz}^s)^2 - I_{zz}^s \left(I_{xy}^s\right)^2$$

$$I_{xx}^s = (I_{xx}^b \cos^2 \alpha + I_{zz}^b \sin^2 \alpha - I_{xz}^b \sin 2\alpha)$$

$$I_{yy}^s = I_{yy}^b$$

$$I_{zz}^s = I_{xx}^b \sin^2 \alpha + I_{zz}^b \cos^2 \alpha + I_{xz}^b \sin 2\alpha$$

$$I_{xy}^s = I_{xy}^b \cos \alpha + I_{yz}^b \sin \alpha$$

$$I_{xz}^s = \tfrac{1}{2}(I_{xx}^b - I_{zz}^b) \sin 2\alpha + I_{xz}^b \cos 2\alpha$$

$$I_{yz}^s = I_{yz}^b \cos \alpha - I_{xy}^b \sin \alpha$$

where I_{xx}^s, I_{yy}^s, I_{zz}^s denote moments of inertia and I_{xy}^s, I_{yz}^s, I_{xz}^s denote products of inertia for the stability-frame

2.6.2 Kinematic Equations

The inertial translational positions (X_s, Y_s, Z_s) of an aircraft referenced at the cg are obtained by relating the stability-frame translational velocities to the inertial velocities by the appropriate transformation matrix. This calculation is accomplished by the Euler angle (ϕ_s, θ_s, ψ_s) transformation as

$$\begin{Bmatrix} \dot{X}_s \\ \dot{Y}_s \\ \dot{Z}_s \end{Bmatrix} = C_{I/s} \begin{Bmatrix} u_s \\ v_s \\ 0 \end{Bmatrix} \tag{2.61}$$

or

$$\begin{aligned} \dot{X}_s &= (\cos\theta_s \cos\psi_s)u_s + (-\cos\phi_s \sin\psi_s + \sin\phi_s \sin\theta_s \cos\psi_s)v_s \\ \dot{Y}_s &= (\cos\theta_s \sin\psi_s)u_s + (\cos\phi_s \cos\psi_s + \sin\phi_s \sin\theta_s \sin\psi_s)v_s \\ \dot{Z}_s &= (-\sin\theta_s)u_s + (\sin\phi_s \cos\theta_s)v_s \end{aligned} \tag{2.62}$$

Alternatively, the same task is accomplished by applying an intermediate transformation between stability-body frames (aerodynamic angles α) and then body-inertial frames (Euler angles ϕ_b, θ_b and ψ_b) as

$$\begin{Bmatrix} \dot{X}_s \\ \dot{Y}_s \\ \dot{Z}_s \end{Bmatrix} = C_{I/b} C_{b/s} \begin{Bmatrix} u_s \\ v_s \\ 0 \end{Bmatrix} \tag{2.63}$$

or, in an expanded form

$$\begin{aligned} \dot{X}_s &= \left(\cos\alpha \cos\theta_b \cos\psi_b + \sin\alpha \left(\sin\phi_b \sin\psi_b + \cos\phi_b \sin\theta_b \cos\psi_b\right)\right)u_s \\ &\quad + (-\cos\phi_b \sin\psi_b + \sin\phi_b \sin\theta_b \cos\psi_b)v_s \\ \dot{Y}_s &= \left(\cos\alpha \cos\theta_b \sin\psi_b + \sin\alpha \left(-\sin\phi_b \cos\psi_b + \cos\phi_b \sin\theta_b \sin\psi_b\right)\right)u_s \\ &\quad + (\cos\phi_b \cos\psi_b + \sin\phi_b \sin\theta_b \sin\psi_b)v_s \\ \dot{Z}_s &= (-\cos\alpha \sin\theta_b + \sin\alpha \cos\phi_b \cos\theta_b)u_s + (\sin\phi_b \cos\theta_b)v_s \end{aligned} \tag{2.64}$$

The orientation of the stability-frame can be described relative to an inertial-frame by a sequence of Euler rotations, as discussed in Section 2.3.3. The Euler angle rates ($\dot{\phi}_s$, $\dot{\theta}_s$, $\dot{\psi}_s$) can be resolved into components relative to the body-fixed angular velocities. Hence, the three Euler body rotation relationships are

$$\begin{aligned}\dot{\phi}_s &= p_s + (\tan\theta_s \sin\phi_s)q_s + (\tan\theta_s \cos\phi_s)r_s \\ \dot{\theta}_s &= (\cos\phi_s)q_s - (\sin\phi_s)r_s \\ \dot{\psi}_s &= (\sin\phi_s / \cos\theta_s)q_s + (\cos\phi_s / \cos\theta_s)r_s\end{aligned} \tag{2.65}$$

Here, the complete motion of an aircraft is described by the two body linear translational velocities and one aerodynamic angle (u_s, v_s, α) and the three body angular velocities (p_s, q_s, r_s). However, to track the path and orientation of the aircraft, three inertial linear positions (X_s, Y_s, Z_s) and three angular attitudes (ϕ_s, θ_s, ψ_s) are used. Therefore, the complete state vector of a nonlinear aircraft model for the stability-frame at the cg is

$$\mathbf{x}_s = [u_s \quad v_s \quad \alpha \quad \phi_s \quad \theta_s \quad \psi_s \quad p_s \quad q_s \quad r_s \quad X_s \quad Y_s \quad Z_s]^T$$

2.7 Wind-Frame Equations of Motion

The wind-frame also is a special aircraft-carried frame that is referenced at the aircraft center of gravity, as shown in Figure 2.1. The wind-frame undergoes a two rotation sequence: a left-handed rotation α about the body y_b-axis, followed by a right-handed rotation β about the stability z_s-axis. Further, the wind-frame experiences an angular velocity of $-\dot{\alpha}$ with respect to the body-frame $x_b y_b z_b$, and an angular velocity of $\dot{\beta}$ with respect to stability-frame $x_s y_s z_s$. The sideslip angle derivative $\dot{\beta}$ can be obtained by direct differentiation and manipulation of Equation (2.2).

$$\dot{\beta} = \frac{(u_b^2 + w_b^2)\dot{v}_b - v_b u_b \dot{u}_b - v_b w_b \dot{w}_b}{(u_b^2 + v_b^2 + w_b^2)\sqrt{u_b^2 + w_b^2}} \tag{2.66}$$

More discussion of this frame was provided in Section 2.2.4. Table 2.4 lists vector and matrix components that are used in the derivation of equations of motion in the wind-frame of reference. Note the velocity vector lies on the x_w-axis, thus the y_w and z_w velocity components are zero ($v_w = 0$, $w_w = 0$) and the x_w component is the aircraft total velocity ($u_w = V_T$).

2.7.1 Kinetic Equations

The derivation here is exactly similar to that found in Section 2.6. Therefore, the linear acceleration vector in the wind-frame $x_w y_w z_w$ can now be expressed explicitly as

$$\dot{\mathbf{v}}_w = -\Omega_{w/b}\mathbf{v}_w - \Omega_w \mathbf{v}_w + \frac{1}{m}\sum \mathbf{F}_w \tag{2.67}$$

The angular velocity of the wind-frame with respect to the body-frame is

$$\boldsymbol{\omega}_{w/b} = \boldsymbol{\omega}_{w/s} + \boldsymbol{\omega}_{s/b} \tag{2.68}$$

where both $\boldsymbol{\omega}_{w/s}$ and $\boldsymbol{\omega}_{s/b}$ must be described in the wind-frame. Thus

$$\boldsymbol{\omega}_{w/b} = \begin{Bmatrix} 0 \\ 0 \\ \dot{\beta} \end{Bmatrix} + C_{w/s} \begin{Bmatrix} 0 \\ -\dot{\alpha} \\ 0 \end{Bmatrix} \tag{2.69}$$

or

$$\boldsymbol{\omega}_{w/b} = \begin{Bmatrix} -\dot{\alpha}\sin\beta \\ -\dot{\alpha}\cos\beta \\ \dot{\beta} \end{Bmatrix} \tag{2.70}$$

Substitute and expand to get three scalar linear accelerations equations.

$$\begin{aligned} \dot{u}_w &= g(-\cos\alpha\cos\beta\sin\theta_b + \sin\beta\sin\phi_b\cos\theta_b + \sin\alpha\cos\beta\cos\phi_b\cos\theta_b) + \frac{1}{m}F_{x,w} \\ \dot{\alpha} &= -\frac{1}{\cos\beta}q_w + \frac{g}{u_w\cos\beta}(\sin\alpha\sin\theta_b + \cos\alpha\cos\phi_b\cos\theta_b) + \frac{1}{mu_w\cos\beta}F_{z,w} \\ \dot{\beta} &= -r_w + \frac{g}{u_w}(\cos\alpha\sin\beta\sin\theta_b + \cos\beta\sin\phi_b\cos\theta_b - \sin\alpha\sin\beta\cos\phi_b\cos\theta_b) \\ &\quad + \frac{1}{mu_w}F_{y,w} \end{aligned} \tag{2.71}$$

If the transformation $C_{w/I}$ is used instead of $C_{w/s}C_{s/b}C_{b/I}$ for the gravity terms, then Equation (2.71) becomes

$$\begin{aligned} \dot{u}_w &= g(\sin\theta_w) + \frac{1}{m}F_{x,w} \\ \dot{\alpha} &= -\frac{1}{\cos\beta}q_w + \frac{g}{u_w\cos\beta}(\cos\phi_w\cos\theta_w) + \frac{1}{mu_w\cos\beta}F_{z,w} \\ \dot{\beta} &= -r_w + \frac{g}{u_w}(\sin\phi_w\cos\theta_w) + \frac{1}{mu_w}F_{y,w} \end{aligned} \tag{2.72}$$

Similarly, the moment equation represented by Equation (2.36) is rewritten here in the wind-frame $x_w y_w z_w$ using a similar derivation as in Section 2.6.

$$\dot{\boldsymbol{\omega}}_w = -\Omega_{w/b}\boldsymbol{\omega}_w + \mathrm{J}_w^{-1}(-\Omega_w \mathrm{J}_w \boldsymbol{\omega}_w + \sum \mathbf{M}_w) \tag{2.73}$$

Substitute and expand to get three scalar angular accelerations equations.

$$\dot{p}_w = \left(r_w\dot{\alpha}\cos\beta + q_w\dot{\beta}\right)$$

$$+ \frac{1}{\Delta^w}\left[k_1^w\left\{\left(I_{yy}^w - I_{zz}^w\right)q_w r_w + I_{yz}^w\left(q_w^2 - r_w^2\right) + \left(I_{xz}^w q_w - I_{xy}^w r_w\right)p_w + L_w\right\}\right.$$

$$+ k_2^w\left\{\left(I_{zz}^w - I_{xx}^w\right)p_w r_w + I_{xz}^w\left(r_w^2 - p_w^2\right) + \left(I_{xy}^w r_w - I_{yz}^w p_w\right)q_w + M_w\right\}$$

$$\left. + k_3^w\left\{\left(I_{xx}^w - I_{yy}^w\right)p_w q_w + I_{xy}^w\left(p_w^2 - q_w^2\right) + \left(I_{yz}^w p_w - I_{xz}^w q_w\right)r_w + N_w\right\}\right]$$

$$\dot{q}_w = \left(-r_w\dot{\alpha}\sin\beta - p_w\dot{\beta}\right)$$

$$+ \frac{1}{\Delta^w}\left[k_2^w\left\{\left(I_{yy}^w - I_{zz}^w\right)q_w r_w + I_{yz}^w\left(q_w^2 - r_w^2\right) + \left(I_{xz}^w q_w - I_{xy}^w r_w\right)p_w + L_w\right\}\right. \quad (2.74)$$

$$+ k_4^w\left\{\left(I_{zz}^w - I_{xx}^w\right)p_w r_w + I_{xz}^w\left(r_w^2 - p_w^2\right) + \left(I_{xy}^w r_w - I_{yz}^w p_w\right)q_w + M_w\right\}$$

$$\left. + k_5^w\left\{\left(I_{xx}^w - I_{yy}^w\right)p_w q_w + I_{xy}^w\left(p_w^2 - q_w^2\right) + \left(I_{yz}^w p_w - I_{xz}^w q_w\right)r_w + N_w\right\}\right]$$

$$\dot{r}_w = \left(q_w\dot{\alpha}\sin\beta - p_w\dot{\alpha}\cos\beta\right)$$

$$+ \frac{1}{\Delta^w}\left[k_3^w\left\{\left(I_{yy}^w - I_{zz}^w\right)q_w r_w + I_{yz}^w\left(q_w^2 - r_w^2\right) + \left(I_{xz}^w q_w - I_{xy}^w r_w\right)p_w + L_w\right\}\right.$$

$$+ k_5^w\left\{\left(I_{zz}^w - I_{xx}^w\right)p_w r_w + I_{xz}^w\left(r_w^2 - p_w^2\right) + \left(I_{xy}^w r_w - I_{yz}^w p_w\right)q_w + M_w\right\}$$

$$\left. + k_6^w\left\{\left(I_{xx}^w - I_{yy}^w\right)p_w q_w + I_{xy}^w\left(p_w^2 - q_w^2\right) + \left(I_{yz}^w p_w - I_{xz}^w q_w\right)r_w + N_w\right\}\right]$$

Table 2.4 Vector and matrix definitions for wind-frame

Force, Moment and Gravity:

$$\Sigma \mathbf{F}_w = \begin{Bmatrix} F_{x,w} \\ F_{y,w} \\ F_{z,w} \end{Bmatrix} + C_{w/I} m\mathbf{g}, \quad \Sigma \mathbf{M}_w = \begin{Bmatrix} L_w \\ M_w \\ N_w \end{Bmatrix}, \quad \mathbf{g} = \begin{Bmatrix} 0 \\ 0 \\ g \end{Bmatrix}$$

Linear Velocity and Angular Velocity:

$$\mathbf{v}_w = \begin{Bmatrix} u_w (= V_T) \\ 0 \\ 0 \end{Bmatrix}, \quad \boldsymbol{\omega}_w = \begin{Bmatrix} p_w \\ q_w \\ r_w \end{Bmatrix}, \quad \boldsymbol{\omega}_{w/b} = \begin{Bmatrix} -\dot{\alpha} \sin\beta \\ -\dot{\alpha} \cos\beta \\ \dot{\beta} \end{Bmatrix}, \quad \mathbf{r} = \mathbf{r}_w = \begin{Bmatrix} X_w \\ Y_w \\ Z_w \end{Bmatrix}$$

Cross-Product Matrix:

$$\boldsymbol{\omega}_w \times (\cdot) = \Omega_w (\cdot) = \begin{bmatrix} 0 & -r_w & q_w \\ r_w & 0 & -p_w \\ -q_w & p_w & 0 \end{bmatrix} (\cdot)$$

$$\boldsymbol{\omega}_w \times \left(\boldsymbol{\omega}_w \times (\cdot)\right) = \Omega_w{}^2 (\cdot) = \begin{bmatrix} 0 & -r_w & q_w \\ r_w & 0 & -p_w \\ -q_w & p_w & 0 \end{bmatrix}^2 (\cdot)$$

$$\boldsymbol{\omega}_{w/b} \times (\cdot) = \Omega_{w/b} (\cdot) = \begin{bmatrix} 0 & -\dot{\beta} & -\dot{\alpha}\cos\beta \\ \dot{\beta} & 0 & \dot{\alpha}\sin\beta \\ \dot{\alpha}\cos\beta & -\dot{\alpha}\sin\beta & 0 \end{bmatrix} (\cdot)$$

Inertia Matrix:

$$\mathrm{J}_w = C_{w/b} \mathrm{J}_b C_{w/b}^T = C_{w/s} C_{s/b} \mathrm{J}_b C_{s/b}^T C_{w/s}^T = \begin{bmatrix} I_{xx}^w & -I_{xy}^w & -I_{xz}^w \\ -I_{xy}^w & I_{yy}^w & -I_{yz}^w \\ -I_{xz}^w & -I_{yz}^w & I_{zz}^w \end{bmatrix}$$

$$\mathrm{J}_w^{-1} = \frac{1}{\Delta^w} \begin{bmatrix} I_{yy}^w I_{zz}^w - \left(I_{yz}^w\right)^2 & I_{yz}^w I_{xz}^w + I_{xy}^w I_{zz}^w & I_{xy}^w I_{yz}^w + I_{xz}^w I_{yy}^w \\ I_{yz}^w I_{xz}^w + I_{xy}^w I_{zz}^w & I_{zz}^w I_{xx}^w - \left(I_{xz}^w\right)^2 & I_{xy}^w I_{xz}^w + I_{yz}^w I_{xx}^w \\ I_{xy}^w I_{yz}^w + I_{xz}^w I_{yy}^w & I_{xy}^w I_{xz}^w + I_{yz}^w I_{xx}^w & I_{xx}^w I_{yy}^w - \left(I_{xy}^w\right)^2 \end{bmatrix} = \frac{1}{\Delta^w} \begin{bmatrix} k_1^w & k_2^w & k_3^w \\ k_2^w & k_4^w & k_5^w \\ k_3^w & k_5^w & k_6^w \end{bmatrix}$$

$$\Delta^w = I_{xx}^w I_{yy}^w I_{zz}^w - 2 I_{xy}^w I_{yz}^w I_{xz}^w - I_{xx}^w \left(I_{yz}^w\right)^2 - I_{yy}^w \left(I_{xz}^w\right)^2 - I_{zz}^w \left(I_{xy}^w\right)^2$$

$$I_{xx}^w = \left(I_{xx}^b \cos^2\alpha + I_{zz}^b \sin^2\alpha - I_{xz}^b \sin 2\alpha\right) \cos^2\beta + I_{yy}^b \sin^2\beta - \left(I_{xy}^b \cos\alpha + I_{yz}^b \sin\alpha\right) \sin 2\beta$$

$$I_{yy}^w = \left(I_{xx}^b \cos^2\alpha + I_{zz}^b \sin^2\alpha - I_{xz}^b \sin 2\alpha\right) \sin^2\beta + I_{yy}^b \cos^2\beta + \left(I_{xy}^b \cos\alpha + I_{yz}^b \sin\alpha\right) \sin 2\beta$$

$$I_{zz}^w = I_{xx}^b \sin^2\alpha + I_{zz}^b \cos^2\alpha + I_{xz}^b \sin 2\alpha$$

$$I_{xy}^w = \tfrac{1}{2}\left(I_{xx}^b \cos^2\alpha + I_{zz}^b \sin^2\alpha - I_{xz}^b \sin 2\alpha - I_{yy}^b\right) \sin 2\beta + \left(I_{xy}^b \cos\alpha + I_{yz}^b \sin\alpha\right) \cos 2\beta$$

$$I_{xz}^w = \left(\tfrac{1}{2}\left(I_{xx}^b - I_{zz}^b\right) \sin 2\alpha + I_{xz}^b \cos 2\alpha\right) \cos\beta + \left(I_{yz}^b \cos\alpha - I_{xy}^b \sin\alpha\right) \sin\beta$$

$$I_{yz}^w = \left(I_{yz}^b \cos\alpha - I_{xy}^b \sin\alpha\right) \cos\beta - \left(\tfrac{1}{2}\left(I_{xx}^b - I_{zz}^b\right) \sin 2\alpha + I_{xz}^b \cos 2\alpha\right) \sin\beta$$

where I_{xx}^w, I_{yy}^w, I_{zz}^w denote moments of inertia and I_{xy}^w, I_{yz}^w, I_{xz}^w denote products of inertia for the wind-frame

2.7.2 Kinematic Equations

The inertial translational positions (X_w, Y_w, Z_w) of an aircraft referenced at the cg are obtained by relating the wind-frame translational velocities to the inertial velocities by the appropriate transformation matrix. This is accomplished by the Euler angle (ϕ_w, θ_w, ψ_w) transformation as

$$\begin{Bmatrix} \dot{X}_w \\ \dot{Y}_w \\ \dot{Z}_w \end{Bmatrix} = C_{I/w} \begin{Bmatrix} u_w \\ 0 \\ 0 \end{Bmatrix} \tag{2.75}$$

or

$$\begin{aligned} \dot{X}_w &= (\cos\theta_w \cos\psi_w)u_w \\ \dot{Y}_w &= (\cos\theta_w \sin\psi_w)u_w \\ \dot{Z}_w &= (-\sin\theta_w)u_w \end{aligned} \tag{2.76}$$

Alternatively, the same task is accomplished by using an intermediate transformation between wind-body frames (aerodynamic angles α and β) and then body-inertial frames (Euler angles ϕ_b, θ_b and ψ_b) as

$$\begin{Bmatrix} \dot{X}_w \\ \dot{Y}_w \\ \dot{Z}_w \end{Bmatrix} = C_{I/b} C_{b/w} \begin{Bmatrix} u_w \\ 0 \\ 0 \end{Bmatrix} \tag{2.77}$$

or in an expanded form

$$\begin{aligned} \dot{X}_w = \big(&\cos\alpha\cos\beta\cos\theta_b\cos\psi_b + \sin\beta\,(-\cos\phi_b\sin\psi_b + \sin\phi_b\sin\theta_b\cos\psi_b) \\ &+ \sin\alpha\cos\beta\,(\sin\phi_b\sin\psi_b + \cos\phi_b\sin\theta_b\cos\psi_b)\big)u_w \\ \dot{Y}_w = \big(&\cos\alpha\cos\beta\cos\theta_b\sin\psi_b + \sin\beta\,(\cos\phi_b\cos\psi_b + \sin\phi_b\sin\theta_b\sin\psi_b) \\ &+ \sin\alpha\cos\beta\,(-\sin\phi_b\cos\psi_b + \cos\phi_b\sin\theta_b\sin\psi_b)\big)u_w \\ \dot{Z}_w = (&-\cos\alpha\cos\beta\sin\theta_b + \sin\beta\sin\phi_b\cos\theta_b + \sin\alpha\cos\beta\cos\phi_b\cos\theta_b)u_w \end{aligned} \tag{2.78}$$

The orientation of the wind-frame can be described relative to an inertial-frame by a sequence of Euler rotations, as discussed in Section 2.3.4. The Euler angle rates ($\dot{\phi}_w$, $\dot{\theta}_w$, $\dot{\psi}_w$) can be resolved into components relative to the body-fixed angular velocities. Hence, the three Euler body rotation relationships are

$$\begin{aligned} \dot{\phi}_w &= p_w + (\tan\theta_w \sin\phi_w)q_w + (\tan\theta_w \cos\phi_w)r_w \\ \dot{\theta}_w &= (\cos\phi_w)q_w - (\sin\phi_w)r_w \\ \dot{\psi}_w &= (\sin\phi_w / \cos\theta_w)q_w + (\cos\phi_w / \cos\theta_w)r_w \end{aligned} \tag{2.79}$$

Here, the complete motion of an aircraft is described by the single body linear translational velocity and two aerodynamic angles (u_w, α, β), and the three body angular velocities (p_w, q_w, r_w). However, to track the path and the orientation of the aircraft, three inertial linear positions (X_w, Y_w, Z_w) and three angular attitudes (ϕ_w, θ_w, ψ_w) are used. Therefore, the complete state vector of a nonlinear aircraft model for the wind-frame at the cg is

$$\mathbf{x}_w = [u_w \quad \alpha \quad \beta \quad \phi_w \quad \theta_w \quad \psi_w \quad p_w \quad q_w \quad r_w \quad X_w \quad Y_w \quad Z_w]^T$$

CHAPTER 3

THEORY OF NONLINEARITY INDEX

3.1 Introduction

One way to systematically assess an aircraft's nonlinearity is to apply nonlinear index theory [27]. Consider a general time-varying nonlinear state-space system with input and initial condition excitation as [36]

$$\begin{aligned} \dot{\mathbf{x}} &= \mathbf{f}(t, \mathbf{x}, \mathbf{u}) \\ \mathbf{y} &= \mathbf{g}(t, \mathbf{x}, \mathbf{u}) \\ \mathbf{x}(t_0) &= \mathbf{x}_0 \end{aligned} \tag{3.1}$$

where $\mathbf{x} \in \Re^n$, $\mathbf{u} \in \Re^p$, $\mathbf{y} \in \Re^m$ denote the state vector, the input vector, and the output vector, respectively. The system nonlinearities are denoted by $\mathbf{f} \in \Re^n$ and $\mathbf{g} \in \Re^m$. Note that the nonlinear aircraft dynamic model considered previously in Chapter 2 lies within this general class of systems.

A time-varying linear state-space model can be obtained by applying the Taylor series expansion to Equation (3.1), yielding

$$\begin{aligned} \delta\dot{\mathbf{x}} &= \bar{A}(t)\delta\mathbf{x} + \bar{B}(t)\delta\mathbf{u} \\ \delta\mathbf{y} &= \bar{C}(t)\delta\mathbf{x} + \bar{D}(t)\delta\mathbf{u} \\ \delta\mathbf{x}(t_0) &= \delta\mathbf{x}_0 \end{aligned} \tag{3.2}$$

where $\bar{A}(t) \in \Re^{n\times n}$, $\bar{B}(t) \in \Re^{n\times p}$, $\bar{C}(t) \in \Re^{m\times n}$, $\bar{D}(t) \in \Re^{m\times p}$ denote the state dynamic, input distribution, output distribution, and direct input-output matrices, respectively. Matrices $\bar{A}(t)$, $\bar{B}(t)$, $\bar{C}(t)$, and $\bar{D}(t)$ are the Jacobians or first partial derivatives of functions **f** and **g** with respect to the variables **x** and **u**, and are evaluated at

the equilibrium reference state $\bar{\mathbf{x}}_0$. Another linear state-space model is obtained at the full or deviated reference state $\mathbf{x}_0$, where $\mathbf{x}_0 = \bar{\mathbf{x}}_0 + \delta\mathbf{x}_0$ and $\delta\mathbf{x}_0$ is a bounded deviation about the equilibrium reference with $\|\delta\mathbf{x}_0\| \leq \delta\mathbf{x}_{\max}$.

$$\begin{aligned} \delta\dot{\mathbf{x}} &= A(t)\delta\mathbf{x} + B(t)\delta\mathbf{u} \\ \delta\mathbf{y} &= C(t)\delta\mathbf{x} + D(t)\delta\mathbf{u} \\ \delta\mathbf{x}(t_0) &= \delta\mathbf{x}_0 \end{aligned} \tag{3.3}$$

3.2 Static Nonlinearity Index

The generalized static nonlinearity indices used to measure the strength of the system nonlinearity are

$$\begin{aligned} \nu_S^A(t,t_0) &= \sup_{\|\delta x_0\| \leq \delta x_{\max}} \frac{\|A(t) - \bar{A}(t)\|}{\|\bar{A}(t)\|} \\ \nu_S^B(t,t_0) &= \sup_{\|\delta x_0\| \leq \delta x_{\max}} \frac{\|B(t) - \bar{B}(t)\|}{\|\bar{B}(t)\|} \\ \nu_S^C(t,t_0) &= \sup_{\|\delta x_0\| \leq \delta x_{\max}} \frac{\|C(t) - \bar{C}(t)\|}{\|\bar{C}(t)\|} \\ \nu_S^D(t,t_0) &= \sup_{\|\delta x_0\| \leq \delta x_{\max}} \frac{\|D(t) - \bar{D}(t)\|}{\|\bar{D}(t)\|} \end{aligned} \tag{3.4}$$

where ν_S^A, ν_S^B, ν_S^C, ν_S^D are the static state, static input, static output, and static direct nonlinearity indices. These four indices capture the deviation of matrices A, B, C, and D across the subregion of equilibrium condition variation relative to the nominal matrices $\bar{A}$, $\bar{B}$, $\bar{C}$, and $\bar{D}$ associated with the center point of this subregion [23]. These deviations give a measure of the nonlinearity strength of the dynamic model, and also indicate the source of the nonlinearity. The static indices ν_S^A and ν_S^C address the nonlinearities associated with initial condition excitation, whereas the static indices ν_S^B and ν_S^D address

the nonlinearities associated with input excitation. Note that, since the linear model is time-varying, the indices are also time-varying.

3.3 Dynamic Nonlinearity Index

In order to account for the dynamic deviation of the system, the state transition matrix of the linear system is utilized. Define the generalized dynamic nonlinearity indices as

$$
\begin{aligned}
\nu_d^x(t,\tau) &= \sup_{\|\delta x_0\| \le \delta x_{\max}} \frac{\|\Phi(t,\tau) - \bar{\Phi}(t,\tau)\|}{\|\bar{\Phi}(t,\tau)\|} \\
\nu_d^u(t,\tau) &= \sup_{\|\delta x_0\| \le \delta x_{\max}} \frac{\|\Phi(t,\tau)B(\tau) - \bar{\Phi}(t,\tau)\bar{B}(\tau)\|}{\|\bar{\Phi}(t,\tau)\bar{B}(\tau)\|} \\
\nu_d^y(t,\tau) &= \sup_{\|\delta x_0\| \le \delta x_{\max}} \frac{\|C(t)\Phi(t,\tau) - \bar{C}(t)\bar{\Phi}(t,\tau)\|}{\|\bar{C}(t)\bar{\Phi}(t,\tau)\|} \\
\nu_d^{y/u}(t,\tau) &= \sup_{\|\delta x_0\| \le \delta x_{\max}} \frac{\|C(t)\Phi(t,\tau)B(\tau) - \bar{C}(t)\bar{\Phi}(t,\tau)\bar{B}(\tau)\|}{\|\bar{C}(t)\bar{\Phi}(t,\tau)\bar{B}(\tau)\|}
\end{aligned}
\tag{3.5}
$$

where ν_d^x, ν_d^u, ν_d^y, $\nu_d^{y/u}$ are the dynamic state, dynamic input, dynamic output, and dynamic input-output nonlinearity indices, respectively. Matrices $\Phi(t,\tau)$ and $\bar{\Phi}(t,\tau)$ are the transition matrices for $A(t)$ and $\bar{A}(t)$ evaluated at $\mathbf{x}_0 = \bar{\mathbf{x}}_0 + \delta\mathbf{x}_0$ and $\bar{\mathbf{x}}_0$, respectively. The four dynamic indices capture the deviation of the four main system transmission paths across the local subregion of the operating point (the term operating point is considered here rather than initial condition). The four main system transmission paths are state-to-state, input-to-state, state-to-output, and input-to-output. Similar to the static indices, the dynamic indices are used to measure the strength and indicate the source of the nonlinearity.

3.4 Parametrized Nonlinearity Index

The previous development is for a single point index analysis at $\bar{\mathbf{x}}_0$. To perform index analysis across multiple points, for example within the traditional speed-altitude flight envelope [27] or within the new aerodynamic attitude flight envelope in Chapters 4 and 5, the indices must be parameterized. Parameter vector $\boldsymbol{\lambda}(t)$ is introduced to extend the concept of the generalized nonlinearity index to a parameterized full-envelope aircraft model. The parameter vector, which is measurable and bounded but may be unknown, is defined to capture the system nonlinearity and can incorporate time-varying characteristics indirectly. Depending on the linearization point $\mathbf{x}_0$ or $\bar{\mathbf{x}}_0$, the nonlinear governing equations of the aircraft model can be approximated by a time invariant but linear parameter-varying (*LPV*) system as

$$\begin{bmatrix}\delta\dot{\mathbf{x}}(t)\\ \delta\mathbf{y}(t)\end{bmatrix} = \begin{bmatrix}\bar{A}(\boldsymbol{\lambda}(t)) & \bar{B}(\boldsymbol{\lambda}(t))\\ \bar{C}(\boldsymbol{\lambda}(t)) & \bar{D}(\boldsymbol{\lambda}(t))\end{bmatrix}\begin{bmatrix}\delta\mathbf{x}(t)\\ \delta\mathbf{u}(t)\end{bmatrix} \qquad (3.6)$$

$$\delta\mathbf{x}(t_0) = \delta\mathbf{x}_0$$

or

$$\begin{bmatrix}\delta\dot{\mathbf{x}}(t)\\ \delta\mathbf{y}(t)\end{bmatrix} = \begin{bmatrix}A(\boldsymbol{\lambda}(t)) & B(\boldsymbol{\lambda}(t))\\ C(\boldsymbol{\lambda}(t)) & D(\boldsymbol{\lambda}(t))\end{bmatrix}\begin{bmatrix}\delta\mathbf{x}(t)\\ \delta\mathbf{u}(t)\end{bmatrix} \qquad (3.7)$$

$$\delta\mathbf{x}(t_0) = \delta\mathbf{x}_0$$

The advantages and disadvantages of different *LPV* methods are discussed in [37]. The most common linearization technique, which is the Jacobian linearization, is implemented in this work to generate the linear approximation model of a high-fidelity aircraft model. The Jacobian method uses the first-dimensional derivatives of the nonlinear state-space model to generate the *LPV* model at different equilibrium points. Depending on the nature of the motion and the *LPV* envelope size, scheduling parameters

such as the angle of attack, sideslip angle, altitude, and/or Mach number are selected. Then the variation of the Jacobians is modeled as functions of one or more scheduling parameters. This process gives a set of linear systems over these equilibrium points approximating the nonlinear dynamics model.

Following Reference [27], in this dissertation, the varying parameter vector $\boldsymbol{\lambda} = [\alpha_0 \quad \beta_0]^T$ is considered to represent the asymmetric level rectilinear attack-sideslip angle flight envelope. The linear system matrices C and D are not considered here. Four parameterized indices in terms of the varying parameter vector $\boldsymbol{\lambda}$ are utilized to measure the nonlinearity strength: two static and two dynamic indices. Using nominal points denoted by $\boldsymbol{\lambda}_j$ and perturbed points denoted by $\boldsymbol{\lambda}_i$, the relevant nonlinearity indices from Equations (3.4) and (3.5) are

$$\begin{aligned} \nu_s^A(\boldsymbol{\lambda}_j) &= \sup_{i=1,\ldots,N} \frac{\|A_i(\boldsymbol{\lambda}_i) - \bar{A}_j(\boldsymbol{\lambda}_j)\|}{\|\bar{A}_j(\boldsymbol{\lambda}_j)\|} \\ \nu_s^B(\boldsymbol{\lambda}_j) &= \sup_{i=1,\ldots,N} \frac{\|B_i(\boldsymbol{\lambda}_i) - \bar{B}_j(\boldsymbol{\lambda}_j)\|}{\|\bar{B}_j(\boldsymbol{\lambda}_j)\|} \end{aligned} \tag{3.8}$$

$$\begin{aligned} \nu_d^x(t, \boldsymbol{\lambda}_j) &= \sup_{i=1,\ldots,N} \frac{\|\Phi_i(t, \boldsymbol{\lambda}_i) - \bar{\Phi}_j(t, \boldsymbol{\lambda}_j)\|}{\|\bar{\Phi}_j(t, \boldsymbol{\lambda}_j)\|} \\ \nu_d^u(t, \boldsymbol{\lambda}_j) &= \sup_{i=1,\ldots,N} \frac{\|\Phi_i(t, \boldsymbol{\lambda}_i)B_i(\boldsymbol{\lambda}_i) - \bar{\Phi}_j(t, \boldsymbol{\lambda}_j)\bar{B}_j(\boldsymbol{\lambda}_j)\|}{\|\bar{\Phi}_j(t, \boldsymbol{\lambda}_j)\bar{B}_j(\boldsymbol{\lambda}_j)\|} \end{aligned} \tag{3.9}$$

where ν_s^A, ν_s^B, ν_d^x, ν_d^u are the static state, static input, dynamic state, and dynamic input nonlinearity indices at operating condition $\boldsymbol{\lambda}_j = [\alpha_{0j} \quad \beta_{0j}]^T$, respectively, and N is the total number of points in the perturbation subregion.

These proposed nonlinearity indices capture the maximum deviation between the nominal linear model $\{\bar{A}_j(\boldsymbol{\lambda}_j), \bar{B}_j(\boldsymbol{\lambda}_j)\}$ and any generated linear model $\{A_i(\boldsymbol{\lambda}_i), B_i(\boldsymbol{\lambda}_i)\}$ at point $\boldsymbol{\lambda}_i = [\alpha_{0i} \quad \beta_{0i}]^T$ within the perturbation subregion. The static state nonlinearity index ν_s^A measures the variation of the state dynamics matrix within the subregion, whereas ν_d^x measures the variation of the time propagation of the state signal. Over the subregion, both nonlinearity indices ν_s^B and ν_d^u measure similar effects associated with the input signal.

CHAPTER 4

AERODYNAMIC ATTITUDE FLIGHT ENVELOPE

4.1 Introduction

The traditional symmetric level speed-altitude envelope is commonly used to describe the operational range of an aircraft. A new nontraditional envelope is developed to assist, in conjunction with the traditional envelope, efforts regarding design requirement specification and satisfication, dynamic analysis over differing flight phases, control synthesis using scheduling principles, or comparison of capabilities of different airframes. An extension of the speed-altitude envelope concept is the asymmetric level aerodynamic attitude envelope, which describes the extent of where the airplane can sustain a slipping horizontal flight condition. This envelope is presented as the angle of attack vs. sideslip angle region where the indicated condition is possible. Fundamentally, this region describes the asymmetric trimability, control power authority, and poststall domain of an aircraft, and thus it can be utilized in similar ways to the traditional flight envelope. The angle of attack vs. sideslip angle flight envelope, which shall be referred to as the $\alpha - \beta$ flight envelope, can be constructed for any altitude, but is restricted to sea level altitude in this dissertation. The main factors which determine the size of the $\alpha - \beta$ flight envelope are aerodynamics, propulsion, structural dynamics, atmospheric conditions, and control surface deflections.

4.2 Envelope Development Methodology

The $\alpha - \beta$ flight envelope can be developed by searching for an equilibrium solution vector to the nonlinear equations of motion of an aircraft. The derivation of the twelve equations of motion of an aircraft was covered thoroughly in Chapter 2. Equations (2.45) and (2.48)-(2.50) are the common 6-DOF nonlinear equations of motion for a body referenced at the center of gravity. Additionally, inertial symmetry about the $x_b z_b$ plane is assumed, so $I_{xy}^b = I_{yz}^b = 0$. These equations are repeated here and numbered individually.

$$\dot{u}_b = r_b v_b - q_b w_b - g \sin\theta_b + \frac{1}{m} F_{x,b} \tag{4.1}$$

$$\dot{v}_b = -r_b u_b + p_b w_b - g \sin\phi_b \cos\theta_b + \frac{1}{m} F_{y,b} \tag{4.2}$$

$$\dot{w}_b = q_b u_b - p_b v_b - g \cos\phi_b \cos\theta_b + \frac{1}{m} F_{z,b} \tag{4.3}$$

$$\begin{aligned} \dot{p}_b = \left(\frac{1}{I_{xx}^b I_{zz}^b - \left(I_{xz}^b\right)^2}\right)\Big[I_{zz}^b\{(I_{yy}^b - I_{zz}^b)q_b r_b + I_{xz}^b p_b q_b + L_b\} \\ + I_{xz}^b\{(I_{xx}^b - I_{yy}^b)p_b q_b - I_{xz}^b q_b r_b + N_b\}\Big] \end{aligned} \tag{4.4}$$

$$\dot{q}_b = \left(\frac{1}{I_{yy}^b}\right)\left[(I_{zz}^b - I_{xx}^b)p_b r_b + I_{xz}^b(r_b^2 - p_b^2) + M_b\right] \tag{4.5}$$

$$\begin{aligned} \dot{r}_b = \left(\frac{1}{I_{xx}^b I_{zz}^b - \left(I_{xz}^b\right)^2}\right)\Big[I_{xz}^b\{(I_{yy}^b - I_{zz}^b)q_b r_b + I_{xz}^b p_b q_b + L_b\} \\ + I_{xx}^b\{(I_{xx}^b - I_{yy}^b)p_b q_b - I_{xz}^b q_b r_b + N_b\}\Big] \end{aligned} \tag{4.6}$$

$$\dot{\phi}_b = p_b + \left(\frac{\sin\theta_b \sin\phi_b}{\cos\theta_b}\right) q_b + \left(\frac{\sin\theta_b \cos\phi_b}{\cos\theta_b}\right) r_b \tag{4.7}$$

$$\dot{\theta}_b = (\cos\phi_b)q_b - (\sin\phi_b)r_b \tag{4.8}$$

$$\dot{\psi}_b = \left(\frac{\sin\phi_b}{\cos\theta_b}\right) q_b + \left(\frac{\cos\phi_b}{\cos\theta_b}\right) r_b \tag{4.9}$$

$$\begin{aligned} \dot{X}_b = {} & (\cos\theta_b \cos\psi_b) u_b + (-\cos\phi_b \sin\psi_b + \sin\phi_b \sin\theta_b \cos\psi_b) v_b \\ & + (\sin\phi_b \sin\psi_b + \cos\phi_b \sin\theta_b \cos\psi_b) w_b \end{aligned} \tag{4.10}$$

$$\begin{aligned} \dot{Y}_b = {} & (\cos\theta_b \sin\psi_b) u_b + (\cos\phi_b \cos\psi_b + \sin\phi_b \sin\theta_b \sin\psi) v_b \\ & + (-\sin\phi_b \cos\psi_b + \cos\phi_b \sin\theta_b \sin\psi_b) w_b \end{aligned} \tag{4.11}$$

$$\dot{Z}_b = (-\sin\theta_b) u_b + (\sin\phi_b \cos\theta_b) v_b + (\cos\phi_b \cos\theta_b) w_b \tag{4.12}$$

These equations of motion are in a derivative decoupled form, since each derivative state is expressed explicitly in terms of only the state variables and inputs. Therefore, these motion equations are representable as

$$\begin{gathered} \dot{\mathbf{x}}_b = \mathbf{f}(\mathbf{x}_b, \mathbf{u}) \\ \mathbf{x}_b = [u_b \quad v_b \quad w_b \quad p_b \quad q_b \quad r_b \quad \phi_b \quad \theta_b \quad \psi_b \quad X_b \quad Y_b \quad Z_b]^T \\ \mathbf{u} = [\delta_1 \quad \delta_2 \quad \cdots \quad \delta_p]^T \end{gathered} \tag{4.13}$$

where $\mathbf{x}_b$ denotes the 12-dimensional state vector, $\mathbf{u}$ denotes the p-dimensional input vector, and $\mathbf{f}(\mathbf{x}_b, \mathbf{u})$ denotes the nonlinear coupled function representing the 12-dimensional state vector derivative.

Equations (4.10)-(4.12) are called the inertial position equations or navigation equations, and their solution depends on the solution of Equations (4.1)-(4.9), but not vice versa, assuming constant gravity and ignoring the weak coupling path of air density on altitude. Thus, Equations (4.10)-(4.12) are not retained for flight envelope calculations. All nine state variables in Equations (4.1)-(4.9) are necessary in order to describe the aircraft motion; however, neither these equations nor the forces and moments depend explicitly on the yaw angle ψ_b. Hence, the first eight equations are

sufficient to completely describe the aircraft motion and thus Equation (4.9) is also discarded from further envelope considerations. For the purpose of this work, it is convenient to replace the translational velocities u_b, v_b, w_b by the total velocity and angle of attack and sideslip angle: V_T, α, β. The relationship between the rectangular coordinates u_b, v_b, w_b and the spherical coordinates V_T, α, β is defined as

$$\begin{aligned} u_b &= V_T \cos\alpha \cos\beta & \alpha &= tan^{-1}(w_b/u_b) \\ v_b &= V_T \sin\beta & \beta &= sin^{-1}(v_b/V_T) \\ w_b &= V_T \sin\alpha \cos\beta & V_T &= (u_b^2 + v_b^2 + w_b^2)^{1/2} \end{aligned} \tag{4.14}$$

To achieve equilibrium, the motion should involve no translational and rotational accelerations. Mathematically speaking, all state derivatives appearing in Equations (4.1)-(4.8) should be identically zero or $\dot{u}_b = \dot{v}_b = \dot{w}_b = \dot{p}_b = \dot{q}_b = \dot{r}_b = \dot{\phi}_b = \dot{\theta}_b = 0$. The motion type considered when developing the $\alpha - \beta$ flight envelope is asymmetric level rectilinear flight, where the body angular rates are also identically zero or $p_b = q_b = r_b = 0$. Consequently, Equations (4.7) and (4.8) are trivially satisfied leaving only (4.1)-(4.6) in algebraic form. Because the aircraft orientation described with angles ϕ_b, θ_b, ψ_b and with angles χ, γ, σ, α, β are not independent, where χ denotes heading angle, γ denotes flight-path angle, and σ denotes aerodynamic bank angle, constraints between angles ϕ_b, θ_b, α, β must be properly accounted for. The extra required constraint equation is

$$\sin\gamma = (\cos\alpha \cos\beta)\sin\theta_b - (\sin\phi_b \sin\beta + \cos\phi_b \sin\alpha \cos\beta)\cos\theta_b \tag{4.15}$$

This equation is sometimes called the rate-of-climb constraint equation [33] where $\gamma = 0$ for the $\alpha - \beta$ envelope consideration. Therefore, the 7 algebraic equations (6 motion equations and 1 constraint equation) relevant to the $\alpha - \beta$ envelope consideration are

$$-g\sin\theta_b + \frac{\bar{q}S}{m}C_{x_{b_T}} + \frac{T}{m} = 0 \tag{4.16}$$

$$-g\cos\theta_b \sin\phi_b + \frac{\bar{q}S}{m}C_{y_{b_T}} = 0 \tag{4.17}$$

$$-g\cos\theta_b \cos\phi_b + \frac{\bar{q}S}{m}C_{z_{b_T}} = 0 \tag{4.18}$$

$$\frac{\bar{q}S\bar{b}}{I_{xx}^b}C_{l_T} = 0 \tag{4.19}$$

$$\frac{\bar{q}S\bar{c}}{I_{yy}^b}C_{m_T} = 0 \tag{4.20}$$

$$\frac{\bar{q}S\bar{b}}{I_{zz}^b}C_{n_T} = 0 \tag{4.21}$$

$$(\cos\alpha\cos\beta)\sin\theta_b - (\sin\phi_b\sin\beta + \cos\phi_b\sin\alpha\cos\beta)\cos\theta_b = 0 \tag{4.22}$$

Note the nongravitational applied loads have been expanded in terms of aerodynamic force and moment coefficients and a propulsion thrust force along the x_b-axis. These equations are representable as

$$\begin{gathered}\mathbf{g}(\mathbf{z}) = 0 \\ \mathbf{z} = [V_T \quad \alpha \quad \beta \quad \phi_b \quad \theta_b \quad \delta_1 \quad \delta_2 \quad \cdots \quad \delta_p]^T\end{gathered} \tag{4.23}$$

The high-performance aircraft (F-16) model studied here was developed in low-speed wind-tunnel facilities by the NASA Langley Research Center in 1979 [30]. The model data covers structural, aerodynamic, and propulsive characteristics. The study focuses on constant mass and inertia, however, the location of the center of mass is variable allowing different configurations to be investigated. The model represents aerodynamic and propulsive data in the form of approximately 50 look-up tables corresponding to a wide range of angle of attack α, sideslip angle β, throttle deflection δ_{th}, and control surface deflections (δ_h, δ_a, and δ_r). Aerodynamic data includes stall and

poststall conditions and propulsive data covers a wide range of altitude H and Mach number M conditions. A static engine is considered here. These data sets represent embedded nonlinearities inside the aerodynamic and propulsive coefficients. Although this model has 6 control inputs ($p = 6$): δ_h, δ_a, δ_r, δ_{th}, δ_{lef}, δ_{sb}; the leading-edge-flap and speed-brake inputs are set to zero ($\delta_{lef} = 0, \delta_{sb} = 0$).

With this, Equation (4.23) represents 7 equations in 9 variables. Trim solutions are computed by specifying 2 excess variables and solving for the remaining 7 unknowns. Two formulations are used and include

$$\mathbf{g}(\mathbf{z}) = 0 \tag{4.24}$$

where

$$\mathbf{z} = [\alpha \quad \beta \quad \theta_b \quad \delta_h \quad \delta_a \quad \delta_r \quad \delta_{th}]^T, \text{ Specified } V_T, \phi_b \tag{4.25}$$

or

$$\mathbf{z} = [V_T \quad \phi_b \quad \theta_b \quad \delta_h \quad \delta_a \quad \delta_r \quad \delta_{th}]^T, \text{ Specified } \alpha, \beta \tag{4.26}$$

A trim point on the $\alpha - \beta$ envelope boundary occurs when an explicit or implicit limit is reached. Explicit limits correspond to control input saturation or dynamic pressure restrictions, and for the F-16 model, these limits correspond to

$$\begin{gathered} -25^\circ \leq \delta_h \leq +25^\circ \\ -21.5^\circ \leq \delta_a \leq +21.5^\circ \\ -30^\circ \leq \delta_r \leq +30^\circ \\ 0 \leq \delta_{th} \leq 1 \\ \bar{q} \leq 2750 \text{ lb/ft}^2 \end{gathered} \tag{4.27}$$

Implicit limits correspond to stall and correlate to an inability of the iteration solver to converge.

4.3 Full-Envelope Results

The $\alpha - \beta$ flight envelope of the high-fidelity F-16 aircraft model is shown in Figure 4.1. This aircraft is very versatile and can sustain equilibrium conditions at both a high angle of attack and sideslip, as shown. Initial expectation was that the $\alpha - \beta$ flight envelope should be symmetric due to the symmetry of the aircraft, but the envelope shows distinct behavior at positive and negative β. At positive angles of attack, the F-16 (or its model) has enhanced ability to maintain equilibrium flight with large negative sideslip angles and a much lesser ability for positive sideslip, whereas the aircraft can maintain large positive sideslip angles with negative angles of attack but no corresponding region for negative sideslip. Another unusual and unanticipated characteristic of the $\alpha - \beta$ envelope in Figure 4.1 is the jagged, non-smooth nature of the boundary curve in certain regions. For attack angles above $+20^{\circ}$ and below -10°, the boundary curve can be quite erratic. The asymmetry trait can be traced to the fact that some of the F-16 model aerodynamic look-up tables are nonsymmetric, possibly originating from an imperfect wind-tunnel test model or measurement error during test. The non-smooth trait can be traced to the fact that although some of the F-16 model aerodynamic look-up tables are relatively flat in the poststall regions, they also feature highly wrinkled curves or surfaces.

Control surfaces, indicated for positive β in Figure 4.1, are the dominant factors limiting the aircraft from trimming beyond the boundary. For example, at $\alpha = -5^{\circ}$ and positive β, the limiting factor is the rudder, i.e., the rudder has reached its maximum deflection capability $\delta_r = 30^{\circ}$. As α increases, the boundary curve rides the δ_r limit until the transition point (α, β)=$(20.63^{\circ}, 20.60^{\circ})$ is reached, at which the rudder and aileron

limits ($\delta_a = 21.5^\circ$, $\delta_r = 30^\circ$) are simultaneously active. For further increases in α, the boundary curve rides the δ_a limit until another transition point is reached. An unexpectedly large number of transitions between the various limiting control surfaces is noted in Figure 4.1. This behavior is also likely due to the flat but wrinkled look-up data in the poststall regions. Stall as a limiting factor is reached at very high angles of attack where $\alpha > 53^\circ$, and the variation of withstanding β is minimum, as indicated in Figure 4.2. An interesting phenomenon is happening between $\alpha = 54^\circ$ and 55°, where there exists a very narrow passage where the airplane almost cannot fly in a straight horizontal equilibrium path with a non-zero sideslip angle. The plot of the narrow passage is shown in the right lower corner of Figure 4.2.

In the speed-altitude flight envelope and near sea level altitude [27], the maximum dynamic pressure an aircraft can tolerate is reached at high supersonic speed. The analogy of this dynamic pressure limitation in the $\alpha - \beta$ flight envelope is shown as a hole in the middle of Figure 4.1, which is better seen in Figure 4.3. The hole boundary represents an ellipse-shaped curve with constant velocity since all calculations are performed at sea level. The interior region of this hole represents trimmed flight that is to be intentionally avoided. It is expected that the F-16 might suffer structural damage if flown for extended periods inside the hole. To maintain equilibrium flight at any location on the dynamic pressure limited boundary, the velocity is unique, but the (α, β) pairs are distinct.

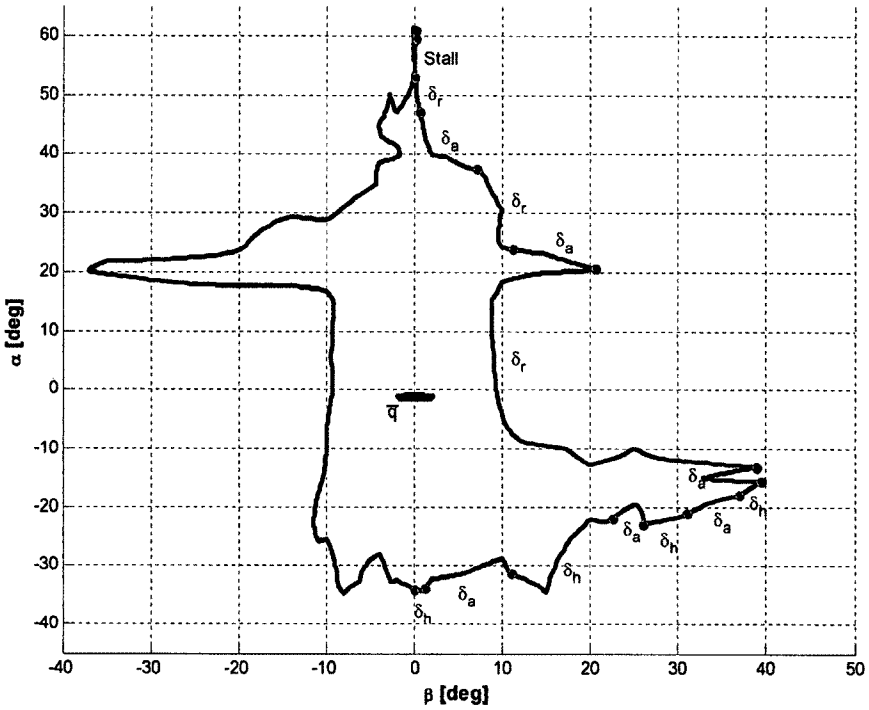

Figure 4.1 α–β flight envelope - complete

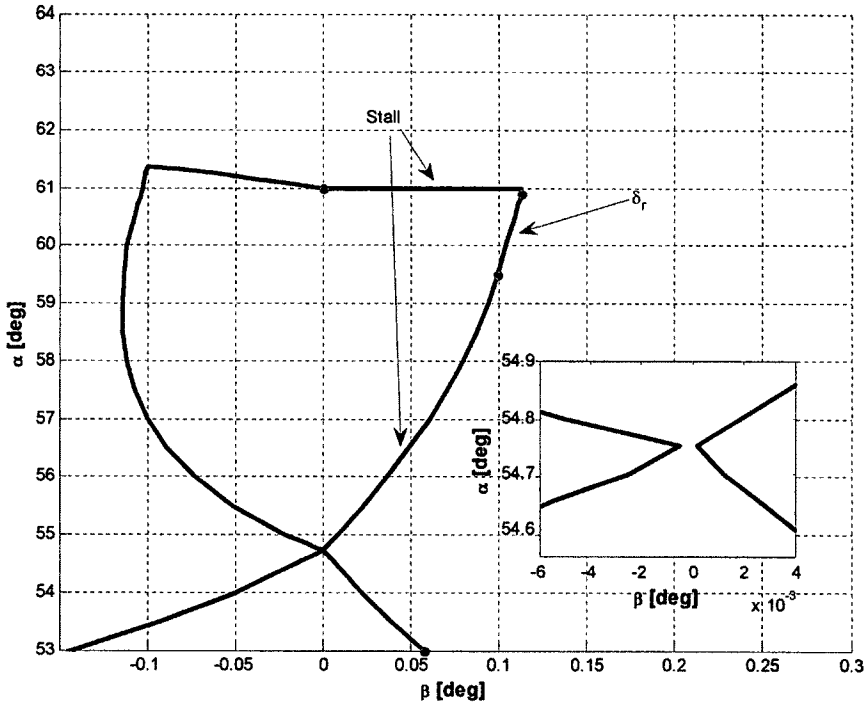

Figure 4.2 α–β flight envelope - enlarged upper region

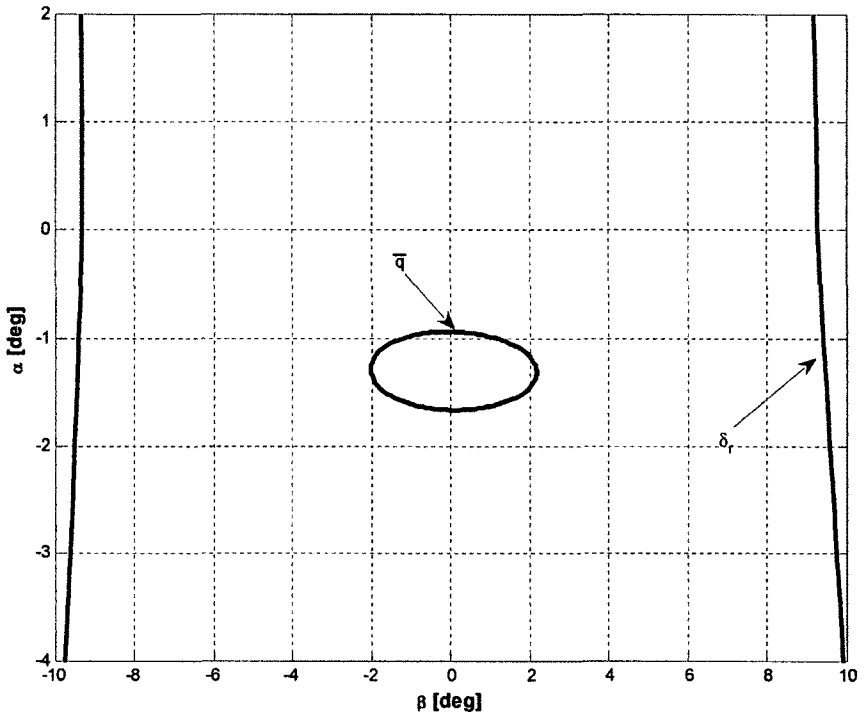

Figure 4.3 α–β flight envelope - enlarged middle region

4.4 Aerodynamic Coefficient Asymmetry

Initial expectation was that the angle of attack vs. the sideslip angle flight envelope would be symmetric due to the symmetry of the aircraft, but the envelope showed distinct behavior at both positive and negative sideslip. The original or non-ideal aircraft aerodynamic model from [30] resulted in a strong irregular $\alpha - \beta$ envelope shape and unusual characteristics such as jagged and non-smooth boundary curves in certain regions. The resulting envelope is shown in Figures 4.1-4.3. This aerodynamic model data exhibits asymmetric and offset behavior in the force and moment coefficients with larger variations for side force, roll moment, and yaw moment coefficients. This behavior is likely due to a combination of factors including experimental measurement error,

model fabrication imperfection, and vortex-dominated flow. The existence and interaction of the vortex-dominated flow with various aircraft surfaces affects all aerodynamic force and moment coefficients and causes asymmetry and offset. At a low angle of attack and a zero sideslip angle, the vortices emanating from the aircraft nose tip are symmetric. As α is increased, one vortex dominates the other and a vortex pattern or vortex-dominated flow is established. This pattern creates different pressures on both sides of the nose, and hence significant lateral net force and moment are produced. Combinations of high α and β complicate numerical and experimental prediction of the aerodynamics coefficients, where the same wind-tunnel aircraft model could produce different results at each run under the exact same conditions [4].

To explain and locate the sources that cause asymmetry in the $\alpha - \beta$ flight envelope, two test points at the same angle of attack but different in sign for sideslip angle, ($\alpha_1 = +21^\circ$, $\beta_1 = -18^\circ$) and ($\alpha_2 = +21^\circ$, $\beta_2 = +18^\circ$), are examined to provide insight into the asymmetry sources. In the vicinity of these points, there is a distinct asymmetry in the envelope boundary (see Figure 4.4). The trimming solutions for both points, as well as the total aerodynamic force and moment coefficients, are shown in Tables 4.1 and 4.2. It is expected, based on aircraft symmetry, that the aircraft will have similar trimming solution magnitudes for both points, in addition to similar total aerodynamic force and moment coefficients. Trim values for the two points in Table 4.1 are approximately equal but are not exact in magnitude with two significant anomalies. The aircraft requires 30% more aileron control surface deflection for $\beta_2 = +18^\circ$ compared to $\beta_1 = -18^\circ$ and 60% more rudder control surface deflection. Also, the total coefficient values for the two points in Table 4.2 are approximately equal in magnitude

but not exact. Although the aileron and rudder related terms appear in the total side force, total rolling moment, and total yawing moment coefficients, only the yawing moment term is considered further.

The total aerodynamic force or moment coefficient is the sum of various aerodynamic contributions. Equation (4.28) shows the total yawing moment coefficient C_{n_T} and each contributing low-level aerodynamic look-up derivative term. The majority of the aerodynamic model data in Reference [30] is represented similarly in look-up tables and are functions of the independent variables α and β. The numerical values for the derivative terms are presented in Table 4.3 at $\alpha = +21^{\circ}$. This table indicates variations in the aerodynamic yawing moment coefficient derivatives depending on the sign of β. Further, the variations are larger in the derivative terms due to rudder and aileron control surfaces (see Table 4.3). At $\beta_1 = -18^{\circ}$, the aerodynamic derivative due to rudder is twice the magnitude at $\beta_2 = +18^{\circ}$, which explains why less rudder deflection is needed for $\beta_1 = -18^{\circ}$, as seen in Table 4.1. A similar observation can be made regarding the aerodynamic derivative due to the aileron. These variations in the aerodynamic derivative data tables explain the origin of the strong asymmetrical $\alpha - \beta$ flight envelope shape. Similar asymmetry in the aerodynamic axial force, side force, normal force, rolling moment, and pitching moment derivative data tables is also observed. Overall, the aerodynamic axial force, normal force, and pitching moment derivative data tables show lesser degree of variations.

$$C_{n_T}(V_T, \alpha, \beta, p_b, r_b, \delta_h, \delta_{lef}, \delta_a, \delta_r)$$

$$= C_n^{\alpha,\beta,\delta_h}(\alpha, \beta, \delta_h) + \Delta C_{n_{\delta_{lef}}}(\alpha, \beta)\left(1 - \frac{\delta_{lef}}{25}\right) + C_{n_\beta}^{\alpha}(\alpha)(\beta)$$

$$+ \Delta C_{n_{\delta_r}}(\alpha, \beta)\left(\frac{\delta_r}{30}\right)$$

$$+ \left\{\Delta C_{n_{\delta_a}}(\alpha, \beta) + \Delta C_{n_{\delta_a \delta_{lef}}}(\alpha, \beta)\left(1 - \frac{\delta_{lef}}{25}\right)\right\}\left(\frac{\delta_a}{20}\right) \quad (4.28)$$

$$+ \left\{C_{n_{p_b}}^{\alpha}(\alpha) + C_{n_{p_b \delta_{lef}}}^{\alpha}(\alpha)\left(1 - \frac{\delta_{lef}}{25}\right)\right\}\left(\frac{\bar{b} p_b}{2V_T}\right)$$

$$+ \left\{C_{n_{r_b}}^{\alpha}(\alpha) + C_{n_{r_b \delta_{lef}}}^{\alpha}(\alpha)\left(1 - \frac{\delta_{lef}}{25}\right)\right\}\left(\frac{\bar{b} r_b}{2V_T}\right)$$

$$- C_{y_{b_T}}(\bar{x}_{cm_R} - \bar{x}_{cm})\left(\frac{\bar{c}}{\bar{b}}\right)$$

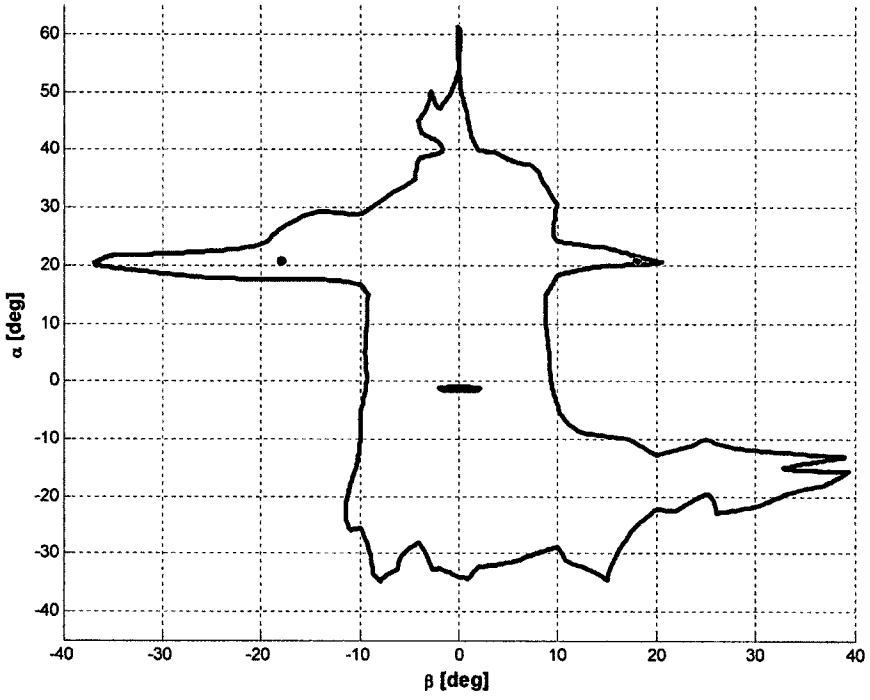

Figure 4.4 Aerodynamic test points

Table 4.1 Trimmed solution at $\alpha = +21^{\circ}$, original data

β	-18°	$+18^{\circ}$
V_T	$205.91\ ft/s$	$202.44\ ft/s$
ϕ_b	-10.9660°	10.1808°
θ_b	23.8962°	23.7177°
δ_h	-8.2649°	-7.8641°
δ_a	14.2629°	-18.4458°
δ_r	-14.6759°	24.3861°
δ_{th}	0.4655	0.4603

Table 4.2 Total aerodynamic force and moment coefficients at $\alpha = +21^{\circ}$, original data

β	-18°	$+18^{\circ}$
$C_{x_{bT}}$	0.0247	0.0269
$C_{y_{bT}}$	0.2359	−0.2271
$C_{z_{bT}}$	−1.2172	−1.2643
C_{l_T}	-5.9821×10^{-9}	2.3710×10^{-8}
C_{m_T}	1.4918×10^{-7}	3.2448×10^{-7}
C_{n_T}	-1.0005×10^{-7}	1.7503×10^{-8}

Table 4.3 Aerodynamic derivatives at $\alpha = +21^{\circ}$, original data

β	-18°	$+18^{\circ}$
$C_n^{\alpha,\beta,\delta_h}(\alpha,\beta,\ \delta_h)$	−0.0277	0.0262
$\Delta C_{n_{\delta_{lef}}}(\alpha,\beta)\left(1-\frac{\delta_{lef}}{25}\right)$	0.0133	−0.0083
$C_{n_\beta}^{\alpha}(\alpha)(\beta)$	$-2.7925 \times 10^{-6}(\beta)$	$-2.7925 \times 10^{-6}(\beta)$
$\Delta C_{n_{\delta_r}}(\alpha,\beta)\left(\frac{\delta_r}{30}\right)$	$-0.0539\left(\frac{\delta_r}{30}\right)$	$-0.0259\left(\frac{\delta_r}{30}\right)$
$\left\{\Delta C_{n_{\delta_a}}(\alpha,\beta)+\Delta C_{n_{\delta_a\delta_{lef}}}(\alpha,\beta)\left(1-\frac{\delta_{lef}}{25}\right)\right\}\left(\frac{\delta_a}{20}\right)$	$-0.0107\left(\frac{\delta_a}{20}\right)$	$0.0012\left(\frac{\delta_a}{20}\right)$
$\left\{C_{n_{p_b}}^{\alpha}(\alpha)+C_{n_{p_b\delta_{lef}}}^{\alpha}(\alpha)\left(1-\frac{\delta_{lef}}{25}\right)\right\}\left(\frac{\bar{b}p_b}{2V_T}\right)$	$0.0468\left(\frac{\bar{b}p_b}{2V_T}\right)$	$0.0468\left(\frac{\bar{b}p_b}{2V_T}\right)$
$\left\{C_{n_{r_b}}^{\alpha}(\alpha)+C_{n_{r_b\delta_{lef}}}^{\alpha}(\alpha)\left(1-\frac{\delta_{lef}}{25}\right)\right\}\left(\frac{\bar{b}r_b}{2V_T}\right)$	$-0.6584\left(\frac{\bar{b}r_b}{2V_T}\right)$	$-0.6584\left(\frac{\bar{b}r_b}{2V_T}\right)$
$C_{y_{bT}}(\bar{x}_{cm_R}-\bar{x}_{cm})\left(\frac{\bar{c}}{\bar{b}}\right)$	$0.2359(\bar{x}_{cm_R}-\bar{x}_{cm})\left(\frac{\bar{c}}{\bar{b}}\right)$	$-0.2270(\bar{x}_{cm_R}-\bar{x}_{cm})\left(\frac{\bar{c}}{\bar{b}}\right)$
Total aerodynamic yawing moment, C_{n_T}	-1.0005×10^{-7}	1.7503×10^{-8}

4.5 Aerodynamic Coefficient Symmetrization

In an ideal world, the aerodynamic force and moment coefficient magnitudes of an ideal model at positive sideslip angles are expected to be identically symmetric with their counterparts at negative sideslip angles. Hence, the $\alpha - \beta$ flight envelope is expected to be symmetric. However, the aerodynamic model in Reference [30] produces asymmetric relationships, as seen in Figure 4.1 and Tables 4.1-4.3. To simplify the analysis and to provide a clearer understanding and a deeper insight into the fundamental relationships, the aerodynamic model from Reference [30] is revisited and modified. The asymmetry and offset in the aerodynamic coefficients that are functions of the independent variables α and β are intentionally removed by data manipulation. This adaptation allows the aircraft to have identical slipping to the right and slipping to the left flight conditions providing an ideal model that is more suitable for analysis.

The data manipulation involves two steps: step 1 and step 2 symmetrization for the aerodynamic force and moment coefficient derivatives. The step 1 symmetrization is carried out using the mathematical arithmetic mean or averaging technique. The aerodynamic data are represented as two-dimensional look-up tables where the rows correspond to angles of attack and the columns correspond to sideslip angles. The asymmetric data in Reference [30] along the sideslip angle range are pre-categorized according to their symmetry resemblance into three types: 1) even symmetry resemblance, 2) odd symmetry resemblance, and 3) neither even nor odd symmetric resemblance. Then, averaging for the even symmetry resemblance data is found using the following expression:

$$\begin{aligned}\left[C_{l_T}(-\beta)\right]_{\text{average}} &= \frac{1}{2}\left\{\left[C_{l_T}(-\beta)\right]_{\text{original}} + \left[C_{l_T}(+\beta)\right]_{\text{original}}\right\} \\ \left[C_{l_T}(+\beta)\right]_{\text{average}} &= \frac{1}{2}\left\{\left[C_{l_T}(-\beta)\right]_{\text{original}} + \left[C_{l_T}(+\beta)\right]_{\text{original}}\right\}\end{aligned} \tag{4.29}$$

On the other hand, averaging for the odd symmetry resemblance data is found using the following expressions:

$$\begin{aligned}\left[C_{l_T}(-\beta)\right]_{\text{average}} &= \frac{1}{2}\left\{\left[C_{l_T}(-\beta)\right]_{\text{original}} - \left[C_{l_T}(+\beta)\right]_{\text{original}}\right\} \\ \left[C_{l_T}(+\beta)\right]_{\text{average}} &= -\frac{1}{2}\left\{\left[C_{l_T}(-\beta)\right]_{\text{original}} - \left[C_{l_T}(+\beta)\right]_{\text{original}}\right\}\end{aligned} \tag{4.30}$$

In Equations (4.29)-(4.30), $\left[C_{l_T}(-\beta)\right]_{average}$ and $\left[C_{l_T}(+\beta)\right]_{\text{average}}$ represent the new averaged columns of data corresponding to negative and positive β, whereas, $\left[C_{l_T}(-\beta)\right]_{\text{original}}$ and $\left[C_{l_T}(+\beta)\right]_{\text{original}}$ represent the original columns of data from Reference [30] corresponding to negative and positive β. Step 1 data manipulation is a standalone process and, using either Equation (4.29) or Equation (4.30), depending on the symmetry resemblance, a new set of symmetrized data is introduced and recorded for future analysis.

Figure 4.5 shows the original asymmetric and the new symmetrized surface plots for the aerodynamic axial force derivative coefficient due to attack angle, sideslip angle, and horizontal tail, $C_{x_b}^{\alpha,\beta,\delta_h}(\alpha, \beta, \delta_h = 0)$. For better visualization, section plots at different angles of attack are shown in Figure 4.6. The relative change for this derivative between the original and new data sets is 2.2% at most. This percentage is small and indicates relatively small asymmetry in the original data. However, for other derivatives, the percentage approaches 20%, indicating relatively large asymmetry. Figures 4.5 and 4.6 are examples of even symmetry resemblance. Odd symmetry resemblances are shown

in Figures 4.7 and 4.8 for the aerodynamic rolling moment derivative coefficient due to attack angle, sideslip angle, and leading-edge-flap, $C_{l_{\delta_{lef}}}^{\alpha,\beta}(\alpha,\beta)$.

As a further analysis, two test points are used to investigate data asymmetry before and after symmetrization. These points are at the same angle of attack but are opposite in sign sideslip angles. The second test point ($\alpha_2 = +20^\circ$, $\beta_2 = +15^\circ$) is an equilibrium point whereas the first point ($\alpha_1 = +20^\circ$, $\beta_1 = -15^\circ$) is not an equilibrium point. However, in order to have a symmetric flight attitude, the first test point is forced to have exactly the same trimming settings of the second point with different sign for aileron and rudder control inputs. The leading-edge-flap control surface deflection, speed-brake control surface deflection, and body angular rates are assumed to be zero. The flight conditions and control settings for the first test point are: $\alpha_1 = +20^\circ$, $\beta_1 = -15^\circ$, $V_{T1} = 202.732$ ft/s, $\delta_{h_1} = -6.8849^\circ$, $\delta_{a_1} = +10.5393^\circ$, $\delta_{r_1} = -29.6584^\circ$. The second test point has the following settings: $\alpha_2 = +20^\circ$, $\beta_2 = +15^\circ$, $V_{T2} = 202.732$ ft/s, $\delta_{h_2} = -6.8849^\circ$, $\delta_{a_2} = -10.5393^\circ$, $\delta_{r_2} = +29.6584^\circ$. These test point values are consistent. Table 4.4 compares the total aerodynamic coefficients for the original and the step 1 symmetrized data. The original total coefficients are clearly asymmetric in magnitude for $\beta = \pm 15^\circ$, whereas the step 1 symmetrized data show symmetries in magnitude for the longitudinal total coefficients only: the axial force, normal force, and pitching moment total coefficients. The lateral total coefficients (the side force, rolling moment, and yawing moment total coefficients) still exhibit asymmetry. Further investigation for the derivative contributions to the total yawing moment coefficient in Equation (4.28) is shown in Table 4.5 and only the first two terms are found to be symmetric. The step 1 manipulation fixes asymmetry only in the longitudinal

coefficients, and asymmetry in the lateral coefficients that are not related to either the rudder or the aileron. Hence, a second step (step 2) manipulation is required to address the asymmetry issues in the data related to these control surfaces.

The aileron and rudder surfaces related aerodynamic derivative coefficients appear only in the lateral total coefficients. Within these derivatives, in addition to the asymmetry, there is an offset in the data. This type of data neither have even nor odd symmetric resemblance. Hence, a step 2 symmetrization is introduced to resolve this issue. This step is performed instantaneously when needed in the analysis. To clarify, this step balances the lateral aerodynamic derivative coefficients related only to aileron and rudder control surface deflections between the positive and its opposite negative sideslip angle. Further, it is implemented corresponding only to a single pair of angle of attack and sideslip angle values. For instance, if an investigation requires calculating coefficients at $p_1 = (\alpha, \beta)$ where α and β are positive, a second hypothetical point $p_2 = (\alpha, -\beta)$ is assumed. Then, the derivative terms related to aileron and rudder surfaces in the total aerodynamic yawing moment coefficient in Equation (4.31), for example, are replaced by averaged terms between p_1 and p_2, as indicated in Equation (4.32).

$$
\begin{aligned}
&C_{n_T}(V_T, \alpha, \beta, p_b, r_b, \delta_h, \delta_{lef}, \delta_a, \delta_r) \\
&\quad = C_n^{\alpha,\beta,\delta_h}(\alpha, \beta, \delta_h) + \Delta C_{n_{\delta_{lef}}}(\alpha, \beta)\left(1 - \frac{\delta_{lef}}{25}\right) + C_{n_\beta}^{\alpha}(\alpha)(\beta) \\
&\quad + \Delta \boldsymbol{C}_{n_{\delta_r}}(\boldsymbol{\alpha}, \boldsymbol{\beta})_{avg}\left(\frac{\delta_r}{30}\right) \\
&\quad + \left\{\Delta \boldsymbol{C}_{n_{\delta_a}}(\boldsymbol{\alpha}, \boldsymbol{\beta}) + \Delta \boldsymbol{C}_{n_{\delta_a \delta_{lef}}}(\boldsymbol{\alpha}, \boldsymbol{\beta})\left(\mathbf{1} - \frac{\boldsymbol{\delta_{lef}}}{\mathbf{25}}\right)\right\}_{\boldsymbol{avg}}\left(\frac{\delta_a}{20}\right) \\
&\quad + \left\{C_{n_{p_b}}^{\alpha}(\alpha) + C_{n_{p_b \delta_{lef}}}^{\alpha}(\alpha)\left(1 - \frac{\delta_{lef}}{25}\right)\right\}\left(\frac{\bar{b} p_b}{2V_T}\right) \\
&\quad + \left\{C_{n_{r_b}}^{\alpha}(\alpha) + C_{n_{r_b \delta_{lef}}}^{\alpha}(\alpha)\left(1 - \frac{\delta_{lef}}{25}\right)\right\}\left(\frac{\bar{b} r_b}{2V_T}\right) \\
&\quad - C_{y_{b_T}}(\bar{x}_{cm_R} - \bar{x}_{cm})\left(\frac{\bar{c}}{\bar{b}}\right)
\end{aligned}
\tag{4.31}
$$

where

$$
\begin{aligned}
&\Delta \boldsymbol{C}_{n_{\delta_r}}(\boldsymbol{\alpha}, \boldsymbol{\beta})_{avg} = \frac{1}{2}\left\{\Delta C_{n_{\delta_r}}(\alpha, -\beta) + \Delta C_{n_{\delta_r}}(\alpha, +\beta)\right\} \\
&\left\{\Delta \boldsymbol{C}_{n_{\delta_a}}(\boldsymbol{\alpha}, \boldsymbol{\beta}) + \Delta \boldsymbol{C}_{n_{\delta_a \delta_{lef}}}(\boldsymbol{\alpha}, \boldsymbol{\beta})\left(\mathbf{1} - \frac{\boldsymbol{\delta_{lef}}}{\mathbf{25}}\right)\right\}_{\boldsymbol{avg}} \\
&\quad = \frac{1}{2}\left\{\Delta C_{n_{\delta_a}}(\alpha, -\beta) + \Delta C_{n_{\delta_a}}(\alpha, +\beta)\right\} \\
&\quad + \frac{1}{2}\left\{\Delta C_{n_{\delta_a \delta_{lef}}}(\alpha, -\beta) + \Delta C_{n_{\delta_a \delta_{lef}}}(\alpha, +\beta)\right\}\left(1 - \frac{\delta_{lef}}{25}\right)
\end{aligned}
\tag{4.32}
$$

Table 4.6 compares the total aerodynamic coefficients for the step 1 and step 1-step 2 symmetrized data. As discussed earlier, the total coefficients using the step 1 symmetrized data are clearly symmetric in magnitude only for the longitudinal coefficients for $\beta = \pm 15^{\circ}$, whereas the second step symmetrization produces exact symmetry in magnitude for the lateral coefficients (see Table 4.6). Further, the derivative contributions to the total yawing moment coefficient in Equation (4.28) are shown in Table 4.7, and all the terms are symmetric.

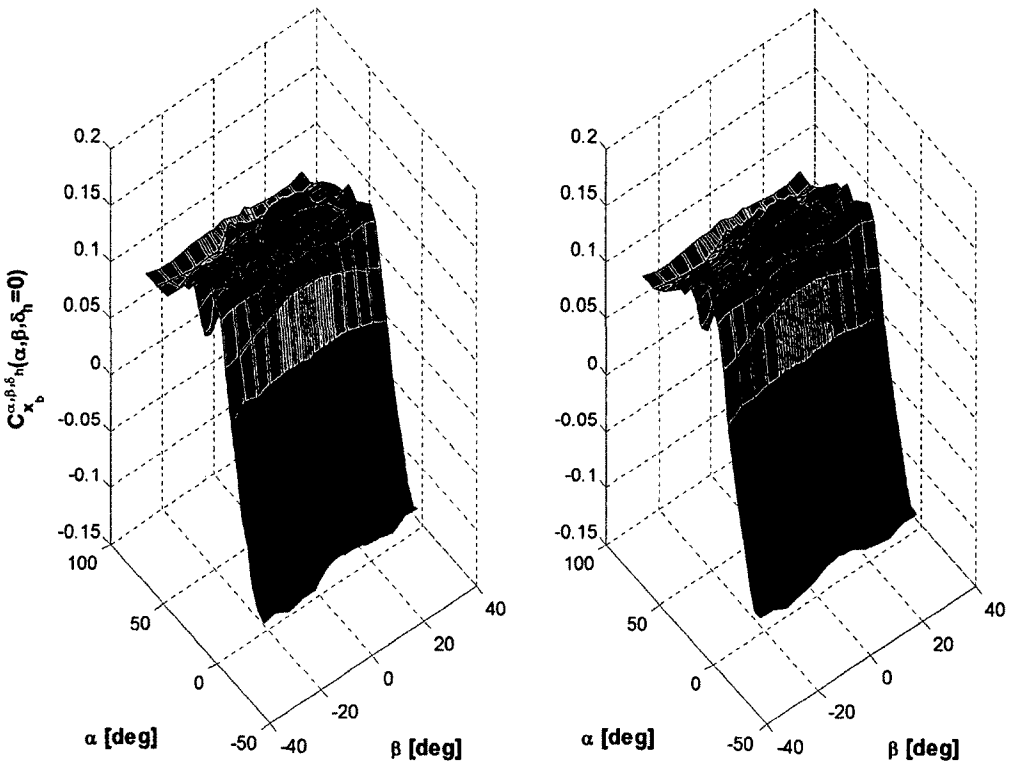

Figure 4.5 Axial force derivative coefficient, asymmetric (left), symmetric (right)

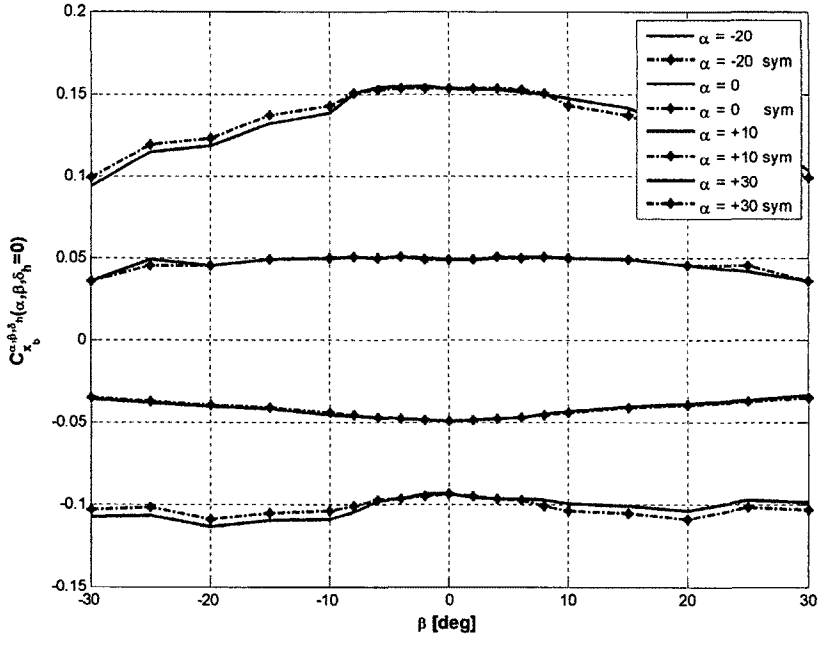

Figure 4.6 Axial force derivative coefficient at different α

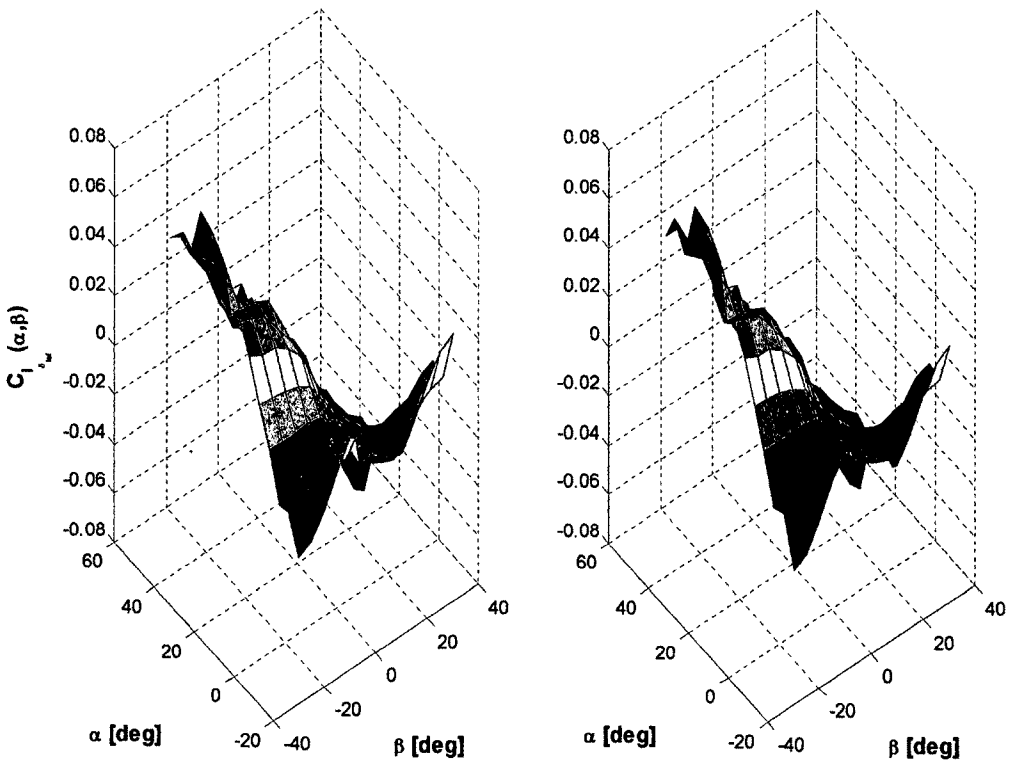

Figure 4.7 Rolling moment derivative coefficient, asymmetric (left), symmetric (right)

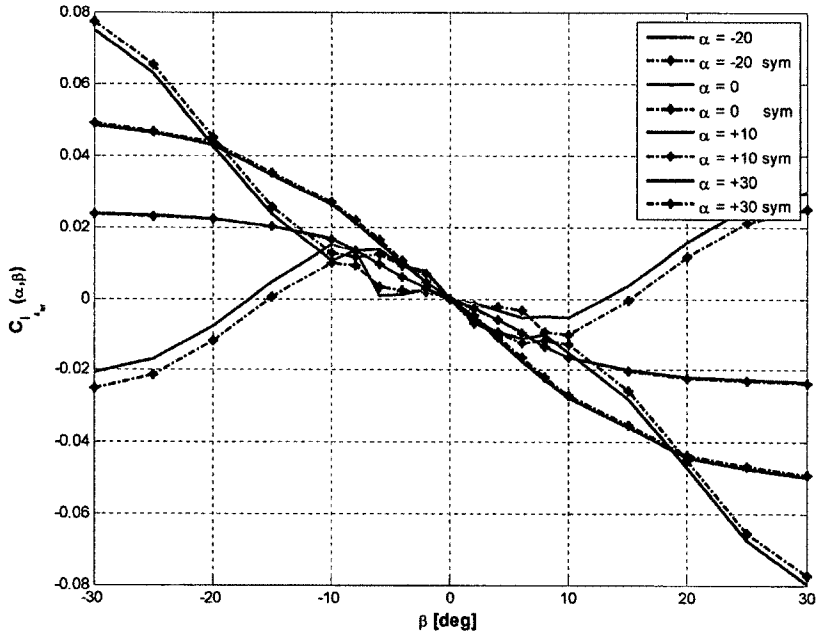

Figure 4.8 Rolling moment derivative coefficient at different α

Table 4.4 Total aerodynamic coefficients at $\alpha = +20^{\circ}$, original vs. step 1

β	Original Data		Step 1 Symmetrized Data	
	-15°	$+15^{\circ}$	-15°	$+15^{\circ}$
$C_{x_{bT}}$	0.0253	0.0277	0.0265	0.0265
$C_{y_{bT}}$	0.1469	−0.1856	0.1435	−0.1669
$C_{z_{bT}}$	−1.2334	-1.2851	−1.2593	−1.2593
C_{l_T}	−0.0054	-5.2×10^{-8}	−0.0077	0.0065
C_{m_T}	−0.0050	1.6×10^{-7}	−0.0026	−0.0026
C_{n_T}	0.0198	-2.5×10^{-8}	0.0255	−0.0112

Table 4.5 Aerodynamic derivatives at $\alpha = +20^{\circ}$, original vs. step 1

β	Original Data		Step 1 Symmetrized Data	
	-15°	$+15^{\circ}$	-15°	$+15^{\circ}$
$C_n^{\alpha,\beta,\delta_h}(\alpha,\beta,\delta_h)$	−0.0309	0.0286	−0.0297	0.0297
$\Delta C_{n_{\delta_{lef}}}(\alpha,\beta)\left(1-\frac{\delta_{lef}}{25}\right)$	0.0091	−0.0017	0.0054	−0.0054
$\Delta C_{n_{\delta_r}}(\alpha,\beta)\left(\frac{\delta_r}{30}\right)$	$-0.0515\left(\frac{\delta_r}{30}\right)$	$-0.0297\left(\frac{\delta_r}{30}\right)$	$-0.0584\left(\frac{\delta_r}{30}\right)$	$-0.0366\left(\frac{\delta_r}{30}\right)$
$\left\{\Delta C_{n_{\delta_a}}(\alpha,\beta)+\Delta C_{n_{\delta_a\delta_{lef}}}(\alpha,\beta)\left(1-\frac{\delta_{lef}}{25}\right)\right\}\left(\frac{\delta_a}{20}\right)$	$-0.0125\left(\frac{\delta_a}{20}\right)$	$0.0020\left(\frac{\delta_a}{20}\right)$	$-0.0098\left(\frac{\delta_a}{20}\right)$	$0.0047\left(\frac{\delta_a}{20}\right)$
$C_{y_{bT}}(\bar{x}_{cm_R}-\bar{x}_{cm})\left(\frac{\bar{c}}{\bar{b}}\right)$	0.0028	−0.0035	0.0027	−0.0031
Total Aerodynamic Rolling Moment, C_{n_T}	0.0198	-2.5×10^{-8}	0.0255	−0.0112

Table 4.6 Total aerodynamic coefficients at $\alpha = +20^{\circ}$, step 1 vs. step 1–2

β	Step 1 Symmetrized Data		Step 1–Step 2 Symmetrized Data	
	-15°	$+15^{\circ}$	-15°	$+15^{\circ}$
$C_{x_{bT}}$	0.0265	0.0265	0.0265	0.0265
$C_{y_{bT}}$	0.1435	−0.1669	0.1581	−0.1581
$C_{z_{bT}}$	−1.2593	−1.2593	−1.2593	−1.2593
C_{l_T}	−0.0077	0.0065	−0.0043	0.0043
C_{m_T}	−0.0026	−0.0026	−0.0026	−0.0026
C_{n_T}	0.0255	−0.0112	0.0123	−0.0123

Table 4.7 Aerodynamic derivatives at $\alpha = +20^{\circ}$, step 1 vs. step 1–2

β	Step 1 Symmetrized Data		Step 1–Step 2 Symmetrized Data	
	-15°	$+15^{\circ}$	-15°	$+15^{\circ}$
$C_n^{\alpha,\beta,\delta_h}(\alpha,\beta,\delta_h)$	-0.0297	0.0297	-0.0297	0.0297
$\Delta C_{n_{\delta_{lef}}}(\alpha,\beta)\left(1-\frac{\delta_{lef}}{25}\right)$	0.0054	-0.0054	0.0054	-0.0054
$\Delta C_{n_{\delta_r}}(\alpha,\beta)\left(\frac{\delta_r}{30}\right)$	$-0.0584\left(\frac{\delta_r}{30}\right)$	$-0.0366\left(\frac{\delta_r}{30}\right)$	$-0.0412\left(\frac{\delta_r}{30}\right)$	$-0.0412\left(\frac{\delta_r}{30}\right)$
$\left\{\Delta C_{n_{\delta_a}}(\alpha,\beta)+\Delta C_{n_{\delta_a\delta_{lef}}}(\alpha,\beta)\left(1-\frac{\delta_{lef}}{25}\right)\right\}\left(\frac{\delta_a}{20}\right)$	$-0.0098\left(\frac{\delta_a}{20}\right)$	$0.0047\left(\frac{\delta_a}{20}\right)$	$-0.0021\left(\frac{\delta_a}{20}\right)$	$-0.0021\left(\frac{\delta_a}{20}\right)$
$C_{y_{b_T}}(\bar{x}_{cm_R}-\bar{x}_{cm})\left(\frac{\bar{c}}{\bar{b}}\right)$	0.0027	-0.0031	0.0030	-0.0030
Total Aerodynamic Rolling Moment, C_{n_T}	0.0255	-0.0112	0.0123	-0.0123

4.6 Full-Envelope Results –Ideal Model

The $\alpha-\beta$ flight envelope of the high-fidelity F-16 aircraft model is reproduced using the ideal aerodynamic model introduced earlier, and is shown in Figure 4.9. This aircraft is very versatile and can sustain equilibrium conditions at both high angle of attack and sideslip, as shown. As expected from the ideal aerodynamic model, the $\alpha-\beta$ flight envelope indicates symmetrical slipping in equilibrium flight due to symmetry of this model data. The envelope shows similar behavior at positive and negative β. At a positive angle of attack, the F-16 has an enhanced ability to maintain equilibrium flight with large sideslip angle at a positive angle of attack and a lesser ability for a negative angle of attack. An unusual characteristic of the $\alpha-\beta$ envelope in Figure 4.9 is the jagged, non-smooth nature of the boundary curve in certain regions. For attack angles above $+20^{\circ}$ and below -10°, the boundary curve again can be quite erratic. The non-smooth trait can be traced to the fact that some of the ideal F-16 model aerodynamic look-up tables are still relatively flat in the poststall regions but also show highly wrinkled curves or surfaces.

Control surfaces, indicated for positive β in Figure 4.9, are the dominant factors limiting the aircraft from trimming beyond the boundary. For example, at $\alpha = -5^{\circ}$ and positive β, the limiting factor is the rudder, i.e., the rudder has reached its maximum deflection capability $\delta_r = 30^{\circ}$. As α increases, the boundary curve rides the δ_r limit until the transition point (α, β)=$(20.9071^{\circ}, 28^{\circ})$ is reached, where the rudder and aileron limits ($\delta_a = 21.5^{\circ}$, $\delta_r = 30^{\circ}$) are simultaneously active. For further increases in α, the boundary curve rides the δ_a limit until another transition point is reached. An unexpectedly large number of transitions between the various limiting control surfaces is noted in Figure 4.9. This behavior is also likely due to the flat but wrinkled look-up data in the poststall regions. Stall as a limiting factor is reached at very high angles of attack where $\alpha > 54.5^{\circ}$ and the variation of withstanding β is minimum, as indicated in Figure 4.10. An interesting phenomenon occurs between $\alpha = 54^{\circ}$ and 55° where there exists a very narrow passage where the airplane almost cannot fly in equilibrium with non-zero sideslip angle. The plot of the narrow passage is shown in the right lower corner of Figure 4.10.

In the speed-altitude flight envelope and near sea level altitude [27], the maximum dynamic pressure that an aircraft can tolerate is reached at high supersonic speed. The analogy of this dynamic pressure limitation in the $\alpha - \beta$ flight envelope is again shown as a hole in the middle of Figure 4.9, which is better seen in Figure 4.11. The hole boundary represents an ellipse-shaped curve with constant velocity since all calculations are performed at sea level. The interior region of this hole represents trimmed flight that is to be intentionally avoided. It is expected that the F-16 might suffer structural damage if flown for extended periods inside the hole. To maintain equilibrium

flight at any location on the dynamic pressure limited boundary, the velocity is unique but the (α, β) pairs are distinct.

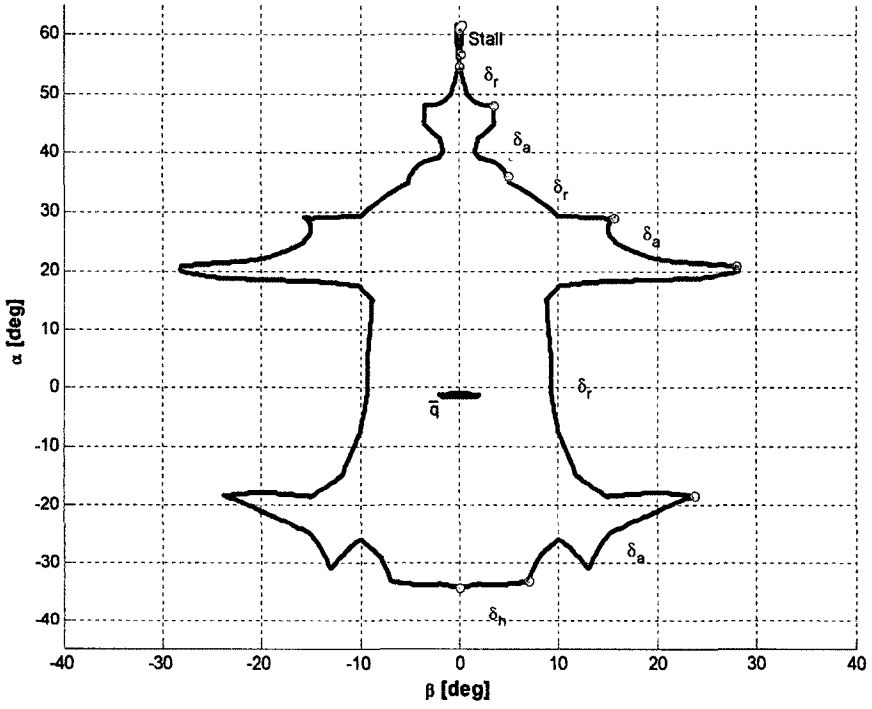

Figure 4.9 Ideal α–β flight envelope – complete

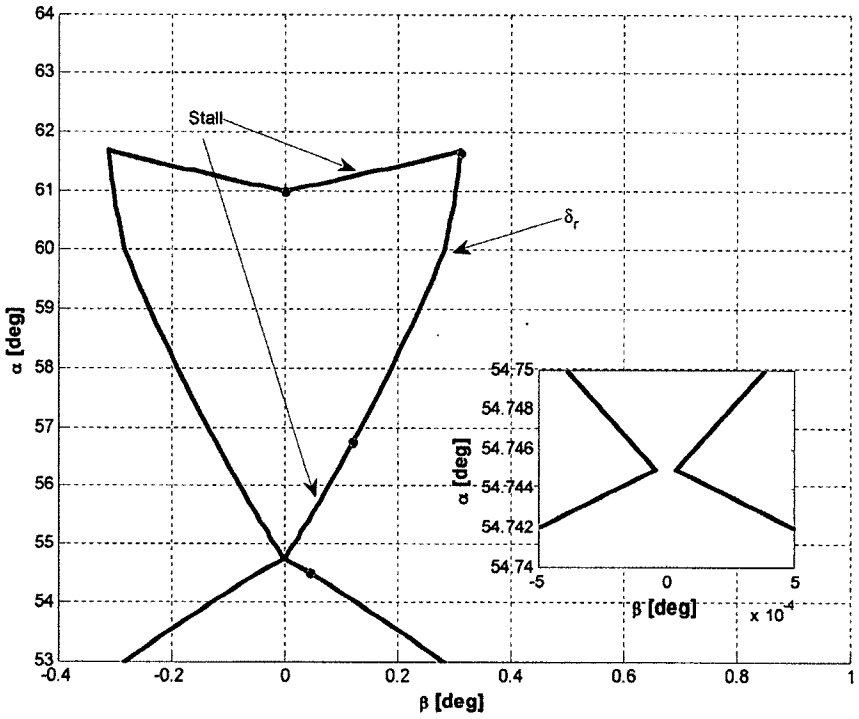

Figure 4.10 Ideal α–β flight envelope - enlarged upper region

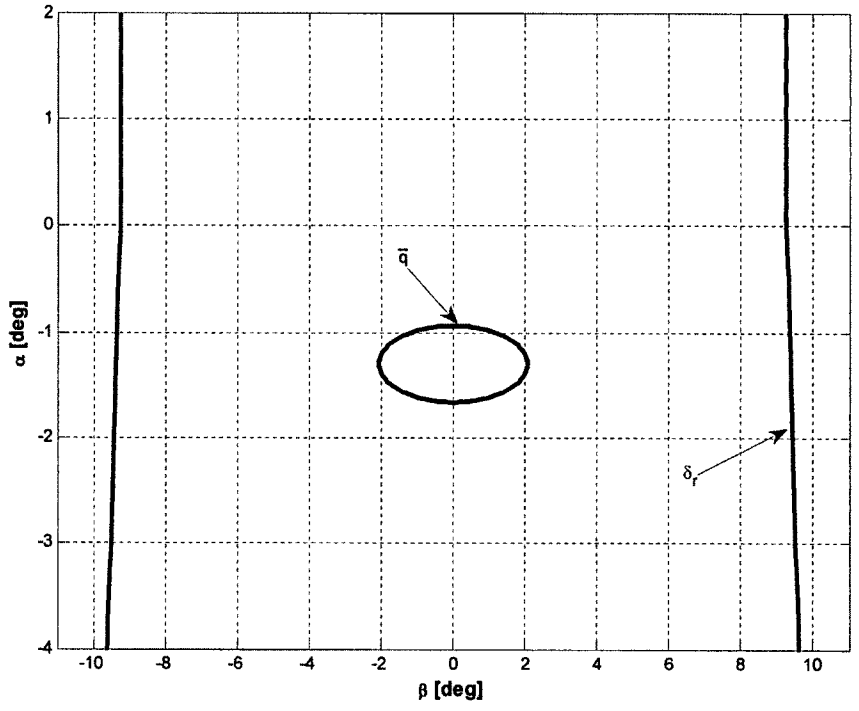

Figure 4.11 Ideal α–β flight envelope - enlarged middle region

CHAPTER 5

NONLINEARITY INDEX ASSESSMENT

5.1 Introduction

Across the $\alpha - \beta$ flight envelope in Figure 5.1, a nominal linear model $\{\bar{A}_j(\boldsymbol{\lambda}_j), \bar{B}_j(\boldsymbol{\lambda}_j)\}$ is generated at each prescribed operating condition parameter vector $\boldsymbol{\lambda}_j = [\alpha_{0j} \quad \beta_{0j}]^T$. At this operating condition, equilibrium states and inputs are obtained by solving a set of nonlinear simultaneous equations (Equation (4.24)). Around each nominal point j, the perturbation subregion is seeded with a set of $N = 16$ points to cover this subregion. At each one of these points, another linear model $\{A_i(\boldsymbol{\lambda}_i), B_i(\boldsymbol{\lambda}_i)\}$ is generated at $\boldsymbol{\lambda}_i = [\alpha_{0i} \quad \beta_{0i}]^T$. The subregion around the operating condition j where the linear model is applicable is chosen as an ellipse with semi-major axis as 10% of the difference between maximum and minimum angle of attack ($0.1\alpha_{\text{band}}$), and semi-minor axis as 10% of the difference between maximum and minimum angle of sideslip ($0.1\beta_{\text{band}}$). Each linear 8^{th} order model for the body-frame coordinate description has the form shown in Equation (5.1). Because of flight asymmetry, the lateral-directional variables are not zero in the linear model. The propulsive input effect has not been considered in the linear model here. The matrices A and B are not defined symbolically here, since there are no explicit expressions for the low-level aerodynamic look-up data to conclude a general linear model for the purpose of analysis. Instead, A and B are developed by numerical finite difference linearization for different operating conditions [33]. Since the maximum singular value or matrix two-norm used in the index expression is unit dependent and thus potentially susceptible to overestimating

nonlinearity strength, Equation (5.1) is normalized with the diagonal matrix T in Equation (5.2) to obtain a normalized linear Equation (5.4) for improved numerical conditioning.

$$\dot{\mathbf{x}}_b = A_b\mathbf{x}_b + B_b\mathbf{u}$$

$$\mathbf{x}_b = [\Delta u_b \quad \Delta v_b \quad \Delta w_b \quad \Delta\phi_b \quad \Delta\theta_b \quad \Delta p_b \quad \Delta q_b \quad \Delta r_b] \tag{5.1}$$

$$\mathbf{u} = [\delta_h \quad \delta_a \quad \delta_r]$$

The diagonal matrices T and T^{-1} are

$$T = \begin{bmatrix} \frac{1}{V_T} & & & & & & & \\ & \frac{1}{V_T} & & & & & 0 & \\ & & \frac{1}{V_T} & & & & & \\ & & & 1 & & & & \\ & & & & 1 & & & \\ & & & & & \frac{\bar{b}}{2V_T} & & \\ & 0 & & & & & \frac{\bar{c}}{2V_T} & \\ & & & & & & & \frac{\bar{b}}{2V_T} \end{bmatrix} \tag{5.2}$$

and

$$T^{-1} = \begin{bmatrix} V_T & & & & & & & \\ & V_T & & & & & 0 & \\ & & V_T & & & & & \\ & & & 1 & & & & \\ & & & & 1 & & & \\ & & & & & \frac{2V_T}{\bar{b}} & & \\ & 0 & & & & & \frac{2V_T}{\bar{c}} & \\ & & & & & & & \frac{2V_T}{\bar{b}} \end{bmatrix} \tag{5.3}$$

The normalized or transformed linear system is

$$\dot{\mathbf{x}}_b' = A_b'\mathbf{x}_b' + B_b'\mathbf{u}$$

$$\mathbf{x}_b' = [\Delta u_b' \quad \Delta v_b' \quad \Delta w_b' \quad \Delta \phi_b' \quad \Delta \theta_b' \quad \Delta p_b' \quad \Delta q_b' \quad \Delta r_b'] \tag{5.4}$$

$$\mathbf{u} = [\delta_h \quad \delta_a \quad \delta_r]$$

where $\mathbf{x}_b' = T\mathbf{x}_b$, $A_b' = TA_bT^{-1}$, $B_b' = TB_b$.

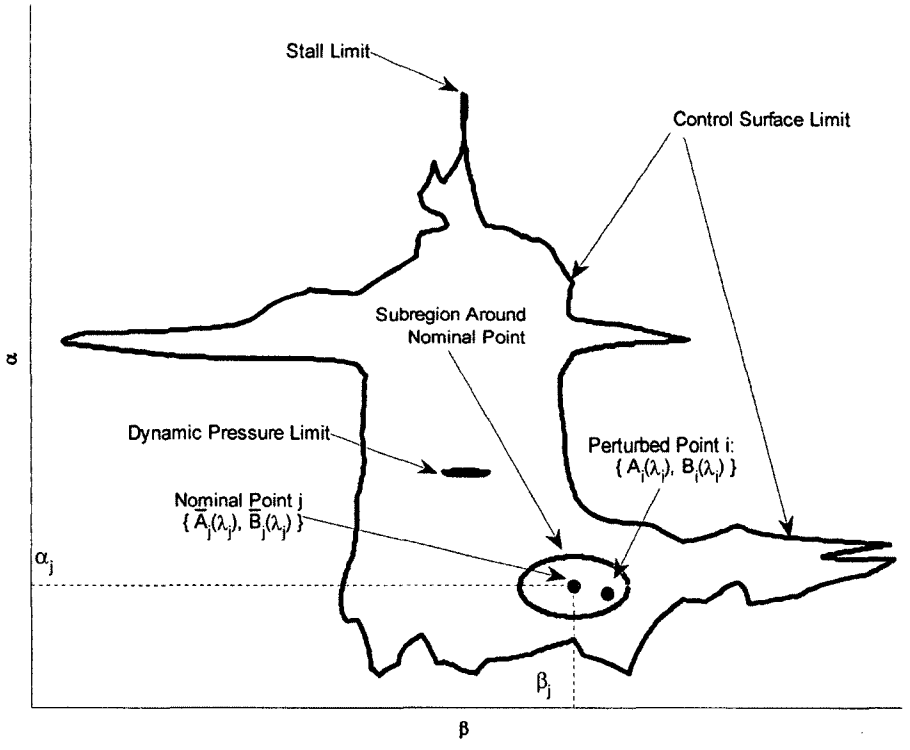

Figure 5.1 α–β flight envelope

5.2 Nonlinearity Sub-Index Using Matrix Partitions

Another way to lessen the overestimation of nonlinearity strength based on a matrix norm measure is to consider matrix partitions. The nonlinearity index assesses the overall variation of linear system matrices A_b and B_b. However, an investigation into A_b and B_b components reveals that these matrices can be partitioned into blocks, according to the system dynamics. In order to assess the contributed weight of each component in the state matrices towards the overall index, matrix A_b is divided into sub-matrix blocks as

$$A_b = \begin{bmatrix} \begin{bmatrix} X_{u_b} & X_{v_b} & X_{w_b} \\ Y_{u_b} & Y_{v_b} & Y_{w_b} \\ Z_{u_b} & Z_{v_b} & Z_{w_b} \end{bmatrix} & \begin{bmatrix} 0 & gC_{\theta_{b_0}} \\ gC_{\phi_{b_0}}C_{\theta_{b_0}} & gS_{\phi_{b_0}}S_{\theta_{b_0}} \\ gS_{\phi_{b_0}}C_{\theta_{b_0}} & gC_{\phi_{b_0}}S_{\theta_{b_0}} \end{bmatrix} & \begin{bmatrix} X_{p_b} & X_{q_b} & X_{r_b} \\ Y_{p_b} & Y_{q_b} & Y_{r_b} \\ Z_{p_b} & Z_{q_b} & Z_{r_b} \end{bmatrix} \\ \begin{bmatrix} 0 & 0 & 0 \\ 0 & 0 & 0 \end{bmatrix} & \begin{bmatrix} 0 & 0 \\ 0 & 0 \end{bmatrix} & \begin{bmatrix} 1 & S_{\phi_{0_b}}T_{\theta_{0_b}} & C_{\phi_{0_b}}T_{\theta_{0_b}} \\ 0 & C_{\phi_{0_b}} & -S_{\phi_{0_b}} \end{bmatrix} \\ \begin{bmatrix} L_{u_b} & L_{v_b} & L_{w_b} \\ M_{u_b} & M_{v_b} & M_{w_b} \\ N_{u_b} & N_{v_b} & N_{w_b} \end{bmatrix} & \begin{bmatrix} 0 & 0 \\ 0 & 0 \\ 0 & 0 \end{bmatrix} & \begin{bmatrix} L_{p_b} & L_{q_b} & L_{r_b} \\ M_{p_b} & M_{q_b} & M_{r_b} \\ N_{p_b} & N_{q_b} & N_{r_b} \end{bmatrix} \end{bmatrix} \tag{5.5}$$

and the transformed matrix A_b' is divided as

$$A_b' = \begin{bmatrix} \begin{bmatrix} X_{u_b} & X_{v_b} & X_{w_b} \\ Y_{u_b} & Y_{v_b} & Y_{w_b} \\ Z_{u_b} & Z_{v_b} & Z_{w_b} \end{bmatrix} & \frac{1}{V_T}\cdot\begin{bmatrix} 0 & gC_{\theta_{b_0}} \\ gC_{\phi_{b_0}}C_{\theta_{b_0}} & gS_{\phi_{b_0}}S_{\theta_{b_0}} \\ gS_{\phi_{b_0}}C_{\theta_{b_0}} & gC_{\phi_{b_0}}S_{\theta_{b_0}} \end{bmatrix} & 2\cdot\begin{bmatrix} \frac{1}{\bar{b}}X_{p_b} & \frac{1}{\bar{c}}X_{q_b} & \frac{1}{\bar{b}}X_{r_b} \\ \frac{1}{\bar{b}}Y_{p_b} & \frac{1}{\bar{c}}Y_{q_b} & \frac{1}{\bar{b}}Y_{r_b} \\ \frac{1}{\bar{b}}Z_{p_b} & \frac{1}{\bar{c}}Z_{q_b} & \frac{1}{\bar{b}}Z_{r_b} \end{bmatrix} \\ \begin{bmatrix} 0 & 0 & 0 \\ 0 & 0 & 0 \end{bmatrix} & \begin{bmatrix} 0 & 0 \\ 0 & 0 \end{bmatrix} & 2V_T\cdot\begin{bmatrix} \frac{1}{\bar{b}} & \frac{1}{\bar{c}}S_{\phi_{0_b}}T_{\theta_{0_b}} & \frac{1}{\bar{b}}C_{\phi_{0_b}}T_{\theta_{0_b}} \\ 0 & \frac{1}{\bar{c}}C_{\phi_{0_b}} & -\frac{1}{\bar{b}}S_{\phi_{0_b}} \end{bmatrix} \\ \frac{1}{2}\cdot\begin{bmatrix} \bar{b}L_{u_b} & \bar{b}L_{v_b} & \bar{b}L_{w_b} \\ \bar{c}M_{u_b} & \bar{c}M_{v_b} & \bar{c}M_{w_b} \\ \bar{b}N_{u_b} & \bar{b}N_{v_b} & \bar{b}N_{w_b} \end{bmatrix} & \begin{bmatrix} 0 & 0 \\ 0 & 0 \\ 0 & 0 \end{bmatrix} & \begin{bmatrix} L_{p_b} & \frac{\bar{b}}{\bar{c}}L_{q_b} & L_{r_b} \\ \frac{\bar{c}}{\bar{b}}M_{p_b} & M_{q_b} & \frac{\bar{c}}{\bar{b}}M_{r_b} \\ N_{p_b} & \frac{\bar{b}}{\bar{c}}N_{q_b} & N_{r_b} \end{bmatrix} \end{bmatrix} \tag{5.6}$$

where $S_{\phi_{b_0}} = \sin\phi_{b_0}$, $C_{\phi_{b_0}} = \cos\phi_{b_0}$, $S_{\theta_{b_0}} = \sin\theta_{b_0}$, $C_{\theta_{b_0}} = \cos\theta_{b_0}$, $T_{\theta_{b_0}} = \tan\theta_{b_0}$.

Matrix A'_b can thus be represented as

$$A'_b = \begin{bmatrix} A'_{b_{F_v}} & A'_{b_G} & A'_{b_{F_\omega}} \\ \mathbf{0} & \mathbf{0} & A'_{b_E} \\ A'_{b_{M_v}} & \mathbf{0} & A'_{b_{M_\omega}} \end{bmatrix} \tag{5.7}$$

where F denotes force coefficients, M denotes moment coefficients, v denotes translational velocity, ω denotes rotational velocity, G denotes gravity, and E denotes Euler. Matrices B_b and B'_b are also divided into sub-matrix blocks as

$$B_b = \begin{bmatrix} \begin{bmatrix} X_{\delta_h} & 0 & 0 \\ 0 & Y_{\delta_a} & Y_{\delta_r} \\ Z_{\delta_h} & 0 & 0 \end{bmatrix} \\ \begin{bmatrix} 0 & 0 & 0 \\ 0 & 0 & 0 \end{bmatrix} \\ \begin{bmatrix} L_{\delta_h} & L_{\delta_a} & L_{\delta_r} \\ M_{\delta_h} & 0 & 0 \\ N_{\delta_h} & N_{\delta_a} & N_{\delta_r} \end{bmatrix} \end{bmatrix} \tag{5.8}$$

and

$$B'_b = \begin{bmatrix} \frac{1}{V_T} \cdot \begin{bmatrix} X_{\delta_h} & 0 & 0 \\ 0 & Y_{\delta_a} & Y_{\delta_r} \\ Z_{\delta_h} & 0 & 0 \end{bmatrix} \\ \begin{bmatrix} 0 & 0 & 0 \\ 0 & 0 & 0 \end{bmatrix} \\ \frac{1}{2V_T} \cdot \begin{bmatrix} \bar{b}L_{\delta_h} & \bar{b}L_{\delta_a} & \bar{b}L_{\delta_r} \\ \bar{c}M_{\delta_h} & 0 & 0 \\ \bar{b}N_{\delta_h} & \bar{b}N_{\delta_a} & \bar{b}N_{\delta_r} \end{bmatrix} \end{bmatrix} \tag{5.9}$$

Therefore, B'_b can be represented as

$$B'_b = \begin{bmatrix} B'_{b_{F_\delta}} \\ \mathbf{0} \\ B'_{b_{M_\delta}} \end{bmatrix} \tag{5.10}$$

where δ denotes control input.

Each block embeds a specific dynamic characteristic to the linear system. For example, the lower left block of matrix A_b or A'_b contains aerodynamic moment coefficients due to translational velocities ($A'_{b_{M_v}}$). These coefficients are referred to as stability derivatives. Blocks $A'_{b_{F_v}}$, $A'_{b_{F_\omega}}$ and $A'_{b_{M_\omega}}$ embed stability derivatives, as well. The top middle block provides gravity rotation components (A'_{b_G}), whereas A'_{b_E} provides Euler rotation components. Matrix B_b or B'_b contains blocks related to aerodynamic force and moment coefficients due to δ_h, δ_a, and δ_r: $B'_{b_{F_\delta}}$ and $B'_{b_{M_\delta}}$. The influence of different state and input system parameters on the index can now be systematically approached.

Block-wise index evaluation further pinpoints the exact dynamics that contribute to increased nonlinearity index values. The partial index, which shall be referred to as *sub-index*, evaluates the variation of a subset of the system dynamics within the overall linear model at a nominal point to that of a perturbed linear model. For example, the sub-index of block $A'_{b_{M_v}}$ measures the nonlinearity of the system specifically regarding the aerodynamic moment coefficients due to translational velocities, and the sub-index for A'_{b_G} reflects the nonlinearity associated with the gravity rotation terms. These sub-indices are denoted as $v_s^{A'}\big|_{M_v}$ and $v_s^{A'}\big|_G$, respectively, and Equations (5.11) and (5.12) provide the precise definitions. Similarly, the sub-indices for blocks $B'_{b_{F_\delta}}$ and $B'_{b_{M_\delta}}$ measure the nonlinearity of the system for the aerodynamic force and moment coefficients due to inputs δ_h, δ_a, δ_r and are denoted as $v_s^{B'}\big|_{F_\delta}$ and $v_s^{B'}\big|_{M_\delta}$, respectively. Finally, the *matrix-index* is simply defined as the matrix of sub-index values representing the various subsets

of system dynamics. Therefore, Equations (5.13) and (5.14) represent the *matrix-indices* for the linear system described by A_b' and B_b'.

$$v_S^{A'}\big|_{M_v} = \sup \frac{\left\| A'_{b_{M_v}} - \bar{A}'_{b_{M_v}} \right\|}{\left\| \bar{A}'_{b_{M_v}} \right\|} \tag{5.11}$$

$$v_S^{A'}\big|_{G} = \sup \frac{\left\| A'_{b_G} - \bar{A}'_{b_G} \right\|}{\left\| \bar{A}'_{b_G} \right\|} \tag{5.12}$$

$$v_S^{A'}\big|_{\text{matrix-index}} = \begin{bmatrix} v_S^{A'}\big|_{F_v} & v_S^{A'}\big|_{G} & v_S^{A'}\big|_{F_\omega} \\ 0 & 0 & v_S^{A'}\big|_{E} \\ v_S^{A'}\big|_{M_v} & 0 & v_S^{A'}\big|_{M_\omega} \end{bmatrix} \tag{5.13}$$

$$v_S^{B'}\big|_{\text{matrix-index}} = \begin{bmatrix} v_S^{B'}\big|_{F_\delta} \\ 0 \\ v_S^{B'}\big|_{M_\delta} \end{bmatrix} \tag{5.14}$$

5.3 Index for Full-Envelope Using Body-Frame

The linear system in Equation (5.4) is based on the nonlinear aircraft model derived in the body-frame of reference. Applying the four index expressions in Equations (3.8) and (3.9) produces four contour plots (Figures 5.2-5.5) and four surface plots (Figures 5.6-5.9) for visualization of the envelope nonlinearity variations. In general, the nonlinearity strength is largest near the internal envelope boundary corresponding to the $\bar{q}$ limit, particularly for the $\alpha < 0$ region. The figures show that for indices $v_S^{A'}$ and $v_d^{x'}$ associated with the states, a single maximum occurs. For indices $v_S^{B'}$ and v_d^{u} associated with the inputs, three strong maximums occur. At the points $(\alpha, \beta) = (-6^\circ, \pm 2^\circ)$, two closely spaced maximums occur with the global maximum occurring at $\beta = -2^\circ$. The

third maximum occurs near the upper region of the envelope boundary in the stall region at $\alpha = 58^{\circ}$. Maximum values are found to be ${v_s^{A'}}_{\max} = 2.73$, ${v_s^{B'}}_{\max} = 2.93$, ${v_d^{x'}}_{\max} = 1.62$, and ${v_d^{u}}_{\max} = 4.30$. In these regions, use of linear models to examine dynamic behavior or design control systems is not feasible. Note that the nonlinearity is also sensitive to both α and β variation in these regions. In the other regions of the $\alpha - \beta$ envelope, the nonlinearity strength is difficult to assess with the displayed data, due to washout from the noted maximum values. The expected index surface behavior was to have been larger values near the envelope edge where the aerodynamic angles are extreme with smaller values at interior regions, which is the opposite of that displayed in Figures 5.2-5.5. To understand the internal region nonlinearity sources, further investigation is needed.

The index $v_s^{A'}$ attains its maximum value at the nominal point $(\alpha_n, \beta_n) = (-6^{\circ}, 0^{\circ})$ where the perturbed point $(\alpha_p, \beta_p) = (-1.6648^{\circ}, 0^{\circ})$ is found to cause the largest deviation around (α_n, β_n). Eigenvalue analysis at both points shows instability in the linear models. However, instability is not a measure or indication of the nonlinearity strength, as an unstable but exactly linear model would produce a zero index value. In Table 5.1, differences between the trimming solutions for both points are insignificant, except for velocity and throttle which reveals large flight condition change for small α and β variations. To assess the contributed weight of each component in the state matrix towards the overall index, A_b' is divided into sub-matrix blocks, as seen in Equation (5.6). The influence of V_T on the index can now be systematically approached. Sub-index evaluation shows that $v_s^{A'}\big|_{M_v} = 5.69$ and $v_s^{A'}\big|_{M_\omega} = 3.36$ exhibit the highest nonlinearity sub-index values, as shown in Equation (5.15). Preliminary investigation indicates that

the large jump in the trimming V_T value associated with the slight variation in α enlarges the moment stability derivative deviation related to the A'_{M_v} and A'_{M_ω} blocks as seen in Equation (5.6). Note the explicit dependence on V_T in A'_b due to the normalized state formulation in Equation (5.6) is not that significant here.

The static input nonlinearity index $\nu_s^{B'}$ in this study indicates the system is also equally sensitive to input excitation near the $\bar{q}$ limit, however, it is further sensitive near the stall region at high α, which explains the large value of $\nu_s^{B'}$ at the spike shown in Figure 5.7. The largest spike occurs at $(\alpha_n, \beta_n) = (-6^\circ, -2^\circ)$ and is caused by the deviation at $(\alpha_p, \beta_p) = (-1.3346^\circ, -2^\circ)$. In Table 5.1, at both points, the only significant difference in the trim solution is the velocity, bank angle, and throttle. Matrix B'_b embeds two blocks related to aerodynamic force and moment coefficients due to δ_h, δ_a, and δ_r: B'_{F_δ} and B'_{M_δ}. The bank angle does not play any role in B'_b, and only V_T determines how large the deviation is. It can be seen in Equation (5.9) that the normalized matrix B'_b is directly multiplied by $1/V_T$. Moreover, the jump in the velocity introduces more drag and lift, such that the trim drag force increases by 104% and the trim lift force increase by 89%. These forces are present in B'_b through the resolved axial, side, and normal force components. Consequently, these forces induce moments as well, and the matrix-index for B'_b shows that sub-indices $\nu_s^{B'}\big|_{F_\delta}$ and $\nu_s^{B'}\big|_{M_\delta}$ contribute equally toward the overall index (Equation (5.15)).

The dynamic nonlinearity indices $\nu_d^{x'}$ and ν_d^{u}, which are now functions of both operating conditions and time, are displayed as contour and surface plots in Figures 5.4-5.5 and Figures 5.8-5.9 at time $t = 0.01$ s. Similar to the static indices, dynamic indices

are sensitive at high-speed flight near the $\bar{q}$ limit for indices $v_d^{x'}$ and v_d^u and is sensitive at high α near the stall limit for index v_d^u and are expected to propagate with time. At very low time, $v_d^{x'}$ tends to be much smaller than $v_s^{A'}$, when comparing Figure 5.2 to 5.4 or Figure 5.6 to 5.8. On the contrary, the dynamic input index v_d^u which measures the propagation of input nonlinearity with time is far more sensitive than static input index $v_s^{B'}$. The transition matrix Φ captures and amplifies the nonlinearities associated with B_b'. Around the high dynamic index region, the aircraft model is unstable and the linear model tends to deviate faster if input excited rather than state excited, but again instability is not a true measure of nonlinearity.

Since the index variation with respect to β appears small except around high index value regions, slices from the surface plots of the four indices at $\beta = 0^\circ$ are shown in Figure 5.10. Furthermore, the corresponding trimming solutions are presented in Figure 5.11. A discontinuity exists between $\alpha = -1.6647^\circ$ and -0.9409° in each plot due to the $\bar{q}$ limit. Note the trimming roll angle ϕ_b exhibits an interesting feature around the unattainable trimmed flight region. For $\alpha \geq -0.9409^\circ$, $\phi_b = 0^\circ$ while for $\alpha \leq -1.6647^\circ$, $\phi_b = 180^\circ$ or -180°. In both cases, the aircraft assumes a wing-level orientation, but in the second case, the aircraft is flying inverted or upside down.

$$v_s^{A'}\big|_{\text{matrix-index}} = \begin{bmatrix} 1.68 & 0.74 & 2.70 \\ 0 & 0 & 2.76 \\ 5.69 & 0 & 3.36 \end{bmatrix}$$

$$v_s^{B'}\big|_{\text{matrix-index}} = \begin{bmatrix} 2.92 \\ 0 \\ 2.93 \end{bmatrix} \tag{5.15}$$

Table 5.1 Trim solutions at nominal and perturbed points

	For A_b'		For B_b'	
	$(\alpha_n, \beta_n) = (-6^\circ, 0^\circ)$	$(\alpha_p, \beta_p) = (-1.6648^\circ, 0^\circ)$	$(\alpha_n, \beta_n) = (-6^\circ, -2^\circ)$	$(\alpha_p, \beta_p) = (-1.3346^\circ, -2^\circ)$
V_T	404.1 ft/s, (M = 0.36)	1520.9 ft/s, (M = 1.36)	402.69 ft/s, (M = 0.36)	1520.98 ft/s, ($M = 1.36$)
ϕ_b	180°	180°	-176.0855°	-97.4596°
θ_b	6°	1.6648°	6.1219°	2.1567°
δ_h	-0.8503°	-1.0903°	-0.8352°	-1.1151°
δ_a	0°	0°	-0.6026°	0.0766°
δ_r	0°	0°	-4.3163°	-4.4087°
δ_{th}	0.1983	0.9107	0.1998	0.9087

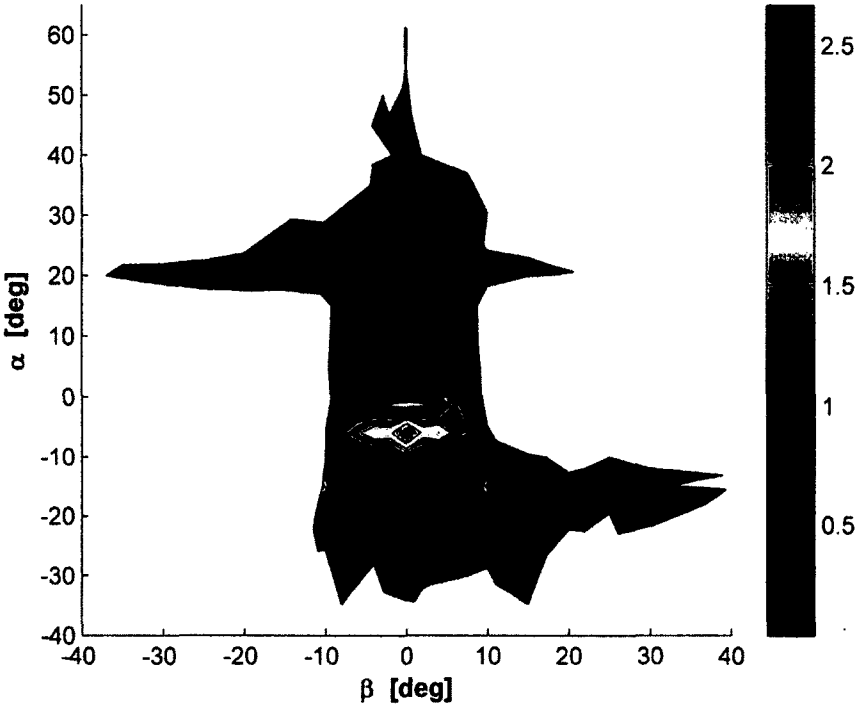

Figure 5.2 Static state nonlinearity index $\nu_S^{A'}$ - contour (body-frame)

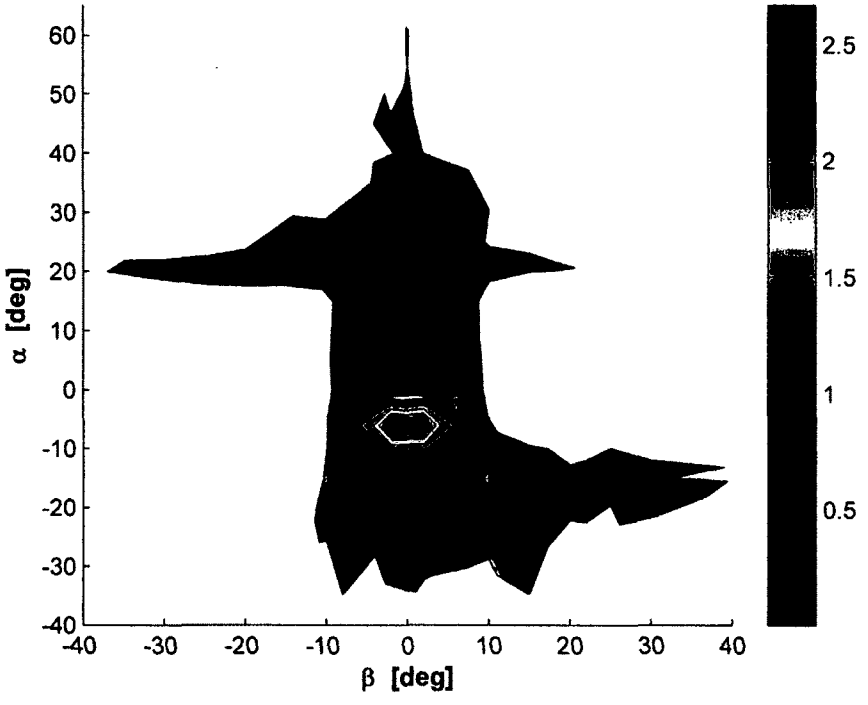

Figure 5.3 Static input nonlinearity index $\nu_S^{B'}$ - contour (body-frame)

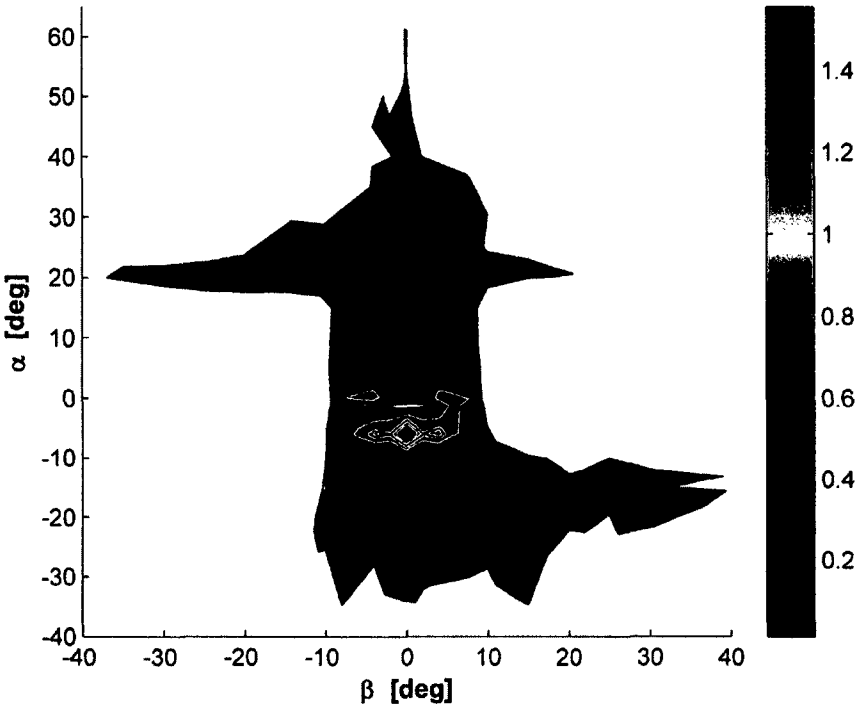

Figure 5.4 Dynamic state nonlinearity index $\nu_d^{x'}$ - contour (body-frame)

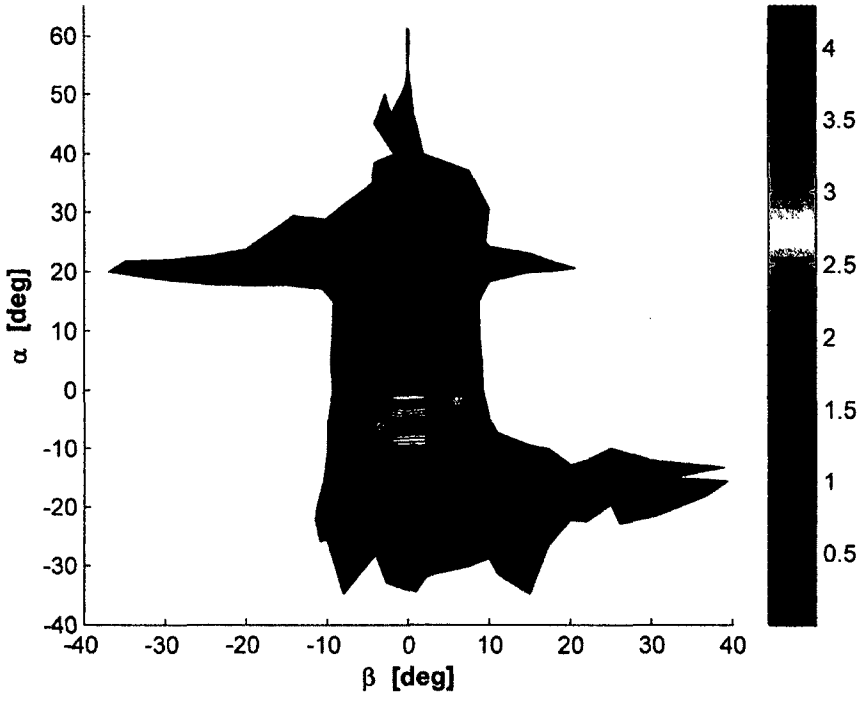

Figure 5.5 Dynamic input nonlinearity index ν_d^u - contour (body-frame)

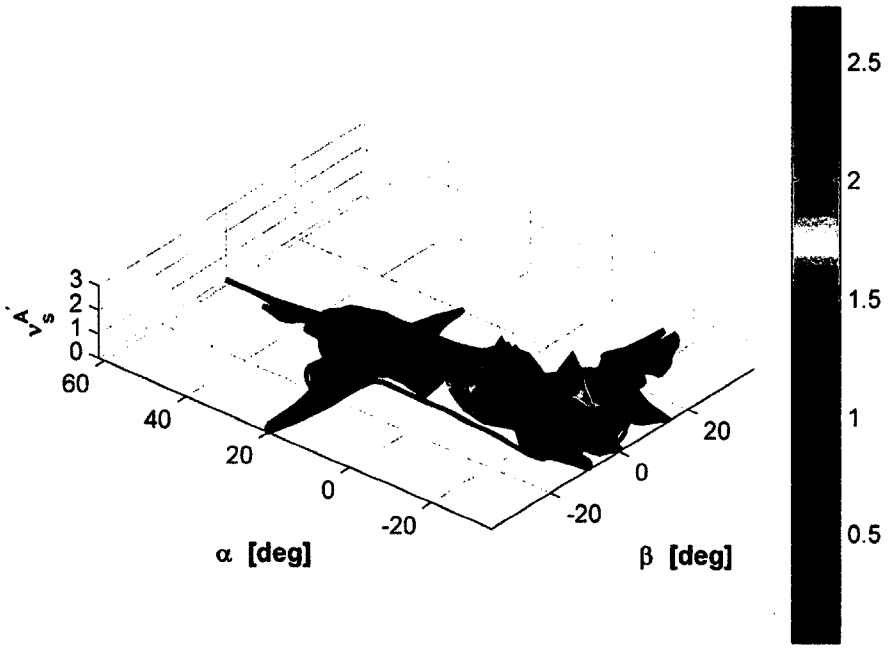

Figure 5.6 Static state nonlinearity index $\nu_s^{A'}$ - surface (body-frame)

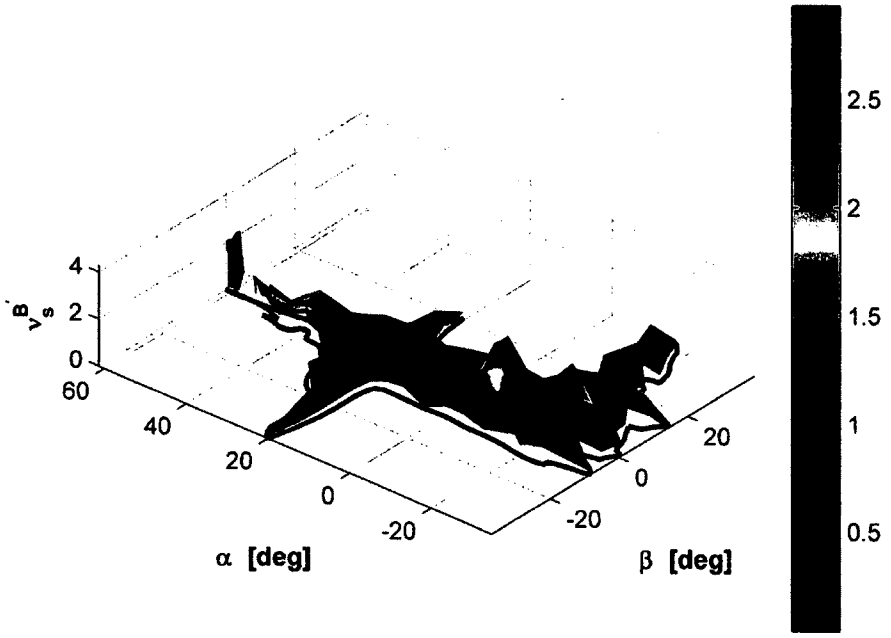

Figure 5.7 Static input nonlinearity index $\nu_s^{B'}$ - surface (body-frame)

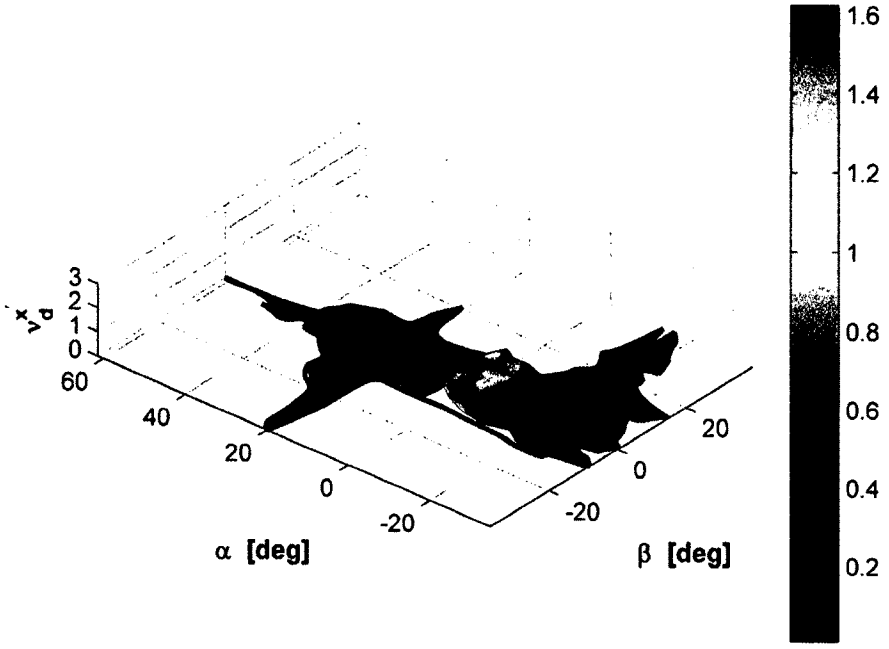

Figure 5.8 Dynamic state nonlinearity index $\nu_d^{x'}$ - surface (body-frame)

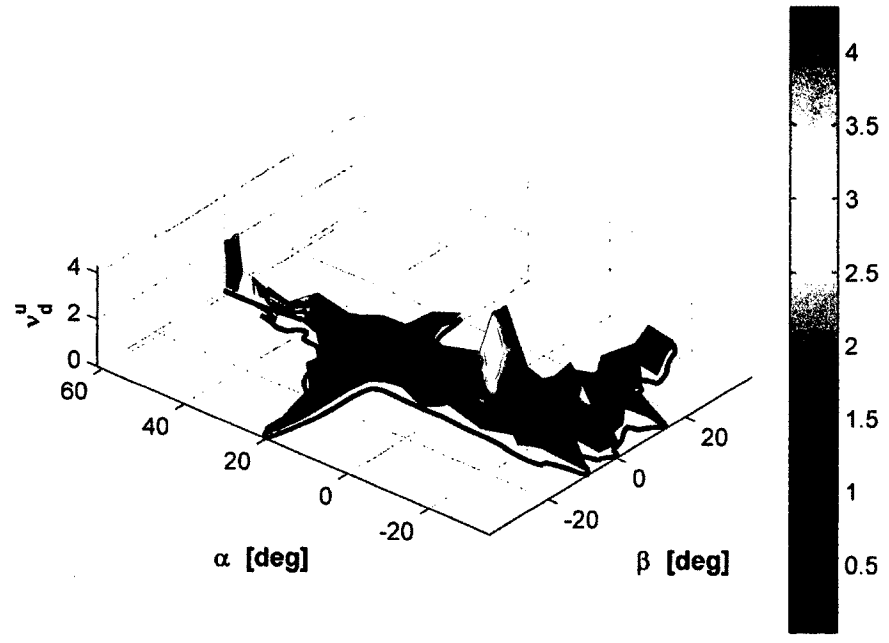

Figure 5.9 Dynamic input nonlinearity index ν_d^u - surface (body-frame)

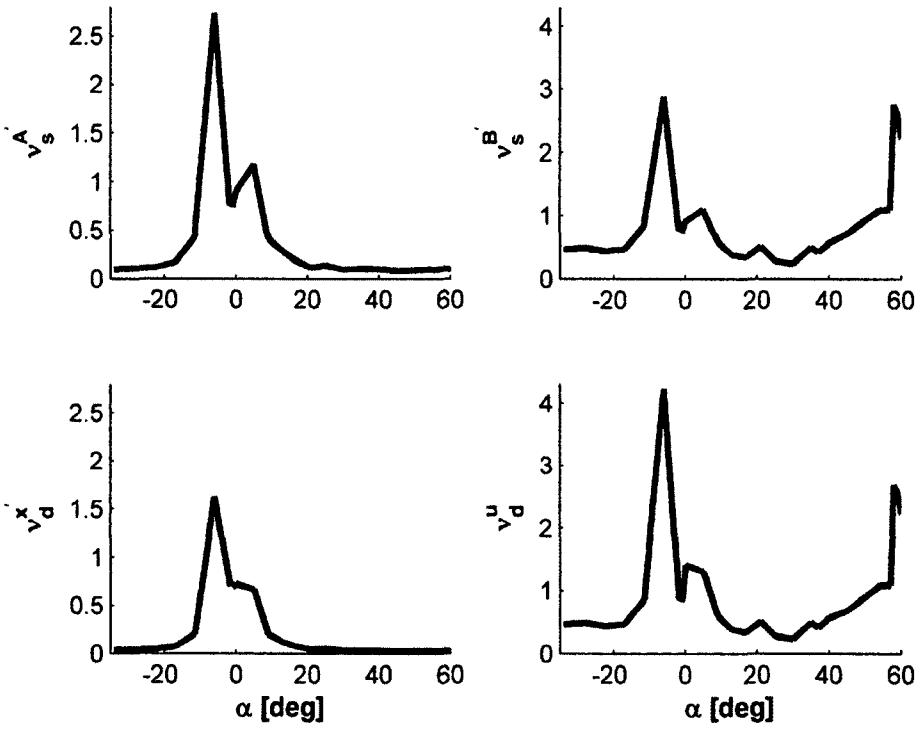

Figure 5.10 Nonlinearity indices at $\beta = 0^\circ$ (body-frame)

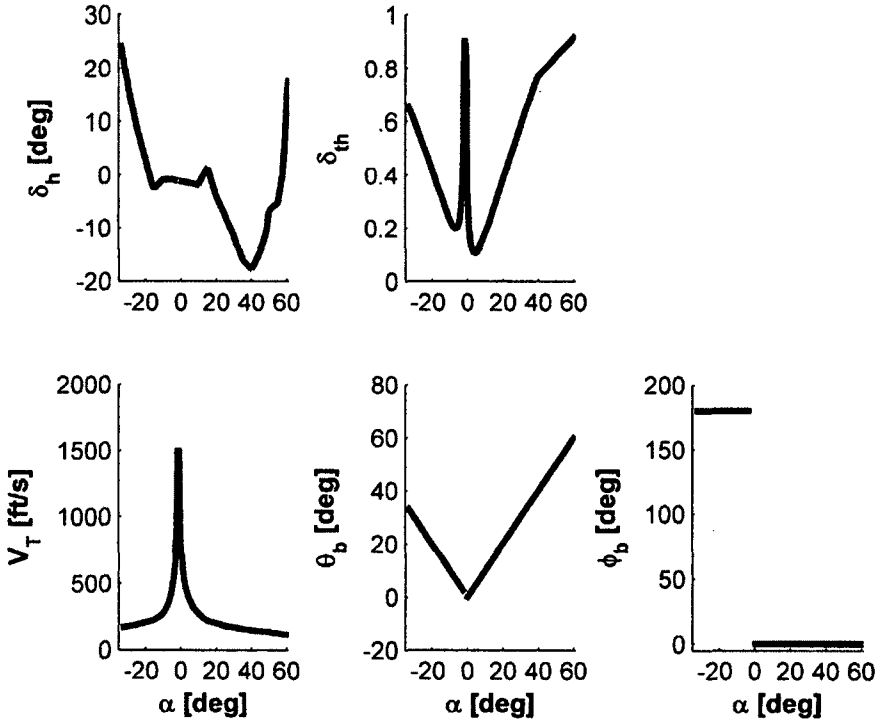

Figure 5.11 Trimming values at $\beta = 0^\circ$ (body-frame)

5.4 Index for Full-Envelope Using Body-Frame – Ideal Model

In Chapter 4, the aerodynamic model is idealized and, in Figure 4.9, an ideal asymmetric flight envelope is developed. Applying the four index expressions in Equations (3.8) and (3.9), on top of this ideal envelope, produces four symmetric contour plots (Figures 5.12-5.15) and four symmetric surface plots (Figures 5.16-5.19) for visualization of the envelope nonlinearity variations. The behavior of the indices on the envelope here is similar, but the values are specifically different, when compared to the results of the non-ideal case in Section 5.3. In general, the nonlinearity strength is largest near the internal envelope boundary corresponding to the $\bar{q}$ limit, particularly for the $\alpha < 0$ region. The figures show that for indices $v_s^{A'}$ and $v_d^{x'}$ associated with the states, a single maximum occurs. For indices $v_s^{B'}$ and v_d^{u} associated with the inputs, three strong maximums occur. At the points $(\alpha, \beta) = (-6^\circ, \pm 2^\circ)$, two closely spaced identical global maximums occur. The third maximum occurs near the upper region of the envelope boundary in the stall region at $\alpha \approx 61^\circ$. Maximum values are found to be ${v_s^{A'}}_{\max} = 2.73$, ${v_s^{B'}}_{\max} = 2.91$, ${v_d^{x'}}_{\max} = 1.62$, and ${v_d^{u}}_{\max} = 4.27$. In these regions, use of linear models to examine dynamic behavior or design control systems is not feasible. Note that the nonlinearity is also sensitive to both α and β variation in these regions. In the other regions of the $\alpha - \beta$ envelope, the nonlinearity strength is difficult to assess with the displayed data, due to washout from the noted maximum values.

The index $v_s^{A'}$ attains its maximum value at the nominal point $(\alpha_n, \beta_n) = (-6^\circ, 0^\circ)$ where the perturbed point $(\alpha_p, \beta_p) = (-1.6648^\circ, 0^\circ)$ is found to cause the largest deviation around (α_n, β_n). Eigenvalue analysis is also utilized here, and at both points, it shows instability in the linear models. In Table 5.2, differences between the

trimming solutions for both points are insignificant except for velocity and throttle which show large differences. To assess the contributed weight of each component in the state matrix towards the overall index, the matrix-index evaluation shows that A'_{M_v}, then A'_{M_ω} exhibit the highest nonlinearity sub-index values, as shown in Equation (5.16). Preliminary investigation indicates that the large jump in the trimming V_T value associated with the slight variation in α enlarges the moment stability derivative deviation related to the A'_{M_v} and A'_{M_ω} blocks, as seen in Equation (5.6). Again note the explicit dependence on V_T in Equation (5.6) is not the important factor here.

The static input nonlinearity index $v_s^{B'}$ in this study indicates the system is equally sensitive to input excitation, which explains the large values of $v_s^{B'}$ at the two identical and third spikes shown in Figure 5.17. One of the largest spikes occurs at $(\alpha_n, \beta_n) = (-6^\circ, +2^\circ)$ and is caused by the deviation at $(\alpha_p, \beta_p) = (-1.3923^\circ, +2^\circ)$. At this nominal point, the aircraft is trimmed to an almost inverted position at $\phi_b = 176.2^\circ$ but at the maximum deviated point the aircraft is nearly in a knife edge position of $\phi_b = 104.6^\circ$. The only other significant difference in the trim solution is the velocity (and throttle) which is 403 ft/s compared to 1521 ft/s. The slight variation in the δ_h, δ_a and δ_r trimming solutions changes the forces and moments acting on the aircraft, and thus contributes towards the overall index. The bank angle does not play any role in B'_b and only V_T and the control surface trimming deflections determine how large the deviation is. Moreover, the jump in the trim velocity introduces more forces and moments. These forces are present in B'_b through the resolved axial, side, and normal force components.

Matrix B_b' embeds two blocks, B_{F_δ}' and B_{M_δ}', and the matrix-index shows that the sub-indices $v_s^{B'}|_{F_\delta}$ and $v_s^{B'}|_{M_\delta}$ contribute equally toward the overall index (Equation (5.16)).

The dynamic nonlinearity indices $v_d^{x'}$ and v_d^u, which are now functions of both operating conditions and time, are displayed as contour and surface plots in Figures 5.14-5.15 and Figures 5.18-5.19 at time $t = 0.01$ s. Similar to the static indices, dynamic indices are sensitive at high-speed flight near the $\bar{q}$ limit for indices $v_d^{x'}$ and v_d^u and are sensitive also at high α near the stall limit for index v_d^u and are expected to propagate with time. At very low time, $v_d^{x'}$ tends to be much smaller than $v_s^{A'}$, when comparing Figure 5.12 to 5.14 or Figure 5.16 to 5.18. On the contrary, the dynamic input index v_d^u, which measures the propagation of input nonlinearity with time, is far more sensitive than the static input index $v_s^{B'}$. The transition matrix Φ captures and amplifies the nonlinearities associated with B_b'. Around the high dynamic index region, the aircraft model is unstable, and the linear model tends to deviate faster if input excited rather than state excited.

Similar to the previous case with non-ideal aerodynamic model, the index variation with respect to β using the ideal model appears small except around high index value regions. Slices from the surface plots of the four indices at $\beta = 0^\circ$ are shown in Figure 5.20. Furthermore, the corresponding trimming solutions are presented in Figure 5.21. A discontinuity exists between $\alpha = -1.6648^\circ$ and -0.9410° in each plot due to the $\bar{q}$ limit. Note that the trimming roll angle ϕ_b exhibits an interesting feature around the unattainable trimmed flight region. For $\alpha \geq -0.9410^\circ$, $\phi_b = 0^\circ$ while for

$\alpha \leq -1.6648^{\circ}$, $\phi_b = 180^{\circ}$ or -180°. In both cases, the aircraft assumes a wing-level orientation, but in the second case the aircraft is flying inverted or upside down.

$$v_S^{A'}|_{\text{matrix-index}} = \begin{bmatrix} 1.68 & 0.74 & 2.70 \\ 0 & 0 & 2.76 \\ 5.72 & 0 & 3.36 \end{bmatrix}$$
$$v_S^{B'}|_{\text{matrix-index}} = \begin{bmatrix} 3.06 \\ 0 \\ 2.91 \end{bmatrix} \tag{5.16}$$

Table 5.2 Trim solutions at nominal and perturbed points (ideal)

	For A_b'		For B_b'	
	$(\alpha_n, \beta_n) = (-6^{\circ}, 0^{\circ})$	$(\alpha_p, \beta_p) = (-1.6648^{\circ}, 0^{\circ})$	$(\alpha_n, \beta_n) = (-6^{\circ}, +2^{\circ})$	$(\alpha_p, \beta_p) = (-1.3923^{\circ}, +2^{\circ})$
V_T	$404.1\ ft/s$, $(M = 0.36)$	$1520.9\ ft/s$, $(M = 1.36)$	$403.01\ ft/s$, $(M = 0.36)$	$1520.9\ ft/s$, $(M = 1.36)$
ϕ_b	180°	180°	176.1981°	104.5954°
θ_b	6°	1.6648°	6.1188°	2.2865°
δ_h	-0.8503°	-1.0903°	-0.8544°	-1.1047°
δ_a	0°	0°	0.6059°	-0.0255°
δ_r	0°	0°	4.3818°	4.5209°
δ_{th}	0.1983	0.9107	0.1996	0.9092

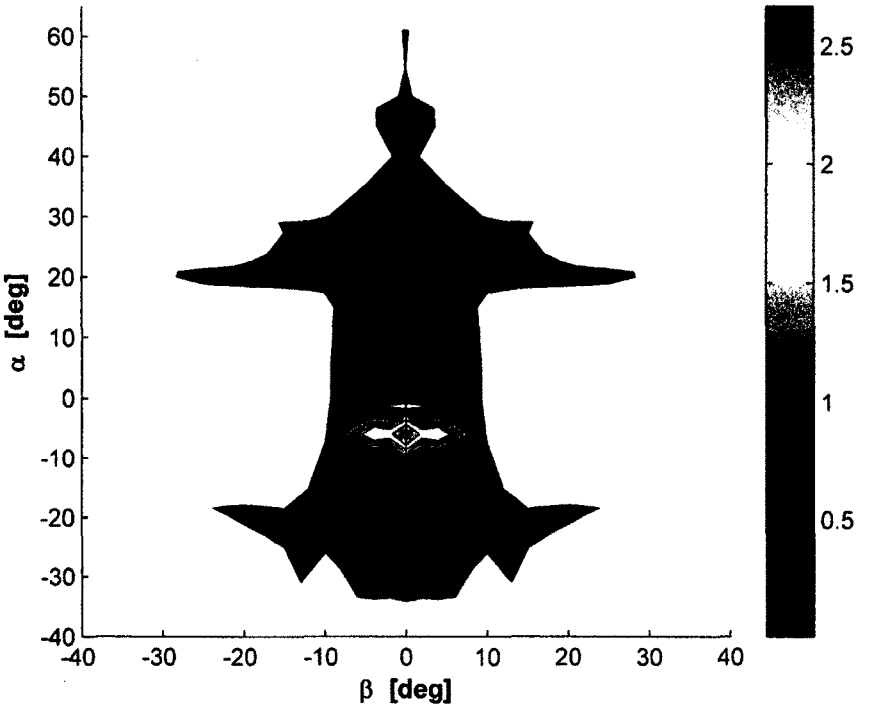

Figure 5.12 Static state nonlinearity index $\nu_S^{A'}$ - contour (body-frame, ideal)

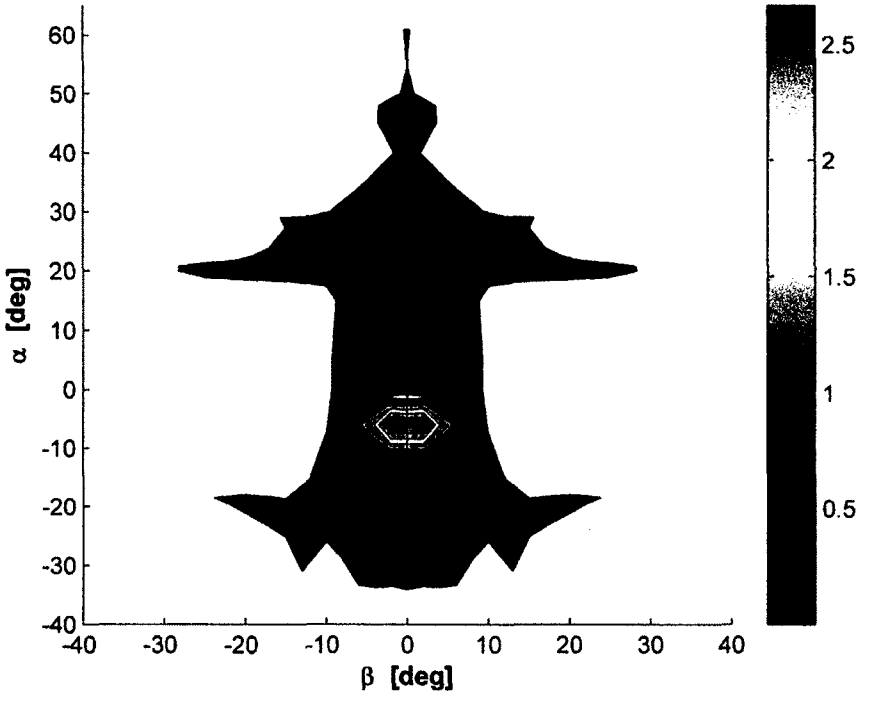

Figure 5.13 Static input nonlinearity index $\nu_S^{B'}$ - contour (body-frame, ideal)

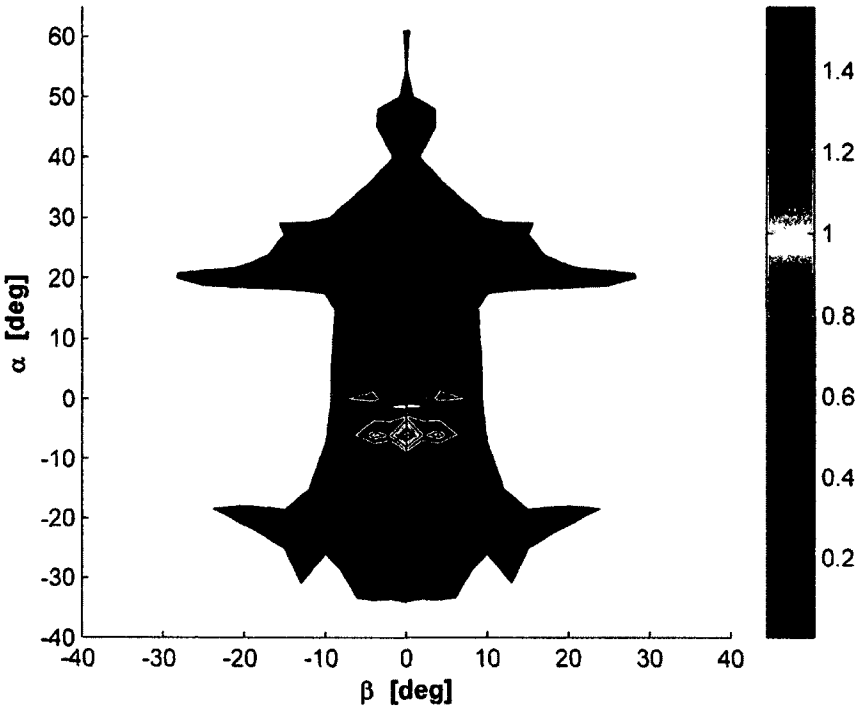

Figure 5.14 Dynamic state nonlinearity index $\nu_d^{x'}$ - contour (body-frame, ideal)

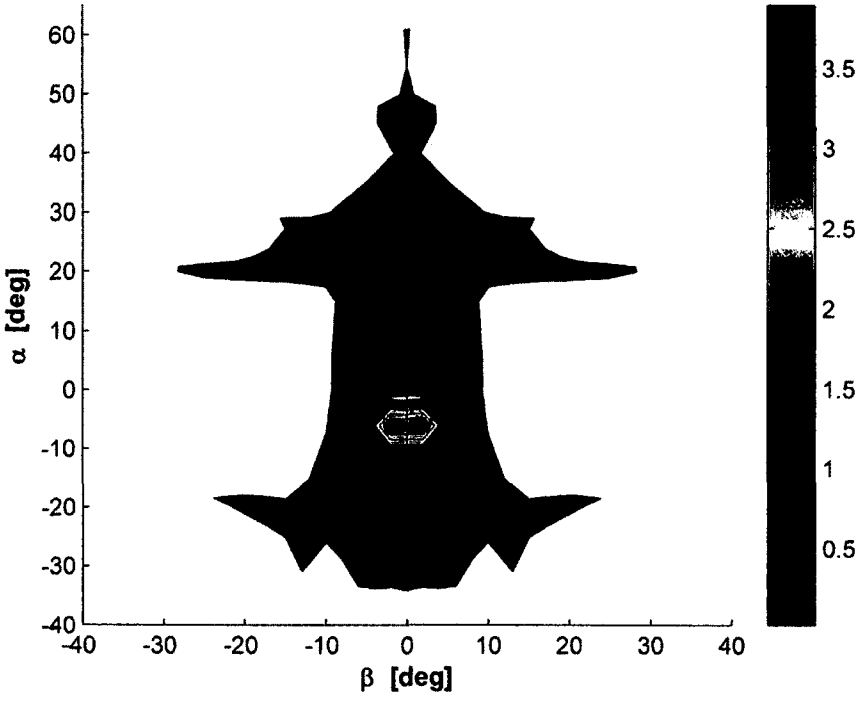

Figure 5.15 Dynamic input nonlinearity index ν_d^u - contour (body-frame, ideal)

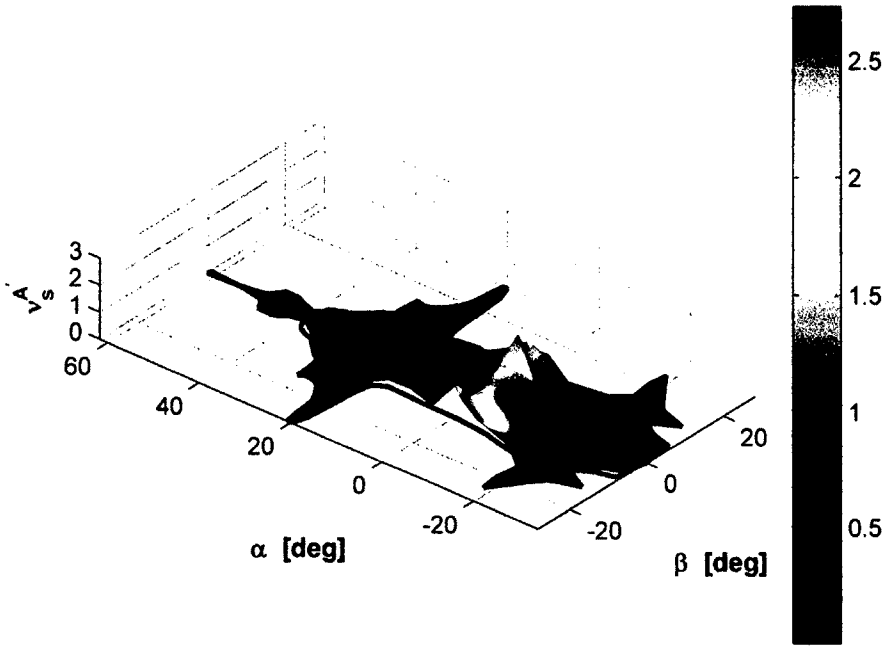

Figure 5.16 Static state nonlinearity index $\nu_s^{A'}$ - surface (body-frame, ideal)

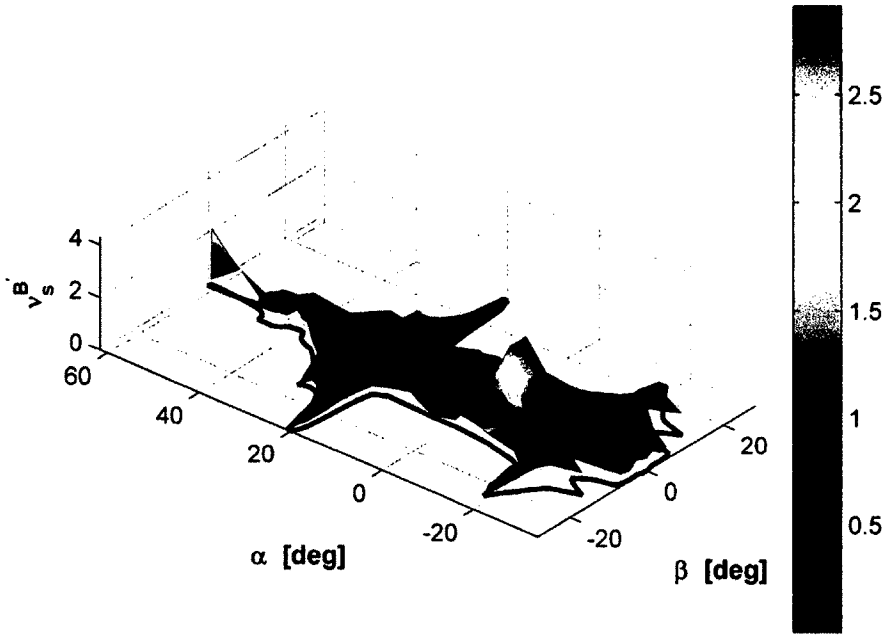

Figure 5.17 Static input nonlinearity index $\nu_s^{B'}$ - surface (body-frame, ideal)

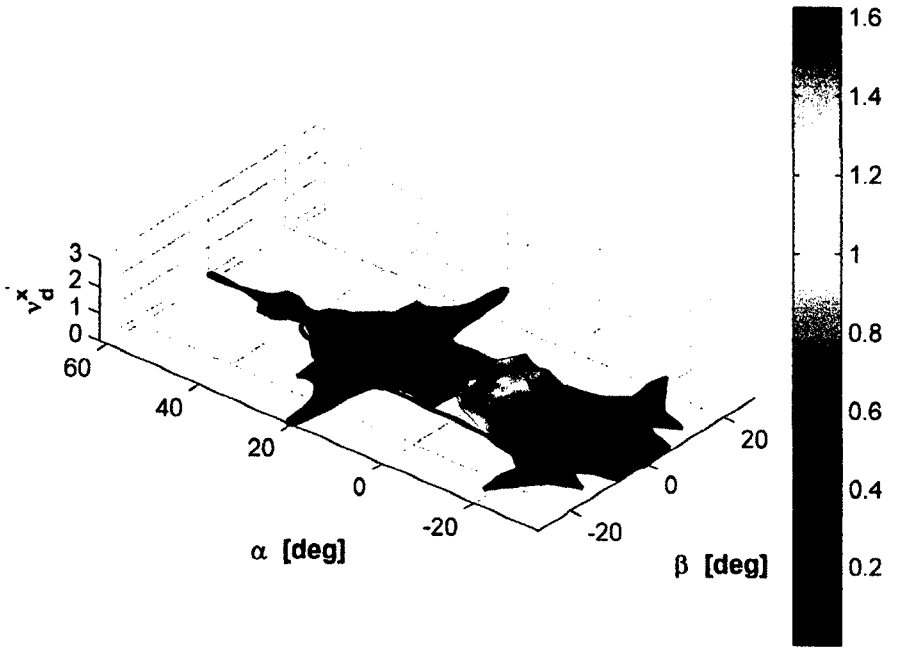

Figure 5.18 Dynamic state nonlinearity index $\nu_d^{x'}$ - surface (body-frame, ideal)

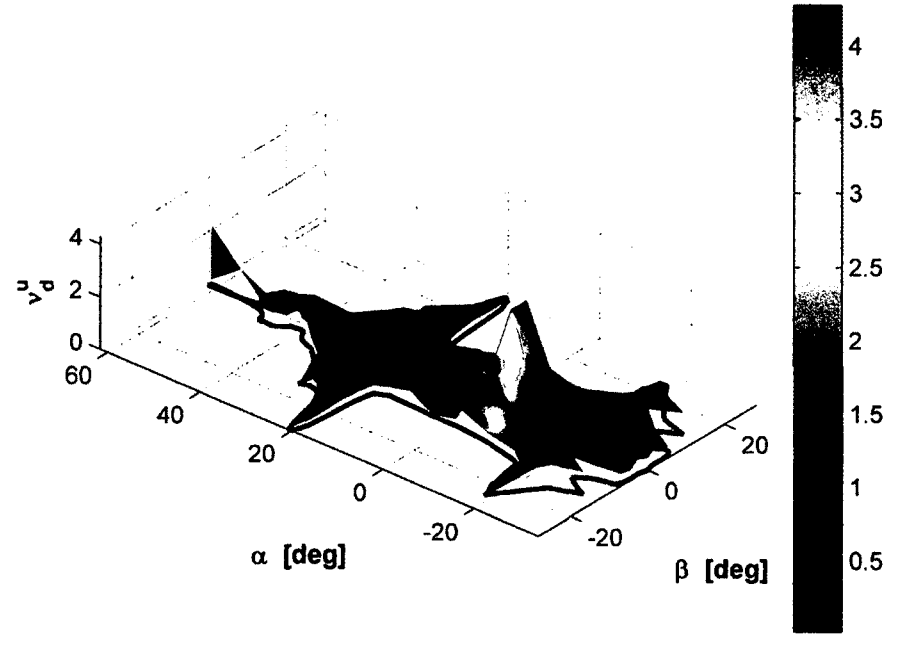

Figure 5.19 Dynamic input nonlinearity index ν_d^u - surface (body-frame, ideal)

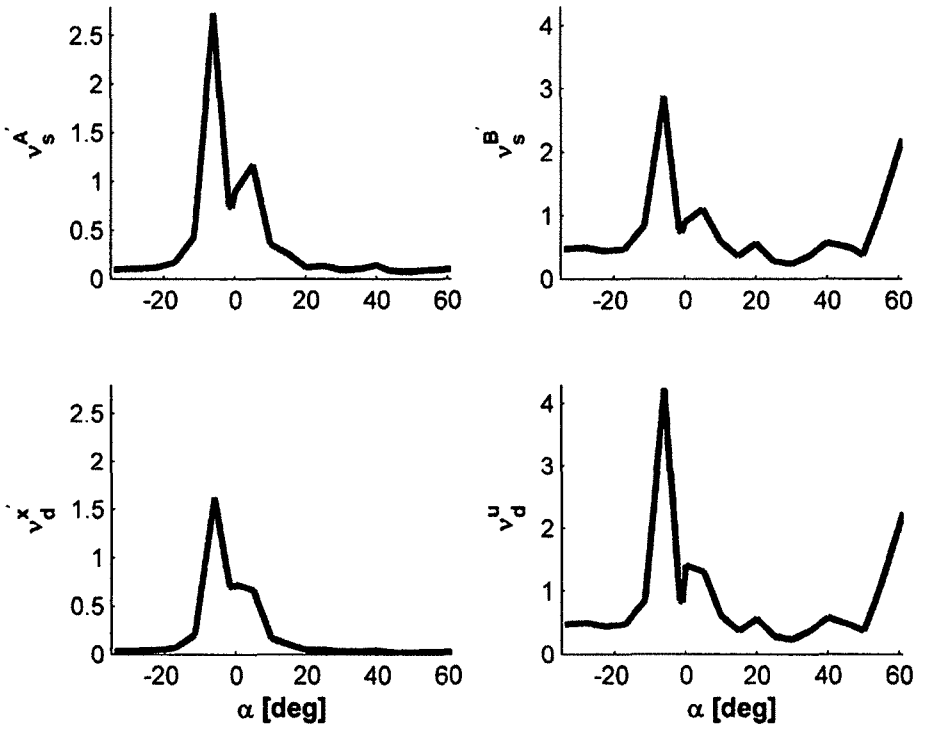

Figure 5.20 Nonlinearity indices at $\beta = 0^\circ$ (body-frame, ideal)

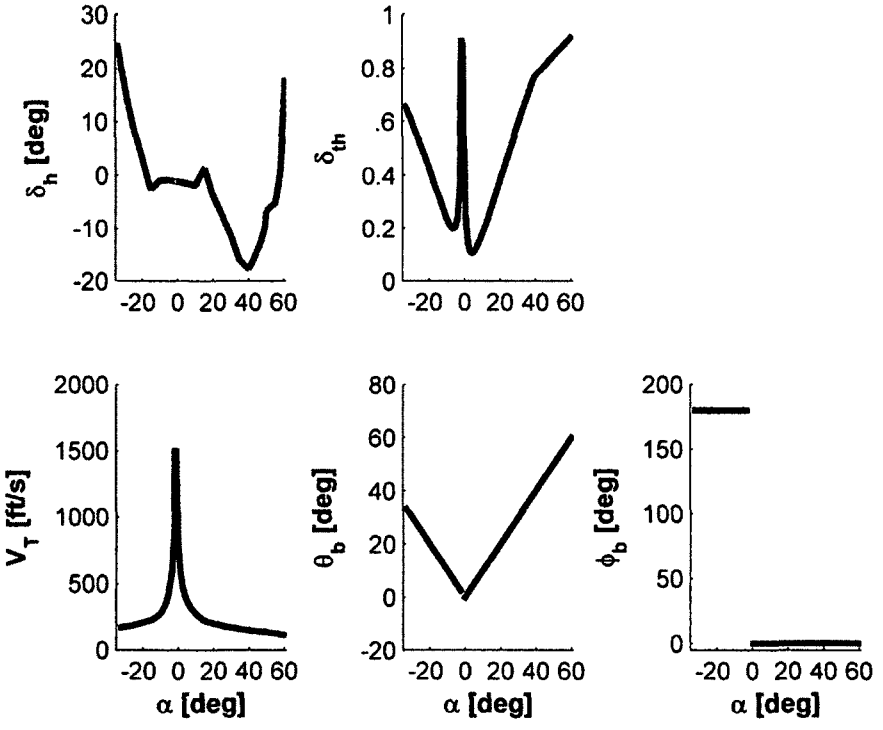

Figure 5.21 Trimming values at $\beta = 0^\circ$ (body-frame, ideal)

5.5 Index for Full-Envelope Using Stability-Frame – Ideal Model

In this section, the ideal envelope in Figure 4.9 produced in Chapter 4 is investigated. A linear model system is developed using the nonlinear equations of motion in the stability-frame of reference discussed in Section 2.6. Hence, the components of the linear system are now described in stability-frame coordinates rather than body-frame coordinates (see Equations (5.17) - (5.19)). Note the transformation matrix T is modified accordingly, where the first three diagonal elements are replaced by $[1/V_T \quad 1/V_T \quad 1]$.

$$\begin{gathered}\dot{\mathbf{x}}_S' = A_S'\mathbf{x}_S' + B_S'\mathbf{u} \\ \mathbf{x}_S' = [\Delta u_S' \quad \Delta v_S' \quad \Delta\alpha' \quad \Delta\phi_S' \quad \Delta\theta_S' \quad \Delta p_S' \quad \Delta q_S' \quad \Delta r_S'] \\ A_S' = TA_ST^{-1} \\ B_S' = TB_S,\end{gathered} \tag{5.17}$$

where

$$A_S' = \begin{bmatrix} \begin{bmatrix} X_{u_s} & X_{v_s} & \frac{1}{V_T}X_\alpha \\ Y_{u_s} & Y_{v_s} & \frac{1}{V_T}Y_\alpha \\ V_TZ_{u_s} & V_TZ_{v_s} & Z_\alpha \end{bmatrix} & \begin{bmatrix} 0 & \frac{1}{V_T}gC_{\theta_{s_0}} \\ \frac{1}{V_T}gC_{\phi_{s_0}}C_{\theta_{s_0}} & \frac{1}{V_T}gS_{\phi_{s_0}}S_{\theta_{s_0}} \\ gS_{\phi_{s_0}}C_{\theta_{s_0}} & gC_{\phi_{s_0}}S_{\theta_{s_0}} \end{bmatrix} & 2\cdot\begin{bmatrix} \frac{1}{\bar{b}}X_{p_s} & \frac{1}{\bar{c}}X_{q_s} & \frac{1}{\bar{b}}X_{r_s} \\ \frac{1}{\bar{b}}Y_{p_s} & \frac{1}{\bar{c}}Y_{q_s} & \frac{1}{\bar{b}}Y_{r_s} \\ \frac{V_T}{\bar{b}}Z_{p_s} & \frac{V_T}{\bar{c}}Z_{q_s} & \frac{V_T}{\bar{b}}Z_{r_s} \end{bmatrix} \\ \begin{bmatrix} 0 & 0 & 0 \\ 0 & 0 & 0 \end{bmatrix} & \begin{bmatrix} 0 & 0 \\ 0 & 0 \end{bmatrix} & 2V_T\cdot\begin{bmatrix} \frac{1}{\bar{b}} & \frac{1}{\bar{c}}S_{\phi_{s_0}}T_{\theta_{s_0}} & \frac{1}{\bar{b}}C_{\phi_{s_0}}T_{\theta_{s_0}} \\ 0 & \frac{1}{\bar{c}}C_{\phi_{s_0}} & -\frac{1}{\bar{b}}S_{\phi_{s_0}} \end{bmatrix} \\ \frac{1}{2}\cdot\begin{bmatrix} \bar{b}L_{u_s} & \bar{b}L_{v_s} & \frac{\bar{b}}{V_T}L_\alpha \\ \bar{c}M_{u_s} & \bar{c}M_{v_s} & \frac{\bar{c}}{V_T}M_\alpha \\ \bar{b}N_{u_s} & \bar{b}N_{v_s} & \frac{\bar{b}}{V_T}N_\alpha \end{bmatrix} & \begin{bmatrix} 0 & 0 \\ 0 & 0 \\ 0 & 0 \end{bmatrix} & \begin{bmatrix} L_{p_s} & \frac{\bar{b}}{\bar{c}}L_{q_s} & L_{r_s} \\ \frac{\bar{c}}{\bar{b}}M_{p_s} & M_{q_s} & \frac{\bar{c}}{\bar{b}}M_{r_s} \\ N_{p_s} & \frac{\bar{b}}{\bar{c}}N_{q_s} & N_{r_s} \end{bmatrix} \end{bmatrix} \\ = \begin{bmatrix} A_{SF_{v,\alpha}}' & A_{SG}' & A_{SF_\omega}' \\ \mathbf{0} & \mathbf{0} & A_{SE}' \\ A_{SM_{v,\alpha}}' & \mathbf{0} & A_{SM_\omega}' \end{bmatrix} \end{bmatrix} \tag{5.18}$$

and

$$B_S' = \begin{bmatrix} \frac{1}{V_T} \cdot \begin{bmatrix} X_{\delta_h} & 0 & 0 \\ 0 & Y_{\delta_a} & Y_{\delta_r} \\ V_T Z_{\delta_h} & 0 & 0 \end{bmatrix} \\ \begin{bmatrix} 0 & 0 & 0 \\ 0 & 0 & 0 \end{bmatrix} \\ \frac{1}{2V_T} \cdot \begin{bmatrix} \bar{b}L_{\delta_h} & \bar{b}L_{\delta_a} & \bar{b}L_{\delta_r} \\ \bar{c}M_{\delta_h} & 0 & 0 \\ \bar{b}N_{\delta_h} & \bar{b}N_{\delta_a} & \bar{b}N_{\delta_r} \end{bmatrix} \end{bmatrix} = \begin{bmatrix} B'_{S_{F_\delta}} \\ \mathbf{0} \\ B'_{S_{M_\delta}} \end{bmatrix} \tag{5.19}$$

Applying the four index expressions in Equations (3.8) and (3.9) on top of this ideal envelope, produces four symmetric contour plots (Figures 5.22-5.25) and four symmetric surface plots (Figures 5.26-5.29) for visualization of the envelope nonlinearity variations. The behavior of the indices on the envelope here is quite similar, but the values are not exactly the same, when compared to the results that are based on body-frame equations with non-ideal/ideal cases in Section 5.3 and 5.3. In general, the nonlinearity strength is largest near the internal envelope boundary corresponding to the $\bar{q}$ limit, particularly for the $\alpha < 0$ region. The figures show that for indices $v_s^{A'}$ and $v_d^{x'}$ associated with the states, a single maximum occurs. For indices $v_s^{B'}$ and v_d^{u} associated with the inputs, three large maximums occur. At the points $(\alpha, \beta) = (-6^\circ, \pm 2^\circ)$, two closely spaced identical global maximums occur. The third maximum occurs near the upper region of the envelope boundary in the stall region at $\alpha \approx 61^\circ$. Maximum values are found to be ${v_s^{A'}}_{\max} = 2.73$, ${v_s^{B'}}_{\max} = 2.90$, ${v_d^{x'}}_{\max} = 1.62$, and ${v_d^{u}}_{\max} = 4.26$. In these regions, use of linear models to examine dynamic behavior or design control systems is not feasible. Note that the nonlinearity is also sensitive to both α and β variation in these regions. In the other regions of the $\alpha - \beta$ envelope, the nonlinearity

strength is difficult to assess with the displayed data, due to washout from the noted maximum values.

The index $v_s^{A'}$ attains its maximum value at the nominal point $(\alpha_n, \beta_n) = (-6^\circ, 0^\circ)$ where the perturbed point $(\alpha_p, \beta_p) = (-1.6648^\circ, 0^\circ)$ is found to cause the largest deviation around (α_n, β_n). Eigenvalue analysis is also utilized here at both points and shows instability in the linear models. The trimming results in Table 5.2 are applicable here, and the table shows differences between the trimming solutions for both points are insignificant except for velocity and throttle which show large differences. To assess the contributed weight of each component in the state matrix towards the overall index, the matrix-index evaluation shows that $A'_{S_{M_{v,\alpha}}}$, and then $A'_{S_{M_\omega}}$, exhibit the highest nonlinearity sub-index values, as shown in Equation (5.20). Preliminary investigation indicates that the large jump in the trimming V_T value associated with the slight variation in α enlarges the moment stability derivative deviation related to the $A'_{S_{M_{v,\alpha}}}$ and $A'_{S_{M_\omega}}$ blocks, as seen in Equation (5.18).

The static input nonlinearity index $v_s^{B'}$ in this study indicates the system is equally sensitive to input excitation, which explains the large values of $v_s^{B'}$ at the two identical and third spikes shown in Figure 5.27. One of the largest spikes occurs at $(\alpha_n, \beta_n) = (-6^\circ, +2^\circ)$ and is caused by the deviation at $(\alpha_p, \beta_p) = (-1.3923^\circ, +2^\circ)$. At this nominal point, the aircraft is trimmed to an almost inverted position at $\phi_b = 176.2^\circ$ but at the maximum deviated point the aircraft is nearly in a knife edge position of $\phi_b = 104.6^\circ$. The only other significant difference in the trim solution is the velocity (and throttle) which is 403 ft/s compared to 1521 ft/s. The slight variation in the δ_h, δ_a and δ_r

trimming solutions changes the forces and moments acting on the aircraft, and thus contributes towards the overall index. The bank angle does not play any role in B_S' and only V_T and the control surface trimming deflections determine how large the deviation is. Moreover, the jump in the velocity introduces more forces and moments. These forces are present in B_S' through the resolved axial, side, and normal force components. Matrix B_S' embeds two blocks $B_{S_{F_\delta}}'$ and $B_{S_{M_\delta}}'$ and the matrix-index shows that sub-indices $v_S^{B'}\big|_{F_\delta}$ and $v_S^{B'}\big|_{M_\delta}$ contribute equally toward the overall index (Equation (5.20)).

The dynamic nonlinearity indices $v_d^{x'}$ and v_d^u, which are now functions of both operating conditions and time, are displayed as contour and surface plots in Figures 5.24-5.25 and Figures 5.28-5.29 at time $t = 0.01$ s. Similar to the static indices, dynamic indices are sensitive at high-speed flight near the $\bar{q}$ limit for indices $v_d^{x'}$ and v_d^u and are sensitive also at high α near the stall limit for index v_d^u and are expected to propagate with time. At very low time, $v_d^{x'}$ tends to be much smaller than $v_S^{A'}$, when comparing Figure 5.22 to 5.24 or Figure 5.26 to 5.28. On the contrary, the dynamic input index v_d^u, which measures the propagation of input nonlinearity with time, is far more sensitive than the static input index $v_S^{B'}$. The transition matrix Φ captures and amplifies the nonlinearities associated with B_S'. Around the high dynamic index region, the aircraft model is unstable and the linear model tends to deviate faster if input excited rather than state excited.

Similar to the previous cases, the index variation with respect to β using the ideal model appears small except around high index value regions. Slices from the surface plots of the four indices at $\beta = 0^\circ$ are shown in Figure 5.30. Furthermore, a discontinuity

exists between $\alpha = -1.6648^{\circ}$ and -0.9410° in each plot, due to the $\bar{q}$ limit. As in the previous section from Figure 5.21, the trimming roll angle ϕ_b for $\alpha \geq -0.9410^{\circ}$ is 0°, while for $\alpha \leq -1.6648^{\circ}$ the angle is $\phi_b = 180^{\circ}$ or -180°. However, in both cases, the aircraft assumes a wing-level orientation, but in the second case, the aircraft is flying inverted or upside down.

$$v_S^{A'}\big|_{\text{matrix-index}} = \begin{bmatrix} 1.68 & 0.73 & 2.69 \\ 0 & 0 & 2.76 \\ 5.68 & 0 & 3.38 \end{bmatrix}$$
$$v_S^{B'}\big|_{\text{matrix-index}} = \begin{bmatrix} 3.06 \\ 0 \\ 2.90 \end{bmatrix} \tag{5.20}$$

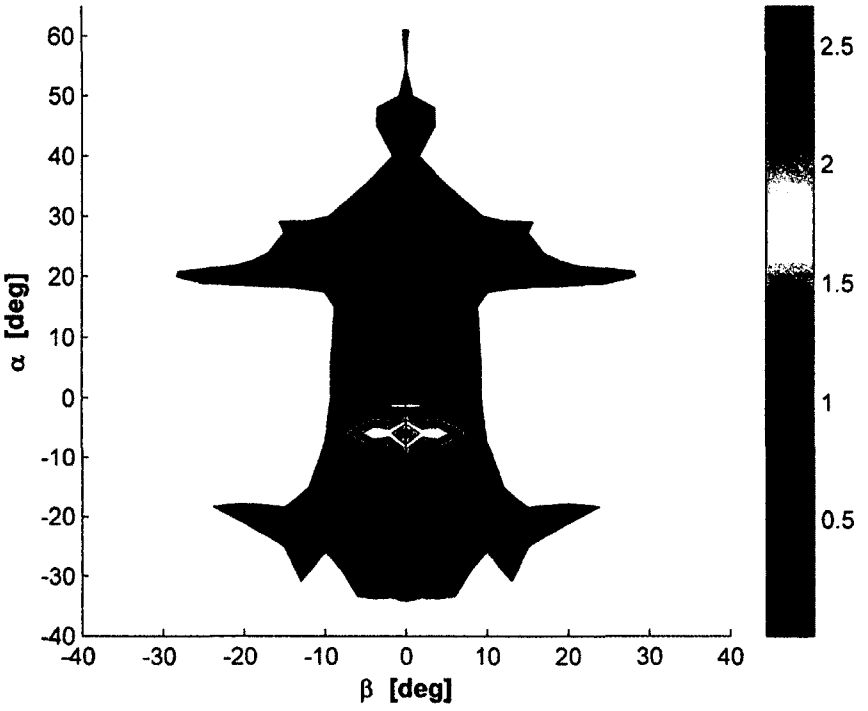

Figure 5.22 Static state nonlinearity index $\nu_S^{A'}$ - contour (stability-frame, ideal)

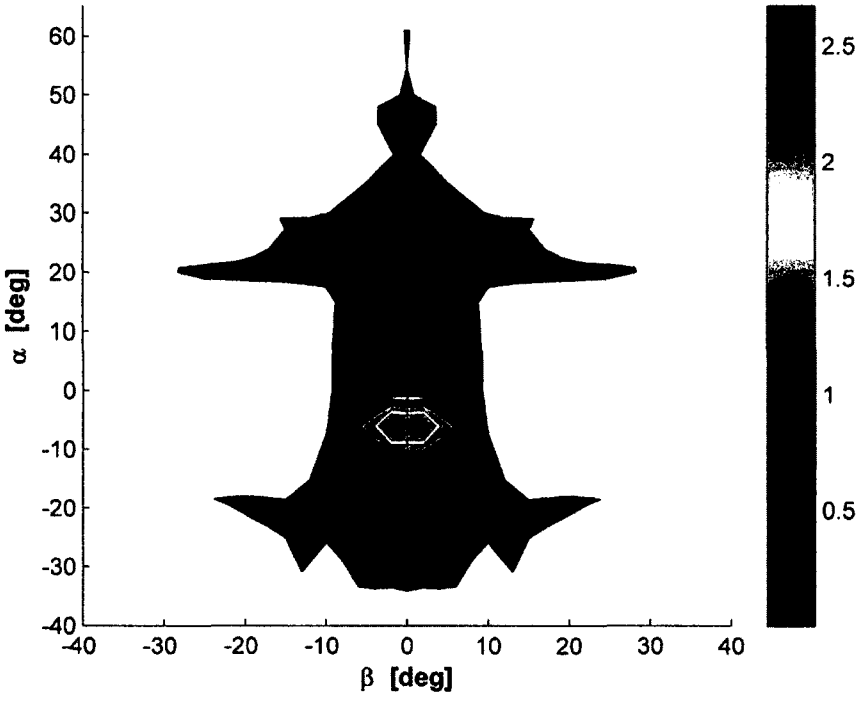

Figure 5.23 Static input nonlinearity index $\nu_S^{B'}$ - contour (stability-frame, ideal)

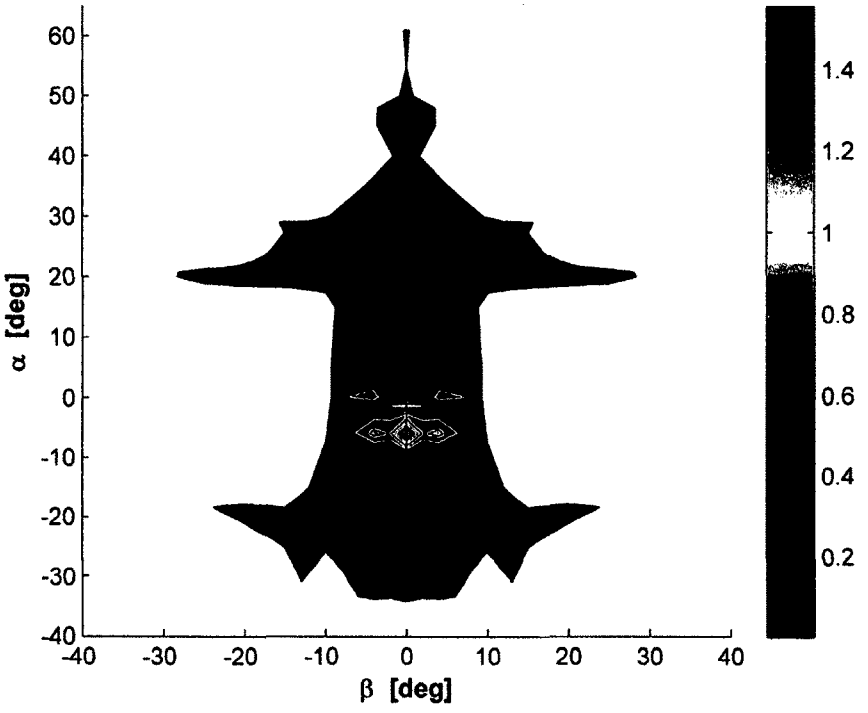

Figure 5.24 Dynamic state nonlinearity index $\nu_d^{x'}$ - contour (stability-frame, ideal)

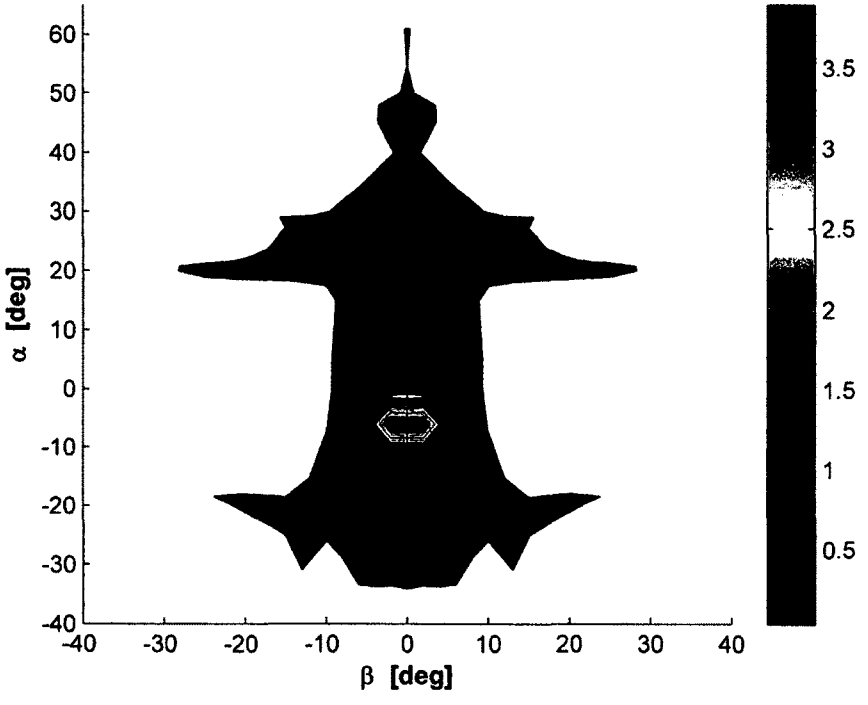

Figure 5.25 Dynamic input nonlinearity index ν_d^u - contour (stability-frame, ideal)

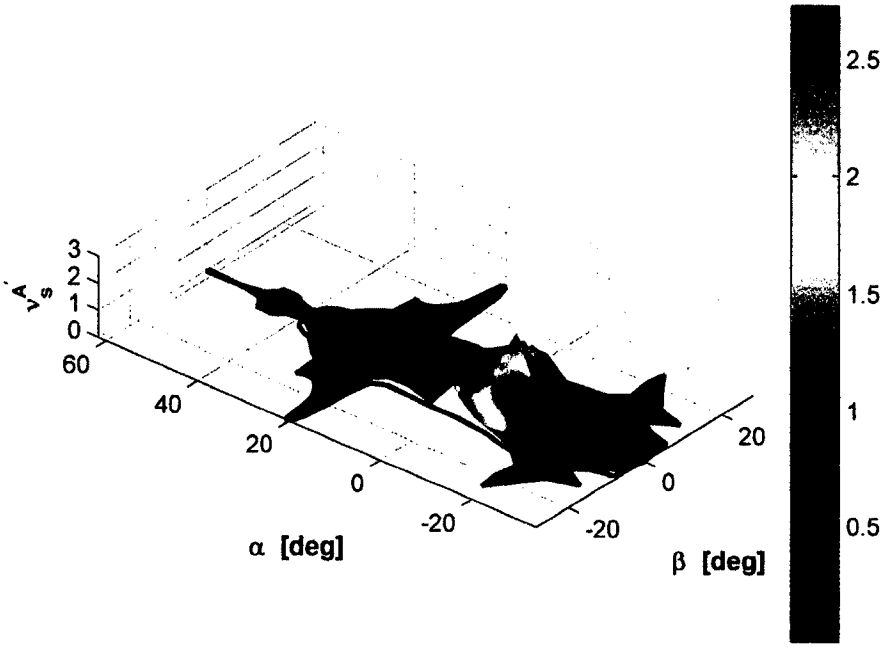

Figure 5.26 Static state nonlinearity index $\nu_s^{A'}$ - surface (stability-frame, ideal)

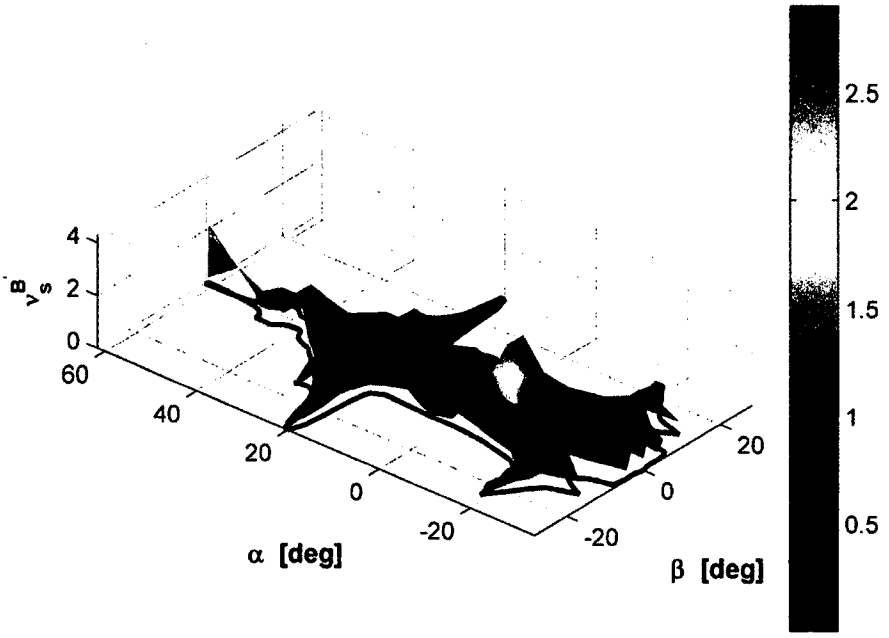

Figure 5.27 Static input nonlinearity index $\nu_s^{B'}$ - surface (stability-frame, ideal)

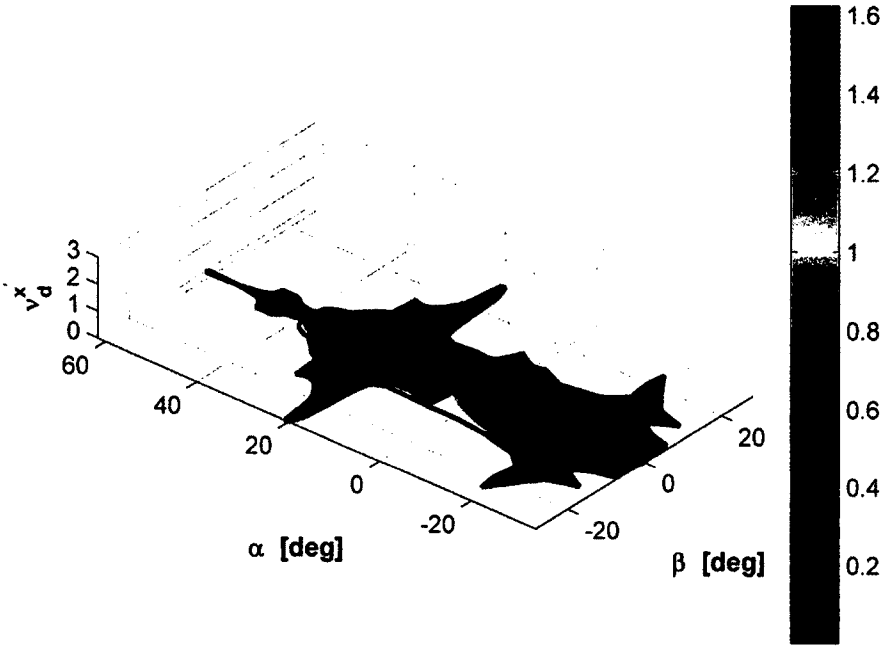

Figure 5.28 Dynamic state nonlinearity index $\nu_d^{x'}$ - surface (stability-frame, ideal)

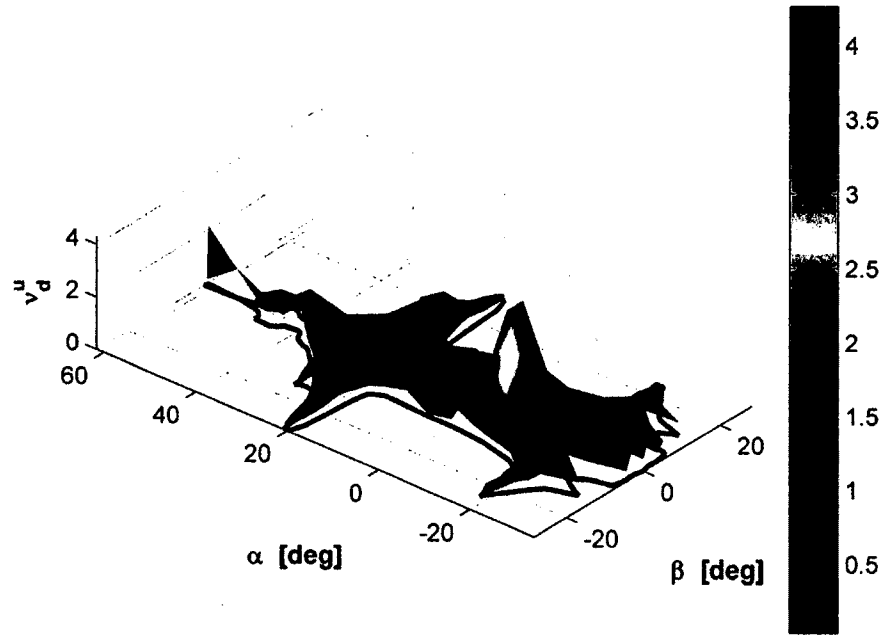

Figure 5.29 Dynamic input nonlinearity index ν_d^{u} - surface (stability-frame, ideal)

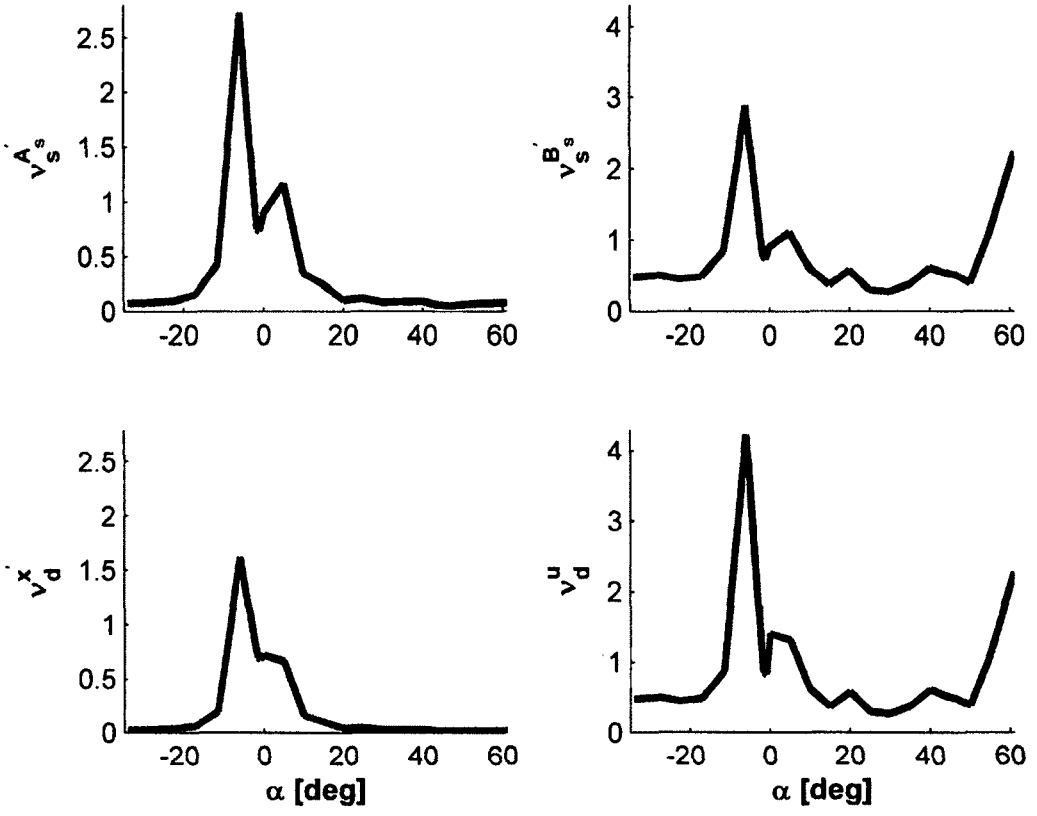

Figure 5.30 Nonlinearity indices at $\beta = 0^{\circ}$ (stability-frame, ideal)

5.6 Index for Full-Envelope Using Wind-Frame – Ideal Model

In this section, the ideal envelope Figure 4.9 produced in Chapter 4 is again investigated. A linear model system is developed using the nonlinear equations of motion in the wind-frame of reference discussed in Section 2.7. The components of the linear system are now described in the wind-frame rather than the body-frame (see Equations (5.21) - (5.23)). The transformation matrix T is modified accordingly, where the first three diagonal elements are replaced by $[1/V_T \quad 1 \quad 1]$.

$$\begin{gathered}\dot{\mathbf{x}}'_w = A'_w\mathbf{x}'_w + B'_w\mathbf{u} \\ \mathbf{x}'_w = [\Delta u'_w \quad \Delta\alpha' \quad \Delta\beta' \quad \Delta\phi'_w \quad \Delta\theta'_w \quad \Delta p'_w \quad \Delta q'_w \quad \Delta r'_w] \\ A'_w = TA_wT^{-1} \\ B'_w = TB_w,\end{gathered} \tag{5.21}$$

where

$$A'_w = \begin{bmatrix} \begin{bmatrix} X_{u_w} & \frac{1}{V_T}X_\alpha & \frac{1}{V_T}X_\beta \\ V_T Y_{u_w} & Y_\alpha & Y_\beta \\ V_T Z_{u_w} & Z_\alpha & Z_\beta \end{bmatrix} & \begin{bmatrix} 0 & \frac{1}{V_T}gC_{\theta_{w0}} \\ gC_{\phi_{w0}}C_{\theta_{w0}} & gS_{\phi_{w0}}S_{\theta_{w0}} \\ gS_{\phi_{w0}}C_{\theta_{w0}} & gC_{\phi_{w0}}S_{\theta_{w0}} \end{bmatrix} & 2\cdot\begin{bmatrix} \frac{1}{\bar{b}}X_{p_w} & \frac{1}{\bar{c}}X_{q_w} & \frac{1}{\bar{b}}X_{r_w} \\ \frac{1}{\bar{b}}Y_{p_w} & \frac{1}{\bar{c}}Y_{q_w} & \frac{1}{\bar{b}}Y_{r_w} \\ \frac{1}{\bar{b}}Z_{p_w} & \frac{1}{\bar{c}}Z_{q_w} & \frac{1}{\bar{b}}Z_{r_w} \end{bmatrix} \\ \begin{bmatrix} 0 & 0 & 0 \\ 0 & 0 & 0 \end{bmatrix} & \begin{bmatrix} 0 & 0 \\ 0 & 0 \end{bmatrix} & 2V_T\cdot\begin{bmatrix} \frac{1}{\bar{b}} & \frac{1}{\bar{c}}S_{\phi_{w0}}T_{\theta_{w0}} & \frac{1}{\bar{b}}C_{\phi_{w0}}T_{\theta_{w0}} \\ 0 & \frac{1}{\bar{c}}C_{\phi_{w0}} & -\frac{1}{\bar{b}}S_{\phi_{w0}} \end{bmatrix} \\ \cdot\frac{1}{2}\cdot\begin{bmatrix} \bar{b}L_{u_w} & \frac{\bar{b}}{V_T}L_\alpha & \frac{\bar{b}}{V_T}L_\beta \\ \bar{c}M_{u_w} & \frac{\bar{c}}{V_T}M_\alpha & \frac{\bar{c}}{V_T}M_\beta \\ \bar{b}N_{u_w} & \frac{\bar{b}}{V_T}N_\alpha & \frac{\bar{b}}{V_T}N_\beta \end{bmatrix} & \begin{bmatrix} 0 & 0 \\ 0 & 0 \\ 0 & 0 \end{bmatrix} & \begin{bmatrix} L_{p_w} & \frac{\bar{b}}{\bar{c}}L_{q_w} & L_{r_w} \\ \frac{\bar{c}}{\bar{b}}M_{p_w} & M_{q_w} & \frac{\bar{c}}{\bar{b}}M_{r_w} \\ N_{p_w} & \frac{\bar{b}}{\bar{c}}N_{q_w} & N_{r_w} \end{bmatrix} \end{bmatrix} \\ = \begin{bmatrix} A'_{wF_{v,\alpha,\beta}} & A'_{wG} & A'_{wF_\omega} \\ \mathbf{0} & \mathbf{0} & A'_{wE} \\ A'_{wM_{v,\alpha,\beta}} & \mathbf{0} & A'_{wM_\omega} \end{bmatrix}\end{bmatrix} \tag{5.22}$$

and

$$B'_w = \begin{bmatrix} \begin{bmatrix} \frac{1}{V_T}X_{\delta_h} & 0 & 0 \\ 0 & Y_{\delta_a} & Y_{\delta_r} \\ Z_{\delta_h} & 0 & 0 \end{bmatrix} \\ \begin{bmatrix} 0 & 0 & 0 \\ 0 & 0 & 0 \end{bmatrix} \\ \frac{1}{2V_T} \cdot \begin{bmatrix} \bar{b}L_{\delta_h} & \bar{b}L_{\delta_a} & \bar{b}L_{\delta_r} \\ \bar{c}M_{\delta_h} & 0 & 0 \\ \bar{b}N_{\delta_h} & \bar{b}N_{\delta_a} & \bar{b}N_{\delta_r} \end{bmatrix} \end{bmatrix} = \begin{bmatrix} B'_{w_{F_\delta}} \\ \mathbf{0} \\ B'_{w_{M_\delta}} \end{bmatrix} \tag{5.23}$$

Applying the four index expressions in Equations (3.8) and (3.9) on top of this ideal envelope, produces four symmetric contour plots (Figures 5.31-5.34) and four symmetric surface plots (Figures 5.35-5.38) for visualization of the envelope nonlinearity variations. The behavior of the indices on the envelope here is quite similar when compared to the results investigated in body- and stability-frame equations in Sections 5.3 and 5.5. Again, the nonlinearity strength is largest near the internal envelope boundary corresponding to the $\bar{q}$ limit, particularly for the $\alpha < 0$ region. The figures show that for indices $v_s^{A'}$ and $v_d^{x'}$ associated with the states, a single maximum occurs. For indices $v_s^{B'}$ and v_d^{u} associated with the inputs, three large maximums occur. At the points $(\alpha, \beta) = (-6^\circ, \pm 2^\circ)$, two closely spaced identical global maximums occur. The third maximum occurs near the upper region of the envelope boundary in the stall region at $\alpha \approx 61^\circ$. Maximum values are found to be ${v_s^{A'}}_{\max} = 2.73$, ${v_s^{B'}}_{\max} = 2.90$, ${v_d^{x'}}_{\max} = 1.62$, and ${v_d^{u}}_{\max} = 4.26$. In these regions, use of linear models to examine dynamic behavior or design control systems is not feasible. Note that the nonlinearity is also sensitive to both α and β variation in these regions. In the other regions of the $\alpha - \beta$

envelope, the nonlinearity strength is difficult to assess with the displayed data, due to washout from the noted maximum values.

The index $\nu_S^{A'}$ attains its maximum value at the nominal point $(\alpha_n, \beta_n) = (-6^\circ, 0^\circ)$ where the perturbed point $(\alpha_p, \beta_p) = (-1.6648^\circ, 0^\circ)$ is found to cause the largest deviation around (α_n, β_n). Eigenvalue analysis is also utilized here at both points and it shows instability in the linear models. Again the results in Table 5.2 are applicable here and show the differences between the trimming solutions for both points are insignificant except for velocity and throttle which show large differences. To assess the contributed weight of each component in the state matrix towards the overall index, the matrix-index evaluation shows that $A'_{W_{M_{v,\alpha,\beta}}}$ largely, and then $A'_{W_{M_\omega}}$, exhibit the highest nonlinearity sub-index values, as shown in Equation (5.24). Preliminary investigation indicates that the large jump in the trimming V_T value associated with the slight variation in α enlarges the moment stability derivative deviation related to the $A'_{W_{M_{v,\alpha,\beta}}}$ and $A'_{W_{M_\omega}}$ blocks.

The static input nonlinearity index $\nu_S^{B'}$ in this study is equally sensitive to input excitation, which explains the large values of $\nu_S^{B'}$ at the two identical and third spikes shown in Figure 5.36. One of the largest spikes occurs at $(\alpha_n, \beta_n) = (-6^\circ, +2^\circ)$ and is caused by the deviation at $(\alpha_p, \beta_p) = (-1.3923^\circ, +2^\circ)$. At this nominal point, the aircraft is trimmed to an almost inverted position at $\phi_b = 176.2^\circ$ but at the maximum deviated point the aircraft is nearly in a knife edge position of $\phi_b = 104.6^\circ$. The only other significant difference in the trim solution is the velocity (and throttle) which is 403 ft/s compared to 1521 ft/s (see Table 5.2). The slight variation in the δ_h, δ_a and δ_r trimming

solutions changes the forces and moments acting on the aircraft and thus contributes towards the overall index. The bank angle does not play any role in B'_w, and only V_T and control surface trimming deflections determine how large the deviation is. Moreover, the jump in the velocity introduces more forces and moments. These forces are present in B'_w through the resolved axial, side, and normal force components. Matrix B'_w embeds two blocks $B'_{w_{F_\delta}}$ and $B'_{w_{M_\delta}}$ and the matrix-index shows that sub-indices $v_s^{B'}\big|_{F_\delta}$ and $v_s^{B'}\big|_{M_\delta}$ contribute equally toward the overall (Equation (5.24)).

The dynamic nonlinearity indices $\nu_d^{x'}$ and ν_d^u, which are now functions of both operating conditions and time, are displayed as contour and surface plots in Figures 5.33-5.34 and Figures 5.37-5.38 at time $t = 0.01$ s. Similar to the static indices, dynamic indices are sensitive at high-speed flight near the $\bar{q}$ limit for indices $\nu_d^{x'}$ and ν_d^u and are sensitive also at high α near the stall limit for index ν_d^u and are expected to propagate with time. At very low time, $\nu_d^{x'}$ tends to be much smaller than $\nu_s^{A'}$, when comparing Figure 5.31 to 5.33 or Figure 5.35 to 5.37. On the contrary, the dynamic input index ν_d^u, which measures the propagation of input nonlinearity with time, is far more sensitive than the static input index $\nu_s^{B'}$. The transition matrix Φ captures and amplifies the nonlinearities associated with B'_w. Around the high dynamic index region, the aircraft model is unstable and the linear model tends to deviate faster if input excited rather than state excited.

Slices from the surface plots of the four indices at $\beta = 0^\circ$ are shown in Figure 5.39, and a discontinuity exists between $\alpha = -1.6648^\circ$ and -0.9410° in each plot, due to the $\bar{q}$ limit. Again, the trimming roll angle ϕ_b for $\alpha \geq -0.9410^\circ$ is 0°, while

for $\alpha \leq -1.6648^{\circ}$ the angle is $\phi_b = 180^{\circ}$ or -180°. However, in both cases, the aircraft assumes a wing-level orientation, but in the second case, the aircraft is flying inverted or upside down (Figure 5.21).

$$v_s^{A'}\big|_{\text{matrix-index}} = \begin{bmatrix} 1.68 & 0.73 & 2.69 \\ 0 & 0 & 2.76 \\ 13.40 & 0 & 3.38 \end{bmatrix}$$
$$v_s^{B'}\big|_{\text{matrix-index}} = \begin{bmatrix} 3.06 \\ 0 \\ 2.90 \end{bmatrix} \tag{5.24}$$

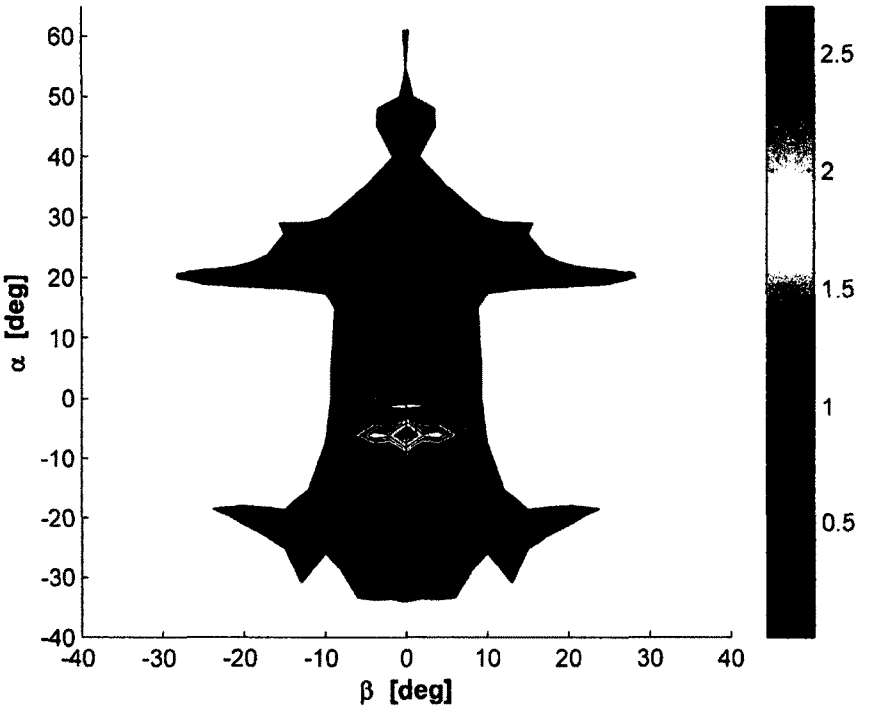

Figure 5.31 Static state nonlinearity index $\nu_s^{A'}$ - contour (wind-frame, ideal)

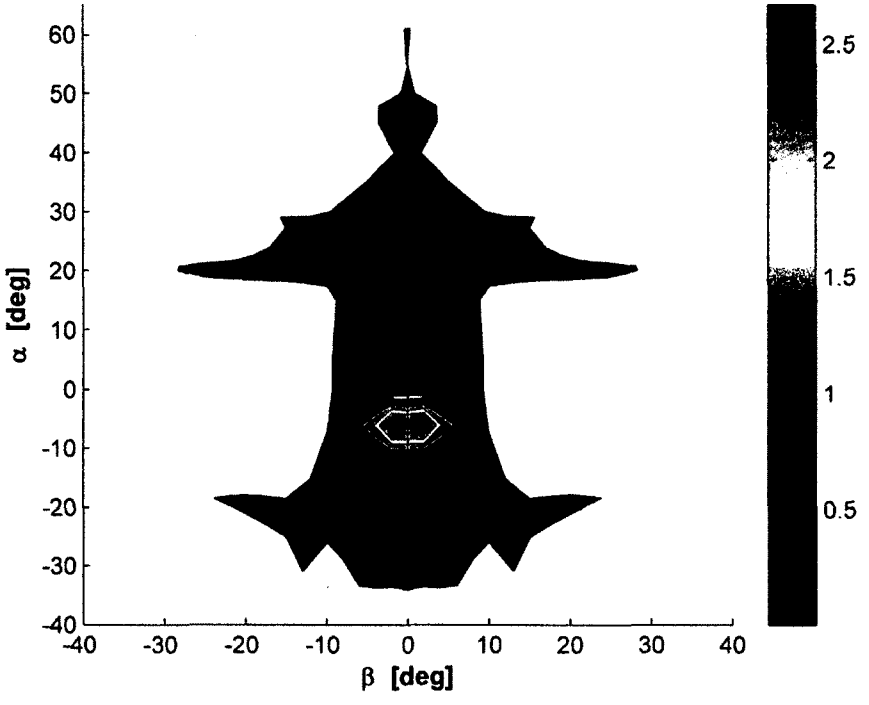

Figure 5.32 Static input nonlinearity index $\nu_s^{B'}$ - contour (wind-frame, ideal)

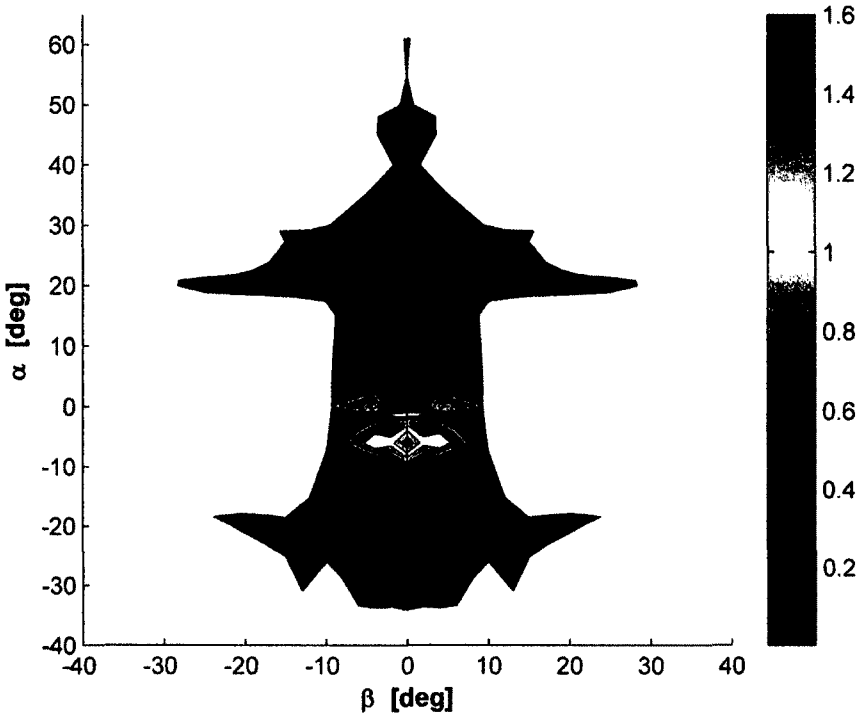

Figure 5.33 Dynamic state nonlinearity index $\nu_d^{x'}$ - contour (wind-frame, ideal)

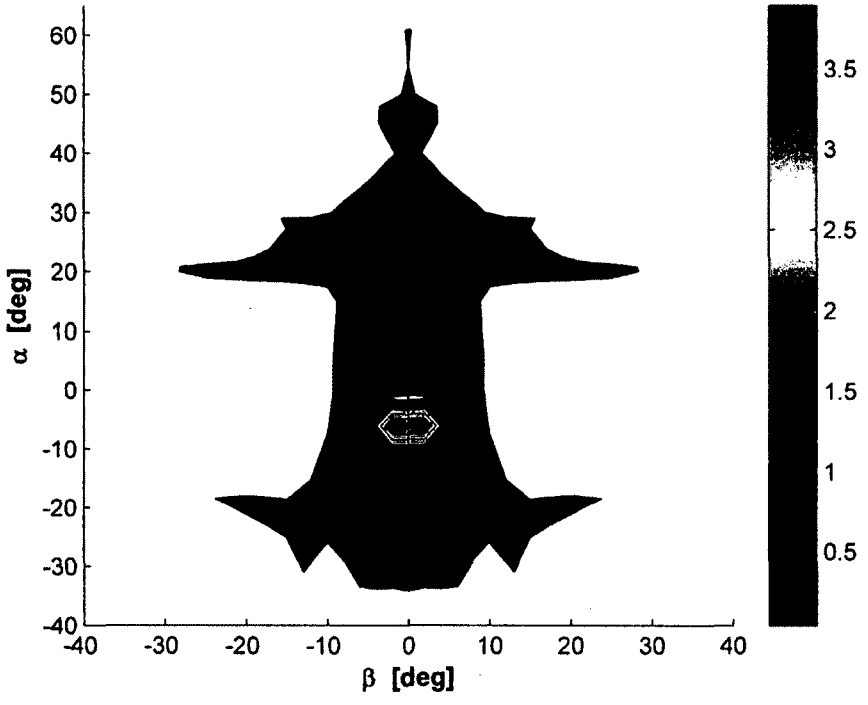

Figure 5.34 Dynamic input nonlinearity index ν_d^u - contour (wind-frame, ideal)

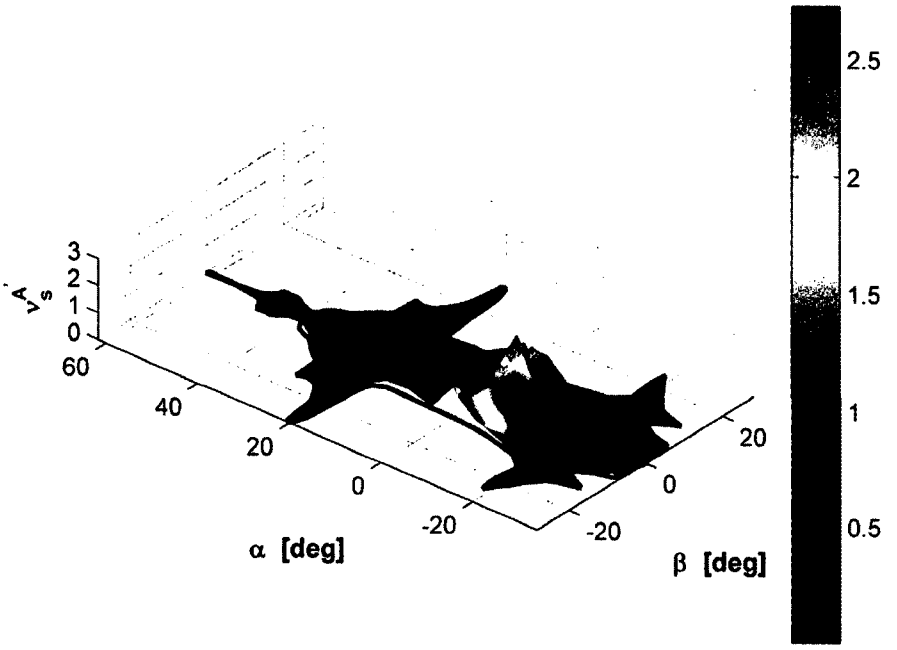

Figure 5.35 Static state nonlinearity index $\nu_s^{A'}$ - surface (wind-frame, ideal)

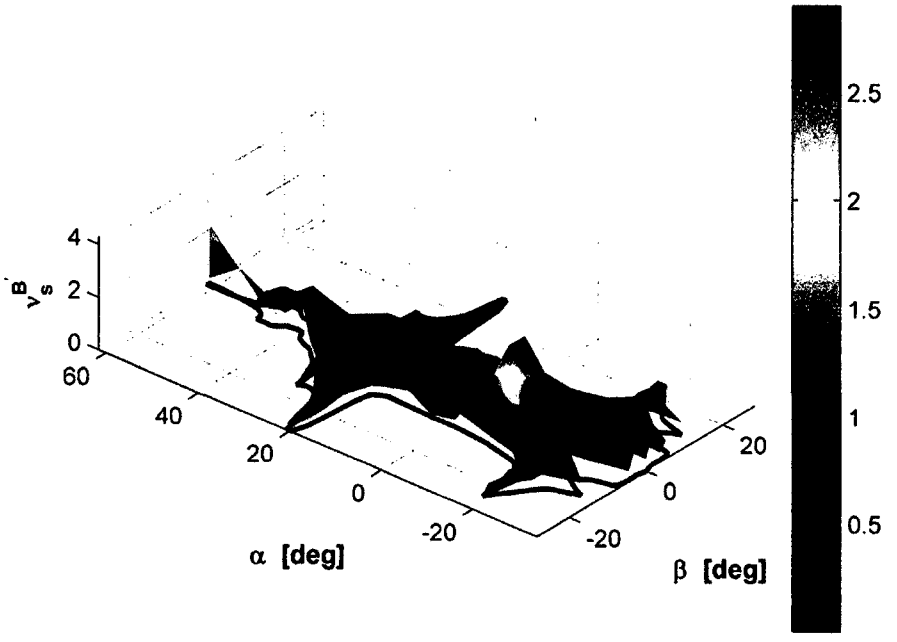

Figure 5.36 Static input nonlinearity index $\nu_s^{B'}$ - surface (wind-frame, ideal)

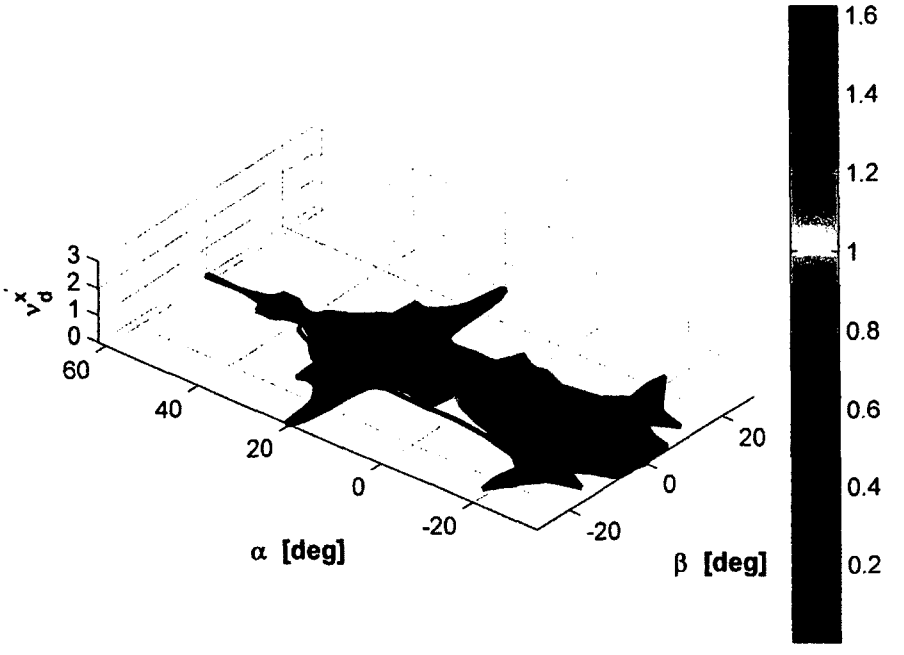

Figure 5.37 Dynamic state nonlinearity index $\nu_d^{x'}$ - surface (wind-frame, ideal)

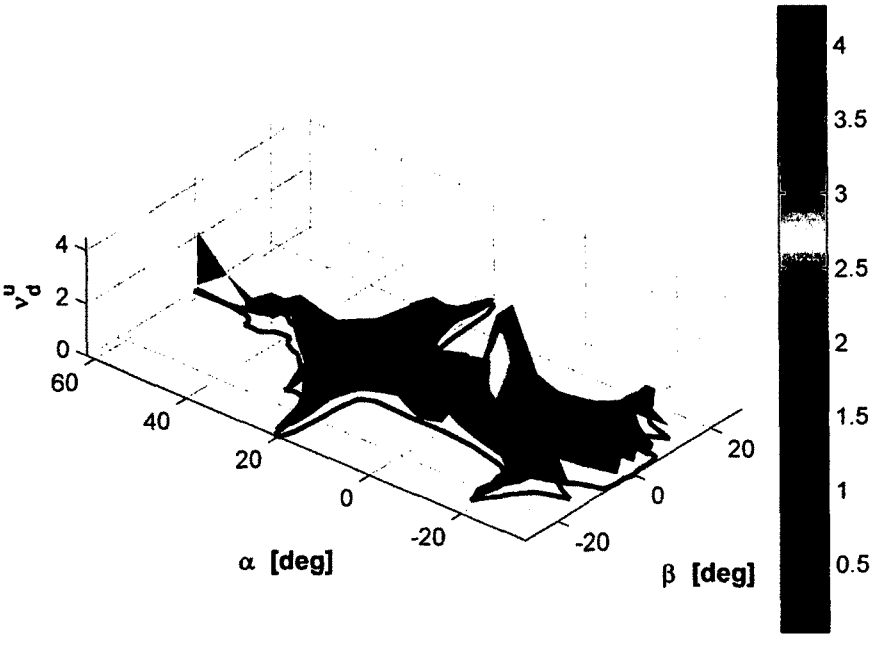

Figure 5.38 Dynamic input nonlinearity index ν_d^u - surface (wind-frame, ideal)

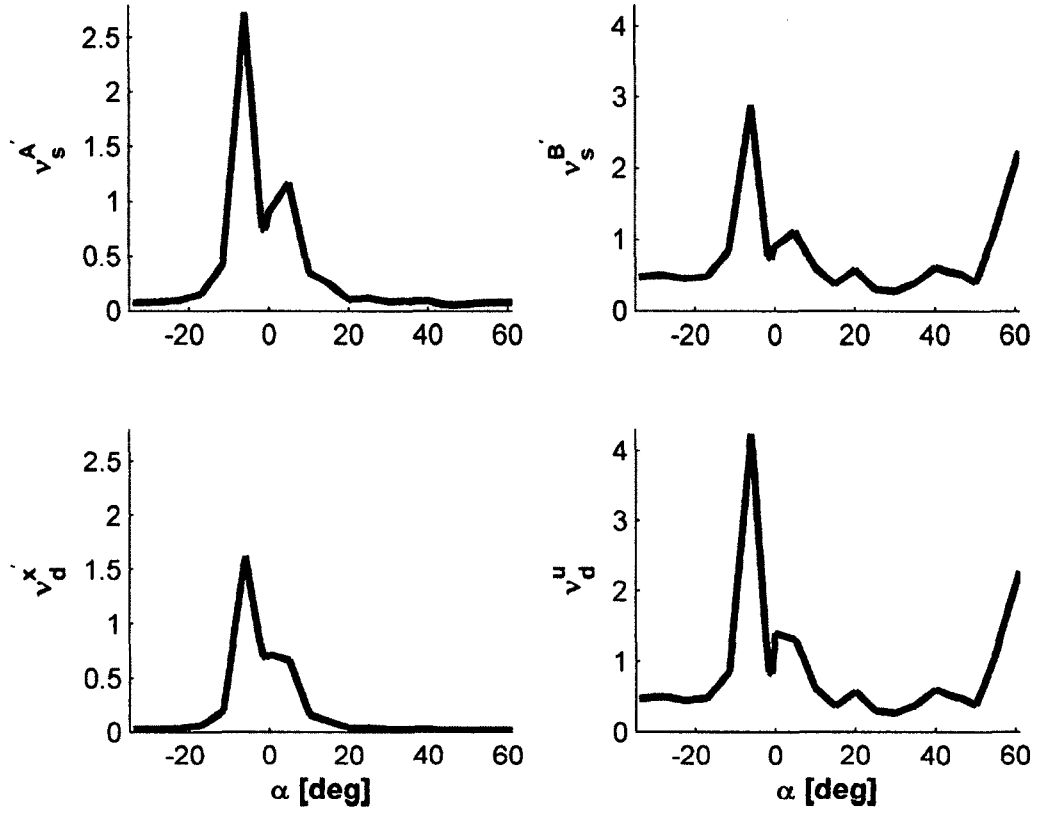

Figure 5.39 Nonlinearity indices at $\beta = 0^\circ$ (wind-frame, ideal)

5.7 Frame of Reference Influence on Index

The nonlinearity index variations with respect to β show small discrepancies, except around high index value regions. Therefore, slices from the surface plots of the four indices $v_s^{A'}$, $v_s^{B'}$, $v_d^{x'}$ and v_d^u are presented and compared in Figures 5.40-5.44, at $\beta = 0^\circ, 2^\circ, 4^\circ, 6^\circ, 8^\circ$. These figures compare indices results over the same ideal envelope developed in Figure 4.9 for different mathematical representations of the nonlinear equations of motion. The compared representations are body-, stability-, and wind-frame coordinates. In all of these frames, the maximum nonlinearities occur around the same neighborhood of $\alpha = -6^\circ$. A comparison of the maximum indices of $v_s^{A'}$, $v_s^{B'}$, $v_d^{x'}$ and

v_d^u over the entire ideal $\alpha - \beta$ envelope among the different frames is offered in Table 5.3. The maximum indices over the entire envelope show highly comparable values among all three representations.

The static state $v_s^{A'}$, static input $v_s^{B'}$, dynamic state $v_d^{x'}$, and dynamic input v_d^u nonlinearity index comparisons for all reference frames in Figure 5.40 at $\beta = 0^\circ$ show no preference of any frame over another. Over the large angle of attack range, all index values are roughly constant except for the α band of $-10^\circ < \alpha < 10^\circ$. In this band, the indices experience the largest values, which is near the inner boundary of the dynamic pressure limit. A notable exception to this rule is for indices $v_s^{B'}$ and v_d^u at $\alpha > 50^\circ$ where the index again becomes large.

With a sideslip angle of $\beta = 2^\circ$, the indices $v_s^{B'}$ and v_d^u for the stability- and wind-frame tend to exhibit more nonlinearity in the lower negative angle of attack region as shown in Figure 5.41. However, the indices $v_s^{A'}$ and $v_d^{x'}$ show no variation in the index values in this same region. These results suggest there is a slight preference for using the body-frame description in specific areas of the flight envelope. In Figure 5.42, for $\beta = 4^\circ$, the index comparison shows similarities among all the frame of reference representations similar to results in Figure 5.40 for $\beta = 0^\circ$.

Figure 5.43 shows that the behavior of the indices $v_s^{A'}$, $v_s^{B'}$, $v_d^{x'}$ and v_d^u for all frames at $\beta = 6^\circ$ are similar to the behavior at $\beta = 2^\circ$. Only the indices $v_s^{B'}$ and v_d^u for the stability- and wind-frame coordinates tend to exhibit more nonlinearity than the body-frame coordinates in the lower negative angle of attack region, whereas indices $v_s^{A'}$ and

$v_d^{x'}$ show no variation in the index values across the various mathematical descriptions of the vehicle dynamics.

At a large sideslip angle of $\beta = 8^\circ$, the different frame comparison in Figure 5.44 shows that the indices $v_s^{B'}$ and v_d^u for the stability- and wind-frame coordinates tend to exhibit more nonlinearity than the body-frame description in the lower negative angle of attack region; whereas for the same indices, the body-frame description tends to exhibit more nonlinearity in the upper angle of attack region. As for the indices $v_s^{A'}$ and $v_d^{x'}$, no variation is observed among the different frames.

Finally, the nonlinearity indices related to matrix A', the static state $v_s^{A'}$ and the dynamic state $v_d^{x'}$, show no difference in the index values as sideslip angle is increased for different frames comparison. However, the nonlinearity indices related to matrix B', the static input $v_s^{B'}$ and the dynamic input v_d^u, show differences in the index values as sideslip angle is increased for different frames comparison. Here, the body-frame shows less nonlinearity than the stability- and wind-frame for negative angles of attack but more nonlinearity for positive angles of attack.

Although not shown in the dissertation, selected results were generated and investigated using the dimensional state formulations without the transformation matrix T. Two important observations were noted. First, index values were much higher than for the normalized state formulations presented here. In other words, the use of a normalized state formulation was very effective in reducing the sensitivity of the index on the units of the linear model. Second, a much wider difference between the index values for various coordinate formulations was observed. Although not universal, the results suggested a strong preference for the body-frame description over the other two frames.

Table 5.3 Maximum index comparison for different frames

	Body-frame	Stability-frame	Wind-frame
$v_s^{A'}$	2.73	2.73	2.73
$v_s^{B'}$	2.91	2.90	2.90
$v_d^{x'}$	1.62	1.62	1.62
v_d^{u}	4.27	4.26	4.26

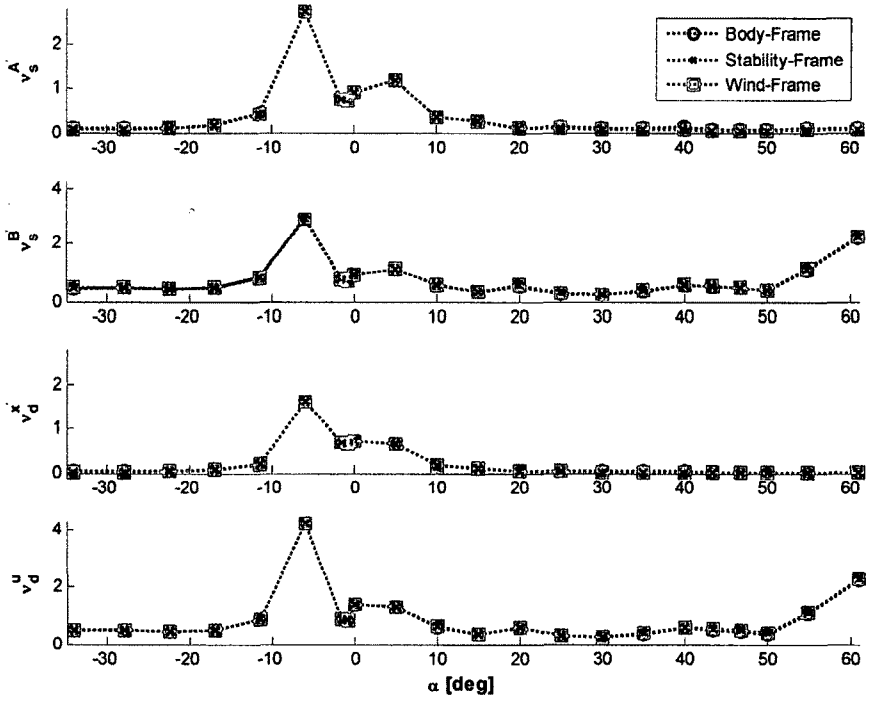

Figure 5.40 Index comparison at $\beta = 0^{\circ}$

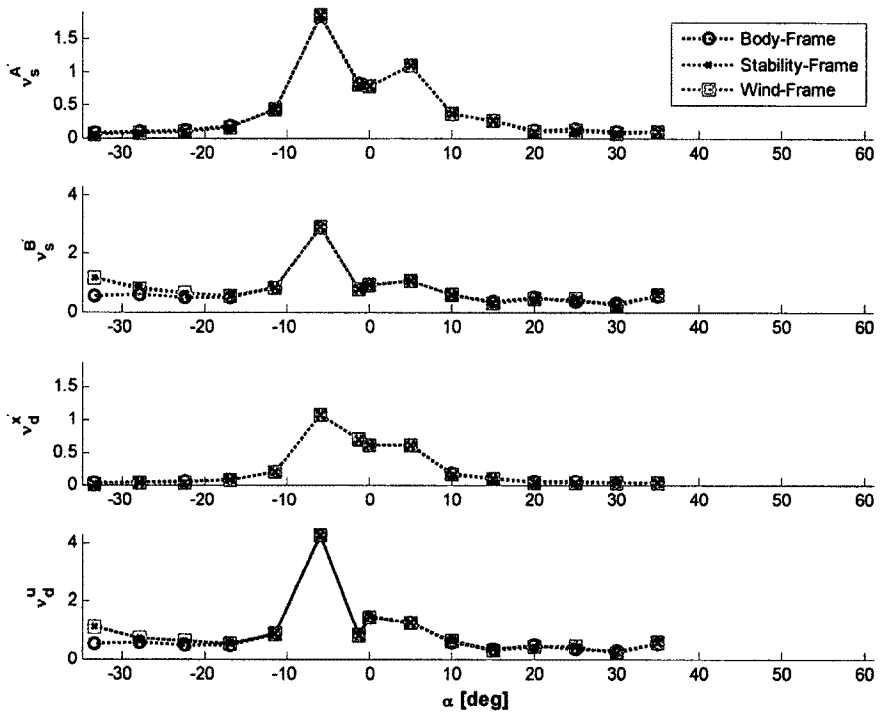

Figure 5.41 Index comparison at $\beta = 2^{\circ}$

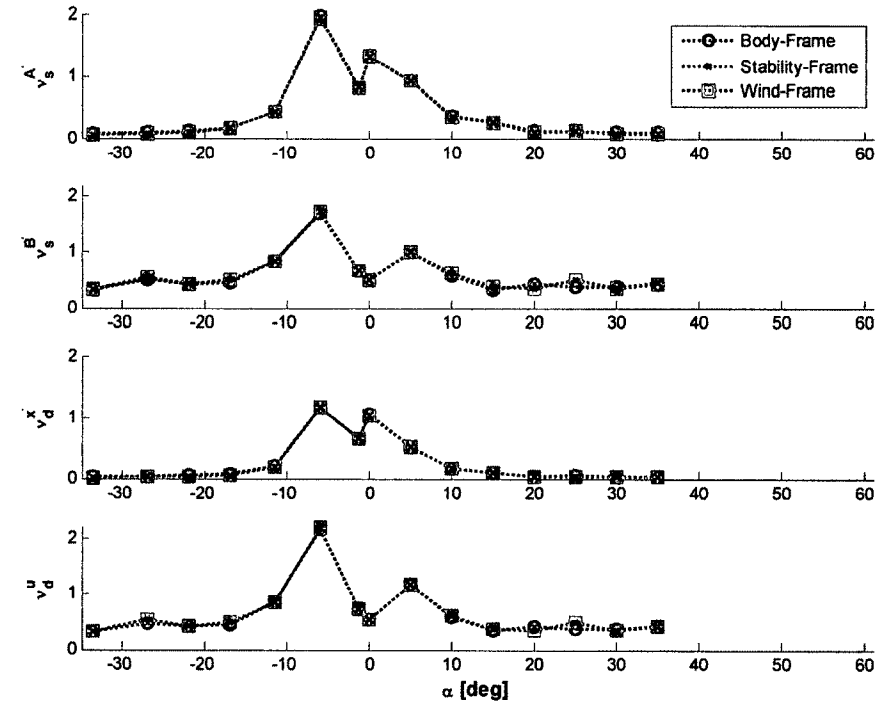

Figure 5.42 Index comparison at $\beta = 4^{\circ}$

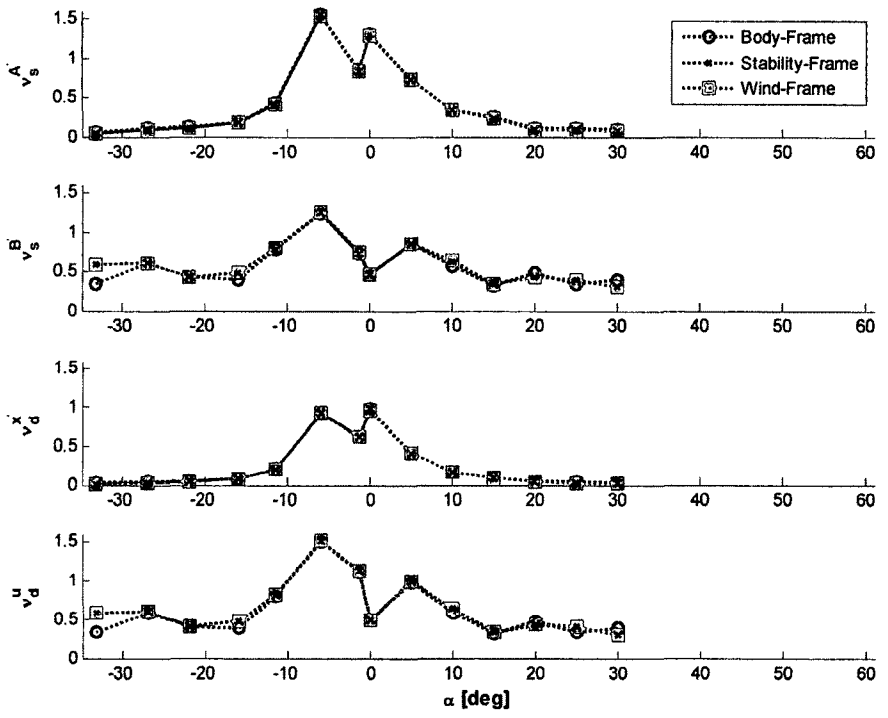

Figure 5.43 Index comparison at $\beta = 6^{\circ}$

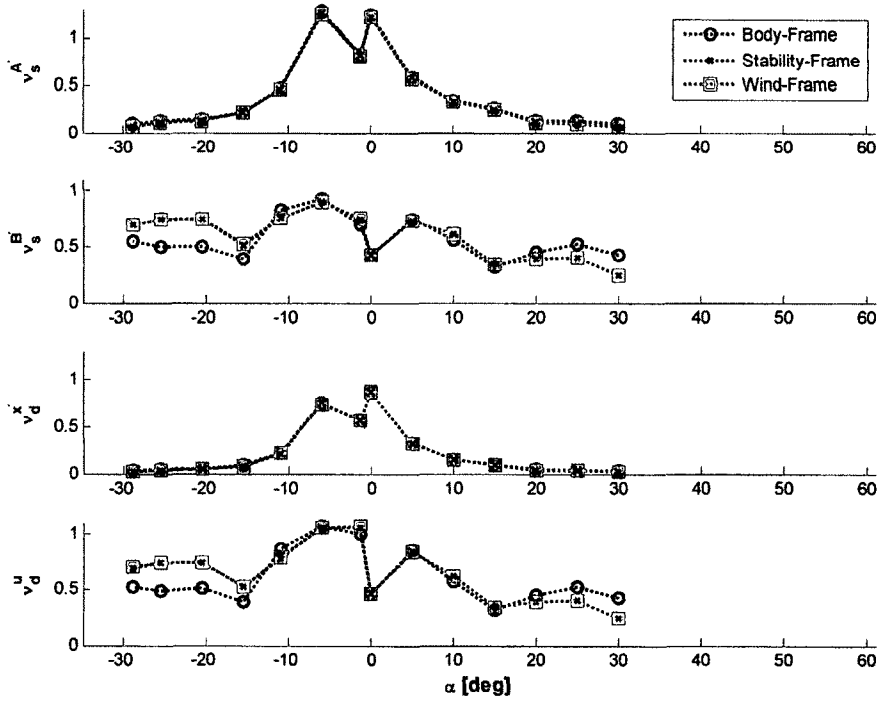

Figure 5.44 Index comparison at $\beta = 8^{\circ}$

CHAPTER 6

SIMULATION CASES AROUND HIGH INDEX

6.1 Introduction

Flight simulations, depending on the mathematical model of the dynamics, are both linear and nonlinear. In flight analysis, linear simulation is typically explored first. The linear model is usually expressed in state variable format, as discussed in Section 3.1, and is derived by numerical methods from the nonlinear model. The linear model is developed around a trimmed operating condition for the aircraft, which prompts the question of whether the trimmed condition is stable when a small perturbation displaces the aircraft from its equilibrium condition. Nonlinear simulation is performed to address the linear model suitability as well as the stability of the trimming condition in a particular domain around a reference operating point. It is important to characterize to what extent nonlinearity is included in the system and whether the system can be regarded as approximately linear. For aircraft dynamic analysis, nonlinear simulation is used to assess the strength of the system's nonlinearity. Further, nonlinear phenomena such as chaos and limit cycling may be predicted or identified by comparing linear and nonlinear simulations.

The linear and nonlinear simulations in this dissertation are carried out at an initial altitude of $H_b = 20{,}000$ ft instead of the sea level altitude $H_b = 0$ ft. This starting altitude is suggested based on the similarity of the nonlinearity index behavior for this altitude, as can be seen in Table 6.1 (different altitude indices are investigated outside of this dissertation). Further, aircraft response is better observed at a higher altitude,

allowing sufficient time for the aircraft to respond to excitations, where the response may present itself as a large altitude change.

The aircraft model in this dissertation is simulated at the (α, β) pairs exhibiting the most nonlinearity over the flight envelope. These pairs are ($\alpha = -6^{\circ}$, $\beta = +2^{\circ}$) and ($\alpha = -6^{\circ}$, $\beta = -2^{\circ}$). These two pairs correspond to untypical and unstable trimming conditions, since the aircraft is trimmed at an inverted position; moreover, they represent common high nonlinearity locations with any of the different frame choices. Since the idealized aerodynamic model is used as the source for the force and moment coefficients here, either one of these pairs reflects exactly the other pair's characteristics. Hence, the pair ($\alpha = -6^{\circ}$, $\beta = +2^{\circ}$) is investigated only, and is designated as pair 1, or (α_1,β_1). The aircraft is excited and perturbed from equilibrium at (α_1,β_1), where index results show the largest nonlinearity exists in all the frames. Comparisons of linear and nonlinear models which are subjected to initial condition angular rates are presented here. Linear and nonlinear simulations for flight dynamic systems are carried out using the tools available in the MATLAB® software suite. All simulations are implemented using the dimensional body-frame of reference formulations.

It is adequate, for comparison purposes, to study the response of the aircraft at a relatively similar flight condition, wherein the aircraft is at a typical and stable trimmed operating condition. Such a condition is satisfied at ($\alpha_2 = +6^{\circ}$, $\beta_2 = +2^{\circ}$), or pair 2. The trim solutions and index values for (α_1 β_1) and (α_2,β_2) for $H_b = 20{,}000$ ft are listed in Tables 6.1 and 6.2. Finally, it should be noted the simulation is performed for an aircraft with fixed control settings; in other words, the control surface deflections are the trimmed angles for that specific operating condition.

6.2 Simulation Results

First, the longitudinal and lateral linear-nonlinear responses to 5, 7 and 10 deg/s perturbations (excitations) on pitch rate at pair 2 ($\alpha_2 = +6^\circ$, $\beta_2 = +2^\circ$) are presented in Figure 6.1 out to $t = 60$ s. Nonlinear simulations and flight-path trajectories for the same perturbations are shown in Figures 6.2 and 6.3 for $t = 120$ s. Comparing the linear results to those for the nonlinear model for $\Delta q_{b_0} = 5$ and 7 deg/s, it can be seen that the differences are quite insignificant for all state variables, although the yaw rate, bank and pitch angles start to deviate slightly after $t = 30$ s. In the case of $\Delta q_{b_0} = 10$ deg/s, the results show many variations between the linear and nonlinear simulation, for example, settling time, peak time, damping rate, and oscillation amplitude. Therefore, it can be concluded that the linear model is adequate, at small pitch rate excitations, $\Delta q_{b_0} < 10$ deg/s, to capture the system behavior at this operating condition. It is found that, for the linear model, increasing the pitch rate $\Delta q_{b_0} \geq 10$ deg/s triggers a divergent transient response from the nonlinear model (see Figure 6.1). In Figure 6.2, the nonlinear response pattern to different initial pitch rates $\Delta q_{b_0} = 5$, 7 and 10 deg/s basically follows similar trends. However, increasing the pitch rate excitation enlarges the overshooting amplitude of the response, as seen clearly in the vertical velocity, pitch angle, and angle of attack. Overall, the pitch rate transient response is well damped.

Figure 6.4 compares the total aerodynamic moments (left) and compares the normalized vertical lift component vs. normalized weight (right) during the complete flight range. The positive Δq_{b_0} excitation produces a nose-up pitching motion, which is countered by a negative restoring pitching moment (see Figure 6.4), and it excites mainly the longitudinal phugoid mode. As a consequence of the pitching moment, there is a

decrease in axial velocity and an increase in altitude and pitch angle, all occurring in the first 30 s (see Figures 6.2 and 6.3). However, the large increase in the angle of attack induces an incremental jump in the lift force, as seen in Figure 6.4, causing the aircraft to accumulate altitude where the initial kinetic energy is transformed into potential energy at $t = 18.3$ s. The conservation of energy law states that kinetic and potential energy continuously exchange over a very long period of time with decaying amplitude rate and at the same period. The vertical velocity, roll rate, and yaw rate perturbed responses are oscillatory in the first 15 s with similar frequency and period. The yaw rate magnitude is steadily offset causing a yaw angle increase, and hence, an increase in the crossrange trajectory. The angle of attack after disturbance remains substantially constant, whereas the total speed, pitch angle, and altitude slowly oscillate around their equilibriums in the long run, thereby indicating a stable long-period low-frequency oscillation mode. It is evident that pitch rate excitation induces larger pitching moment smaller fluctuations in the rolling and yawing moments (Figure 6.4), and hence, the lateral mode is excited only slightly.

The three-dimensional (3-D) aircraft attitude is better visualized in Figure 6.5, with top and side views included, where the aircraft position and orientation is snapshotted every 11.99 s. The aircraft wings are colored differently for better attitude visualization: green for left wing and blue for right wing. The phugoid mode can be better explained by referring to Figures 6.2-6.5. When the aircraft is initially at the trimmed condition at $t = 0$ s, the vertical lift force is balanced by the weight. The moment the aircraft is perturbed by Δq_{b_0} the angle of attack jump results in a spike in the lift and a similar spike of induced drag due to lift; hence, the aircraft is no longer in a vertical or

longitudinal equilibrium. It is important to note that the angle of attack settles down quickly and remains constant throughout the simulation time period. The rapid build-up in lift, inertia, and momentum causes the aircraft to pitch-up steadily and climb-up; meanwhile, it starts losing lift and speed. As the aircraft decelerates, it pitches down steadily until the vertical lift is significantly less than the weight at $t = 18$ s at which the descending acceleration begins. The vertical lift and speed continue to build-up as the aircraft passes through equilibrium altitude at $t = 35$ s, and during the descent, the aircraft starts to pitch-up steadily at $t = 38$ s, around which the vertical lift and speed are equal to their trimmed values. At $t = 56$ s, the aircraft gains its local maximum build-up of lift and speed, and thus an excess of kinetic energy, inertia, and momentum, causing it to climb-up. The cycle repeats itself again, such that the aircraft decelerates and loses lift and speed, and pitches down, reaching to a local minimum lift and speed. During the motion progress, the maximum and minimum peak magnitudes reduce slowly until the oscillations eventually damps out. To conclude, it is evident from the response that pair (α_2,β_2) is a stable equilibrium operating point and does not exhibit any strong nonlinear behavior for the perturbation excitations considered.

Now, the longitudinal and lateral linear-nonlinear responses to -5 deg/s perturbation on pitch rate for $(\alpha_1 = -6^\circ, \beta_1 = +2^\circ)$, whereby the nonlinearity index is at the largest value, are compared in Figure 6.6. The time scale is restricted to $t = 15$ s due to nonlinear amplitudes being washed out by the quickly deviated linear amplitudes. Comparing the linear to the nonlinear results, it can be seen that the differences are significantly large for all state variables. Hence, at this operating point, the linear model is not suitable to represent the aircraft motion. Nonlinear simulations for the perturbed

response for a longer period of time out to $t = 68$ s are shown in Figures 6.7 and 6.8. The initial pitch rate introduces asymmetry in the response since the aircraft is initially trimmed asymmetrically. The aircraft is trimmed at $\phi_{b_0} = 176.3^{\circ}$; that is an inverted aircraft orientation, and the negative pitch perturbation produces nose-down pitching from an aircraft-fixed perspective, or nose-up from an inertial perspective. Note that, in Figure 6.7, in the first 15 s, the pitch rate is moderately damped and the side velocity and sideslip angle experience a moderate decaying oscillatory transient response from their equilibriums; however, the sideslip angle response shows insignificant variation. There is no evidence of the phugoid long-period mode. Also, the pitch rate jump induces a sudden positive jump in the roll rate and then undergoes a steadily increasing rate with negative slope; meanwhile, it induces a yaw rate that alternates slope. The yaw rate causes a quadratic yaw angle increase for $t < 40$ s, leading to an increase in the crossrange trajectory. As a consequence of the pitching moment, the total velocity decreases due to gravity effect, whereas altitude, pitch angle, and angle of attack increase.

There is a notable increase in the lift component that counteracts the aircraft weight, which explains the altitude gain (Figure 6.9 on the right). The left side of Figure 6.9 indicates that lateral rolling and yawing moments are induced as well, due to lift and drag asymmetry on both wings and due to side force developed by the vertical tail. The yawing moment exhibits a damped oscillatory behavior and a sudden continuous increase at the moment the aircraft pitches down with negative pitch angle into a descending position. The aircraft reaches maximum perturbed altitude at around $t = 16$ s. Afterwards, the aircraft represents a diving attitude, with increasing bank and pitch attitude angles and increasing total speed into the supersonic regime. By this time, the

aircraft begins to lose altitude and descends at a rapid rate starting at 403 ft/s and increasing until sea level. It is apparent that the aircraft is entering a high-speed steeply banked turn and it is entering a spiral dive due to its increasing roll rate, yaw rate, and speed. The initial and propagated aircraft attitude is visualized better in the top and side views in Figure 6.10, and in 3-D in Figure 6.11, where the aircraft position and orientation is snapshotted every 6.79 s. The spiral dive motion can be easily recognized in these plots.

Unlike level flight, in which the lift produced by the wings is cancelled by the downwards gravity force, the aircraft requires more lift to support its weight when banking, since lift is divided between pulling the aircraft towards the turn and balancing the weight. In order to compensate for the lift required, assuming no piloting interference, the aircraft speeds up until the vertical component of the lift is balancing the weight (see Figures 6.7 and 6.9). If the vertical lift curve is above the weight line, the aircraft is gaining altitude; otherwise, it is descending. The speed-up is related to the combined effect of directional damping and angle of attack stability. Additionally, the aircraft's overbanking tendency increases the bank angle further, and accordingly, speed, descent rate, and load factor increase dramatically. To conclude, responses at pair (α_1,β_1) indicate strong nonlinear behavior as predicted by the nonlinear index results from Chapter 5.

Now consider a roll axis excitation at pair 1. An initial roll rate of 5 deg/s applied to pair 1 (α_1,β_1) is rapidly damped out, but it triggers a moderately damped oscillation that is seen in the side velocity, sideslip angle, and yaw rate, as presented in Figure 6.12, which compares linear and nonlinear simulation to $\Delta p_{b_0} = 5$ deg/s for a 30 s window. The linear results cannot accurately duplicate the nonlinear dynamics at the trimming

equilibrium of ($\alpha_1 = -6^\circ$, $\beta_1 = +2^\circ$) after approximately 10 s. The nonlinear responses over a much larger time window are given in Figures 6.13-6.14. From Figure 6.15 (left), the initial roll perturbation produces a well damped rolling moment, due to large roll damping of the aircraft. On the other side, the roll coupling effect introduces high frequency fluctuations in the yaw moment with a decaying rate of amplitude in the transient period, and its effect is clearly seen in the yaw rate and the heading angle (see Figures 6.13 and 6.15). The initial roll rate induces a wing spanwise asymmetric local angle of attack variation that produces asymmetric lift force. This asymmetry reduces lift on one wing (the right wing in this case), and initiates the rolling moment. In the same time, the positive Δp_{b_0} increases the linearly varying angle of attack, and that in turn increases the profile drag on the left wing and the drag difference induces a yawing moment. The transient responses of the remaining state variables, translational velocities, angle of attack, pitch rate, bank angle, and pitch angle, are almost flat and maintain close to equilibrium position. Around $t = 50$ s, where the aircraft has slightly elevated to a maximum altitude, the yaw rate changes sign and induces linearly increasing roll and pitch rates, causing the aircraft to bank and pitch simultaneously. The combined roll and yaw rates position the aircraft nose to level with the horizon, and the pitch rate jump develops a pitching moment causing a nose-up orientation from the pilot's perspective (Figure 6.15). Consequently, the aircraft loses altitude and enters a high-speed descending flight starting at 367 ft/s on average until it approaches sea level at $t =$ 103 s. This descending flight motion can be seen clearly in Figures 6.16 and 6.17 where the aircraft attitude is depicted every 9.35 s. A longer time simulation would reveal that

the aircraft is entering a spiral dive, but it does not add any useful contribution. It is noted that the sideslip angle variation during the total nonlinear simulation time remains small.

Now consider a yaw axis excitation at pair 1. For an initial yaw rate of 5 deg/s perturbation at pair 1, linear vs. nonlinear results are compared in Figure 6.18 out to $t = 30$ s, and nonlinear simulations are presented in Figures 6.19 and 6.20 for $t = 93$ s. Moments and normalized forces are given in Figure 6.21. Figures 6.22 and 6.23 show views for the aircraft attitude at a 9.29 s period. The linear model again shows invalid results when compared to the nonlinear model (Figure 6.18). The oscillatory transient response to the yaw perturbation is moderately damped, and it induces equal frequency oscillations in the side velocity, roll rate, bank angle, and yaw angle. However, the bank and yaw angles show smaller amplitudes. Perturbation in the yaw rate does not induce any pitching moment, but it introduces a noticeable yawing moment and ten times smaller-in-magnitude rolling moments in the first 10 s, and then dies out and has minimum effect in the transient period on vertical velocity, pitch rate, and pitch angle; however, the yaw angle and crossrange increase (see Figures 6.19 and 6.20). The aircraft's axial velocity slightly decreases and it gains some altitude until $t \approx 35$ s, around which the yaw rate changes direction and induces linearly increasing roll and pitch rates that cause the aircraft to bank and pitch simultaneously. Due to gravity's effect and the increased pitching moment (Figure 6.21), the aircraft loses altitude and enters a high-speed descending flight motion starting at 356 ft/s on average until it approaches sea level at $t = 93$ s. Strong nonlinear behavior is again observed.

It can be observed from the previous results for an aircraft initially perturbed from equilibrium at pair 1 with an angular rate, that the resulting motion response is a

nonlinear coupled interaction between the other two angular rates. The trimming solution at (α_1,β_1), without doubt, is highly nonlinear, due to its sensitivity to initial condition excitation. The sideslip angle variation due to Δp_{b_0}, Δq_{b_0} or Δr_{b_0} is minimum; hence, note that the large response in the body roll, pitch, or yaw rates are not primarily caused by large aerodynamic variation, but rather by the so-called nonlinear inertial coupling. However, the aircraft in all of the cases enters a gradual high-speed diverging spiraling descending motion, due to the high increased roll rate with increasing bank and changing heading angles. In all of the cases, the gradual negative increase of the pitch angle points the aircraft nose toward the ground, and hence diverts more of the gravity component into the aircraft body x_b-axis and reduces the lift force tremendously in the second-half phase of the flight. The non-oscillatory divergence leads to the nonlinear high-speed spiral dive phenomenon as time proceeds. Usually this path divergence occurs for aircraft with large directional stability and small lateral stability.

The aircraft model in the study is a high-performance category aircraft, and the nonlinear inertial coupling cannot be ignored in the analysis. The mass of such an aircraft is concentrated in its fuselage; therefore, the roll mass moment of inertia I_{xx}^b is much smaller than the pitch and yaw mass moment of inertias, I_{yy}^b and I_{zz}^b. Numerical values show that I_{yy}^b and I_{zz}^b are 5.88 and 6.64 times larger than I_{xx}^b, respectively. The inertia coupling can be best understood by looking at the moment equations of motion. Equation (2.37) is repeated here with the necessary assumptions of $I_{xy}^b = I_{yz}^b = \Delta x = \Delta y = \Delta z = 0$,

$$L_b = I_{xx}^b \dot{p}_b - (\dot{r}_b + p_b q_b) I_{xz}^b + \left(I_{zz}^b - I_{yy}^b\right) q_b r_b$$

$$M_b = I_{yy}^b \dot{q}_b + (p_b^2 - r_b^2) I_{xz}^b + (I_{xx}^b - I_{zz}^b) p_b r_b \tag{6.1}$$

$$N_b = I_{zz}^b \dot{r}_b - (\dot{p}_b - q_b r_b) I_{xz}^b + \left(I_{yy}^b - I_{xx}^b\right) p_b q_b$$

Looking at the last terms of the second and third equations, one notes that the inertia difference is large, such that, for example, a rapid rolling may result in uncontrollable pitching and yawing motions. This significant roll coupling can lead to divergence from the trimmed trajectory, as seen earlier.

Nonlinear simulation results to an initial 10 ft/s side velocity perturbation and a -5 deg rudder deflection impulse are shown in Figures 6.24-6.27. The perturbations Δv_{b_0} and $\Delta \delta_{r_0}$ produce a similar overall response when compared to Δr_{b_0} (see Figures 6.19 and 6.20). The same analysis as before applies here and is not repeated.

Table 6.1 Index comparison for selected pairs at different altitudes*

	$H_b = 0$ ft		$H_b = 20{,}000$ ft	
	$(\alpha_1, \beta_1) = (-6^\circ, +2^\circ)$	$(\alpha_2, \beta_2) = (+6^\circ, +2^\circ)$	$(\alpha_1, \beta_1) = (-6^\circ, +2^\circ)$	$(\alpha_2, \beta_2) = (+6^\circ, +2^\circ)$
v_s^A	3.29	0.99	3.30	0.99
v_s^B	56.80	7.82	56.80	7.82
v_d^x	3.24	0.98	3.26	0.98
v_d^u	114.17	10.63	129.43	11.33

* Computation performed with a dimensional state formulation using the body-frame

Table 6.2 Trim solutions for selected pairs at $H_b = 20{,}000$ ft

	$(\alpha_1, \beta_1) = (-6^\circ, +2^\circ)$	$(\alpha_2, \beta_2) = (+6^\circ, +2^\circ)$
V_T	551.96 *ft/s*, $(M = 0.53)$	472.75 *ft/s*, $M = 0.46$
ϕ_b	176.2742°	2.8893°
θ_b	6.1167°	6.0927°
δ_h	-0.8544°	-1.5533°
δ_a	0.57°	-1.0717°
δ_r	4.4176°	4.6608°
δ_{th}	0.3823	0.2465

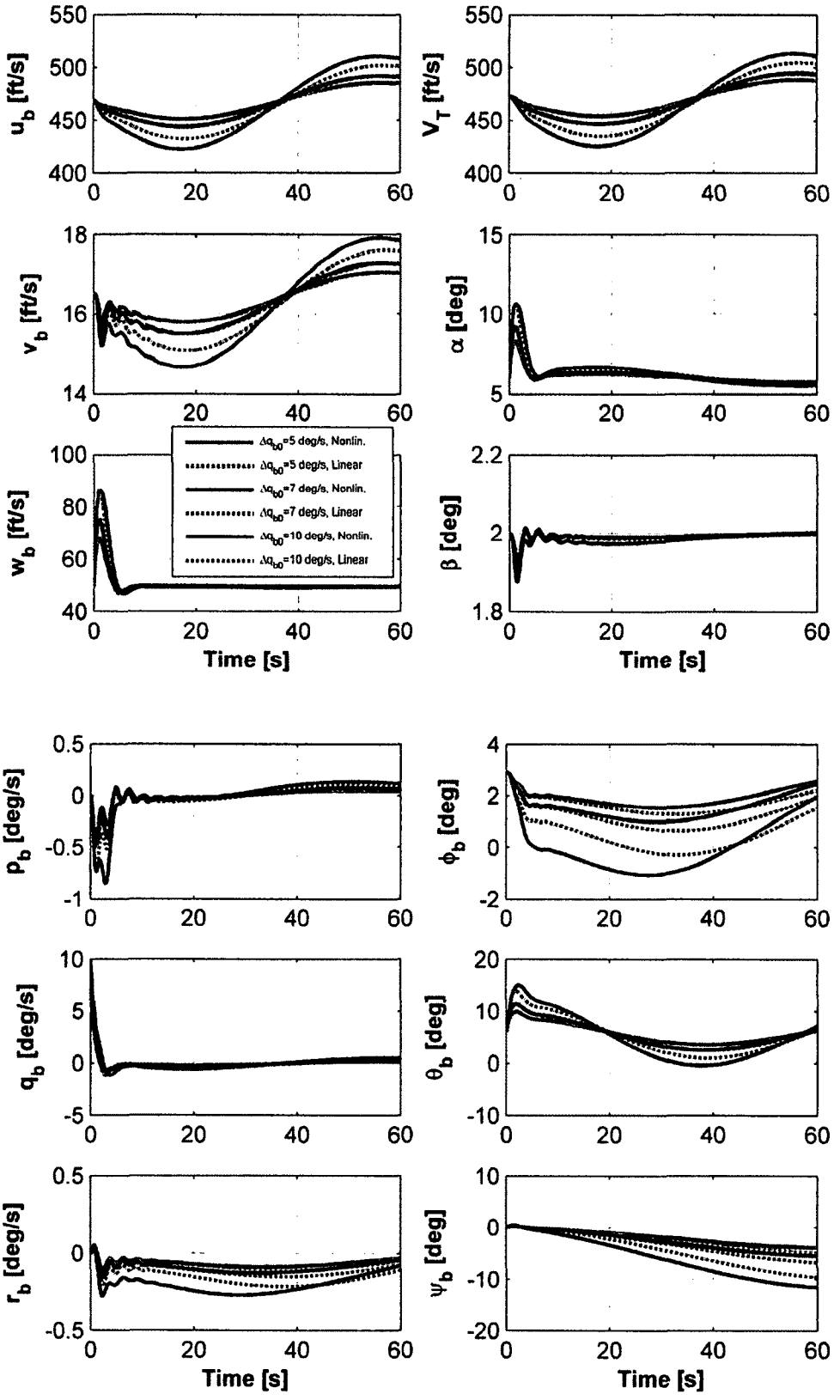

Figure 6.1 Linear-nonlinear response to initial pitch rate at pair 2, $\Delta q_{b_0} = 5, 7, 10$ deg/s

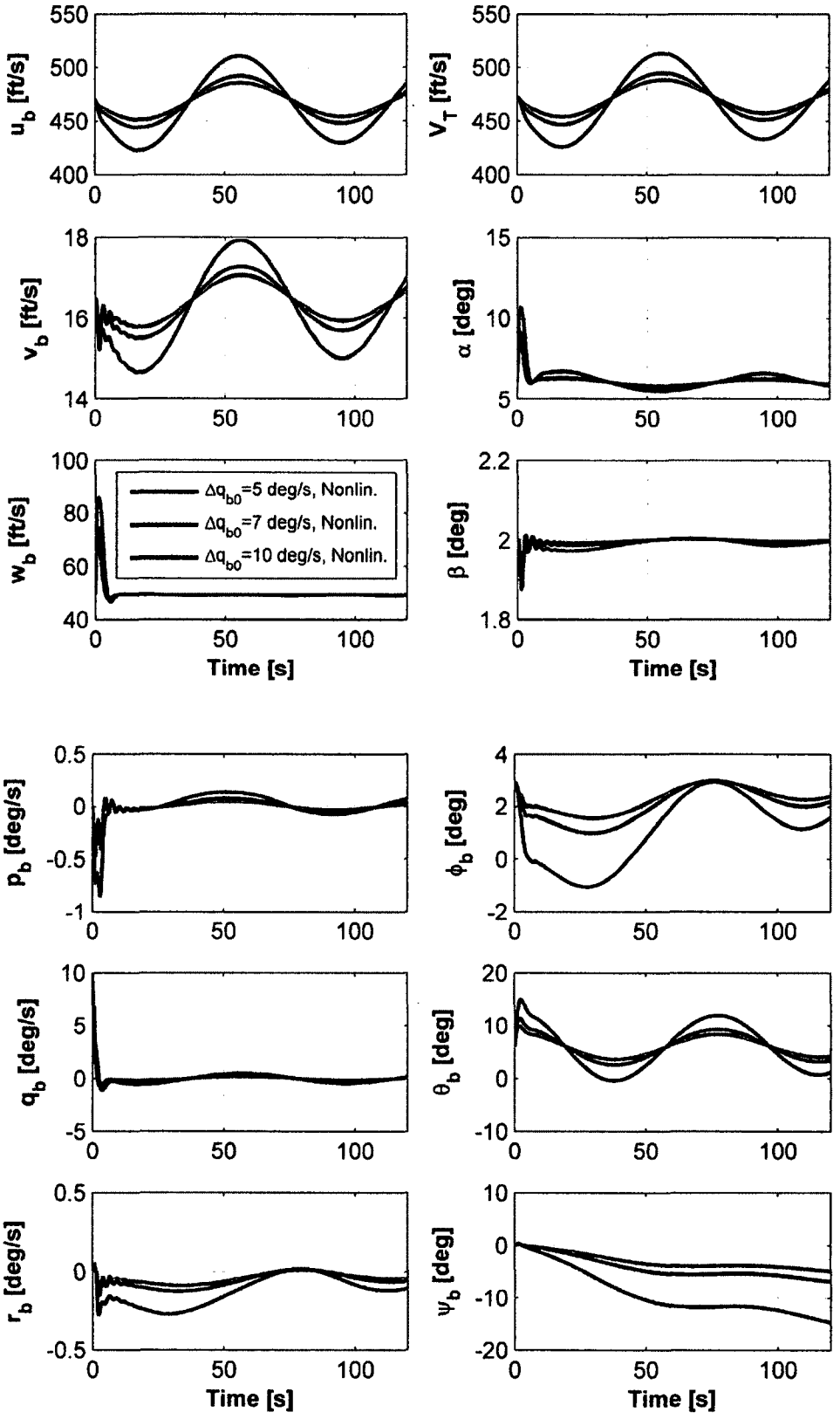

Figure 6.2 Nonlinear response to initial pitch rate at pair 2, $\Delta q_{b_0} = 5, 7, 10$ deg/s

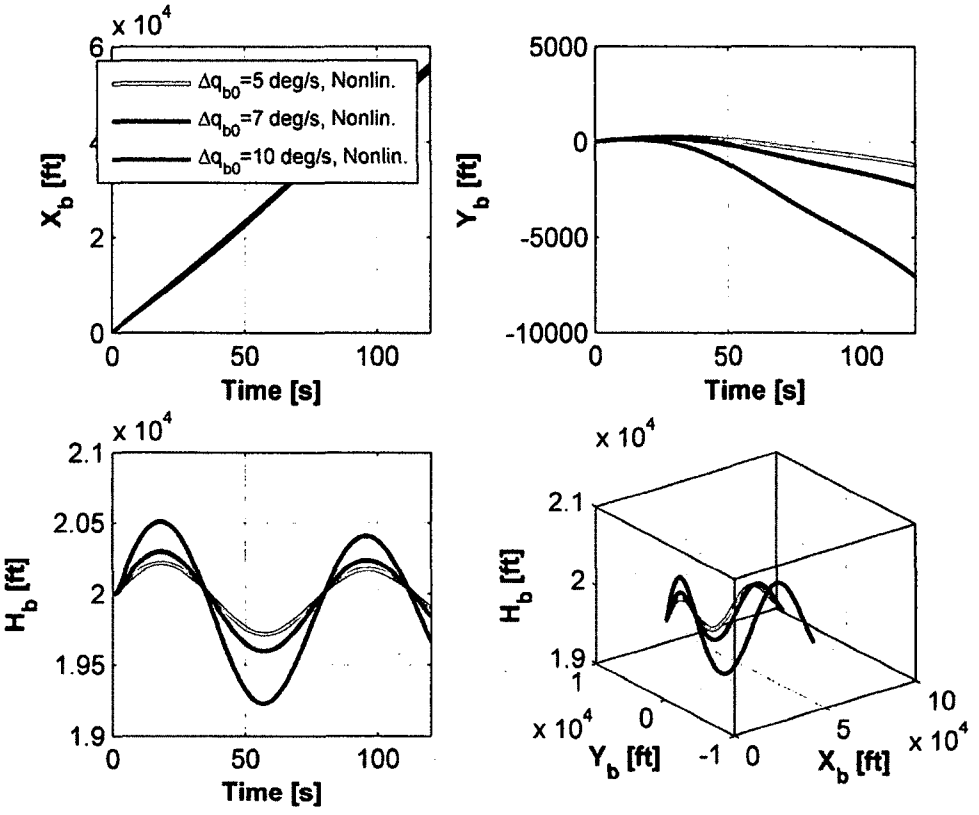

Figure 6.3 Trajectory response to initial pitch rate at pair 2, $\Delta q_{b_0} = 5, 7, 10$ deg/s

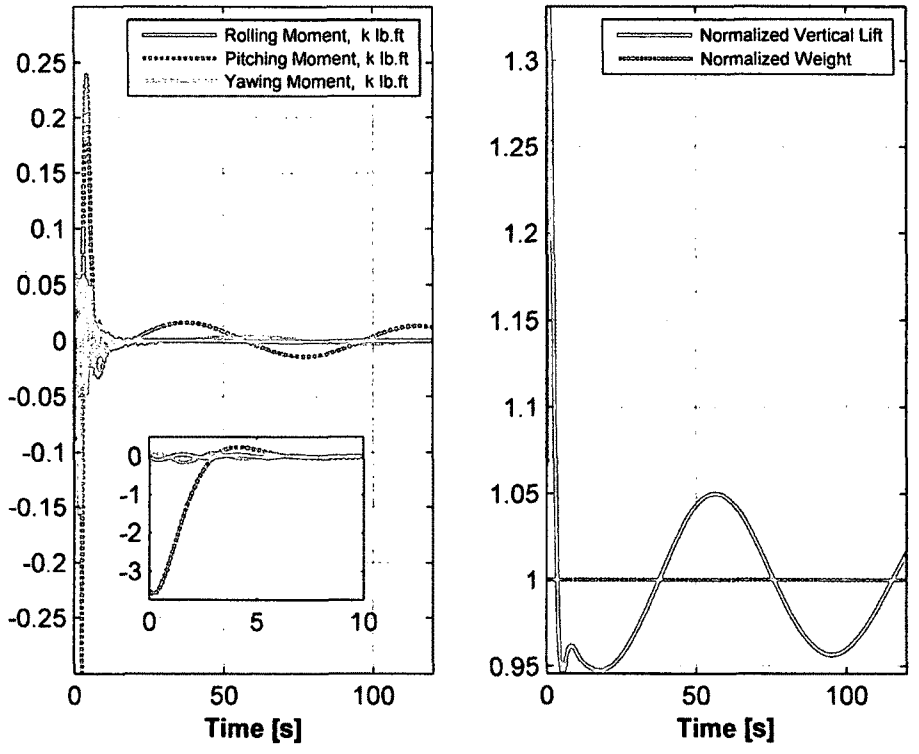

Figure 6.4 Force and moment variations to initial pitch rate at pair 2, $\Delta q_{b_0} = 5$ deg/s

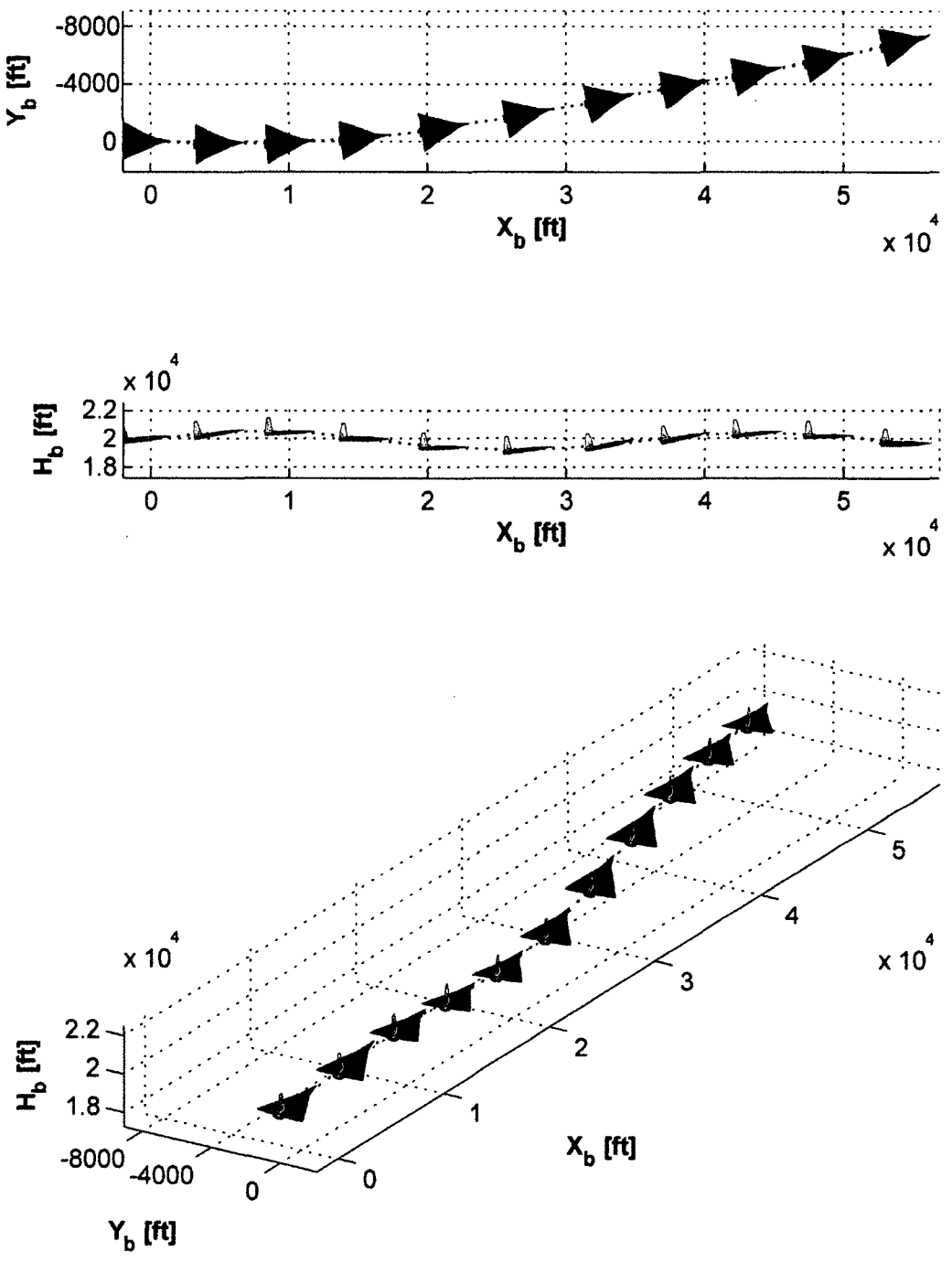

Figure 6.5 Top, side, and 3-D visual attitude to initial pitch rate at pair 2, $\Delta q_{b_0} = 10$ deg/s

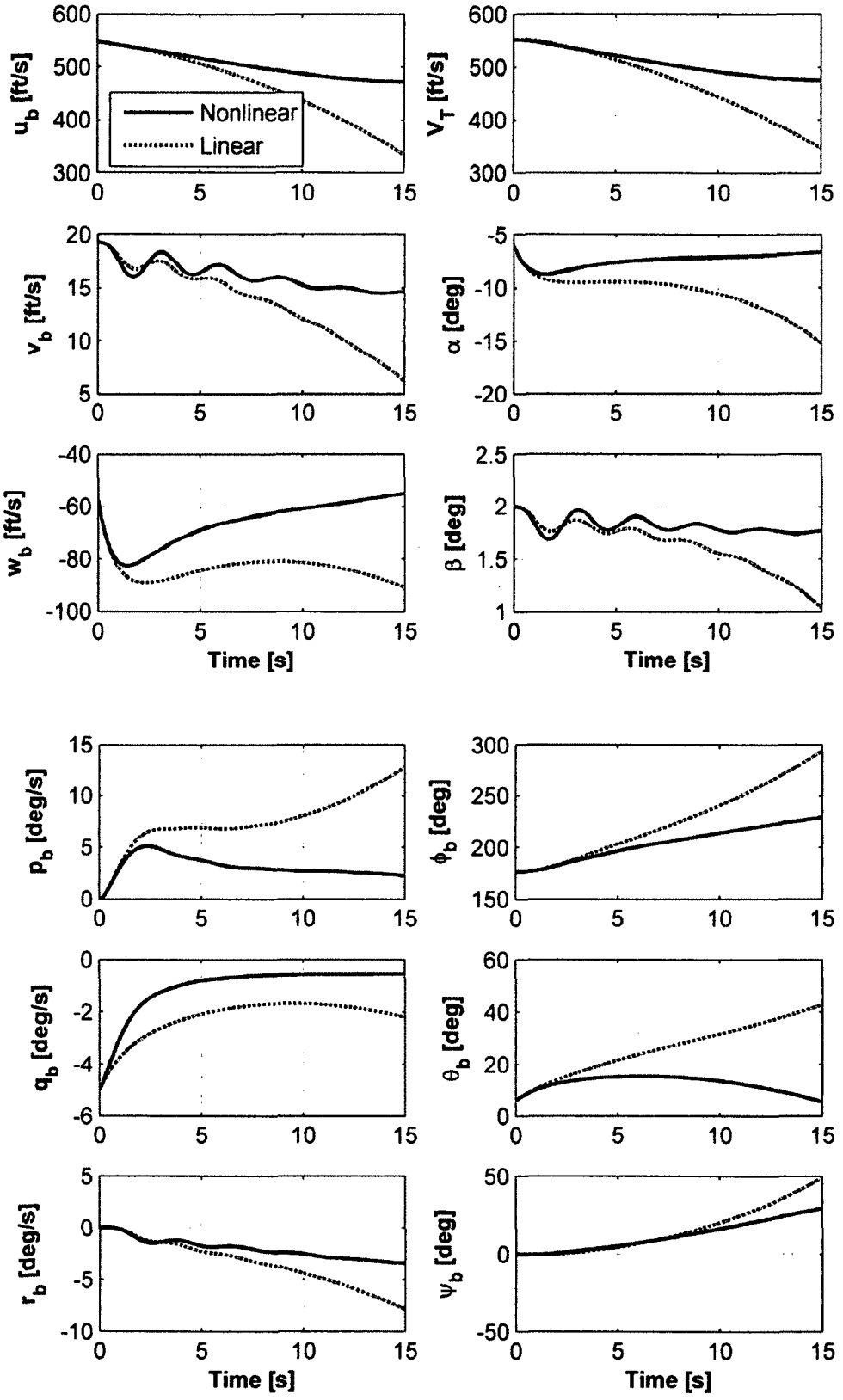

Figure 6.6 Linear-nonlinear response to initial pitch rate at pair 1, $\Delta q_{b_0} = -5$ deg/s

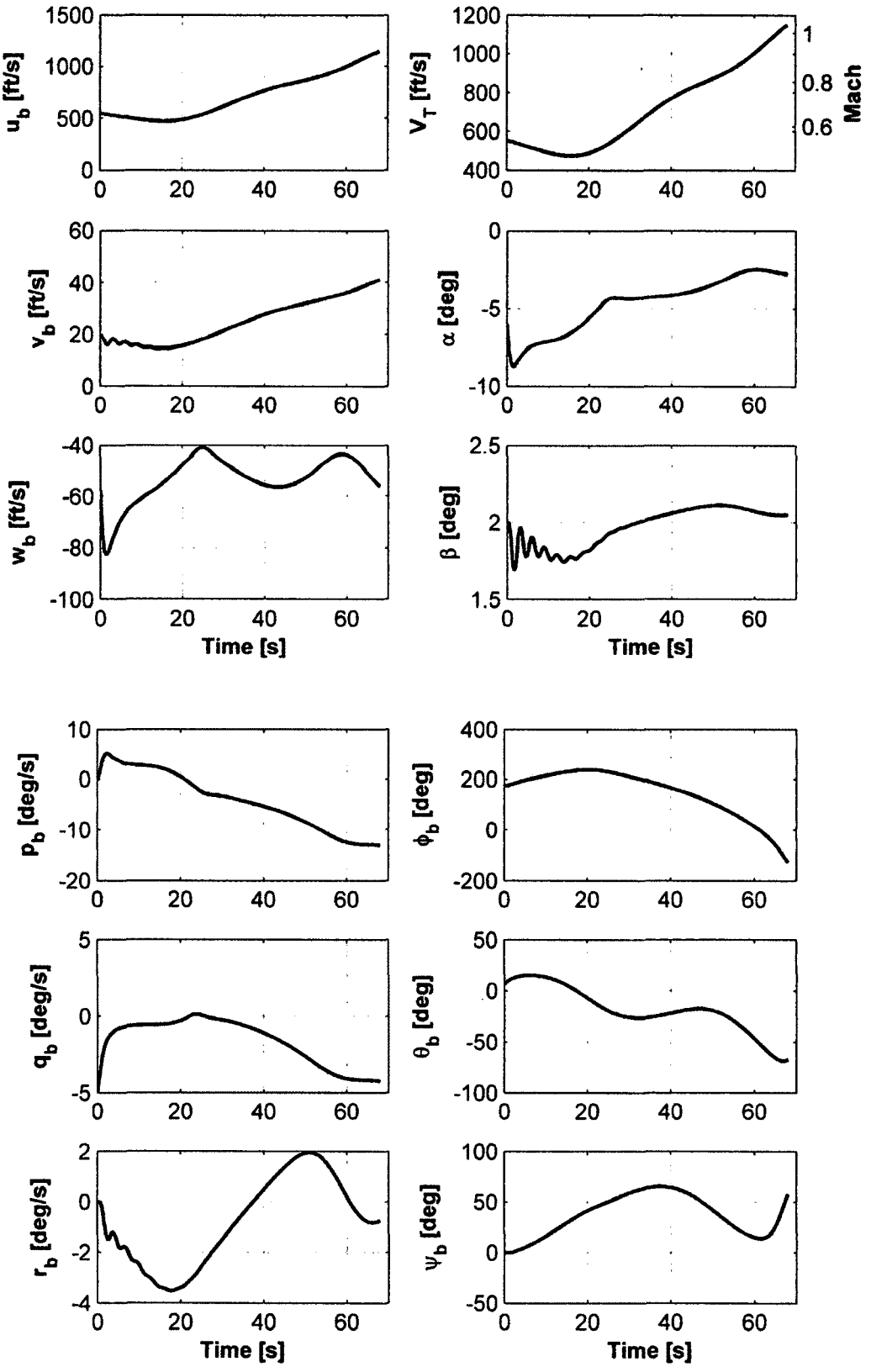

Figure 6.7 Nonlinear response to initial pitch rate at pair 1, $\Delta q_{b_0} = -5$ deg/s

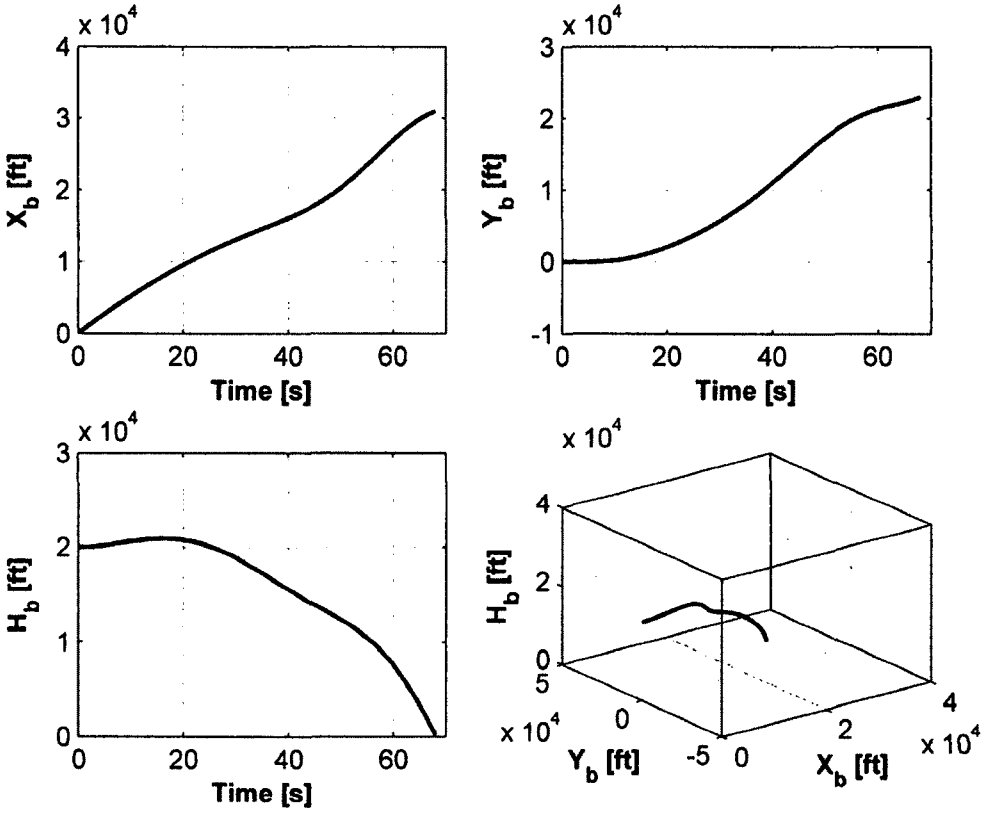

Figure 6.8 Trajectory response to initial pitch rate at pair 1, $\Delta q_{b_0} = -5$ deg/s

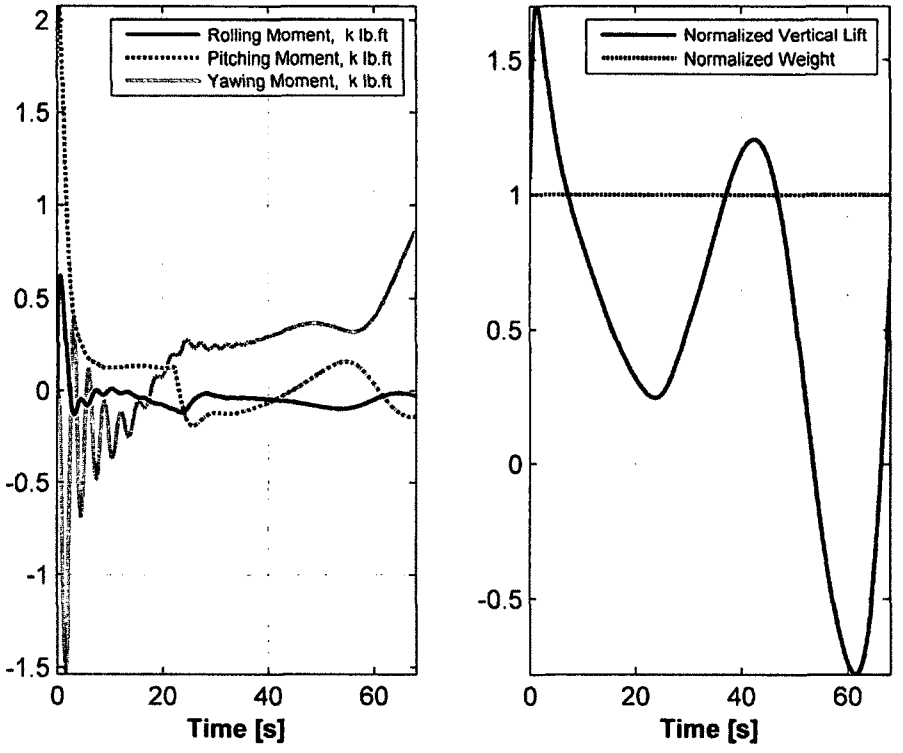

Figure 6.9 Force and moment variations to initial pitch rate at pair 1, $\Delta q_{b_0} = -5$ deg/s

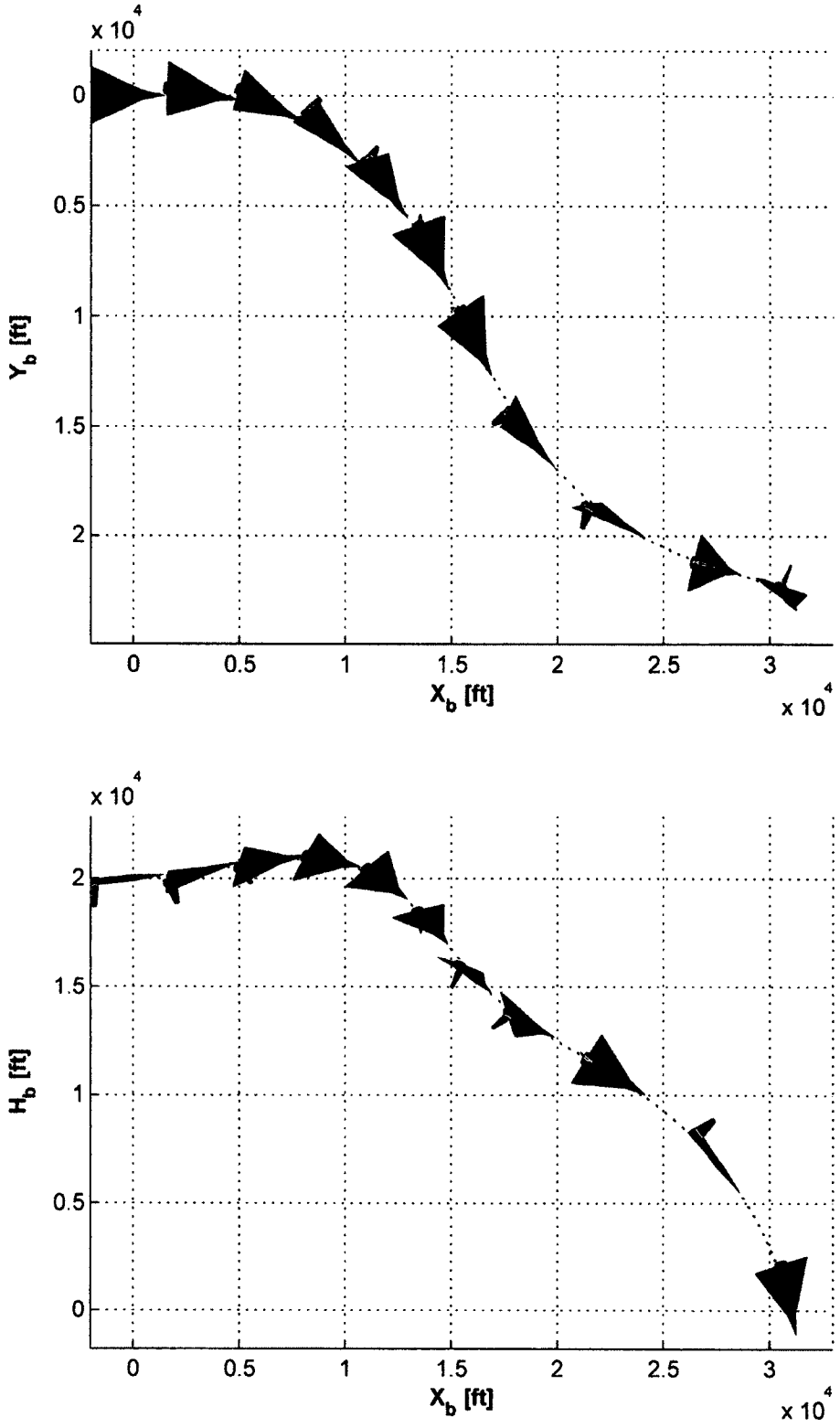

Figure 6.10 Top and side visual attitude to initial pitch rate at pair 1, $\Delta q_{b_0} = -5$ deg/s

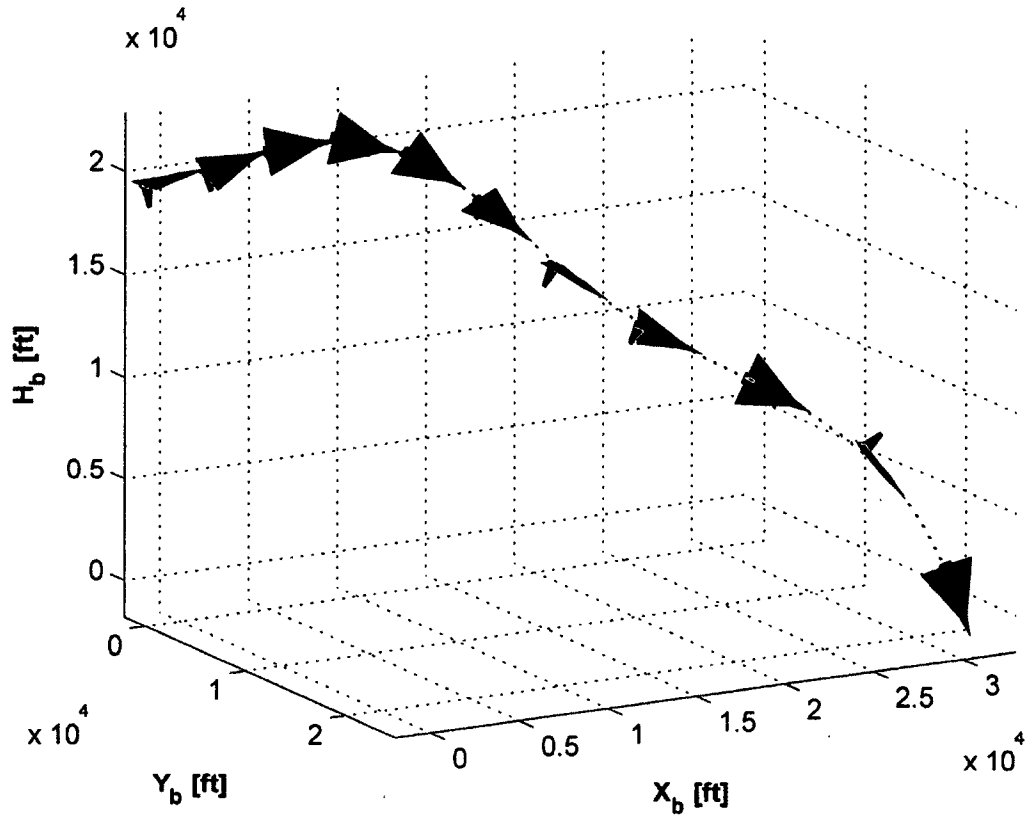

Figure 6.11 3-D visual attitude to initial pitch rate at pair 1, $\Delta q_{b_0} = -5$ deg/s

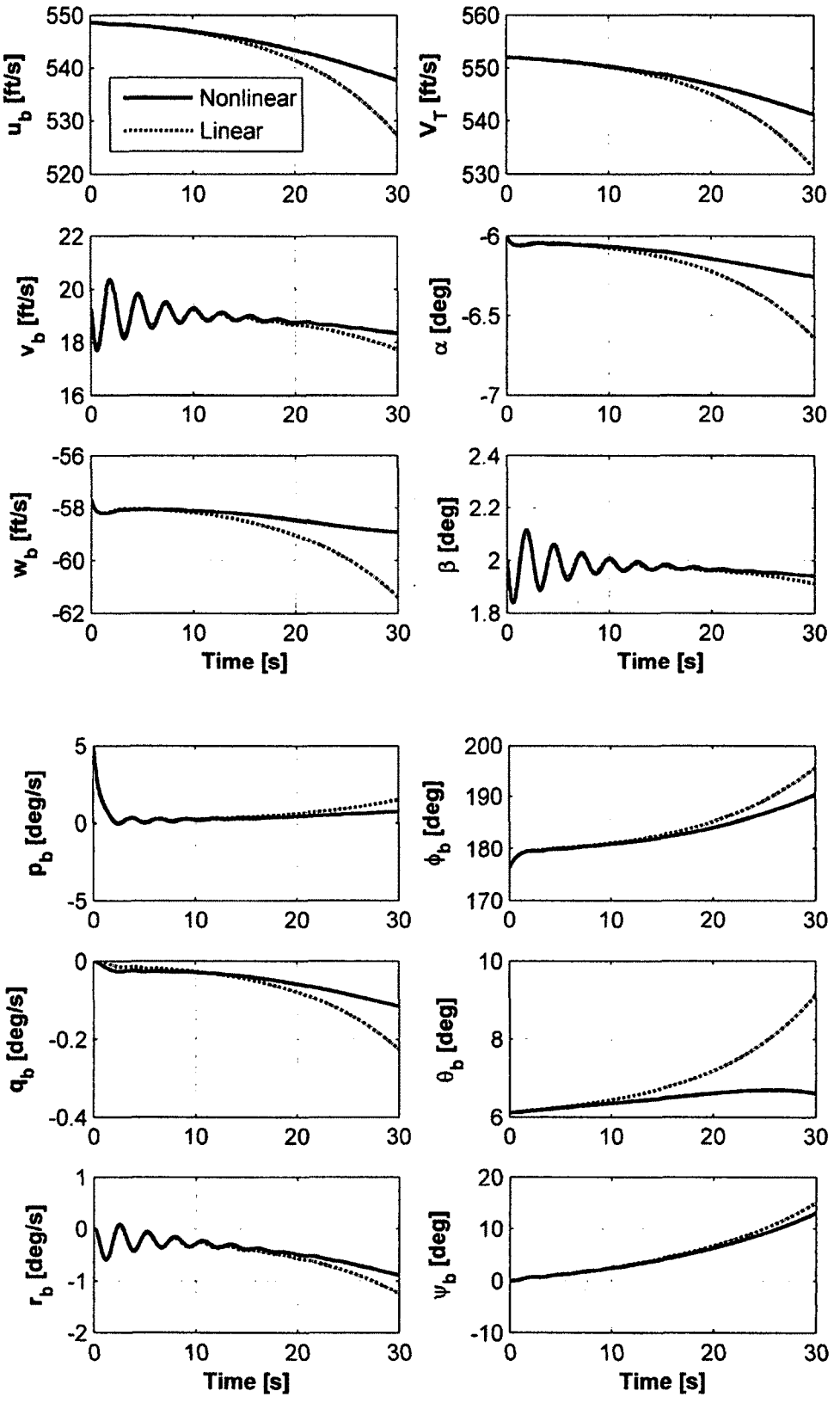

Figure 6.12 Linear-nonlinear response to initial roll rate at pair 1, $\Delta p_{b_0} = 5$ deg/s

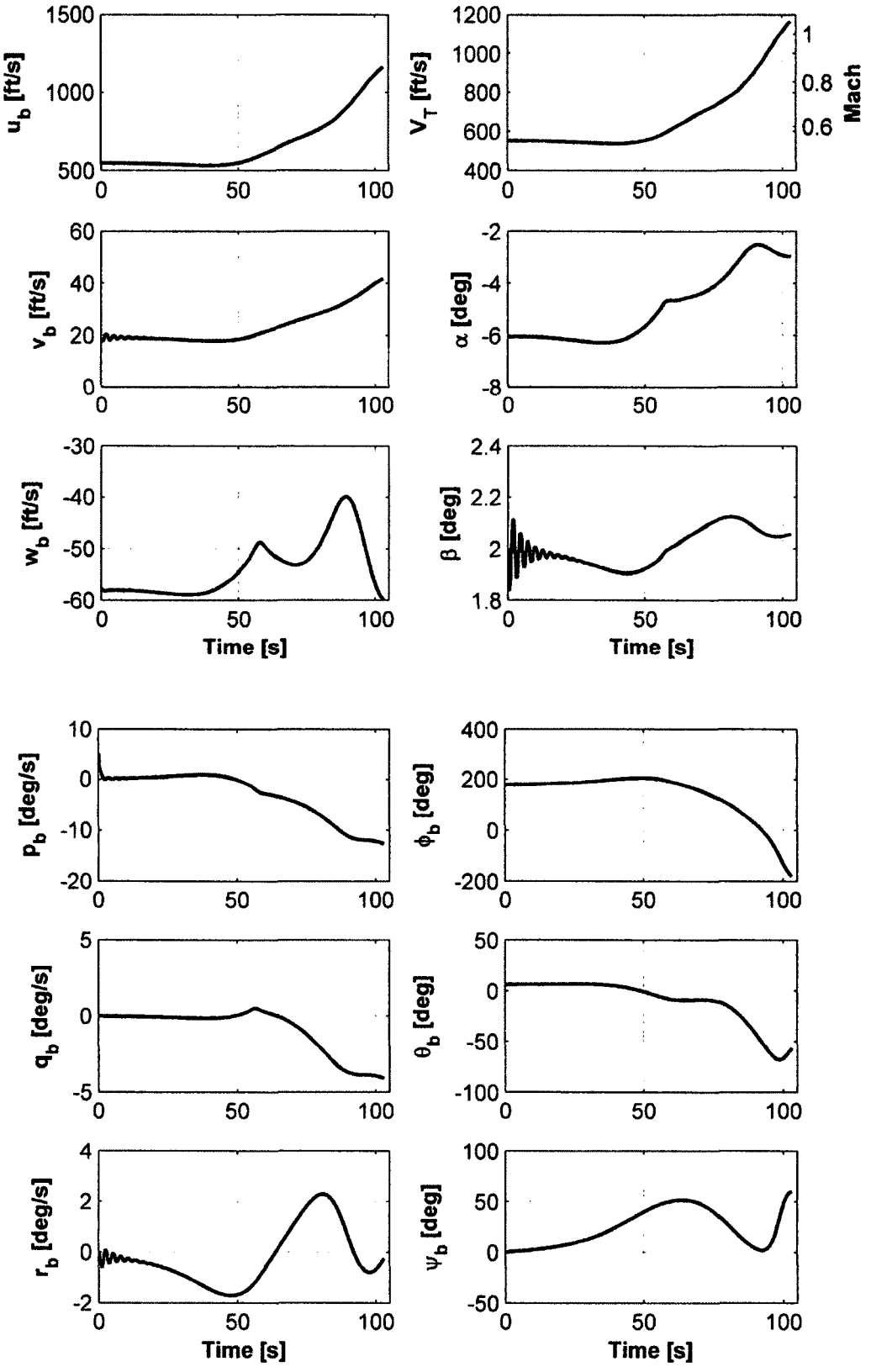

Figure 6.13 Nonlinear response to initial roll rate at pair 1, $\Delta p_{b_0} = 5$ deg/s

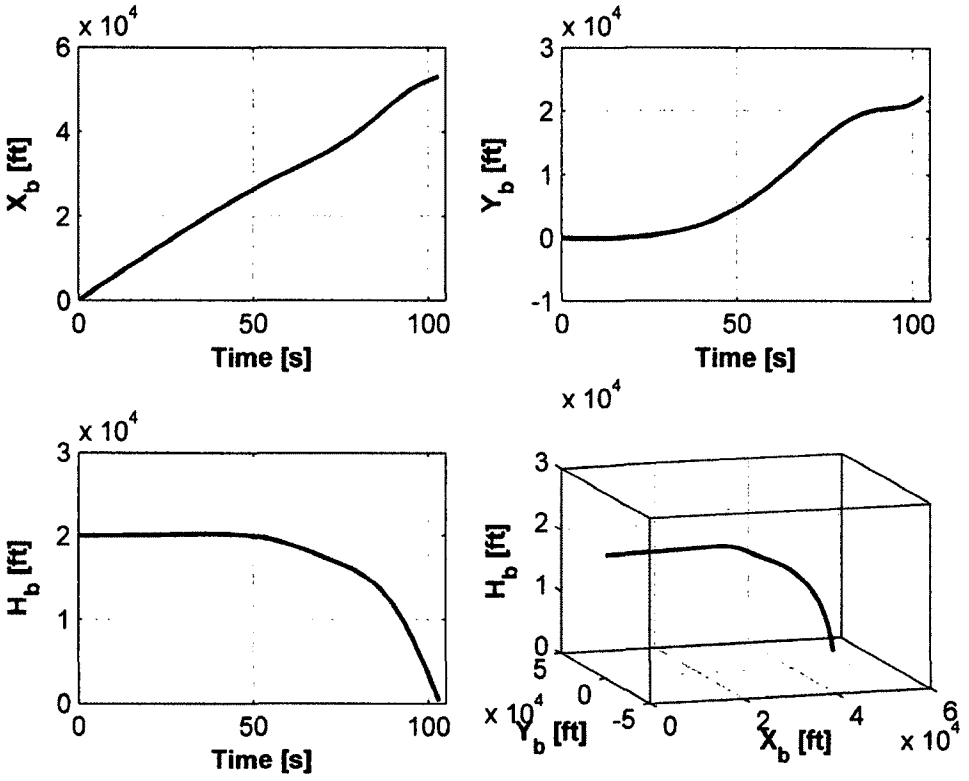

Figure 6.14 Trajectory response to initial roll rate at pair 1, $\Delta p_{b_0} = 5$ deg/s

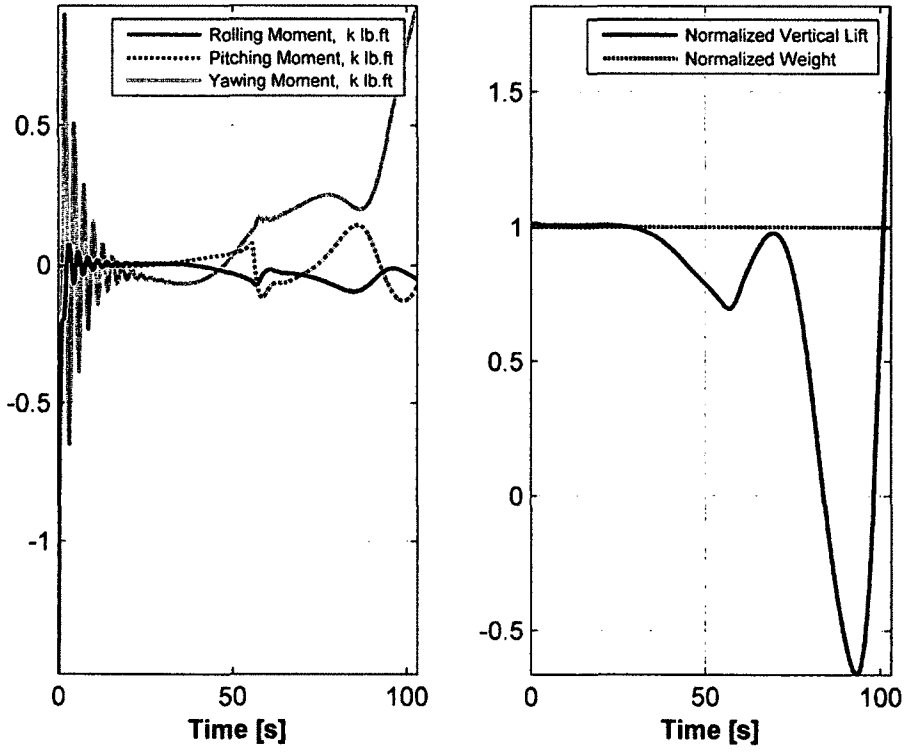

Figure 6.15 Force and moment variations to initial roll rate at pair 1, $\Delta p_{b_0} = 5$ deg/s

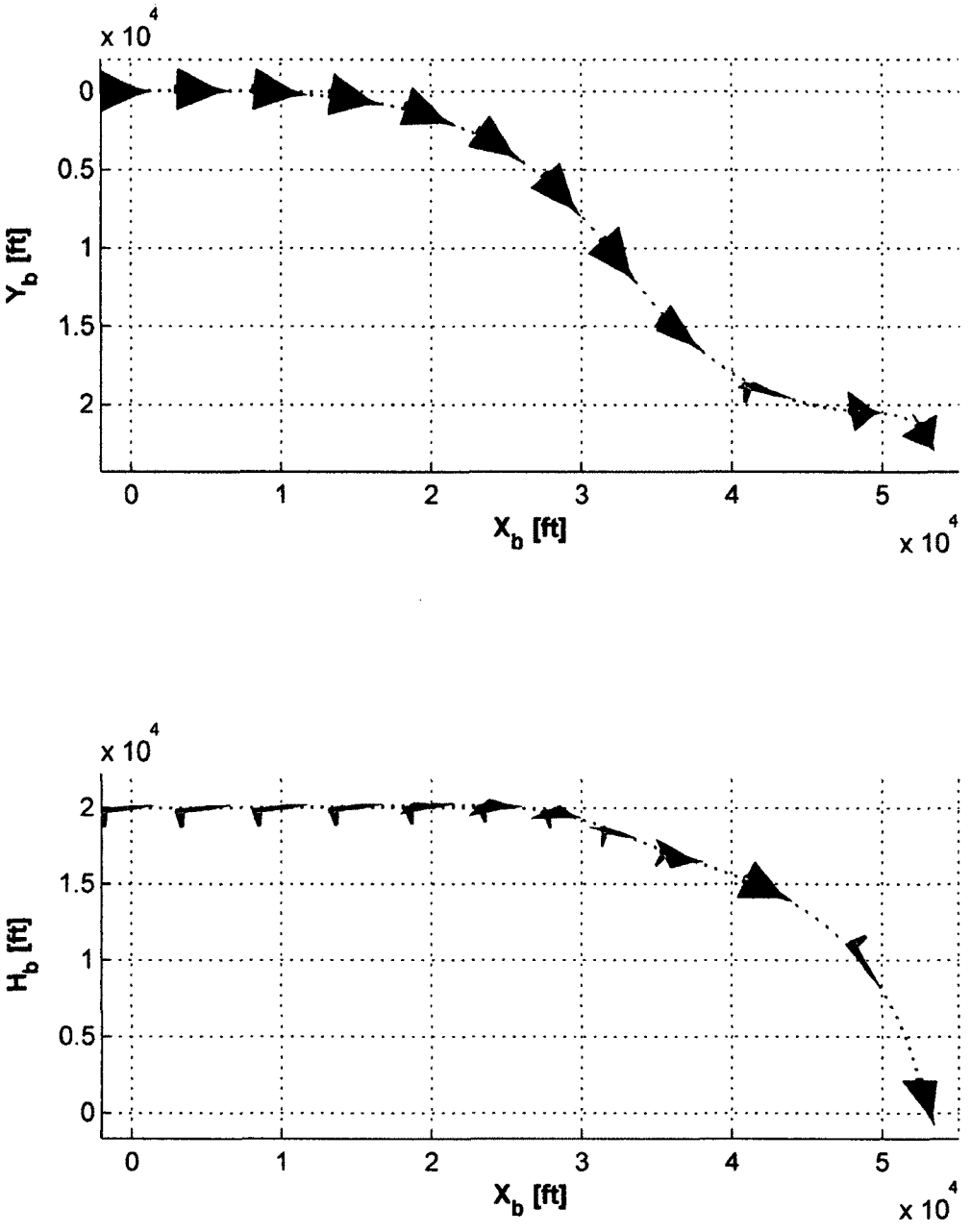

Figure 6.16 Top and side visual attitude to initial roll rate at pair 1, $\Delta p_{b_0} = 5$ deg/s

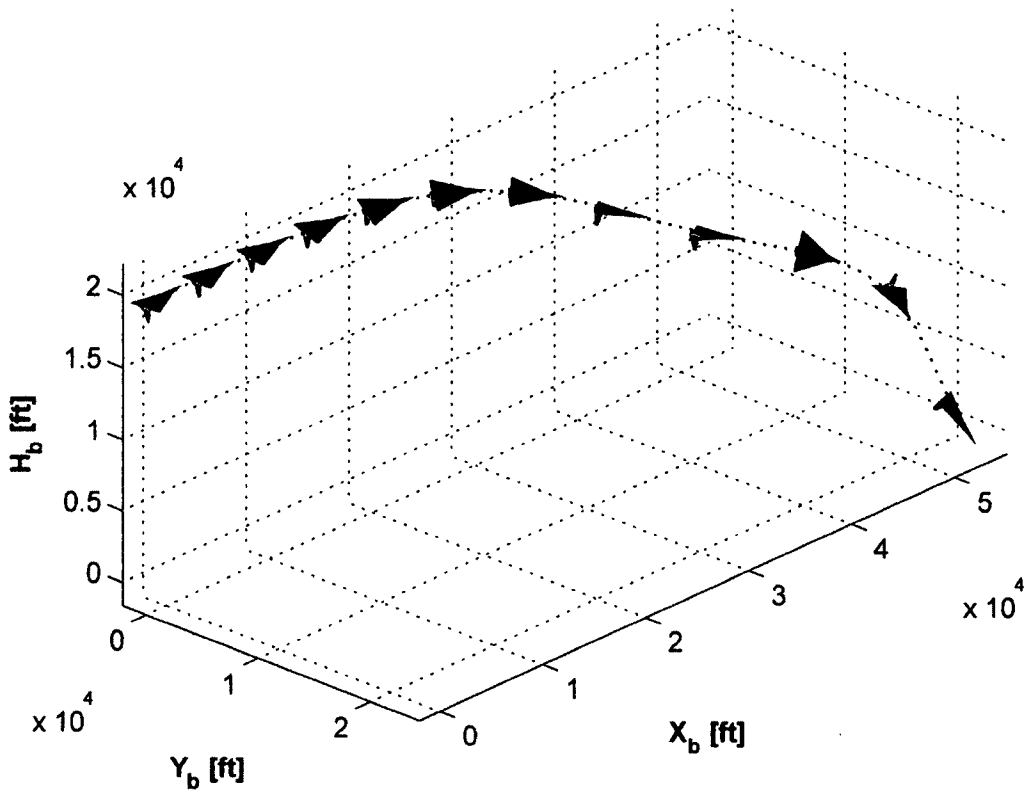

Figure 6.17 3-D visual attitude to initial roll rate at pair 1, $\Delta p_{b_0} = 5$ deg/s

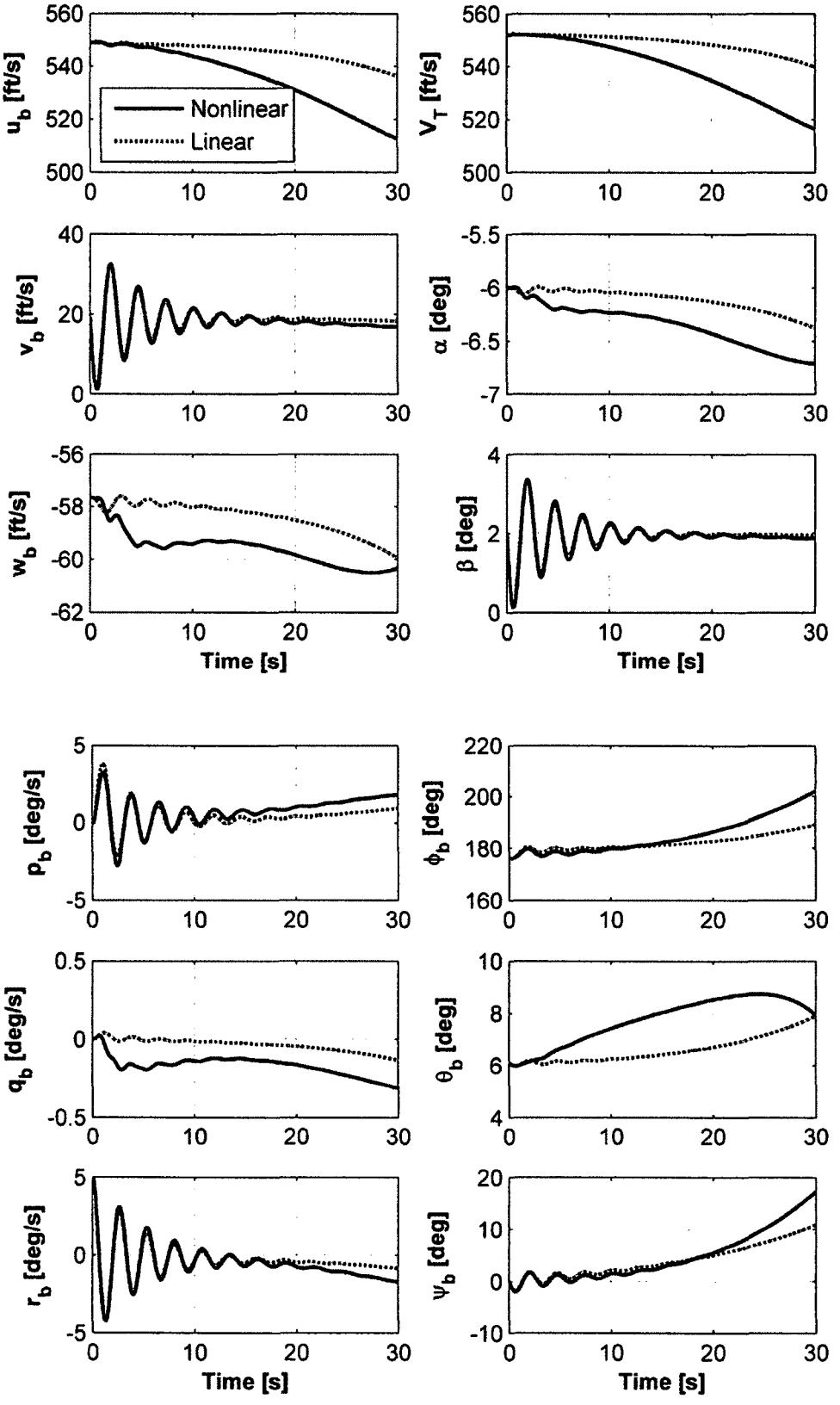

Figure 6.18 Linear-nonlinear response to initial yaw rate at pair 1, $\Delta r_{b_0} = 5$ deg/s

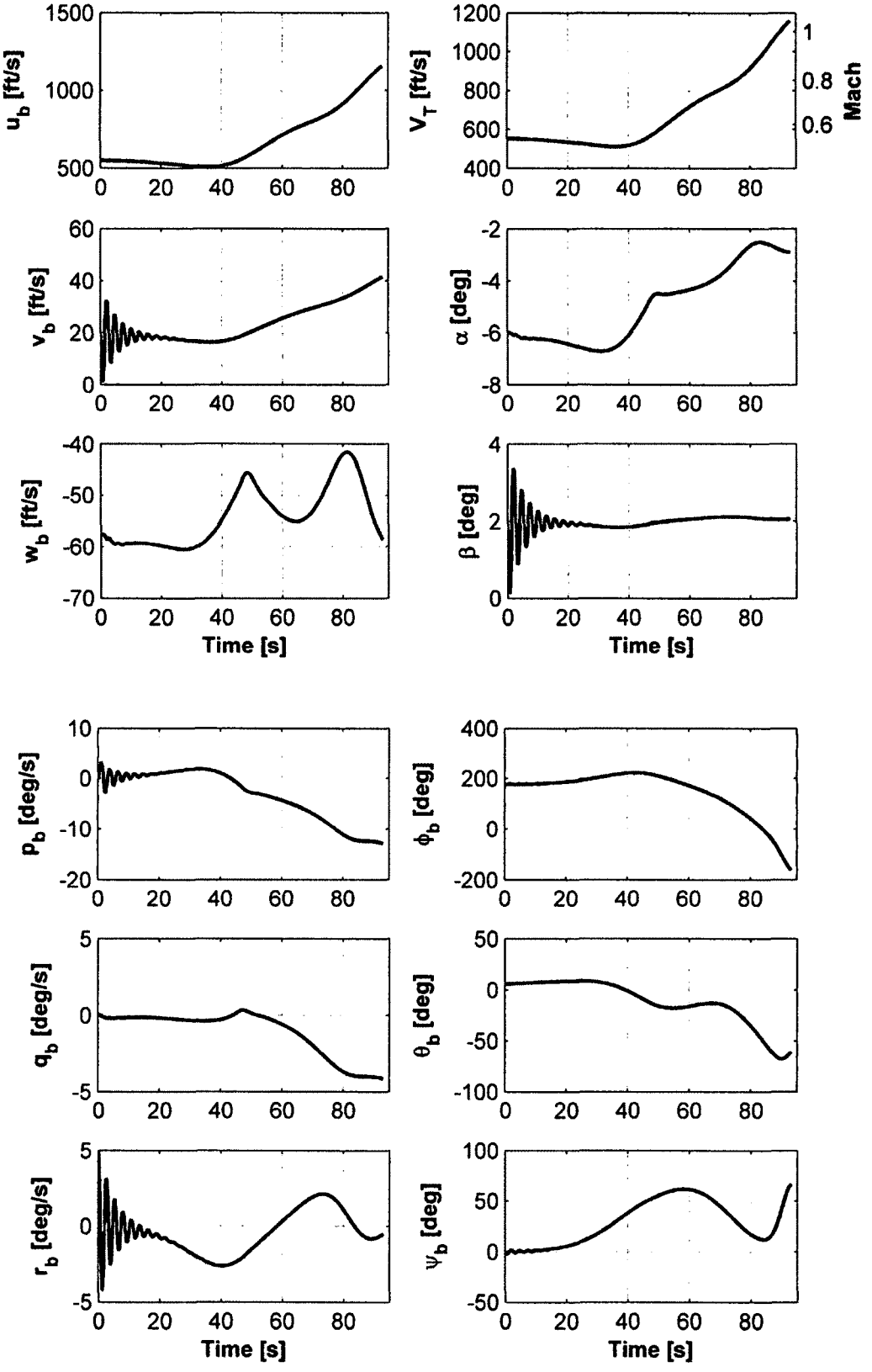

Figure 6.19 Nonlinear response to initial yaw rate at pair 1, $\Delta r_{b_0} = 5$ deg/s

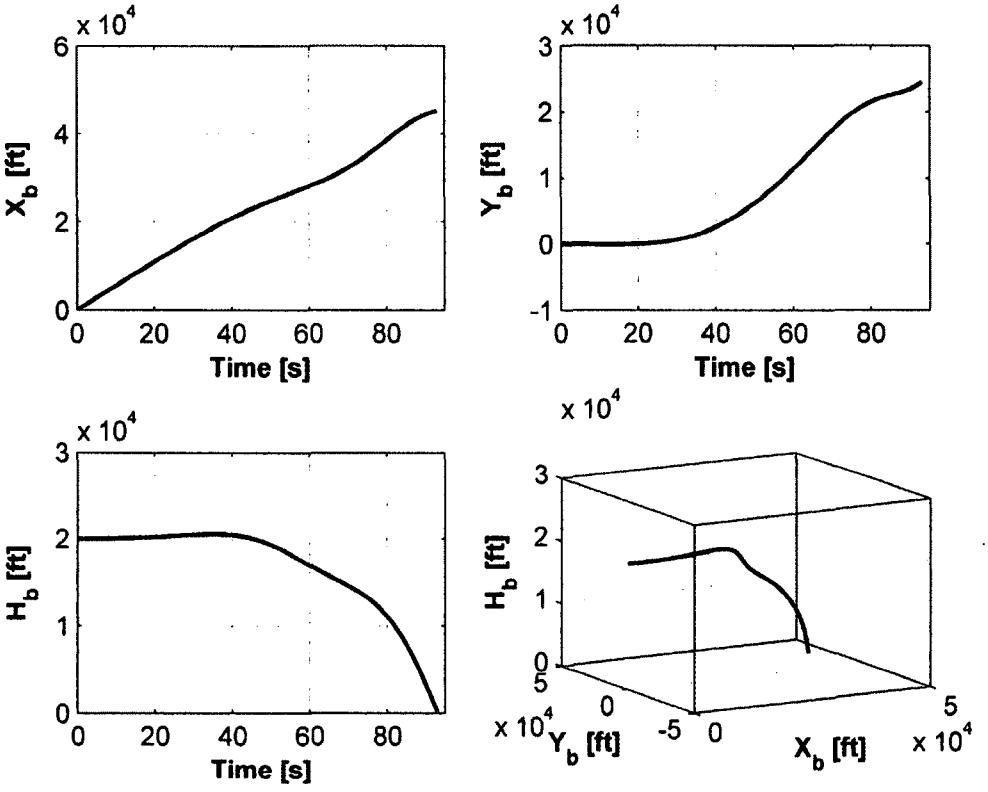

Figure 6.20 Trajectory response to initial yaw rate at pair 1, $\Delta r_{b_0} = 5$ deg/s

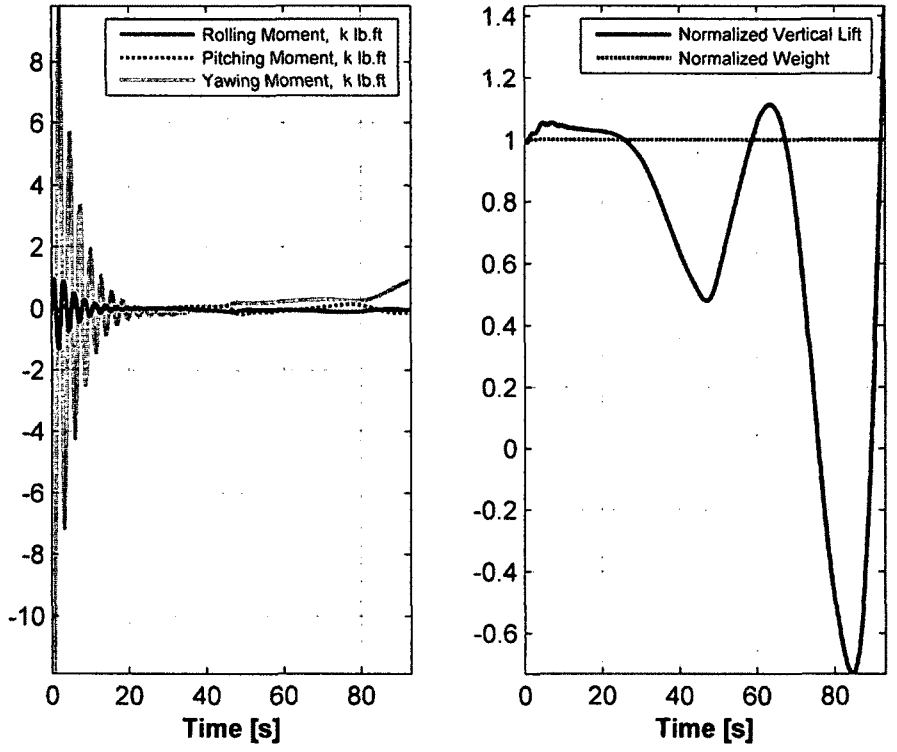

Figure 6.21 Force and moment variations to initial yaw rate at pair 1, $\Delta r_{b_0} = 5$ deg/s

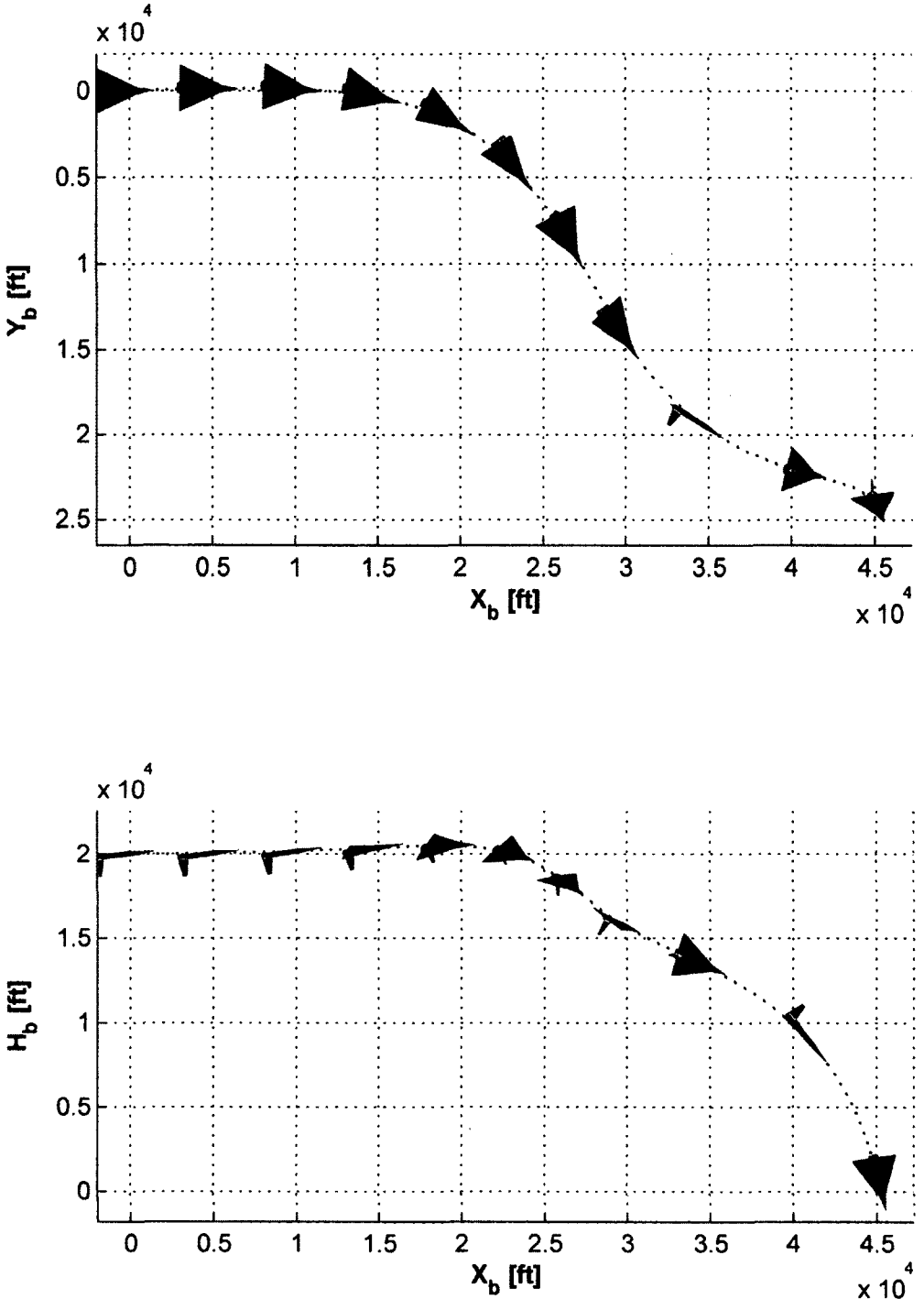

Figure 6.22 Top and side visual attitude to initial yaw rate at pair 1, $\Delta r_{b_0} = 5$ deg/s

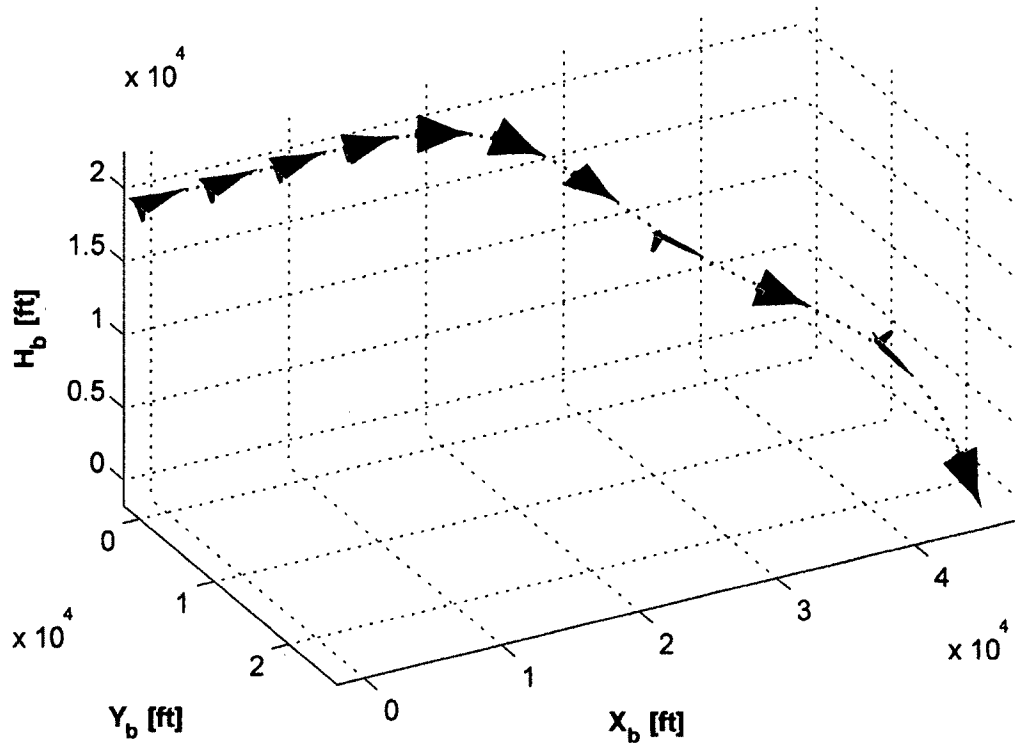

Figure 6.23 3-D visual attitude to initial yaw rate at pair 1, $\Delta r_{b_0} = 5$ deg/s

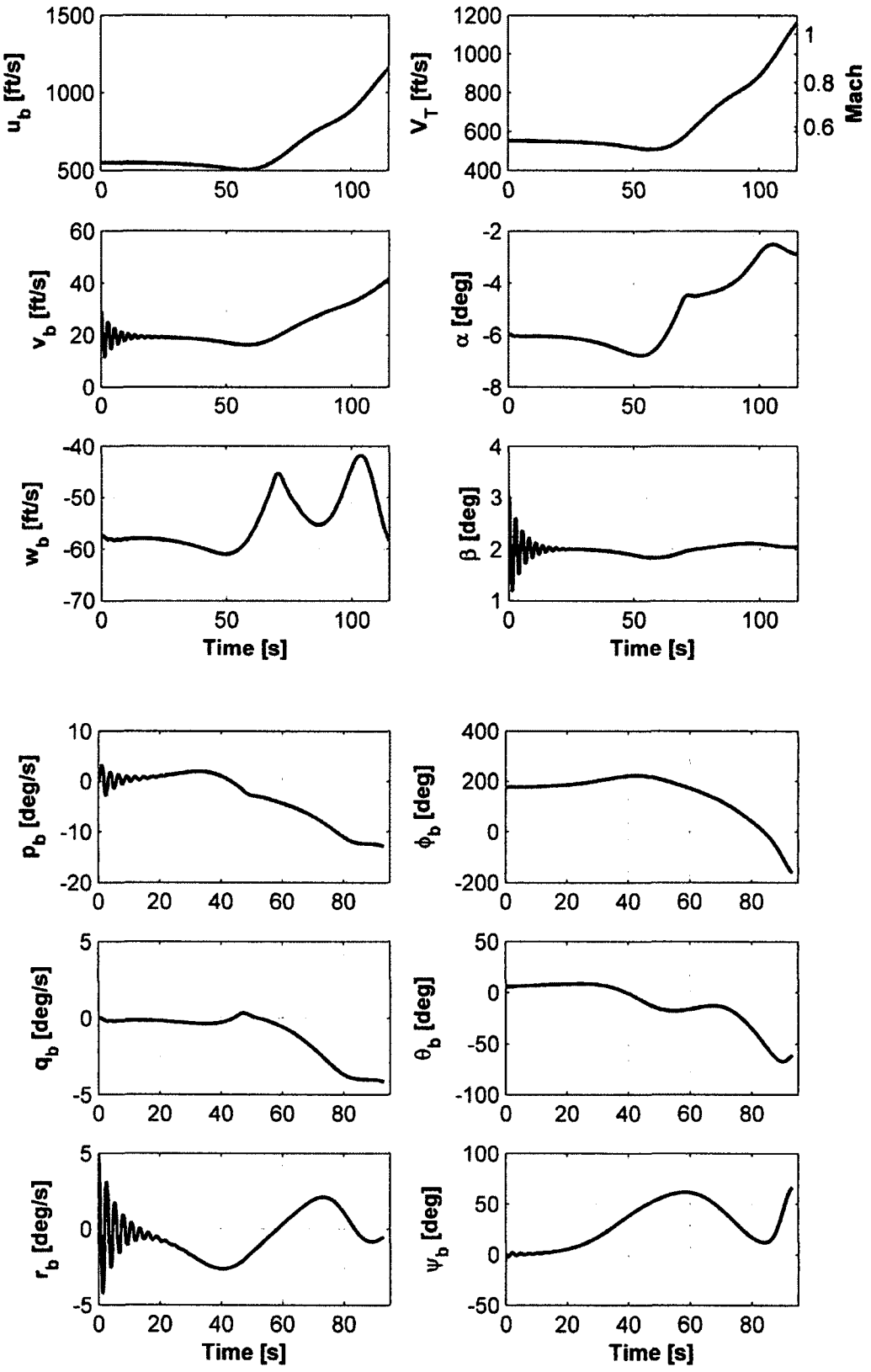

Figure 6.24 Nonlinear response to initial side velocity at pair 1, $\Delta v_{b_0} = 10$ ft/s

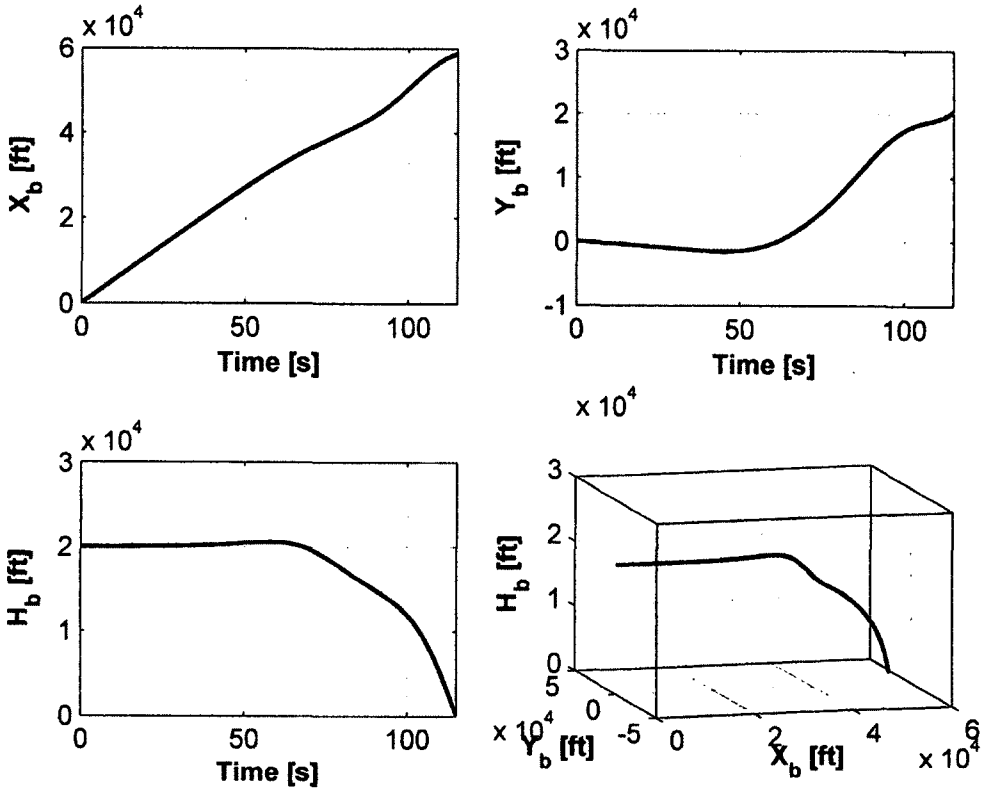

Figure 6.25 Trajectory response to initial side velocity at pair 1, $\Delta v_{b_0} = 10$ ft/s

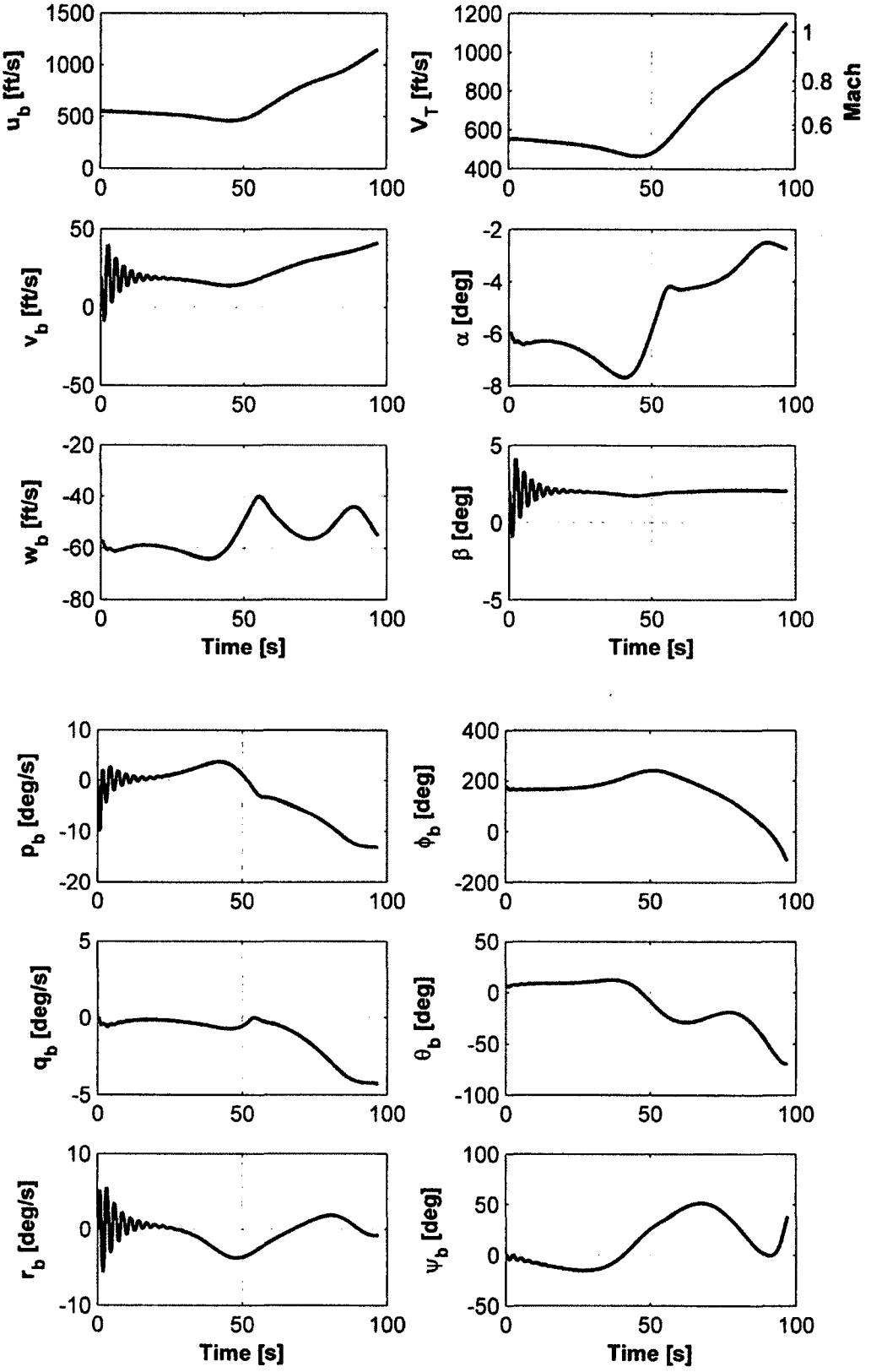

Figure 6.26 Nonlinear response to rudder deflection impulse at pair 1, $\Delta\delta_{r_0} = -5$ deg

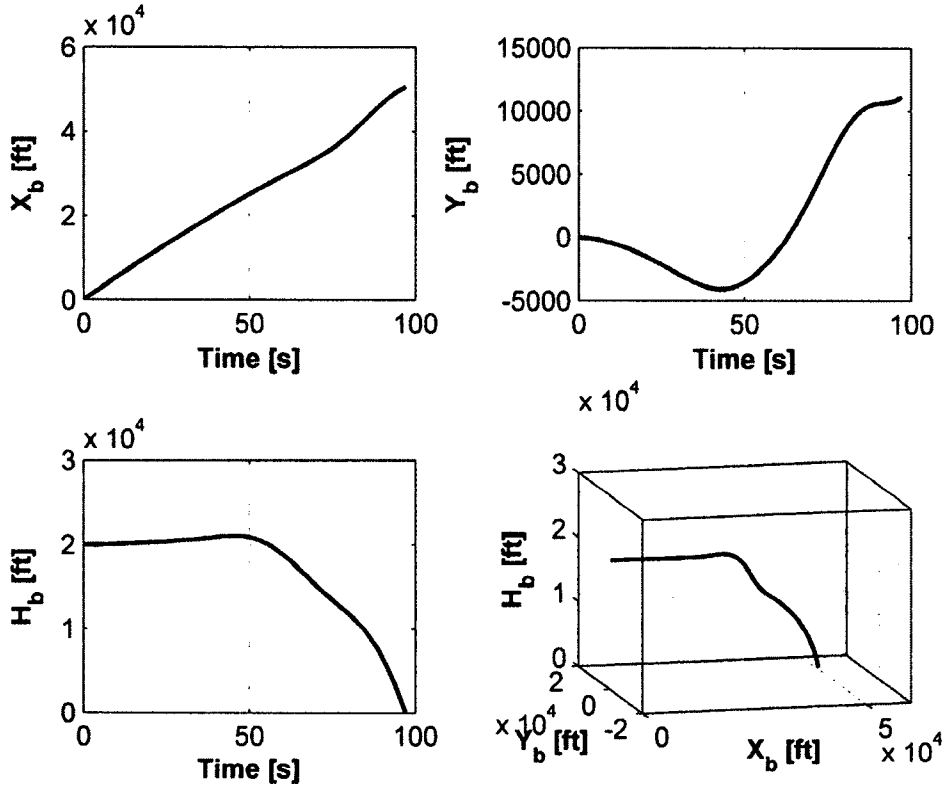

Figure 6.27 Trajectory response to rudder deflection impulse at pair 1, $\Delta\delta_{r_0} = -5$ deg

CHAPTER 7

CONCLUSIONS AND RECOMMENDATIONS

7.1 Conclusions

In this dissertation, a new generalized asymmetric nontraditional angle of attack vs. sideslip angle flight envelope for asymmetric flight conditions has been developed. Some of the results have been published [38],[39]. The asymmetry and offset in the aerodynamic model in Reference [30] has been idealized by data manipulation. A new ideal symmetric aerodynamic model was produced, in which the symmetrization procedure involves step 1 and step 2 averaging steps. This ideal aerodynamic model assists analysis so that fundamental relationships can be more easily observed. Using this model, a new generalized and symmetric angle of attack vs. sideslip angle flight envelope for a symmetric flight conditions has been developed.

Parameterized nonlinearity index theory has also been presented. Four index expressions have been implemented to evaluate the nonlinearity strength embedded in the F-16 nonlinear aircraft dynamics over the new nontraditional angle of attack vs. sideslip angle flight envelope. The concepts of sub-index and matrix-index are introduced. These concepts provided a systematic means to link specific dynamics of the aircraft that contribute towards increasing the overall nonlinearity index.

Application to the angle of attack vs. sideslip angle flight envelope showed that the nonlinearity strength is high at a high-speed flight regime, where the aircraft is near the structural flight boundary. The maximum nonlinearity occurred at negative angles of attack, where the aircraft is at an inverted equilibrium flight orientation. Nonlinearity of

different mathematical descriptions of the aircraft model has been investigated. Body-, stability-, and wind-frame descriptions, when formulated with normalized states, exhibited essentially the same nonlinearity for static and dynamic state indices across a wide range of attack angles. Further, the body-frame description exhibited the least nonlinearity for lower negative angles of attack whereas stability- and wind-frame descriptions dominated the upper region due to static input excitation. Fundamentally, high nonlinearity appears to be caused by vastly different but closely spaced equilibrium points lying within the envelope. Also, these high index values may be exaggerated due to the singular value norm used in the index computation. Additional investigation is required to assess this effect, using structured singular value concepts.

The new angle of attack vs. sideslip angle envelope provides enhanced insight to trimability-controllability regions. The envelope may be useful for parameterized dynamic analysis and for scheduled control design. The new nonlinearity index theory is a promising tool, since it not only quantifies the dynamic's nonlinearity strength but it also identifies the source of that nonlinearity. The index may also detect hidden nonlinear phenomena, such as limit cycles, which ordinary linear analysis fails to detect. Further, the index assesses the suitability of linear analysis.

Linear and nonlinear simulations are carried out on the common angle of attack and sideslip angle pair that exhibited the most nonlinearity over the flight envelope with different frame choices. The linear results correlated well to the index results; the linear model at a high index showed inconsistency with the nonlinear results, in addition to instability and divergent behavior to perturbation. For even moderate perturbations in the state variables or the control input, the nonlinear simulation reveals the tendency of the

aircraft model toward a high body angular rate with increasing speed accompanied by fast altitude loss, all leading into divergent steep spiral mode motion. The simulation showed a significant nonlinear inertial coupling interaction between the longitudinal and lateral dynamics. In other words, the nonlinear simulation results also correlated well to the index results.

7.2 Recommendations

The current research provides a solid base to extend the new generalized nontraditional angle of attack vs. sideslip angle flight envelope for asymmetric flight conditions. A few recommendations could be considered in future work. For example, a third dimension, i.e., altitude, could be added to the envelope; this would provide insightful details on a specific aircraft model. Additional boundaries may be discovered limiting this aircraft model's trimability. Utilizing a simpler aircraft model with an analytically well expressed aerodynamic model may facilitate predicting the asymmetric flight envelope. Further, application of the nonlinearity index theory on the simplified model may provide a clearer picture of nonlinearity sources.

REFERENCES

[1] Filippone, A., *Advanced Aircraft Flight Performance*, Cambridge University Press, New York, New York, 2012.

[2] Raymer, D., *Aircraft Design: A Conceptual Approach*, American Institute of Aeronautics and Astronautics, Reston, Virginia, 2012.

[3] Phillips, W., *Mechanics of Flight*, Wiley, Hoboken, New Jersey, 2010.

[4] Stengel, R., *Flight Dynamics*, Princeton University Press, Princeton, New Jersey, 2004.

[5] Pamadi, B., *Performance, Stability, Dynamics, and Control of Airplanes*, American Institute of Aeronautics and Astronautics, Reston, Virginia, 2004.

[6] Schmidt, L., *Introduction to Aircraft Flight Dynamics*, American Institute of Aeronautics and Astronautics, Reston, Virginia, 1998.

[7] Stengel, R. and Berry, P., "Stability and Control of Maneuvering High-Performance Aircraft," NASA CR-2788, Washington, District of Columbia, April, 1977.

[8] Wu, Y., Wang, X., and Wu, Y., "Dynamic Flight Envelope Estimation for Damaged Asymmetric Aircraft," *RNIS: Research Notes in Information and Service Sciences*, Vol. 12, 2013, pp. 209-214.

[9] Richardson, J., Atkins, E., Kabamba, P., and Girard, A., "Envelopes for Flight Through Stochastic Gusts," *Journal of Guidance, Control, and Dynamics*, Vol. 36, No. 5. September-October, 2013, pp. 1464-1476.

[10] Dale, D., Bolender, M., Torres, S., and Driscoll, J., "Flight Envelope Calculation of a Hypersonic Vehicle Using a First Principles-Derived Model," AIAA-2011-2368, *Proceedings of the AIAA International Space Planes and Hypersonic Systems and Technologies Conference*, San Francisco, California, April, 2011.

[11] Fialho, I., Balas, G., Packard, A., Renfrow, J., and Mullaney, C., "Gain-Scheduled Lateral Control of the F-14 Aircraft During Powered Approach Landing", *Journal of Guidance, Control, and Dynamics*, Vol. 23, No. 3, May-June, 2000, pp. 450-458.

[12] Stilwell, D., "State-Space Interpolation for a Gain-Scheduled Autopilot", *Journal of Guidance, Control, and Dynamics*, Vol. 24, No. 3, May-June, 2001, pp. 460-465.

[13] Kwatny, H., Dongmo, J., Chang, B., Bajpai, G., Yasar, M., and Belcastro, C., "Nonlinear Analysis of Aircraft Loss of Control", *Journal of Guidance, Control, and Dynamics*, Vol. 36, No. 1, January–February, 2013, pp. 149-162.

[14] Engelbrecht, J., Pauck, S., and Peddle, I., "Bifurcation Analysis and Simulation of Stall and Spin Recovery for Large Transport Aircraft," AIAA-2012-4801, *Proceedings of the AIAA Atmospheric Flight Mechanics Conference*, Minneapolis, Minnesota, August, 2012.

[15] Antonini, E., Bedon, G., De Betta, S., Michelini, L., Castelli, M., and Benini, E., "Innovative Discrete-Vortex Model for Dynamic Stall Simulations," *AIAA Journal*, Vol. 53, No. 2, 2015, pp. 479-485.

[16] Mohan, A., Gaitonde, D., and Visbal, M., "Model Reduction and Analysis of Deep Dynamic Stall on a Plunging Airfoil using Dynamic Mode Decomposition," AIAA-2015-1058, *Proceeding of the AIAA Aerospace Science Meeting*, Kissimmee, Florida, January, 2015.

[17] Kokolios, A., Cook, S., and Niewoehner, R., "Use of Piloted Simulation for Evaluation of Abrupt-Wing-Stall Characteristics," *Journal of Aircraft*, Vol. 42, No. 3, May–June, 2005, pp. 641-646.

[18] Zuccher, S. and De Ponte, S., "Post-Stall Motions Evolving Toward Chaos," *Journal of Aircraft*, Vol. 44, No. 3, May–June, 2007, pp. 833-844.

[19] Arena, A. and Nelson, R., "Experimental Investigations on Limit Cycle Wing Rock of Slender Wings," *Journal of Aircraft*, Vol. 31, No. 5, September-October, 1994, pp. 1148-1155.

[20] Ananthkrishnan, N. and Sudhakar, K., "Inertia-Coupled Coordinated Roll Maneuvers of Airplanes," *Journal of Aircraft*, Vol. 32, No. 4, 1995, pp. 883-884.

[21] Ananthkrishnan, N. and Sudhakar, K., "Prevention of Jump in Inertia-Coupled Roll Maneuvers of Aircraft," *Journal of Aircraft*, Vol. 31, No. 4, 1994, pp. 981-983.

[22] Yana, K., Yoshida, H., and Komai, M., "Measurement and Estimation of System Nonlinearity via a Neural Network," *Electronics & Communications in Japan, Part 3: Fundamental Electronic Science*, Vol. 77, No. 2, 1994, pp. 35-44.

[23] Junkins, J. L. and Singla, P., "How Nonlinear Is It?: A Tutorial on Nonlinearity of Orbit and Attitude Dynamics," Journal of the Astronautical Sciences, Vol. 52, No. 1-2, January-June, 2004, pp. 7–60.

[24] Junkins, J. L., Singla, P., Sinclair, A. J., and Hurtado, J. E., "On Coordinate Choices, Regularization, and Degree of Nonlinearity for Dynamical Systems," International Conference on Computational & Experimental Engineering and Sciences, India, December, 2005.

[25] Sinclair, A. J., Hurtado, J. E., and Junkins, J. L., "Nonlinearity Index of the Cayley Form," The Malcolm D. Shuster Astronautics Symposium, Grand Island, New York, June, 2005.

[26] Sinclair, A. J., Hurtado, J. E., and Junkins, J. L., "A Nonlinearity Measure for Estimation Systems," 16th AAS/AIAA Spaceflight Mechanics Meeting, Tampa, Florida, January, 2006.

[27] Omran, A. and Newman, B., "Nonlinearity Index Theory for Aircraft Dynamic Assessment," *Journal of Guidance, Control, and Dynamics*, Vol. 36, No. 1, January-February, 2013, pp. 293–303.

[28] Tapolcai, D., Omran, A., and Newman, B., "Aircraft Stall Phenomenon Analysis Using Nonlinearity Index Theory," AIAA-2012-4403, *Proceedings of the AIAA Atmospheric Flight Mechanics Conference*, Minneapolis, Minnesota, August, 2012.

[29] Tapolcai, D., Omran, A., and Newman, B., "Aircraft Spin Phenomenon Analysis Using Nonlinearity Index Theory," AIAA-2012-4401, *Proceedings of the AIAA Atmospheric Flight Mechanics Conference*, Minneapolis, Minnesota, August, 2012.

[30] Nguyen, L. T., Ogburn, M. E., Gilbert, W. P., Kibler, K. S., Brown, P. W., and Deal, P. L., "Simulator Study of Stall/Post-Stall Characteristics of a Fighter Airplane With Relaxed Longitudinal Static Stability," *NASA-TP-1538*, NASA Langley Research Center, Hampton, Virginia, December 1979.

[31] Abzug, M. J., *Computational Flight Dynamics*, American Institute of Aeronautics and Astronautics, Reston, Virginia, 1998.

[32] Zipfel, P. H., *Modeling and Simulation of Aerospace Vehicle Dynamics*, American Institute of Aeronautics and Astronautics, Reston, Virginia, 2007.

[33] Stevens, B. L. and Lewis, F. L., *Aircraft Control and Simulation*, Wiley, Hoboken, New Jersey, 2003.

[34] Schmidt, D. K., *Modern Flight Dynamics*, McGraw-Hill, New York, New York, 2012.

[35] Bacon, B. and Gregory, I., "General Equations of Motion for a Damaged Asymmetric Aircraft," AIAA-2007-6306, *Proceedings of the AIAA Atmospheric Flight Mechanics Conference*, Hilton Head, South Carolina, August, 2007.

[36] Khalil, H. K., *Nonlinear Systems*, Prentice Hall, Upper Saddle River, New Jersey, 2002.

[37] Marcos, A. and Balas, G. J., "Development of Linear-Parameter-Varying Models for Aircraft," *Journal of Guidance, Control, and Dynamics* Vol. 27, No. 2, March-April, 2004, pp. 218–228.

[38] Abdallah, A., Newman, B., and Omran, A., "Measuring Aircraft Nonlinearity Across Aerodynamic Attitude Flight Envelope," AIAA-2013-4985, *Proceedings of the AIAA Atmospheric Flight Mechanics Conference*, Boston, Massachusetts, August, 2013.

[39] Abdallah, A., Newman, B., and Omran, A., "Measuring Aircraft Nonlinearity Across Aerodynamic Attitude Flight Envelope- Revisited With Symmetrized Aerodynamics," AIAA-2014-2193, *Proceedings of the AIAA Atmospheric Flight Mechanics Conference*, Atlanta, Georgia, June, 2014.

VITA

Ayman Muhammad Abdul-Sattar Khalil Abdallah

Education

Doctor of Philosophy, Aerospace Engineering
Old Dominion University, Norfolk, Virginia, USA, 2015
- Major: Flight dynamics and Control (Performance and Nonlinearity Enhancement)
- Dissertation: Flight Dynamics Nonlinearity Assessment Across A New Aerodynamic Attitude Flight Envelope

Master of Science, Aerospace Engineering
King Fahd University of Petroleum & Minerals, Dhahran, KSA, 2007
- Major: Flight dynamics and Control (Performance Enhancement)
- Dissertation: On Rocket Performance, Stability and Control

Bachelor of Science, Aerospace Engineering
King Fahd University of Petroleum & Minerals, Dhahran, KSA, 2002

Publications

- "*Experimental and Numerical Investigation of 65-deg Delta and 65/40-deg Double-Delta Wings*," 44th AIAA Aerospace Sciences Meeting and Exhibit, Reno, Nevada, January 2006.
- "*Aerodynamic-Shape Optimization of Supersonic-Missiles Using Monte-Carlo*," International Review of Aerospace Engineering. February 2008.
- "*Measuring Aircraft Nonlinearity Across Aerodynamic Attitude Flight Envelope*," AIAA Atmospheric Flight Mechanics (AFM) Conference, Boston, Massachusetts, August 2013.[38]
- "*Measuring Aircraft Nonlinearity Across Aerodynamic Attitude Flight Envelope Revisited With Symmetrized Aerodynamics*," AIAA Aviation and Aeronautics Forum and Exposition, Atlanta, Georgia, June 2014.[39]

Experience

Graduate Assistant, *King Fahd University of Petroleum & Minerals*, Dhahran, KSA, 2002 to 2008.
- Co-assisting Aerospace Engineering professors in many ways in teaching, research and administrative work.
- Teaching Aerospace Engineering Laboratory courses.
- Exposing students to practical applications of Aerospace Engineering by visiting industry and showing real applications of what they study.

Trainee Engineer, Arabian-American Oil Company (ARAMCO) - Aviation Department, Dammam, KSA, 2001.
- Trainee Engineer in hangar maintenance, line maintenance and Engineering unit.
- Worked on Dash-8, Twin-Otter and Boeing 737-200/700 airplanes.